

ISTITUTO UNIVERSITARIO DI
STUDI SUPERIORI DI PAVIA



Dipartimento di Ingegneria Civile ed Architettura

**Selective Laser Melting process
simulation:
advancements towards a
cost-effective model**

A Thesis submitted in Fulfilment of the Requirements for the
Degree of Doctor in Philosophy in

Computational Mechanics and Advanced Materials
at Istituto Universitario degli Studi Superiori di Pavia, Italy

Supervisor: Professor
Ferdinando Auricchio

Author:
Isabella Sani

Academic year 2015/2016
XXIX PhD Course

A mio nonno Alberto

*"Intelligence is the ability to adapt to change."
Stephen Hawking, A Briefer History of Time*

Acknowledgments

A new experience is always so positive and we discover at the end that we have changed so much personally. The period of three years here in Pavia was a great opportunity for me to change, to grow up, and to expand my experiences. This was possible thanks to the presence of professors, colleagues and friends that I met during my way.

First, I would thank Prof. Ferdinando Auricchio and Prof. Alessandro Reali for giving me the opportunity to take part of the research group of Computational Mechanics of University of Pavia and especially my Supervisor for his great guidance and forward-looking advices.

I would really thank Prof. Elio Sacco to give me the occasion of beginning this new experience with enthusiasm and curiosity, and for his special support and confidence shown in me.

I would really thank Prof. Ernst Rank and Prof. Stefan Kollmannsberger to give me the opportunity to spend a period as visiting PhD student at Technische Universität München (TUM) and to collaborate with such expert and skilled research group, as the CiE group. I would give special gratitude to Stefan, for his precious advices and support, and for his contagious enthusiasm for research.

This period in Pavia would not be the same without my colleagues. passed and current, for their friendship and presence: Simone, Michele, Paolo, Tuong, Alice, Alberto C., Anna, Sonia, Giulia, Elisa, Massimo, Alberto S., Lorenzo, Margherita, Giorgione, Stefania, Gianluca. Really thanks to Chiara for the countless confidences and conversations, to Mauro and Giuseppe for the precious suggestions and help.

I would thank my 'German' friends, Davide, Nastia and Alex, to make my period in Munich memorable and make me feel like at home.

A special thank to my friends of TTF group, Marco, Elena, Rodrigo, Valentina and Andrea, for the kind moments and laughs, the special dinners which improve my culinary and writing skills. Special thanks to Andrea, who was a good lab-mate and present confidant, despite the noisy small trumpet.

I would thank my flatmate and friend Veronica to offer me a warm cup of tea against the cold and foggy weather and to be always present for a chat.

I am very thankful to my parents, a reference point and an example, my sister Ilaria and my brother Lorenzo, for their deep encouragement and support.

Last but not least, I really thank Eric for his patience, positivity and love.

Abstract

In the last decades, Additive Manufacturing (AM) has received an outstanding interest as an additive production technology for producing parts layer-by-layer. The potential on AM technologies is related to the high degree of design and shape freedom with a significant reduction of waste material. Among AM technologies, Selective Laser Melting (SLM) is a valid alternative to the conventional manufacturing, particularly used to produce complex metal components for a large number of application fields. In SLM technology, the part is constructed layer-by-layer using a moving laser beam which hits the powder material and binds together the powder particles; when the laser moves away the part starts cooling and a new powder layer is placed upon the others. SLM technology is able to produce metal and ceramics components with high density ($>99\%$) without the need of post-processing.

The continuous ambition from industries on producing complex and competitive parts with SLM technology leads to the necessity of a standardization of process parameters and conditions, i.e. laser power, scanning strategy, thickness of the layer, etc. Indeed, SLM is a complex process which involves a large number of physical phenomena: heat conduction, phase transformation, fluid flow, 'balling' effect, evaporation, oxidation, etc. which are highly influenced by the choice of input parameters. Furthermore, the high energy input of laser beam produces high temperature gradients, with consequent formation of residual stresses, which can cause undesired deformations, cracking of the part and delamination.

In such scenario, the role of computational modelling becomes essential to provide better understanding of SLM process and to identify the optimal process parameters. SLM modelling is still an ongoing challenge, due to the multitude of time and spatial scales involved in the process, the high level of nonlinearity due to the phase transformation and large-scale domains.

Finite Element Analysis (FEA) is a reliable and efficient numerical technique widely employed to simulate physical problems. Commercial software, like Abaqus, use finite element method to predict the macroscopic behaviour of parts and are recently used to simulate SLM process. Anyway the SLM modelling lacks of an efficient computational tool: the high computational costs are against the definition of an efficient and accurate simulation model of the process.

A possibility to decrease the computational burden can come from Model Order Reduction (MOR) techniques, which permit to reduce large-scale problems with a good level of accuracy. Such techniques can be used in combination of Dynamic Substructuring (DS) to divide the large domain in individual components which are computed separately and then combined with the rest of the model.

The present thesis aims to develop an advanced FE three-dimensional numerical model of SLM process which would be, at the same time, efficient from a computational point

of view. Numerical simulations of thermal and mechanical behaviour of SLM parts are developed in the software Abaqus and possible enhancements of speeding-up the process are presented. In particular the definition of a simplified heat input to simulate the moving laser beam and its effect on computational burden are presented. Furthermore, the use of a set of Lanczos vectors and their derivatives constitute a suitable basis to reduce large-scale linear and nonlinear heat conduction problems. Numerical examples are developed to show the accuracy of using such projection basis to reduce linear and non-linear heat conduction problems.

A first application of this suitable basis with dynamic substructuring to reduce large-scale SLM simulation models is developed for the linear case. The reduction procedure is integrated within the software Abaqus by the definition of an in-house user subroutine written in Fortran which is able to reduce directly the global matrices.

Sommario

Negli ultimi anni, la stampa 3D, o 'Additive Manufacturing' (AM), ha ottenuto un notevole interesse come tecnologia additiva per la produzione di oggetti stampati strato dopo strato. Il successo delle tecnologie a stampa 3D è dovuto principalmente alla grande libertà di produrre oggetti di varia forma e dimensione, con una notevole riduzione di material di scarto. Tra le diverse tecnologie di stampa 3D, Selective Laser Melting (SLM) rappresenta una valida alternativa alle tecnologie convenzionali, specialmente per la produzione di complessi componenti metallici destinati a diversi campi di applicazione. Nel processo SLM il componente viene stampato strato dopo strato utilizzando un fascio laser che investe la superficie e fonde insieme le singole particelle di polvere; quando il fascio laser si allontana la parte fusa inizia a raffreddarsi ed un nuovo strato di polvere viene posizionato sugli strati sottostanti. Tramite la tecnologia SLM è possibile produrre componenti di materiale metallico e ceramico con una elevata densità (vicina al 99 %) senza la necessità di utilizzare processi aggiuntivi.

La continua tendenza da parte di aziende e imprese di produrre sempre più complessi e competitivi componenti tramite la tecnologia SLM conduce alla necessità di ottenere una standardizzazione del processo di stampa ed, in particolare, dei parametri di ingresso, come la potenza del laser, la strategia di stampa, lo spessore dello strato, ecc. Questo perchè la tecnologia SLM è una tecnica complessa che comprende una moltitudine di fenomeni fisici, quali conduzione del calore, trasformazione di fase, moti dei fluidi, effetto 'balling', evaporazione, ossidazione, che sono fortemente influenzati dalla scelta delle tecniche di stampa. Inoltre, alti valori di intensità del laser producono, all'interno del prodotto stampato, elevati gradienti di temperatura e formazione di tensioni residue che possono condurre a indesiderati effetti deformativi, rottura del pezzo e delaminazione. In questo contesto, gli strumenti di modellazione computazionale sono essenziali per fornire una più profonda conoscenza del processo di stampa e per identificare la scelta dei parametri 'ottimali'. La modellazione del processo di stampa SLM risulta uno stimolante oggetto di ricerca, specialmente per gli aspetti complessi che riguardano il processo, come le diverse scale temporali e spaziali che caratterizzano il fenomeno e la non linearità del problema dovuta al cambiamento di fase.

Tecniche numeriche basate su analisi agli elementi finiti (FEA) rappresentano uno strumento affidabile ed efficiente per la simulazione di diversi processi fisici. In particolare, software commerciali agli elementi finiti, come Abaqus, permettono di modellare con accuratezza gli aspetti fisici del processo e di prevedere il comportamento macroscopico termico e meccanico del componente durante la sua costruzione. Una simulazione numerica accurata del processo risulta di contro onerosa e poco efficiente dal punto di vista dei costi computazionali.

Una possibile soluzione agli elevati costi computazionali proviene dalla formulazione di tecniche di riduzione del modello (MOR) che permettono di ridurre il numero di gradi di

libertà del sistema. Tali tecniche di riduzione possono essere utilizzate in combinazione con la definizione di sottostrutture (DS) che permettono di decomporre il modello in parti distinte, di risolverle separatamente ed in seguito di assemblarle.

La presente tesi si pone come obiettivo quello di definire un modello tridimensionale agli elementi finiti che simuli il processo di stampa SLM e che sia, allo stesso tempo, efficiente dal punto di vista computazionale. Le simulazioni numeriche mirano alla previsione del comportamento termico e meccanico, e possibili avanzamenti nella riduzione dei costi computazionali verranno inoltre presentati. In particolare la definizione di un modello semplificativo del laser e il suo effetto in termini di riduzione dei costi computazionali verranno presentati. Inoltre, l'utilizzo di metodi di riduzione basati su particolari vettori (Lanczos vectors) e delle loro derivate costituiscono una buona base per ridurre problemi di conduzione del calore per casi lineari e non lineari. Diversi esempi numerici saranno presentati al fine di dimostrare che la scelta di tale base conduce a risultati accurati.

Tale tecnica di riduzione sarà inoltre applicata al modello termico agli elementi finiti tramite la definizione di sottostrutture lineari. Il metodo di riduzione verrà integrato all'interno del software tramite la definizione di una subroutine in grado di ridurre direttamente le matrici assemblate del sistema.

Contents

List of Tables	IX
List of Figures	XIV
1 Introduction	1
1.1 Additive Manufacturing technologies and materials	2
1.1.1 Selective Laser Sintering/Selective Laser Melting	4
1.2 Selective Laser Melting modelling	5
1.3 Aim of the thesis	8
1.4 Organization of the dissertation	9
2 SLM technology	11
2.1 Physical Phenomena	11
2.2 Residual stresses	15
2.3 Process parameters	17
2.3.1 Melt pool: stability analysis	18
2.3.2 Temperature gradients, deformation, and residual stress	21
2.3.3 Porosity and microstructure	28
2.3.4 Mechanical properties	31
2.4 Summary	35
3 SLM modelling	37
3.1 A description of physical models	37
3.1.1 Heat conduction models	39
3.1.2 Fluid flow models	43
3.2 Phase change models	44
3.2.1 Physical phenomena during phase change	44
3.2.2 Front tracking models: the Stefan problem	45
3.2.3 Numerical methods	47
3.2.4 Front-tracking methods	49
3.2.5 Fixed domain methods	50
3.3 Residual stresses: theoretical models	54
3.3.1 Shrinkage	60
3.4 Material properties	62
3.4.1 Thermo-physical properties	63
3.4.2 Thermo-mechanical properties	70
3.5 Summary	71

4	Finite Element simulation of SLM process	72
4.1	State of art	73
4.2	Problem definition	74
4.3	Finite Element formulation	76
4.4	Numerical examples	78
4.4.1	Effect of material model selection	79
4.4.2	Comparison with analytical model	79
4.4.3	Titanium alloy: Ti-6Al-4V	86
4.4.4	Melt pool analysis	87
4.4.5	Thermo-mechanical analysis	90
4.4.6	Results and discussions	94
4.4.7	Computational times and limitations	102
4.5	Improvements of numerical model	105
4.5.1	Simplified source model	105
4.6	Summary	108
5	Substructuring and model order reduction technique	110
5.1	Linear transient problems	111
5.1.1	Eigenmodes and linear modal truncation	112
5.1.2	Craig-Bampton Method	112
5.1.3	Rayleigh-Ritz Approximation	115
5.1.4	Lanczos vectors	115
5.1.5	Convergence criterion and loss of orthogonality	118
5.1.6	Lanczos vectors as reduced basis	119
5.2	Nonlinear Transient problems	119
5.2.1	Modal derivatives	120
5.2.2	Derivatives of Lanczos vectors	121
5.2.3	Derivatives of Lanczos vectors as reduced basis	123
5.2.4	Numerical example using Matlab	123
5.2.5	Summary	127
6	A new user subroutine implementation for model order reduction in Abaqus	129
6.1	Substructuring applied to SLM	129
6.2	Model order reduction subroutine	131
6.2.1	Application examples	134
7	Final remarks	139
7.1	Future developments	140
	Appendices	142
A	User subroutines for FE thermal model of SLM process	143
A.1	User subroutines	143

B	Compressed Row Storage format for sparse matrices	149
C	New user subroutine for	
	nonlinear model order reduction in Abaqus	150
C.1	Input file	150
C.2	User subroutines	152
	Bibliography	171

List of Tables

2.1	Mechanical properties of SLM and reference material.	32
2.2	Tensile properties of SLM built parts using different laser scanning speeds [118].	35
2.3	Mechanical properties of SLM built parts at different building directions [63].	35
2.4	Mechanical properties of SLM built Ti6Al-7Ng alloy at different building directions [28].	35
3.1	Main advantages and disadvantages of front tracking and fixed domain methods	49
3.2	Values of thermal conductivity of powder beds measured at room temperature in air atmosphere [107].	66
3.3	Relative densities, coordination number and normalised contact conductivity for diamond, SC, BCC and FC unit cell, [51].	67
4.1	Input parameters used in analytical solution and numerical model [41] .	83
4.2	Thermal properties of Ti-6Al-4V alloy [106].	86
4.3	Specific heat of Ti-6Al-4V alloy [90].	86
4.4	Thermal conductivity and density of solid Ti-6Al-4V alloy [90].	87
4.5	Thermal conductivity and density of powder Ti-6Al-4V alloy [46].	87
4.6	Laser beam parameters [46].	88
4.7	Laser beam parameters [106]	91
4.8	Thermal properties of AISI 1015 [106].	91
4.9	Thermal conductivity and density of AISI 1015 [106].	92
4.10	Specific heat of AISI 1015 [106].	92
4.11	Mechanical properties of Ti64 [106].	93
4.12	Mechanical properties of AISI 1015 [106].	93
4.13	Computational times of three-dimensional SLM simulation.	104
4.14	Comparison of computational times between the three-dimensional models with the old and new meshes.	106
5.1	Linear case: Input parameters for 2D bar [60].	124
6.1	Comparison between computation times before and after linear substructuring.	131
6.2	Nonlinear case: Input parameters for 2D square.	138
6.3	Comparison between the solutions obtained with the full model and with the reduced model by the reduction tool in Fig. 6.4.	138

List of Figures

1.1	Additive manufacturing (AM) process chain [47].	1
1.2	Research publications on SLM from 1999 to 2014. [142].	2
1.3	Typical configuration of a SLS/SLM machine. <i>Source: www.popular3dprinters.com.</i>	4
1.4	Medical products processed by SLM. (a) <i>Source: concept-laser.de.</i> (b) <i>Source: layerwise.com</i>	6
1.5	The injection moulding tools manufactured by SLM [103].	6
1.6	Aerospace (a) and automotive (b) products processed by SLM. <i>Source: concept-laser.de</i>	6
1.7	Research publications on SLM of metals, ceramics, and composite materials and between different metallic materials. Data are based on research publications on SLM, LaserCusing, and DMLS indexed by Web of Science and ScienceDirect [142].	7
1.8	Challenges of SLM modelling.	7
2.1	Physical phenomena during selective laser melting.	12
2.2	Schematic representation of heat transfer [147].	12
2.3	Main process defects [146].	13
2.4	Schematic presentation of Marangoni convection in a melt due to the presence of a surface tension gradient $d\gamma_{LV}/dT$ [108].	13
2.5	Schematic representation of wetting of liquid on substrate.	14
2.6	Schematic model of layer removal method [115].	16
2.7	Schematic description of Crack Compliance Method (CCM)[88].	17
2.8	Schematic model of Bridge Curvature Method (BCM) [72].	17
2.9	Typical cross-section of a laser sintered track from metal powder on steel substrate [141].	19
2.10	Influence of scanning speed to remelted depth and width of melt pool from SS grade 904L(-16 μm) for different values of laser power $P = 25$ W and $P = 50$ W [141].	20
2.11	Effect of laser scanning and laser power on scanning condition of stainless steel 316L [77].	21
2.12	Comparison between experiments (a-b) and calculations (c-d) at various scanning velocities [52].	22
2.13	Different types of tracks from tests with -150/+75 μm M2 steel powder in an argon atmosphere with 1.1 mm laser beam diameter, [27].	23
2.14	M2, H13, and 314S-HC process map examples, for different powder size ranges and laser beam diameters, [27].	24
2.15	Different temperatures through different scan vector length [71].	25
2.16	Different scanning strategies [71].	25

2.17	The average curvature along (a)X-direction and (b)Y-direction for different scanning strategies [71].	25
2.18	Different scanning strategies [88].	26
2.19	Measured stress distributions of stainless steel 316L samples for: (a) different exposure strategies (Fig 2.18), (b) different sector exposure orders [88].	27
2.20	Principle of BCM method for identifying the residual stresses in the test parts [73].	28
2.21	Influence of scan vectors length on curling of Ti-6Al-4V test parts; REF.: reference part, [73].	28
2.22	Influence of scan vectors orientation on curling of Ti-6Al-4V test parts; [73].	29
2.23	Influence of island size and orientation on curling of steel parts; [73].	29
2.24	Residual stresses on stainless steel 316L sample with: (a) random sector scanning exposure, (b) Y-direction scanning exposure, [88].	29
2.25	Results of post-scanning and pre-scanning with different scan speeds [73].	30
2.26	Temperature cycle for heat treatment [73].	30
2.27	Balling increases with higher scanning speed [4].	31
2.28	Microstructures of etched samples: (a) adjacent melt pool, (b) vicinity of a keyhole pore and (c) keyhole pore enclosing non-molten powders [4].	31
2.29	Effect of scan speed on the relative density for AISI 316L stainless steel, [72].	32
2.30	Influence of scanning strategy on relative density of Ti6Al4V material, [72].	32
2.31	Stress-strain curves for SLM material and reference material.	33
2.32	(a) Monotonic stress-strain curves for 316L processed by 1000 W (solid lines) and by 400 W (dashed lines), the inset shows the initial response of both conditions upon loading, with significant differences of Young's moduli [93]; (b) Typical stress-strain curves of parts processed at different laser scan speeds[148].	34
2.33	(a) Typical stress-strain curves of SLM-processed iron specimens at the laser power of 100 W using different scanning speeds [118]; (b) Stress-strain curves for parts produced with different directions [63].	34
3.1	SLM process principle [46].	38
3.2	Heat conduction problem formulation.	39
3.3	Transverse electromagnetic modes of Gaussian profile [106].	40
3.4	Gaussian heat distribution for $C = 2/R^2$	41
3.5	Irradiance profile for Gaussian TEM ₀₀ mode [106].	41
3.6	Intensity distribution of the tailored TEM _{mixed} mode laser heat sources, [124].	43
3.7	Typical enthalpy versus temperature relations: (a) isothermal phase change and non-isothermal phase change.	45
3.8	Possible solid-liquid interfaces: planar, columnar and dendritic [10].	45
3.9	Stefan model for a single phase.	46
3.10	Numerical techniques: a) front tracking method; b) fixed domain method	48
3.11	Dependence of specific heat to temperature for equivalent heat capacity model.	52

3.12	Dependence of enthalpy on temperature for phase change occurring over a range of temperature.	53
3.13	Schematic description of the formation of residual stresses during TGM [73].	55
3.14	Simplified representation of stress-strain curves during TGM [73]. . . .	55
3.15	Simplified theoretical model of SLM process [88].	56
3.16	Residual stress within the SLM part and the base plate (simplified model) [73].	57
3.17	Residual stress before and after removing the SLM part from the base plate, [73].	57
3.18	Influence of number of layers on residual stress profile in SLM part before and after base removal [88].	58
3.19	Influence of base plate height on residual stress profile in SLM part before and after base removal [88].	59
3.20	Influence of materials yield strength on residual stress profile in SLM part before and after base removal [88].	59
3.21	Effect of process parameters on shrinkage, Wang et al. [129].	61
3.22	Variation of shrinkage with scan length, [94].	62
3.23	Schematic model of volume shrinkage [85].	62
3.24	Typical pattern powder-liquid-solid of thermal conductivity versus temperature.	64
3.25	Cubic unit cell: simple cubic (SC), body centered cubic (BCC), and face centered cubic (FCC), [21].	65
3.26	Radiative thermal conductivity as a function of the temperature T and the extinction coefficient β , [107].	66
3.27	Two solid powder particles sintering zone.	67
3.28	Effect of increase of thermal conductivity on temperature profile [107]. .	67
3.29	Absorptance profile of Ni-alloy I metal powder during laser processing (laser wavelength of $\lambda = 1.06\mu m$), [122].	69
3.30	Temperature profile on an iron powder bed for different values of laser absorptance α and laser power P , [107].	69
3.31	Dependence of specific heat to temperature for equivalent heat capacity model.	70
3.32	Variation of Young's modulus with temperature for Ti-6Al-4V material, [106].	70
4.1	Temperature distribution $T(x,t)$ for 2D problem.	72
4.2	Flow chart of numerical model in Abaqus	75
4.3	Flow chart of user subroutine USDFLD and UMATHT called for i -th Gauss point ($i = 1, \dots, N_g$) at a specific time increment t	77
4.4	Temperature distribution of a single scanning track over a Ti64 layer with an elliptical heat source: powder-liquid-powder ('p-l-p'); solid-liquid-solid ('s-l-s'); powder-liquid-solid ('p-l-s' case).	80
4.5	Time derivative of temperature at the center point of the scan path: powder-liquid-powder ('p-l-p'); solid-liquid-solid ('s-l-s'); powder-liquid-solid ('p-l-s' case).	81
4.6	Double ellipsoidal heat source, [41].	81
4.7	Dimensions of infinite layer (mm).	82

4.8	Mesh size used in numerical model (mm).	82
4.9	Ellipsoidal heat source: temperature distribution.	84
4.10	Elliptical heat source: temperature distribution.	85
4.11	Geometry of melt pool analysis. a) Dimensions of geometry (mm); b) Scanning path along layer i (with $i=1,2,3$) with middle point $P_i = (x_P, y_{P_i}, z_P)$.	88
4.12	FE mesh of multiple layers.	88
4.13	Temperature field (K) and melt pool (gray region) in Layer 1, 2, 3.	89
4.14	Half melt pool in the first layer; dimensions: depth (D), width (W/2), and length (L/2).	89
4.15	Temperature field (Kelvin) along the depth, width and scanning direction.	90
4.16	Dimensions of Ti64 layer on steel base plate (mm).	90
4.17	Scanning strategy of laser beam	91
4.18	FE Mesh size of Example 2.	92
4.19	Boundary condition in the base plate for stress analysis.	92
4.20	Temperature distribution (K) of the layer for different time steps.	94
4.21	Temperature profiles along the first scan track for different time steps.	95
4.22	Temperature history of point P ($x=1.5$ mm, $z=1.5$ mm).	95
4.23	Solution and material properties at 3.675 ms: (a) Temperature solution (K); (b) Temperature dependent thermal conductivity (W/(m K)); (c) Solidified material (red part).	96
4.24	Longitudinal transient stresses σ_{xx} (MPa) for different time steps.	96
4.25	Transverse transient stresses σ_{zz} (MPa) for different time steps.	97
4.26	Temperature profile along depth at 3.675 ms.	97
4.27	Residual stresses profile at 600 s: (a) longitudinal stresses (b) transverse stresses.	98
4.28	Residual stresses profile along path OF: (a) longitudinal stresses; (b) transverse stresses.	99
4.29	(b) Longitudinal residual stresses (σ_{xx}) along depth (black line); (c) Longitudinal residual stresses along depth obtained by Roberts [106].	100
4.30	Displacement (magnitude) of base plate at 8 ms (deformation scale factor: 150).	101
4.31	Displacement (magnitude) of base plate at 600 s (deformation scale factor: 150).	101
4.32	View of base plate and cross sections.	101
4.33	Vertical displacement (mm) of base plate along cross sections A-A' and B-B' at 8 ms.	102
4.34	Vertical displacement (mm) of base plate along cross sections A-A' and B-B' at 600 s.	103
4.35	New mesh for the thermal problem.	105
4.36	Temperature profile on the powder layer at 4 ms.	105
4.37	Temperature distributions at different time steps along the first scanning track.	106
4.38	Temperature solution imposed as boundary condition on the powder layer.	107
4.39	Residual stresses profile along path OF: (a) longitudinal stresses; (b) transverse stresses. <i>Simplified heat source</i> : model with imposed temperature solution; <i>Reference solution</i> : model with Gaussian moving heat flux.	108

5.1	Representation of substructuring for a FE model [3]	110
5.2	Thermal system composed by one substructure	113
5.3	Component modes for CBM [2].	114
5.4	2D bar exposed to a time dependent heat flux.	124
5.5	Nonlinear case: Input parameters for 2D bar.	124
5.6	Linear case: Temperature distribution and heat flux along the 2D bar for three different time steps: 5, 10, 40 s.	125
5.7	Nonlinear case: Temperature distribution and heat flux along the 2D bar for t=10 s.	126
5.8	Nonlinear case: (a) Eigenmodes, (b) Lanczos vectors	126
5.9	Nonlinear case: Lanczos vectors derivatives	127
5.10	Root mean square (RMS) error of temperature solution for: Eigenmodes solution, Lanczos vectors solution and Lanczos vectors (3)+ Lanczos derivatives (<i>Reference solution: full system</i>).	127
6.1	Substructuring of thermal model in Abaqus.	130
6.2	Generation of substructuring using User Element (UEL).	131
6.3	Sparsity pattern of stiffness and capacity matrices of the system before and after projection.	132
6.4	Algorithm to reduce the nonlinear matrices in Abaqus.	135
6.5	2D square exposed to a time dependent heat flux.	136
6.6	Linear case: temperature field (°C).	136
6.7	Nonlinear case: temperature field (°C).	137
7.1	Future developments: sequentially substructuring.	141

Chapter 1

Introduction to the thesis

Additive Manufacturing (AM) is a layer-based automated fabrication process started in 1980s for making three-dimensional physical objects by adding material in layers. A schematic representation of the process steps is depicted in Fig. 1.1. First, the 3D CAD data is converted to STL file to slice the virtual model; a set of contoured virtual slices is obtained. Each layer is a thin cross-section of the part derived from the original CAD data so increasing the thickness of the layer, the final part will be closer to the original. The STL file is then transferred to the AM machine where the part is built after setting some process parameters. Once the part is built, it is removed from the machine and then it is exposed to post-process treatments, such as cleaning or removing supporting features.

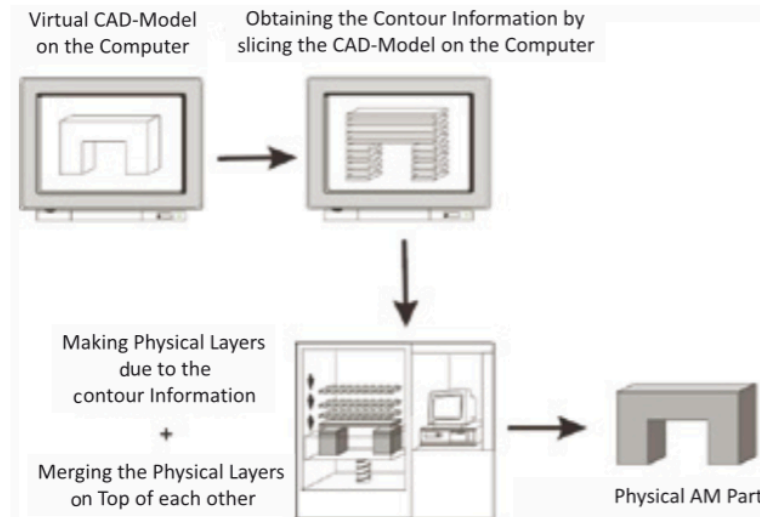


Figure 1.1: Additive manufacturing (AM) process chain [47].

In the last few decades AM is becoming a powerful technology for its innovative and non-conventional manufacturing processes, widely developed in industries for automotive, aerospace and medical applications. The interest in AM is especially due to its shape and design freedom, e.g. producing complex internal channels or complicated lattice structures, adaptivity to customer's demand, reducing the large stock of manufactured parts, healthcare products customized, and reduction of waste material with an optimization of the final shape. The common will from industries of producing efficient and competitive products maintaining low costs and high speed

is in contrast with the high level of complexity. Indeed the variability of process parameters, enviromental conditions, number of processed materials, etc. do not allow a full standardization of AM processes. The interest of AM from academic community is also increasing: in the last decade the number of scientific papers per year about Selective Laser Melting (SLM) intensified a lot; in 2014 the number of publications are more than ten times the number observed in 2004 (Fig. 1.2). The research activities around experimental and material tests and numerical simulations try to face the several challenges and drawbacks that involved AM. For example, the lack of process credibility and design rules, the generation of a large number of measurements, the missing of efficient computational tools, the low part quality and productivity, size limitations and imperfections, etc. The entry level cost of 3D printers is still too high, it can go from 5000\$ to 50000 \$, not including the cost of accessories and materials [112]. In

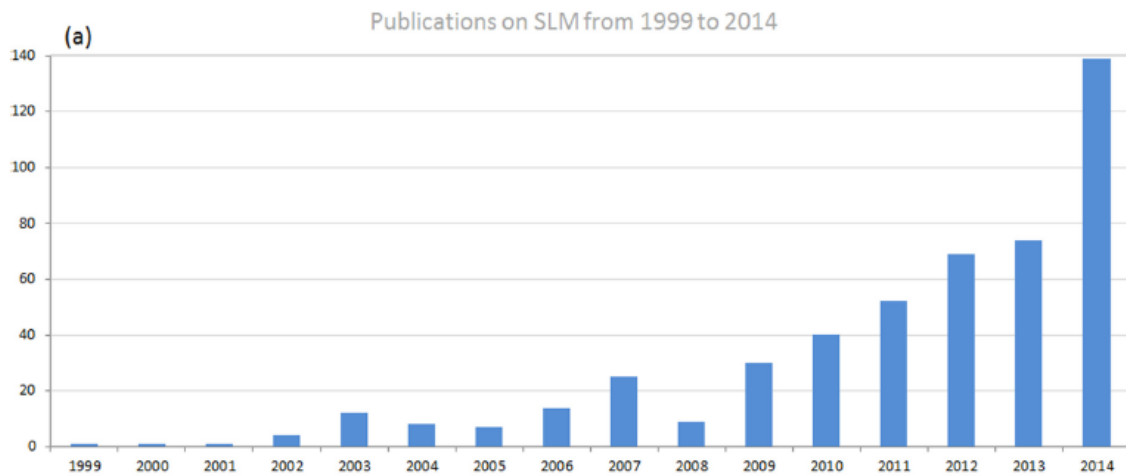


Figure 1.2: Research publications on SLM from 1999 to 2014. [142].

such scenario the role of the scientific research is giving a fundamental contribution to overcome these limitations and to develop a competitive alternative to the conventional manufacturing processes, with a substantial positive impact in terms of costs, like reduction of material waste, and time.

1.1 Additive Manufacturing technologies and materials

Today, there are considerably more than 100 different AM machines following the process chain in Fig. 1.1 which essentially differ from each others in the way the layers are made and merged together. The most common used ways to bind the layers together are [47]:

- lasers with galvo-type scanning devices, optical switches, or gantry-type handling systems;
- electron beams;
- single- or multi-nozzle print heads;

- knives, extruders, or infrared heaters with plotters or DLP projectors.

For the classification of AM technologies we follow the procedure taken by Gibson et al. [48], which subdivides the systems in liquid polymer, discrete particles, molten material, and laminated sheets. In the following we summarize some of the most common AM technologies belonging to these four categories:

- *Liquid Polymer System.* In liquid polymer systems the parts are built from a (photo)-polymerization of a photosensitive liquid or resin which solidifies at the exposition of an ultra-violet (UV) radiation. Examples are Laser-Stereolithography (SLA), Polymer Printing and –Jetting, and Digital Light Processing (DLP) [47]. In SLA (1986) the laser beam traces the cross-section on the surface of the liquid resin to solidify the pattern. This process is repeated for each layer of the design until the 3D object is complete. Once the part is completed, the support structures may be removed manually. SLA is most used in the manufacturing industry but has some disadvantages, such small size and high costs.
- *Molten Material Systems.* The most well-known method of molten material systems is the Fused Deposition Modeling (FDM, 1992) developed by the US company Stratasys [48]. In FDM a liquid thermoplastic material is deposited through a nozzle in a controlled manner to form ultra-thin layers with final part accuracy of ± 0.05 mm. The material is heated to 1 °C above its melting temperature in order to solidify immediately after the extrusion. The cost of FDM is quite low and the equipment has small size, on the contrary FDM requires long process times and creates possible delamination between layers. There are many plastic materials available for FDM processes, including engineering materials such as ABS, PC-ABS, and grades for medical modelling.
- *Solid Sheet Systems.* The Laminated Object Manufacturing (LOM, 1988) system from Helisys USA is an example of solid sheet systems [48]. LOM consists of a series of adhesive-coated sheet materials, e.g. paper, metals, plastics, fabrics, synthetic materials, manufactured by 2D cross sections. A moving laser beam cuts the sheets and adjusts the thickness of the single layer. This technology is not expensive but produces some Z-axis accuracy problems [112].
- *Discrete Particle System.* Discrete particles are normally powders with relatively uniform size and shape and narrow distribution. There exist different technologies belong to such category, diversifying between the way of powder binding. 3D printing (3DP, 1993) is a discrete particle system technology where the powders are joined together using a binder sprayed through a nozzle, while the unbound powder is removed. Before the material is hit by the binder it is misting with water droplets to avoid excessive disturbance. The process presents some advantages, such as process speed and low material cost, and some drawbacks such low surface accuracy and high costs. The process may be applied to the production of metal, ceramic, and metal/ceramic composite parts [112].

Selective Laser Sintering (SLS, 1989) and Selective Laser Melting (SLM, 1995) are two examples of discrete particle systems using a moving laser beam to connect together the powder particles. These two processes belong to the category of Powder Bed Fusion (PBF) processes, which offer a wide variety of material

possibilities with polymers, metals and ceramics all available on current commercial systems. When the process consists of an electron beam instead of a laser is called Electron Beam Melting (EBM) and when the energy is provided by a radiator through a mask, it is called Selective Mask Sintering (SMS).

1.1.1 Selective Laser Sintering/Selective Laser Melting

SLS was developed in 1989 at University of Texas at Austin, USA, and was the first commercialized PBF process. SLS is commercialized by 3D Systems, Rock Hill, SC, USA and EOS FmbH, Munich, Germany [47].

SLM started in 1995 at the Fraunhofer Institute ILT in Aachen, Germany and the most of the SLM machines come from Germany: EOS-GmbH of Munich, Realizer- GmbH of Borcheln, Concept Laser GmbH of Lichtenfels, and SLM-Solutions of Lübeck [47].

SLS and SLM machines are very similar and a description of the machine configuration is shown in Fig.3.1. A powder bed with grain size of up to $50\ \mu m$ is placed on a build chamber, which is preheated to decrease laser power and protected by shielding gas (e.g. nitrogen or argon) to prevent oxidation. On the top of the powder bed a laser scanner unit generates the x-y contour, meanwhile on the bottom, a movable piston can be adjusted at any z-level. The top of the powder bed defines the build area in which the actual layer is built. Most machines are equipped with a Nd:YAG or CO₂

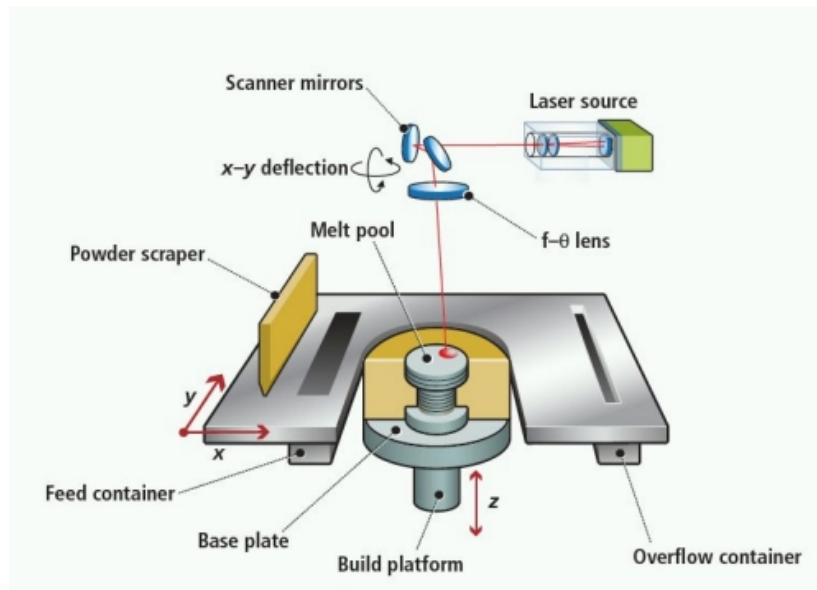


Figure 1.3: Typical configuration of a SLS/SLM machine.

Source: www.popular3dprinters.com.

laser having a Gaussian energy distribution. The laser beam is deflected by galvano mirrors, which control the movement of the laser beam over the surface of a powder bed. The velocity of the laser ranges typically from 50 to 600 mm/s. The laser beam hits the surface and melts the powder bed. The geometry of the melted region depends on the power and the scan speed of laser beam. Once the laser beam travels further, the melted region starts cooling and the liquid part solidifies. After solidification of one layer, the build cylinder moves down one step, typically between 30 and 100 μm , and the next powder layer is placed upon the previous one by means of a powder coater

mechanism: a roller rotates counter-clock wise to its linear movement in order to spread the powder uniformly; this procedure is called recoating. Then the process is repeated for each layer and the part is completed. After the build is finished and the top layer is processed, the whole part, including the surrounding powder, is covered by some layers of powder. This procedure makes a so-called powder cake which has to be cooled down before removing the part from the surrounding powder. The cool-down can be done in the machine but using a separate chamber can allow the use of the machine for a new process.

SLS and SLM machines present the same process technique but SLM procedure is developed in particular to process metal parts that need to be very (>99 %) dense without the need for post-processing, other than the removal of supports and parts from the substrate. The full dense parts are achieved using an high-intensity laser without any binder material; this provides a high improvement in product quality, processing time and manufacturing reliability compared to SLS.

Both SLS and SLM processes can fabricate ceramic, metal and polymer parts. Many classes of materials can be used with sintering process: plastics, metals and ceramics. These include polymers such as nylon (neat, glass-filled, or combined with other fillers such as carbon fiber) or polystyrene; for all metals machines a wide variety of metals, including carbon steel, stainless steel, CoCr, titanium, aluminum, gold and proprietary alloys are available.

In particular, the use of metals leads to an increasing interest from industries and makes SLM a very demanding and widespread technology. The metal composites manufactured by SLM are characterized by full density, strength and micro-hardness, which make metals, and in particular titanium and steel, very valued materials.

Metal materials are involved in different research fields: medical and dental applications, to produce customized and biocompatible products, uses steel-based alloys [74], cobalt-chrome [43] and titanium [28] which presents high specific strength and elastic moduli closer to bone than Co-Cr alloys and stainless steel [142] (Fig. 1.4); industrial applications, such the production of heat exchangers in steel [135] and copper, due to its high thermal conductivity of 401 W/(m K), or the manufacturing of injection moulding tools [103] (Fig. 1.5); aerospace and automotive applications to produce structures with high temperature performance and light weight, especially with titanium alloys [113] (Fig. 1.6).

The trend of number of publications about SLM from 1999 to 2014 has varied a lot: the interest from academic community is increased especially for metal materials (Fig. 1.7). Among the metallic materials, the application of iron and steel alloys on SLM started early while the research interests in titanium-based alloys started in 2010 when was found the compatibility of titanium for medical applications.

1.2 Selective Laser Melting modelling

The nature of Selective Laser melting (SLM) is rather complex and it is characterized by a multitude of different physical phenomena. The heat supply over the powder surface is transferred by heat conduction to the underlying layers and by convection and radiation to the environment; at the hit of the laser beam the powder particles reach the melting temperature and the material becomes liquid leading to the so-called melt pool; in the melt pool the fluid can flow due to different surface tensions (Marangoni

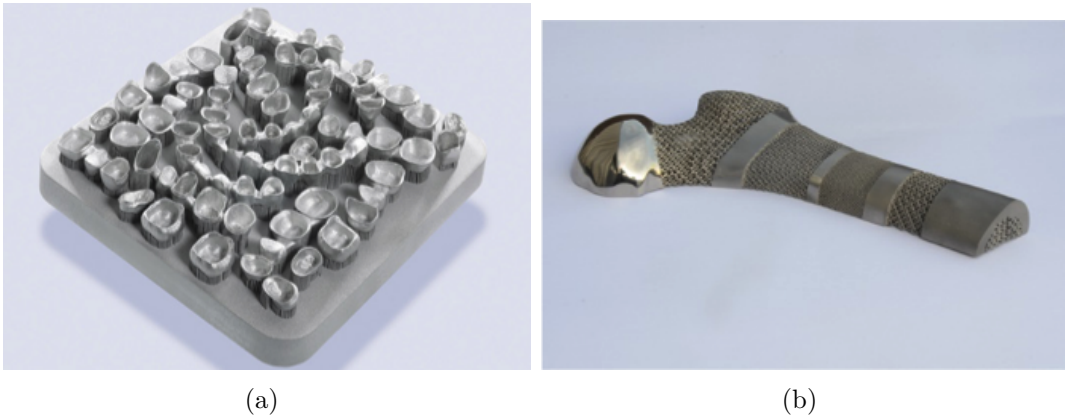


Figure 1.4: Medical products processed by SLM. (a) *Source: concept-laser.de.* (b) *Source: layerwise.com*

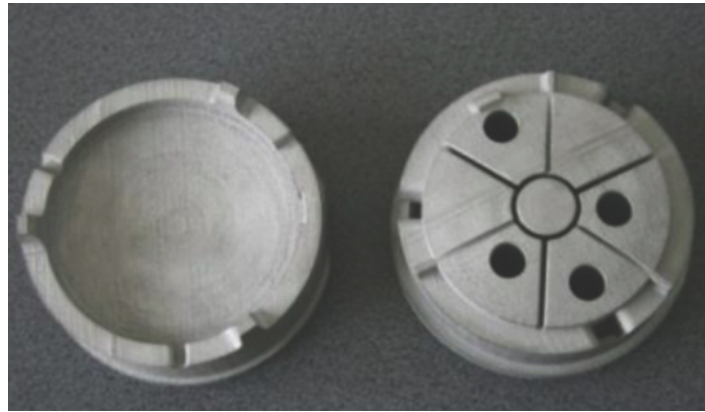


Figure 1.5: The injection moulding tools manufactured by SLM [103].

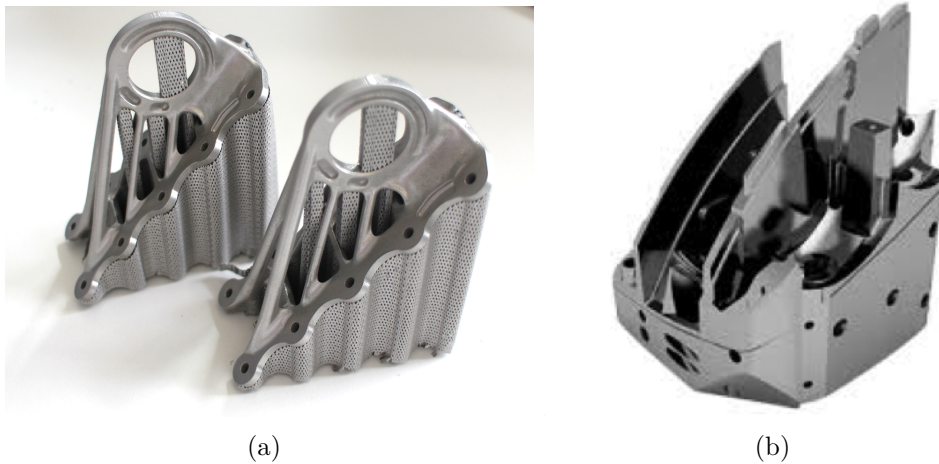


Figure 1.6: Aerospace (a) and automotive (b) products processed by SLM. *Source: concept-laser.de*

effect); after the laser beam goes further the melted region starts cooling and finally solidifies. The scanned material during the process experiences a phase transformation

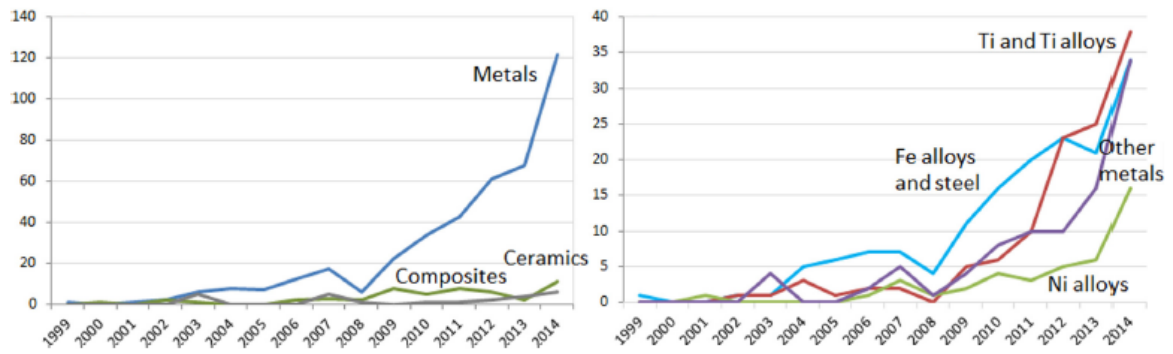


Figure 1.7: Research publications on SLM of metals, ceramics, and composite materials and between different metallic materials. Data are based on research publications on SLM, LaserCusing, and DMLS indexed by Web of Science and ScienceDirect [142].

from powder to liquid during heating and from liquid to solid during cooling. Inside the melt region the so-called Rayleigh instabilities can lead to the undesired 'balling' effect with formation of micro-balls. The balling effect determinates a lack of connection between the different layers, with consequent delamination.

The transient temperature gradients generates transient thermal stresses in the portions of the geometry which are not free to expand or contract in response to temperature changes. After cooling the stresses remain inside the domain under the shape of residual stresses. Steep temperature gradients during heating-cooling cycles are not always unwanted (e.g., for annealing, hardening and tempering), but in case of SLM the consequent formation of residual stresses can lead to deformations, damage and part crack.

SLM process involves multi-physics aspects, thermal and mechanical behaviour, and multi-scale aspects, from submicrons, e.g. the characteristic length of the solid-liquid interface, to order of meters, e.g. the entire domain. Furthermore, the time scales are different during the process; the laser beam can move very quickly over the layer (e.g. 120 cm/s) and the phase transformation inside the material occurs in few microsecond, while the entire process may invest many hours.

The development of an accurate numerical model able to describe the entire process and capture the multifaceted nature of SLM is still a big challenge. In Fig. 1.8 we summarize some of the most important challenges regarding the SLM modelling.

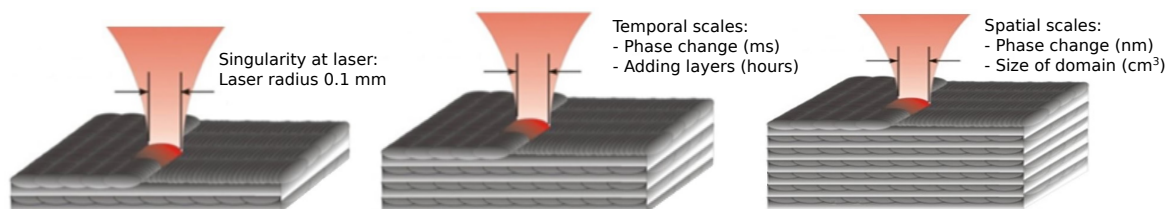


Figure 1.8: Challenges of SLM modelling.

The physics of SLM involves many scientific fields: fluid dynamics, solid mechanics, heat conduction, laser propagation, phase transformation and chemical reactions, etc.; and different modelling approaches can be assumed with several hypothesis and simplifications. The role of computational modelling is essentially focused on the assessment

of the temperature evolution, with the prediction of the melt pool shape, the residual stress profile and the topological and shape optimisation of components. The thermal modelling is essential to control the levels of porosity and the formation of the microstructures giving an insight into the resulting material properties, from elastic anisotropy to tensile strength. An accurate thermal model should be comprehensive of several aspects: melting and solidification, free surface re-construction, multiple phases (liquid, solid and powder), force and natural convection, moving laser beam, temperature dependent material properties (i.e., thermal conductivity, density), temperature dependent surface tension (i.e. Marangoni convection), alloy phase changes. Thermal modelling is also important as input for the stress analysis.

SLM modelling from a microscale point of view ($\approx 10\mu\text{m}$ up to 1 mm) is rarely modelled and only recent papers are presented [13, 86], while many authors face to the macroscopic behaviour ($\approx 100\mu\text{m}$ up to 10 cm) with the simulation of temperature and stress evolutions [45] and fluid flow [145]. Other authors investigate the SLM process from a meso-scale ($\approx 100\mu\text{m}$ up to 1 mm), modelling the sintering and melting of the single powder particles, and the mass transfer and fluid flow, especially with Volume of fluid method (VOF) [50]. The melting and solidification of randomly packed powder bed are also investigated using the Lattice Boltzmann mode (LBM), where particles exist on a set of discrete points that are spaced at regular intervals to form a lattice [8, 69]. Modelling is typically developed using analytical solutions [150] and numerical solutions [30, 46, 98] using self-developed codes or finite element, finite difference commercial codes (i.e., Abaqus, Ansys).

1.3 Aim of the thesis

The previous section shows the importance of developing a numerical model to assess and predict the real behaviour of manufactured parts to select the optimal process parameters and to face the high requirements derived from industries. For this reason appropriate modelling assumptions have to be evaluated to handle the several numerical challenges: the most important is surely the development of a suitable, fast and cost-effective numerical model.

The aim of this doctoral research is the development of an efficient finite element numerical model of selective laser melting process, which is able to predict the thermal and mechanical behaviour with reasonable computational time. In particular, we conduct separately thermal and stress analyses using finite element commercial software Abaqus. The main advantage of using a sequentially-coupled thermal-stress analysis is the time step regulation which could be different between the two analyses, saving a large quantity of required storage. The thermal simulation is performed and the temperature solution is stored at each time step; after this solution is applied as a load into the stress analysis. The thermal analysis requires a high computational effort due to the strong nonlinearity came from the phase transformation of scanned material. For this reason we focus the activity research on reducing the time consuming of the thermal analysis. In particular we develop different model reduction strategies: we develop a simplified heat input model to replace the presence of the moving heat flux over the scanning track. First a detailed numerical simulation of a one track with moving heat source is performed, modelling the presence of phase transformation, the temperature dependent material properties and the heat loss by convection. After, a steady-state

temperature solution is selected and imposed as a Dirichlet moving boundary condition in the thermal analysis; after the effect on residual stress distribution is investigated. In literature the development of an equivalent cheap model for the heat source is being quite common [79, 80], but rarely its effect is measured in terms of residual stress distribution.

Furthermore we introduce the concept of substructures and model order reduction techniques in order to further decrease the large number of degrees of freedom (DOFs) of the thermal system. We adopt the Craig-Bampton method to condense linear elements into substructures with a reduced number of DOFs. In particular a suitable projection basis with a set of vectors, called Lanczos vectors, is constructed for the heat conduction problem and possible extensions to the nonlinear reduction model techniques are also presented with the use of some derivatives of these vectors.

1.4 Organization of the dissertation

The dissertation is organized as follows:

- *Chapter 2.* Selective Laser Melting technology. The chapter is developed to better understanding the whole selective laser melting process. A description of the main physical phenomena is presented showing the complex nature of SLM process. Furthermore such physical phenomena are greatly affected by the choice of process input parameters, e.g. laser power, scanning velocity, and an extended overview is shown.
- *Chapter 3.* Selective Laser Melting modelling. The understanding of the physics permits to perform an accurate model of the process, which is clearly multi-disciplinary. In this chapter an overview of the models and its governing equations of heat conduction, phase-field and mechanical models is presented.
- *Chapter 4.* Finite Element Simulation of Selective Laser Melting process. Finite element analysis (FEA) is performed in Abaqus to simulate the thermal and mechanical behaviour of manufactured parts. Some modelling assumptions are adopted and justified by the author; the FE model is validated comparing the numerical solution with an analytical solution of temperature field of a linear transient heat conduction problem [41]. The following physical aspects are simulated: melt pool geometry, temperature distribution, build-up layers, residual stresses, deformation.
- *Chapter 5.* Substructuring and model order reduction techniques. In this chapter we introduce some model order reduction (MOR) techniques to reduce large-scale linear and nonlinear problems. In particular we describe the use of a particular set of vectors referred to the Krylov sequence, called Lanczos vectors, to construct a suitable projection basis. The use of this basis is applied to the Craig-Bampton method to reduce linear portions of large-scale problems. A possible nonlinear extension of the Craig-Bampton method is by the definition of the derivatives of the Lanczos vectors that can be added to enrich the projection basis.
- *Chapter 6.* A new user subroutine implementation for model order reduction in Abaqus. This chapter presents the application of model order reduction techniques

over the SLM simulation model. In particular the Craig-Bampton method with a suitable reduction basis is adopted for 'linear' portions of the thermal problem. Furthermore a new in-house user subroutine is performed inside the software Abaqus to reduce directly the nonlinear system.

- *Chapter 7.* Final remarks. In this final chapter, the conclusions are drawn highlighting the original aspects of the doctoral research and future research developments are outlined.

Chapter 2

Selective Laser Melting technology

Selective Laser Melting technology (SLM) is a rather complex process with, even now, not fully investigated facets. The multitude of physical aspects characterizing the process makes arduous the definition of the best selection of process parameters. The present chapter is the result of an accurate literature review with the objective of giving to the reader an overview of the main physical phenomena and possible choices of SLM process parameters.

2.1 Physical phenomena

SLM process involves the melting of powder particles and the re-solidification of melted material to form the desirable component. Besides these classical mechanisms, SLM presents very peculiar and specific physical phenomena: absorption of the beam in the powder bed and the melt pool or the re-solidified melt, melting and re-solidification of a melt pool, wetting of the powder particles with the liquid, diffusive and radiative heat conduction in the powder, diffusive and convective heat conduction in the melt pool, capillary effects, gravity, etc. The efficiency of processed material is strongly influenced by the interplay between the physical phenomena; typical process defects associated with SLM processes are loss of porosity, melt ball formation, residual powder and not connected layers (Fig. 2.3).

The heat transfer takes place an important role during SLM process: the laser scans on the top of the powder bed following a prescribed scan pattern. This involves absorption of the laser radiation by the target material, which can be powder, liquid or solid. Part of the heat is lost for convection between powder bed and the environment while the amount of heat that is subsequently conducted to the surrounding material depends on the thermal conductivity of the material. The complexity brought about by the powder phase change and the corresponding variation of thermal properties during SLM also complicates the heat transfer problem. A schematic description of the heat transfer processes is showed in Fig. 2.2. The beam absorption process for laser radiation is complicated due to multi-reflection processes causing radiation transport in much deeper powder layers. Körner et al. [68] presented a model in which the reflection processes are neglected but the transient nature of the absorbing surface is considered. The moving beam is always described by a Gaussian distribution:

$$I(x, t) = \frac{P}{\sqrt{2\pi}\sigma} \exp\left(-\frac{(x - vt)^2}{2\sigma^2}\right) \quad (2.1)$$

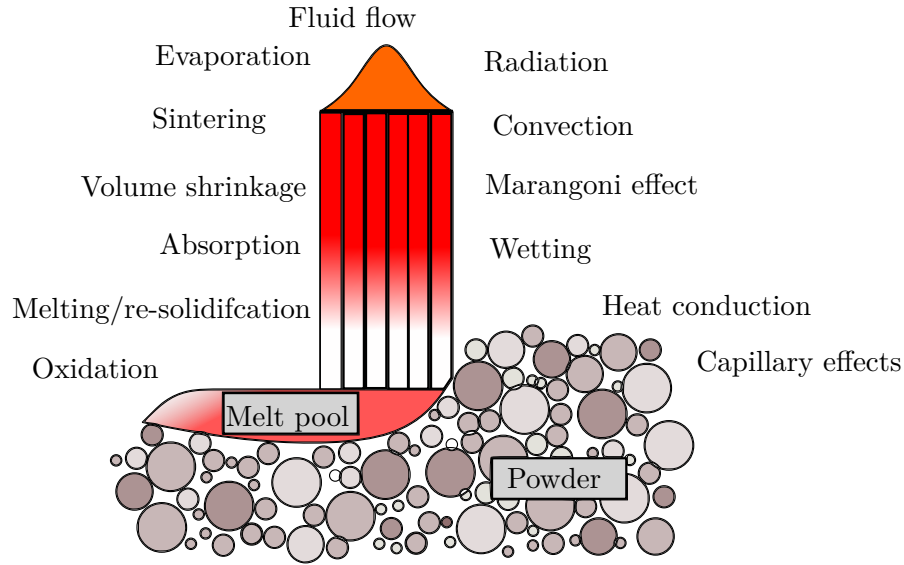


Figure 2.1: Physical phenomena during selective laser melting.

where I is the beam power density, v is the velocity of the beam, x is the location, t is time, σ is the standard deviation and P is the total beam power. In literature a surface heat flux is more used [40, 46, 105] than a volumetric heat flux [61] due to a very small thickness of powder layers (30-100 μm).

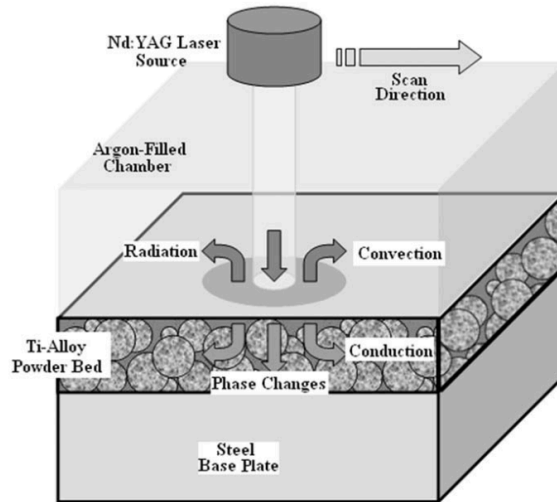


Figure 2.2: Schematic representation of heat transfer [147].

Volumetric shrinkage is a phenomenon connected to the porous character of the powder: during melting the liquid phase needs to collect and drive the interstitial gasses out of the powder bed, effectively shrinking the volume. A significant density change and motion of the surface occur during the melting process. The influence of powder shrinkage and molten pool fluid flow has been widely investigated in literature [22, 62, 139]; for example Zhang and Faghri [151] analytically solved a one dimensional melting problem in a powder bed containing a powder mixture. The results showed that the shrinkage effect on the melting of the powder bed is not negligible.

In general, the binding mechanism in full melting is strongly driven by the fluid behaviour

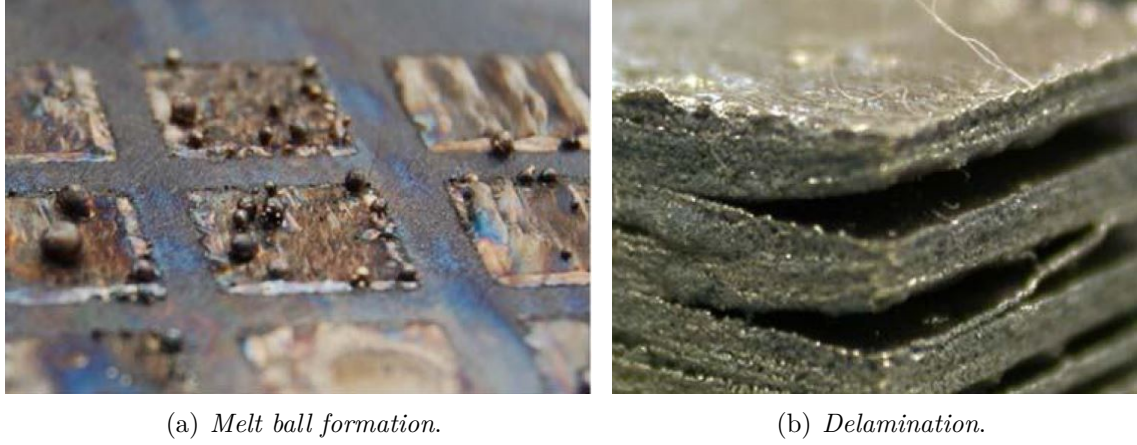


Figure 2.3: Main process defects [146].

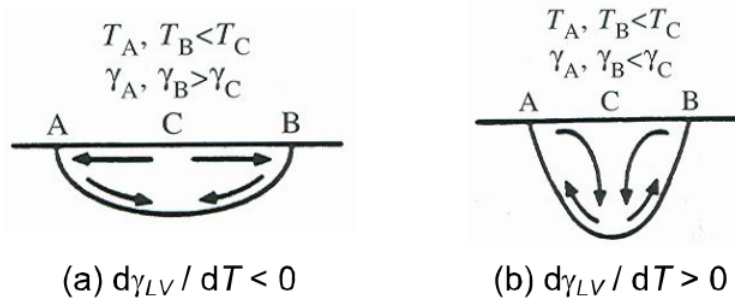
of the melt which is related to surface tension (Rayleigh instabilities), viscosity, wetting, thermo-capillary effects (Marangoni convection), evaporation, and oxidation.

Rayleigh instabilities imply the break up of a liquid cylinder with high aspect ratio in order to lower the surface energy. This type of instability was first studied by Plateau and later by Rayleigh for liquids with negligible viscosity.

Marangoni convection is the thermocapillary flow of a fluid from regions with a low surface tension to regions with a high surface tension. The sign of the surface tension gradient associated with liquid-vapour interface ($d\gamma_{LV}/dT$ in Eq. 2.2) determines the direction of the fluid flow: if the flow is radially outward a shallow and broad melt pool results (Fig. 2.4a); if the flow is radially inward a deep but narrow pool is formed (Fig. 2.4b). The surface tension gradient of pure metals and many alloys is negative; however, positive tension gradient is reported for alloys containing a sufficiently high content of surface active elements. The magnitude of the flow can be estimated from the dimensionless Marangoni number M_a :

$$M_a = \frac{d\gamma_{LV}}{dT} \frac{dT}{dr} \frac{L}{2\eta\delta} \quad (2.2)$$

where dT/dr is the temperature gradient, L is the characteristic length of the melt pool, δ is the thermal diffusivity and η is the liquid viscosity. Marangoni convection

Figure 2.4: Schematic presentation of Marangoni convection in a melt due to the presence of a surface tension gradient $d\gamma_{LV}/dT$ [108].

is relevant at low scanning velocities while it disappears at higher scanning velocities.

Xiao and Zhang [140] developed a three dimensional model considering the thermal behaviour and fluid dynamics in the molten pool caused by Marangoni and buoyancy forces. Fan and Liou [42] presented a two dimensional continuum model to simulate the free-surface flow of the melt pool also considering Marangoni effect.

During SLM also evaporation is observed when applying high heat inputs. This can cause a deviation between the chemical composition of the material before and after processing. A second effect of evaporation is the induction of a recoil pressure that acts on the surface of the melt. Finally, the formation of a vapour above the melt surface can affect the amount of laser energy that is absorbed during SLM. Verhaeghe et al. [125] considered the effect of evaporation on the dimension of the bath width and remelting depth.

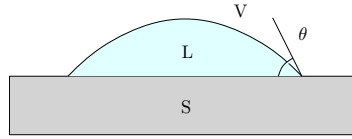


Figure 2.5: Schematic representation of wetting of liquid on substrate.

The wetting characteristics of the solid phase by the liquid phase are crucial for a successful processing since it determines the spreading behaviour of the melt and affects the infiltration characteristics of the system. The wetting of the melt pool on the previously consolidated material ensures the connection of the underlying layers and prevents delamination. Wetting of a liquid on a substrate is described by the equation of Young:

$$\cos\theta = \frac{\gamma_{SV} - \gamma_{LS}}{\gamma_{LV}} \quad (2.3)$$

where $\gamma_{SV}, \gamma_{LV}, \gamma_{LS}$ are the surface tensions associated with respectively solid-vapour, liquid-vapour and liquid-solid interface. The liquid wets the substrate as $\cos(\theta) \rightarrow 1$ or equivalently if $\gamma_{SV} - \gamma_{LS} > \gamma_{LV}$. The wettability of a solid by a liquid can be influenced by the material temperature, impurities, contamination, and atmosphere. Also capillarity is governed by the surface and interface energies and the capillary force (\mathbf{F}_{cap}) exists if the surface curvature k does not vanish according with [68]:

$$\mathbf{F}_{cap} = k \sigma dA \mathbf{n} \quad (2.4)$$

where k is the curvature, σ is the surface tension, dA is a surface element, and \mathbf{n} is the normal vector belonging to dA .

A well-known phenomenon during SLM processes is the break up of thin melt pools into spherical droplets called "balling". Commonly, balling is explained by the Plateau-Rayleigh capillary instability of a cylinder at length to diameter ratio greater than π but also a strong non wetting condition amplifies balling effect. The balling phenomenon can be avoided by using a pulsed laser beam with very small beam spot size at very high scanning velocity to complete melting of single-component metal powders. Another method to reduce the balling phenomenon is to use two-component powder, in which two types of powder with different melting points are employed. The high-melting-point powder does not melt in the sintering process and plays a role as the structure necessary to avoid the balling in the sintering process. A molten liquid that is formed by melting the lower melting point powders infiltrates into the voids between the higher melting

point solid powders and binds them together. The solid particles move downward while only the low-melting point powder melts and resolidifies. The use of a mixture of low and high melting temperature powders also produces higher viscosity of the melt pool which is relevant to avoid balling effect. It is also the reason behind developing alloys with a wide solidus melting temperature to liquid melting temperature, for which it is easier to maintain a partially molten state within the irradiated layer [27].

In literature many authors considered two-component metal powder [25, 66]. Körner et al. [68] developed a two dimensional model at a mesoscopic scale and provided the influence of the relative powder density, the stochastic effect of randomly packed powder bed, capillary and wetting phenomena; the model was able to predict experimental observations such as balling effect. Gusarov et al. [52] considered the balling effect at different scanning velocities over a thin powder layer deposited on a dense substrate. Experimental and numerical results showed that balling effect increased with higher scanning velocities while lower velocities can reduce the length-to-diameter ratio and the width of the contact of the melt pool with the substrate.

SLM of metal powders is often accompanied by oxidation due to the presence of oxygen in the processing chamber, for instance trapped in the pores of the powder bed, and the high temperatures involved. Since oxidation is present, the laser absorptance of oxides differs significantly from that of metals. Furthermore, oxidation of the substrate results in a lower solid surface tension γ_{SV} and thus, according to the equation of Young (Eq. 2.3) to worse wetting by the liquid melt. Oxidation also causes delamination induced by poor interlayer bonding in combination with thermal stresses. In order to mitigate oxidation as well as to ensure good wetting and successful layer-by-layer consolidation, processing must be conducted in a vacuum or protective atmosphere using high purity inert gases.

2.2 Residual stresses

Residual stresses in a body are those which are not necessary to maintain equilibrium between the body and its environment. As illustrated by Withers and Bhadeshia [134], the residual stresses can be classified by the characteristic length l_0 over which they self-equilibrate. Long range stresses (type I) equilibrate over macroscopic dimensions ($l_{0,I} \approx$ the scale of the structure); such stresses can be estimated using continuum models which ignore the polycrystalline or multiphase nature of the material, often calculated using finite element. Type II residual stresses equilibrate over a number of grain dimensions ($l_{0,II} \approx 3-10 \times$ grain size) and they nearly always exist in polycrystalline materials from the fact that the elastic and thermal properties of differently oriented neighbouring grains are different. Also, grain scale stresses occur when the micro-structure contains several phases or phase transformations take place. Type III stresses exist over atomic dimensions and balance within a grain ($l_{0,I} \approx$ the scale of the structure ($l_{0,III} <$ grain size)); type III category typically includes stresses due to coherency at interfaces and dislocations stress fields.

Residual stresses are not always disadvantageous, e.g. glass plates are many times rapidly cooled to introduce compressive stress in the surface area of the plate, thus increasing the overall loading resistance and preventing crack growth at the surface. However, in most cases, residual stresses are unwanted, since they result in deformations from the intended shape. For example, in SLM parts the high temperature gradients

produce internal stresses which can cause undesired warping and failure of the part. For this reason it is necessary to understand the typology, the origin and the experimental measurements of residual stresses. The experimental tests to measure the residual stresses are performed by many researchers to verify the results of theoretical and numerical models. Many techniques for measuring the residual stresses in the part are available and they can be distinguished into two groups, whether the measurement is destructive or not.

Destructive methods are the layer removal method, the Crack Compliance Method (CCM) [88], the contour method, the hole drilling method, and the Bridge Curvature Method (BCM) [73]. Non-destructive methods include X-ray diffraction, neutron diffraction, ultrasonic and magnetic measuring methods. Shiomi et al. [115] estimated the residual stresses of a chrome molybdenum steel powder blend made by SLM using the layer removal method. After the SLM process the surface layer was removed from the part with a milling machine and the strain in the longitudinal direction of the base plate was measured. This process was made until the whole model is removed. From the equilibrium equations of force and moment before and after layer removal, the residual stress changes were calculated assuming a linear stress-strain relationship (Fig. 2.6). Mercelis and Kruth [88] measured the residual stresses on aluminium samples

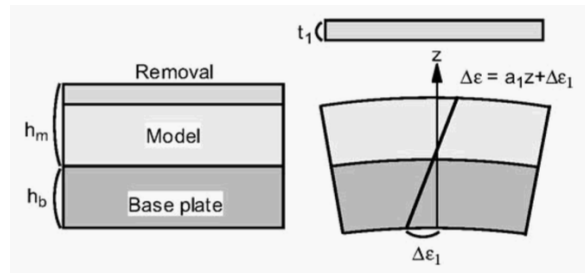


Figure 2.6: Schematic model of layer removal method [115].

adopting the CCM which can do through-thickness measurements, compared to X-ray diffraction and hole drilling. The strain gauges were connected to the sample's surface; next the part is cut in subsequent small steps using wire electric discharge machining (EDM) while the strain was measured. From the measured strain the original residual stress can be calculated by theoretical means (Fig. 2.7).

Kruth et al. [73] measured the residual stresses with the experimental approach of bridge curvature method: the method is based on removing a bridge-shape part from its base plate and consequently calculating a curvature angle α which is a measure for residual stress (Fig. 2.8). This approach was used to investigate the influence of process parameters on the residual stress within Ti6Al4V samples.

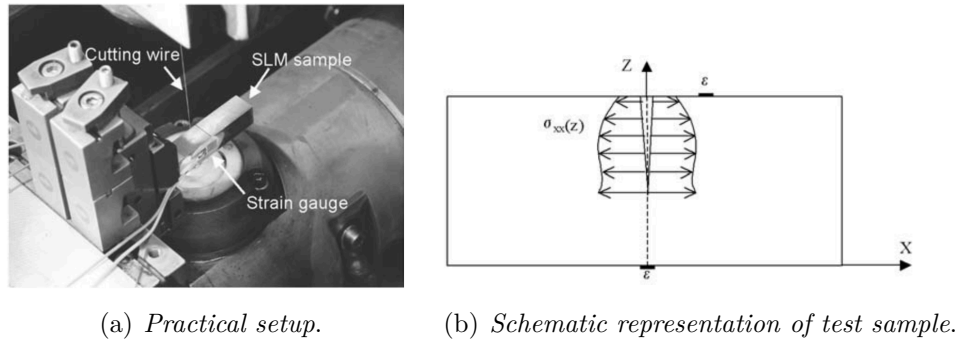


Figure 2.7: Schematic description of Crack Compliance Method (CCM)[88].

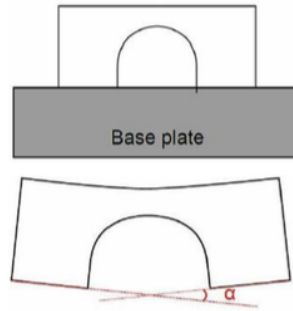


Figure 2.8: Schematic model of Bridge Curvature Method (BCM) [72].

2.3 Process parameters

The described physical phenomena can critically influence the accuracy of manufactured parts affecting the microstructure and the mechanical properties. A good control of machine input process parameters can improve the effects of the physics over the outcomes. The process parameters can be divided into four main categories, principally related to the laser beam, the scanning of the laser, the powder properties and the thermal inputs:

1. Laser-related
 - (a) Laser power
 - (b) Spot size
 - (c) Pulse duration
 - (d) Pulse frequency
2. Scan-related
 - (a) Scan speed
 - (b) Scan spacing
 - (c) Scan pattern
3. Powder related
 - (a) Particle size

- (b) Particle shape and distribution
 - (c) Powder bed density
 - (d) Layer thickness
 - (e) Material properties
 - (f) Building direction
4. Temperature-related
- (a) Powder bed temperature
 - (b) Powder feeder temperature
 - (c) Temperature uniformity

In the following a brief report of the influence of such process parameters on microstructure, melt pool dimensions, stability analysis, temperature gradients, deformation, residual stresses, mechanical properties, etc. will be described.

2.3.1 Melt pool: stability analysis

During SLM process the laser beam scans the powder surface and the material starts heating, after it reaches the melting temperature a melt pool is visible on the surface. The dimension of the molten pool can impact the quality of the track formation and it is greatly affected by the average applied energy per unit volume, which is mainly controlled by the laser power and the scanning speed. For example, it has been reported that higher laser power produces larger melt pool dimensions, in terms of depth, width and length and higher scanning velocity yields to an increasing length-to-diameter ratio, leading to the undesired 'balling effect' [52].

Yadroitsev et al. [141] showed how the zone of powder consolidation and the remelted depth decrease with the scanning speed (Fig. 2.10(a)). Furthermore a lower scanning speed decreases the length and increases the width of the molten pool (Fig. 2.10(b)). Molten pools with lower length-to-circumference ratio ($L/2\pi r$) are supposed to show a more stable behaviour. Therefore, the upper stability limit of the scanning speed can be related to the loss of the contact between the molten powder and the substrate. Yadroitsev et al. [141], in the range of the studied parameters of laser irradiation, observe that continuous single tracks from SS grade 904L (-16 μm) powder may be formed by choosing $P=50$ W, $V=0.06-0.18$ m/s and that for $P=25$ W the substrate remelting depth is absent for all the range of the scanning speeds. The instability of molten pool of SS grade 316L (-25 μm) is also considered, showing that, increasing the energy input per unit length (P/v) at a relatively high laser power and small scanning speed, the volume of melt pool increases. Also at smaller laser power for small scanning speed, energy becomes insufficient to melt the substrate, and the penetration of powder into substrate, which is an additional stabilizing effect for sintering, disappears. The range of the optimal scanning speed is larger for higher laser power, and it narrows for material with high thermal conductivity.

Laohaprapanon et al. [77] investigated the optimal scanning condition of stainless steel 316L for different process parameters, i.e. laser power, scanning speed, and scan spacing. For a single line scanning, the appearance of scan tracks is categorized into five models: unmelted, balling, smooth, irregular, and over-melted (Fig. 2.11). Balling effect is

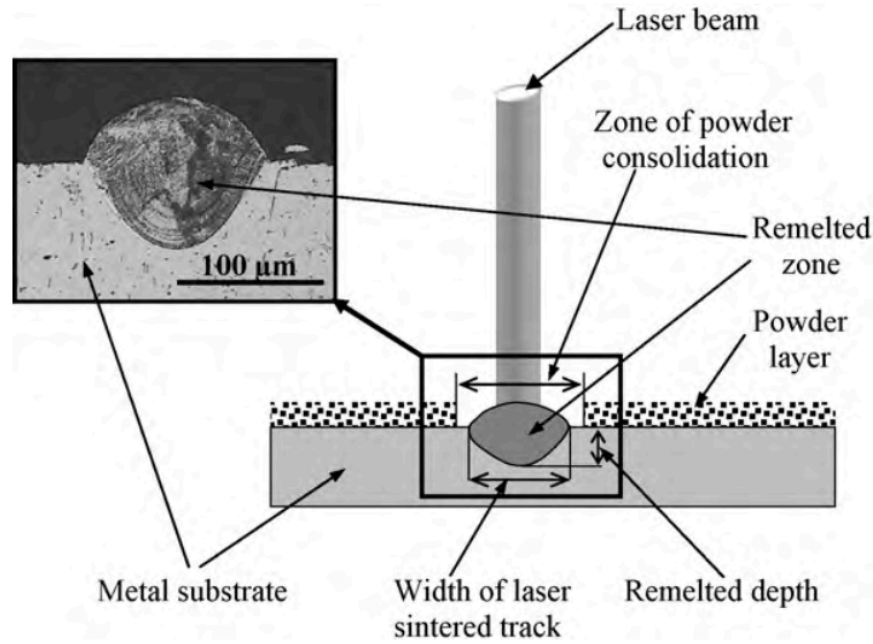
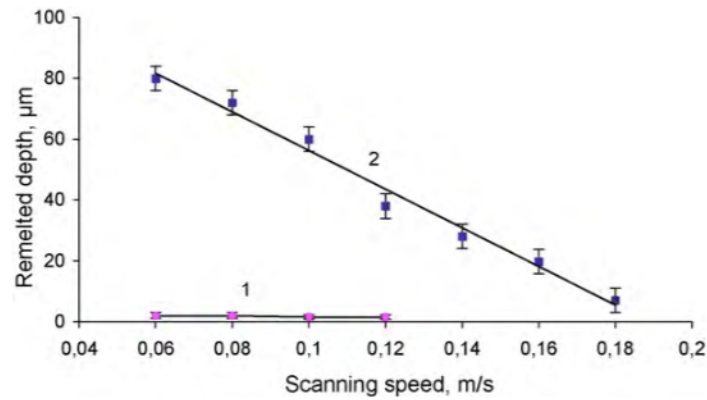


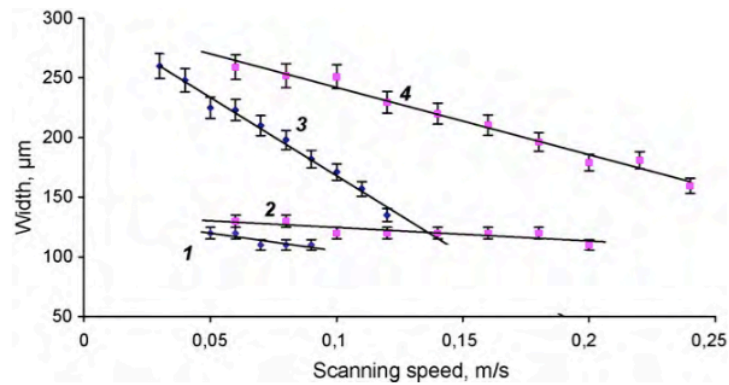
Figure 2.9: Typical cross-section of a laser sintered track from metal powder on steel substrate [141].

visible for low values of laser power (25-50 W) and scan speed (50-140 mm/s) due to high viscosity, and for high values of laser power (75-225 W) and scan speed (> 290 mm/s) because of higher length-to-circumference ratio. Smooth tracks can be formed by values of laser power between 75-225 W and scanning speed at 90-200 mm/s. These phenomena can be described as sufficient liquid stability, continuous and smooth melted tracks without balling formation. Irregular tracks are caused by high scanning speed (170-260 mm/s) and high laser power (75-150 W). The appearance of track is generally distorted and uncontinued for reduction of surface energy and instability of liquid. Over-melted tracks generally occur at low scan speed (50-80 mm/s) and high laser power (75-225 W) with overheating of powder, oxidation, and tracks widening. Gusarov et al. [52] observed that decreasing the scanning speed two main factors can stabilize the process: the reduction of the length-to-width ratio and the growth of the contact width with the substrate. The experiments and the calculations are made for stainless steel type 316L with thickness of powder layer of $50\ \mu\text{m}$. For 316L stainless steel the balling effect is visible for scanning velocities higher than ~ 20 cm/s. For example, the length of the melt pool at the stability limit ($v = 24$ cm/s) is about $300\ \mu\text{m}$ and its width about $150\ \mu\text{m}$ (Fig 2.12d). The surface tension transforms this liquid volume to a shape similar to a circular cylinder with the length of $300\ \mu\text{m}$ and the diameter about $100\ \mu\text{m}$ estimated from volume conservation. The circumference of this cylinder is about its length, which is the limit of the Plateau-Rayleigh capillary instability of a liquid cylinder: the cylinder breaks into two droplets if the length exceeds the circumference. However, the crucial stabilizing factor could be the contact between the melt cylinder and the substrate, which disappears at $v \sim 20$ cm/s, and increases fast with decreasing the velocity.

Childs et al. [27] studied the effect of laser power and scan speed on the tracks formed from melting M2 and H13 tool steel and 314S-HC stainless steel powders (Fig. 2.13).



(a) Substrate remelted depth for laser power.



(b) Width of the melt pool (curves 1–2) and of zone of powder consolidation (curves 3–4).

Figure 2.10: Influence of scanning speed to remelted depth and width of melt pool from SS grade 904L(-16 μm) for different values of laser power $P = 25 \text{ W}$ and $P = 50 \text{ W}$ [141].

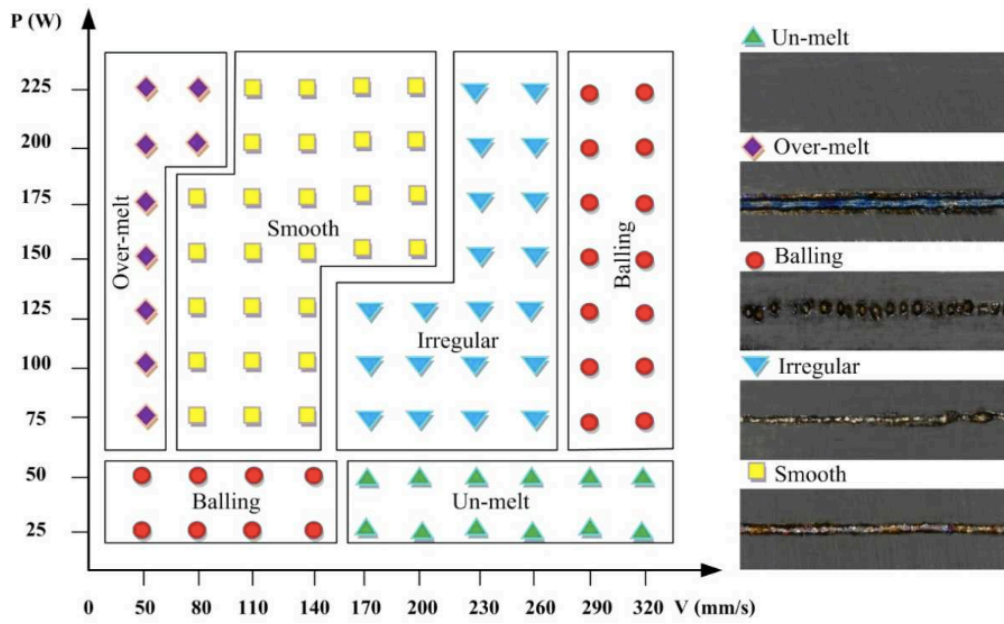


Figure 2.11: Effect of laser scanning and laser power on scanning condition of stainless steel 316L [77].

The combination of laser power and scan speed affects the typology of the tracks (Fig. 2.14): at low scan speed the track is continuous and flat (type A) increasing the velocity the track becomes round and sank (type B) and then occasionally broken (type C); with higher velocities the balling effect is evident (type D) and later the maximum temperatures are not exceeded with partially melted material (type E); in the extreme case no melting occurred in the region (type F).

2.3.2 Temperature gradients, deformation, and residual stress

Temperature gradients within the component leads to the formation of internal stresses which can cause the distortion and part failure of the part by delamination or cracking. The material properties of the powder and the process parameters like scanning strategy, laser power, layer thickness, energy distribution etc. influence the appearance of thermal stresses in the part. Other internal stresses can be induced by time-varying processing temperatures, which can differ depending on the part geometry and the scan strategy used. Generally cross-sections of the part are scanned with vectors parallel to each other. If the area to be scanned is small, short scan tracks are deposited rapidly one after the other, leaving little cool down time in between thus resulting in high temperatures. Instead for larger areas the laser beam travel distance is much longer leading to an higher cooling time and to a lower temperature of scanning area (Fig. 2.15). This can induce worse wetting conditions on the molten pool leading to a lower density of the material. Differences in temperature can be attributed also to differences in heat conductivity between loose powder and solidified material. Indeed during melting of powder bed, the material density increases from 40 to 95 %. Small scanned areas surrounded by loose material present less heat sink than large scanned areas due to isolation of the surrounding powder. This phenomenon is especially clear for zones at the corner of the part which can lead to better wetting and higher material densities [71].

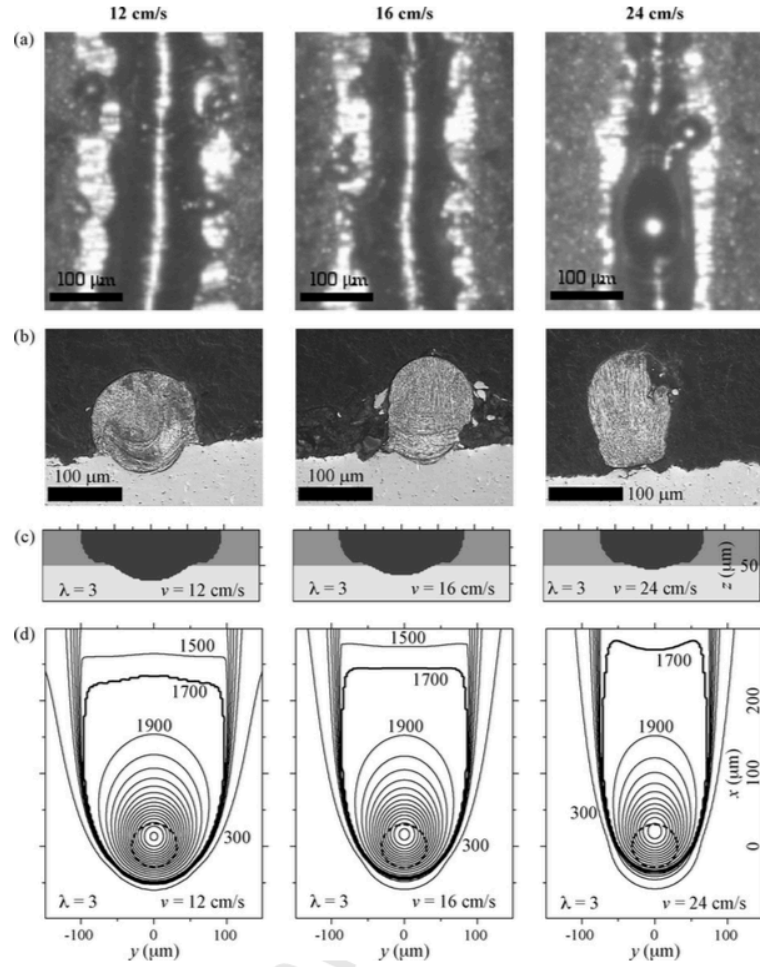


Figure 2.12: Comparison between experiments (a-b) and calculations (c-d) at various scanning velocities [52].

Scanning strategy

Kruth et al. [71] experimentally investigated the deformation during SLM on a mixture of different types of particles (Fe, Ni, Cu and Fe_3P) scanned with different scanning strategies (Fig. 2.16). The first two scanning strategies are applied along X and Y; the other scanning patterns are applied considering the area divided into 'island' sectors of 5 mm x 5 mm for strategy (3) and (4) and 2.5 mm x 2.5 mm for (5) and (6). The scanning order of the sectors can be 'successive' or according to the 'least heat influence' (LHI) between the scanned sectors. The LHI method starts at a randomly selected sector; next the sector which is least heated, thus farthest away from the last one, is scanned and so on. As shown in Fig. 2.17, scanning along X direction (and Y direction) produces the smallest curvature in the X direction (Y direction), but the largest curvature in the Y direction (X direction). Less deformation is visible for scanning strategies (3)-(6) meanwhile no striking differences can be found between strategies with different 'island sector' size. Comparing the 'successive' (3), (5) and the LHI procedure (4), (6) the first one is preferable. A possible reason could be the higher thermal gradient obtained during LHI scanning due to the lack of preheating (typical of 'successive' procedure) of the sector before scanning.

The influence of the scanning strategy on the residual stresses is experimentally investi-

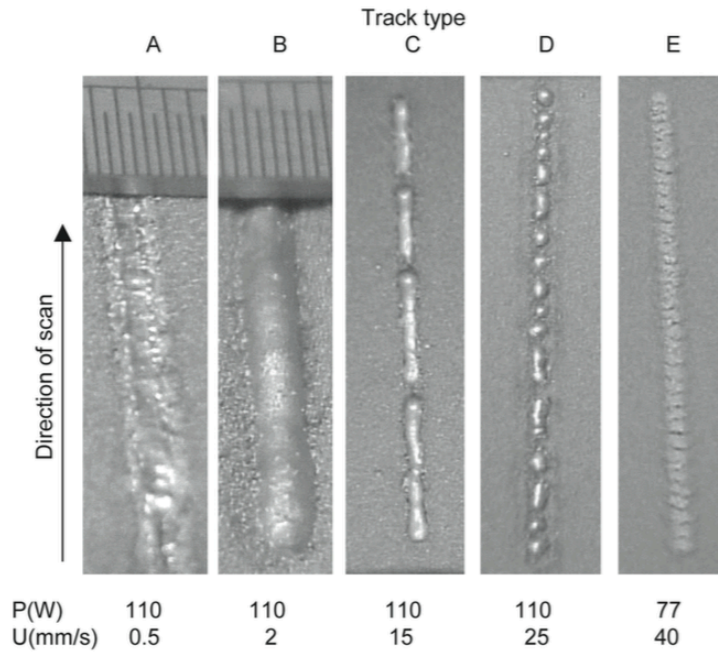


Figure 2.13: Different types of tracks from tests with $-150/+75 \mu\text{m}$ M2 steel powder in an argon atmosphere with 1.1 mm laser beam diameter, [27].

gated by Mercelis and Kruth [88]. The residual stresses are experimentally measured by the Crack Compliance Method (CCM) for a set of samples of 316L steel powder. The different scanning patterns are depicted in Fig. 2.18, where the strategies along the Y ('short track') and X ('long track') directions are compared to the sector scanning strategies of $5 \times 5 \text{ mm}$ and $10 \times 10 \text{ mm}$. The scanning pattern of the sector parts is chosen to minimize the thermal influence of previous scanned sectors on the next scanned sector. As shown in Fig. 2.19(a), for all scanning strategies the stress profile presents a zone with high tensile stresses at the top of the part, followed by broad zone of compressive stresses and a small zone of tensile residual stresses. Also the 'short track' along Y direction presents the largest values of σ_{xx} , the 'long track' along X direction the smallest σ_{xx} values, and the others with 'island' sectors present an intermediate stress level between 'short' and 'long' profiles.

The sector scanning order also affects the residual stress profile. Three different exposure orders are tested: along the width of the part, along the length of the part, and in a randomized order to minimize the mutual thermal influence of the sectors.

Fig. 2.19(b) shows that the scanning order along the width of the part yields a larger σ_{xx} value at the top of the part, than scanning along the part's length. The stress level in case of the randomized scanning order is comparable to the stress level when scanning along the length of the part. So the scanning vector length influences the amount of thermal stresses. This effect is also validated by the experimental observations of Kruth et al. [73], where the amount of residual stresses is calculated by the Bridge Curvature Method (BCM), considering the amount of resulting curvature, in terms of a curvature angle α , after removing a bridge-like structure from the base plate (Fig. 2.20). The results show that at lower vector lengths the measured angle decreases (Fig. 2.21(a)) for the scan pattern depicted in Fig 2.21(b). In this case, vector lengths of 2 mm record the largest improvement with a 13 % reduction of curling angle α , as compared with the curling angle of the reference part.

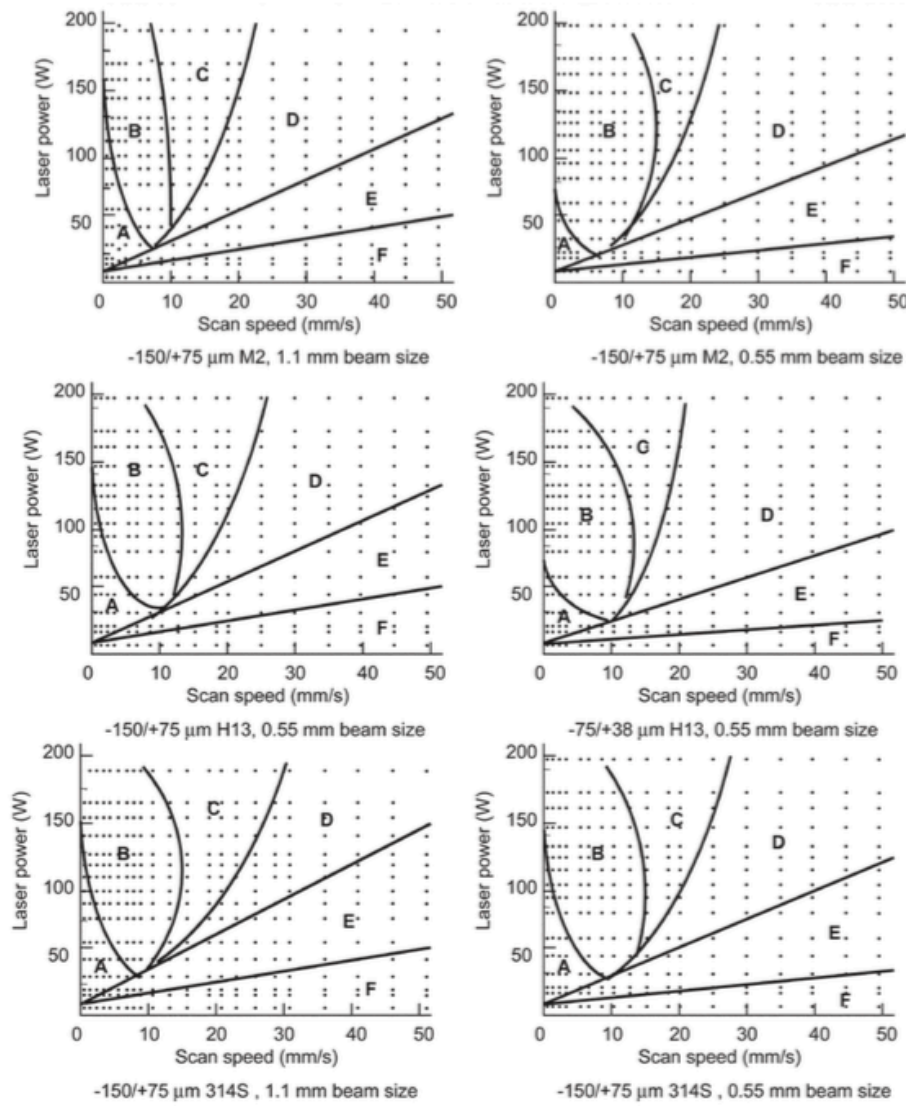


Figure 2.14: M2, H13, and 314S-HC process map examples, for different powder size ranges and laser beam diameters, [27].

The orientation of the parallel scan vectors has a clear effect on the measured angle α . This fact is clear varying the angle between the parallel scan vectors and the measurement datum: the results show that the measured angle α decreases as the rotational angle reaches 90° (Fig 2.22(a)). The bending of the test part reduces by 59 % if the scan vectors are oriented 90° from the curling measurement datum. If the parallel scan vectors are layer-wise alternated ($0^\circ - 90^\circ$), the reduction of the measured angle is found to be 45 %.

As it is described before, island scanning consists to divide the area to be scanned into small square islands. The effect of the island size, scanned with a randomized order, is shown in Fig. 2.23(a) for islands rotated $\gamma = 15^\circ$ from the x-direction. The use of island scanning reduces the measured angle α , but the size of the islands does not seem to influence the results. Fig. 2.23(b) illustrates the effect of the rotation γ for islands of 5×5 mm. If the rotation γ is 45° instead of 15° , the measured angle further decreases. Island scanning with islands of 5×5 mm, rotated 45° from the x-direction reduces the

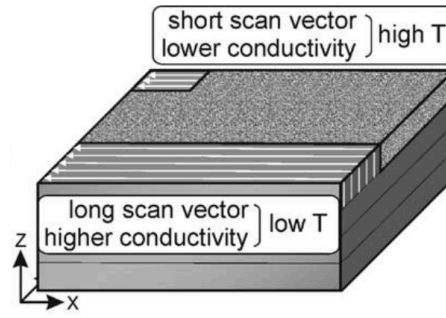


Figure 2.15: Different temperatures through different scan vector length [71].

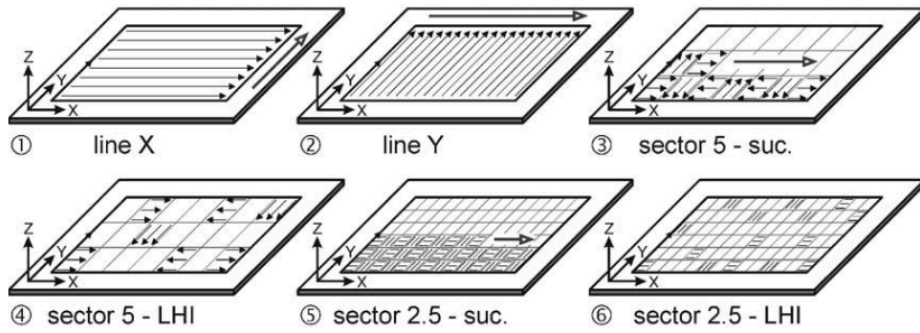


Figure 2.16: Different scanning strategies [71].

measured angle by 36 %.

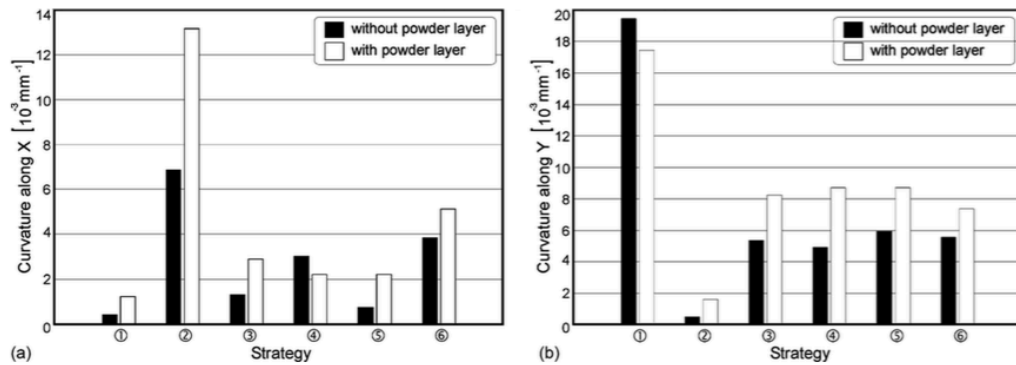


Figure 2.17: The average curvature along (a)X-direction and (b)Y-direction for different scanning strategies [71].

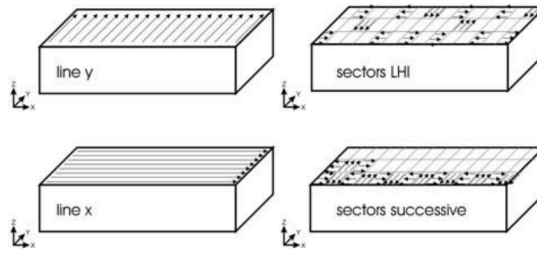


Figure 2.18: Different scanning strategies [88].

Base plate removal and sample height

Differences on residual stresses values are visible between parts connected to their base plate and parts that are removed afterwards. In general, parts that stay connected to the base plate contain very high stress levels, in the range of the yield strength of the material. Parts that are removed from the base plate, contain much lower stress levels, but they suffer from deformation during part removal (Fig. 2.24(a)).

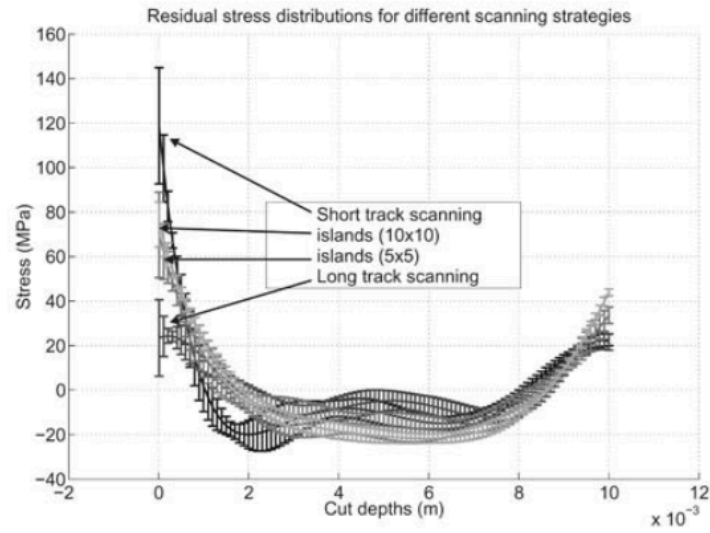
Experimental tests showed that stresses perpendicular to the scanning direction are significantly larger than the stresses along the scanning direction for the samples produced by one-directional strategy and cut from the substrate; for example for a 10 mm sample the perpendicular stresses are 302 MPa and along the scanning direction are 209 MPa. Furthermore, residual stresses increase with the height of samples, e.g. from 20-30 MPa for 2.5 mm sample to 200-300 MPa for 10 mm sample (Fig. 2.24(b)).

Post-scanning and pre-scanning

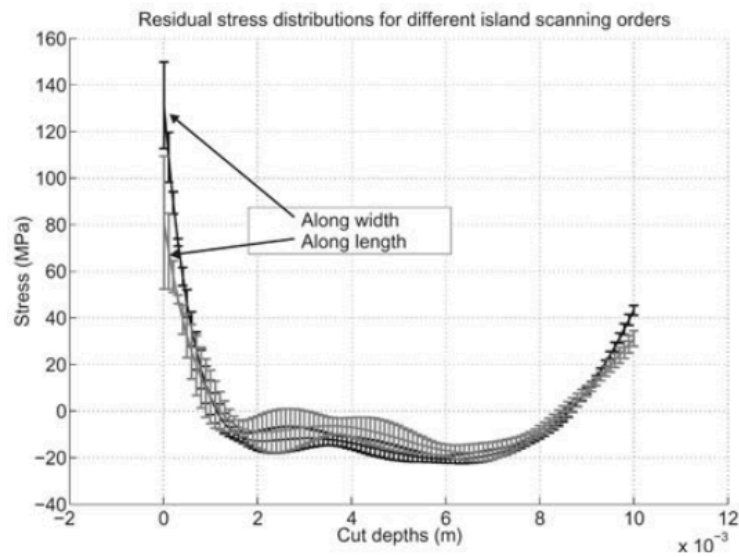
Post-scanning means re-scanning a melted and consolidated layer with the same scan pattern and spot size of melting procedure. Only low scan speeds reduce the measured angle (Fig.2.25(a)): a post-scanning speed of 100 mm/s gives the maximum reduction of 8%. When pre-scanning is applied, the laser first sinters the powder material before melting the material completely. Pre-scanning strategies reduces the measured angle only slightly, with a maximum reduction of 6% obtained at 800 mm/s (Fig. 2.25(b)).

Pre-heating of the base plate and heat treatment

Pre-heating of the base plate has a positive effect to the residual stresses: according with Kruth et al. [73] pre-heating the vase plate of 180 °C can induce a reduction of 10 % of the measured angle of curvature. Also heat treatment as a post-processing technique allows the reduction of residual stresses. Kruth et al. [73] showed how the heat treatment applied to a Ti-6Al-4V reference part on the baseplate, reduces the measured angle by 80 % (Fig.2.26).



(a) Measured stress distributions for different exposure strategies.



(b) Measured stress distributions for different sector exposure orders.

Figure 2.19: Measured stress distributions of stainless steel 316L samples for: (a) different exposure strategies (Fig 2.18), (b) different sector exposure orders [88].

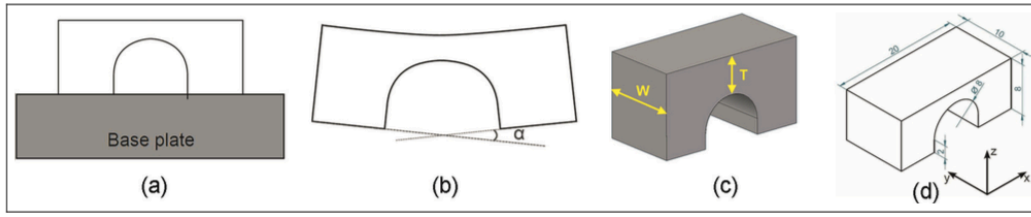
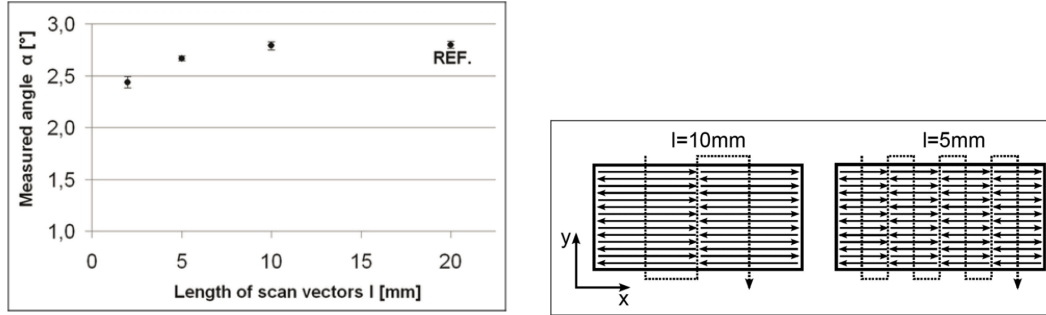


Figure 2.20: Principle of BCM method for identifying the residual stresses in the test parts [73].



(a) Scan vectors length effect on curvature angle α . (b) Scan pattern to investigate short scan vectors.

Figure 2.21: Influence of scan vectors length on curling of Ti-6Al-4V test parts; REF.: reference part, [73].

2.3.3 Porosity and microstructure

Density of the material has a significant impact on the mechanical properties of the component and for this reason density represents the most important physical property in the process. The difficulty to achieve full dense parts is often related to the presence of gas bubbles entrapped in the material during the solidification; a reason could be the decrease in the solubility of the dissolved elements in the melt pool. The roughness of the powder bed has a significant influence on porosity: rough surface causes the entrapment of gas upon deposition of a new powder layer. Indeed when a new non-homogeneous layer is deposited the laser energy may be not enough to melt the new layer completely, since the depth of the powder in some regions will be thicker. Aboulkhair et al. [4] studied the effect of scanning strategy on density of Al alloy specimens (5 mm x 5mm x 5mm). In particular, they observed the influence of hatch spacing (50, 100, 150, 200, 250 μm), scanning speed (from 250 mm/s to 1000 mm/s with 250 mm/s intervals) and scan orientation on test cubes (layer thickness of 40 μm and laser power at 100 W) to minimize porosity. They deduced that the type of pores (metallurgical pores and keyhole pores), formed during SLM process, is related to the scanning speed used. The best combination is found to be a speed of 500 mm/s, hatch spacing 50 μm , and employing the pre-sinter scan strategy (scan the layer with half power followed by a second scan with full power) yielding a relative density of 99.77 ± 0.08 %.

The balling phenomenon is also observed on the top surface of samples and it increases with scanning speed (Fig. 2.27). The reason is related to capillary instability in the molten metal pool which promotes balling. A microstructural analysis is also taken when different forms of grain structure are visible (Fig. 2.28): a fine microstructure

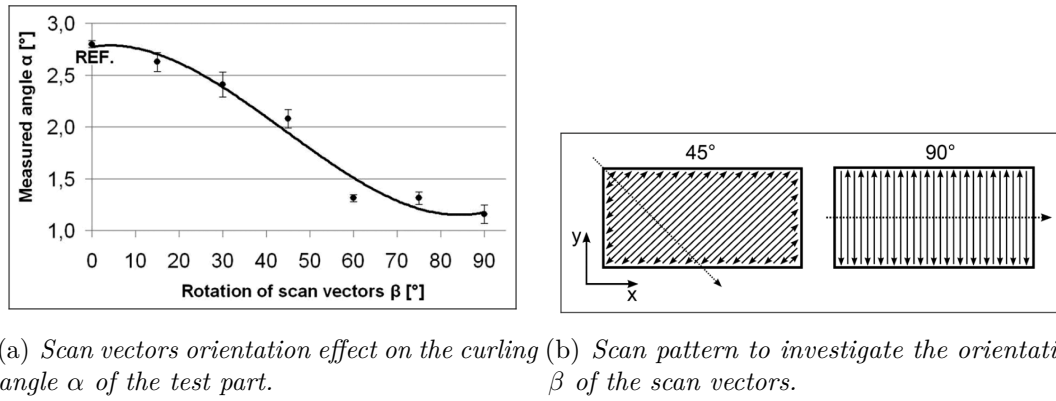


Figure 2.22: Influence of scan vectors orientation on curling of Ti-6Al-4V test parts; [73].

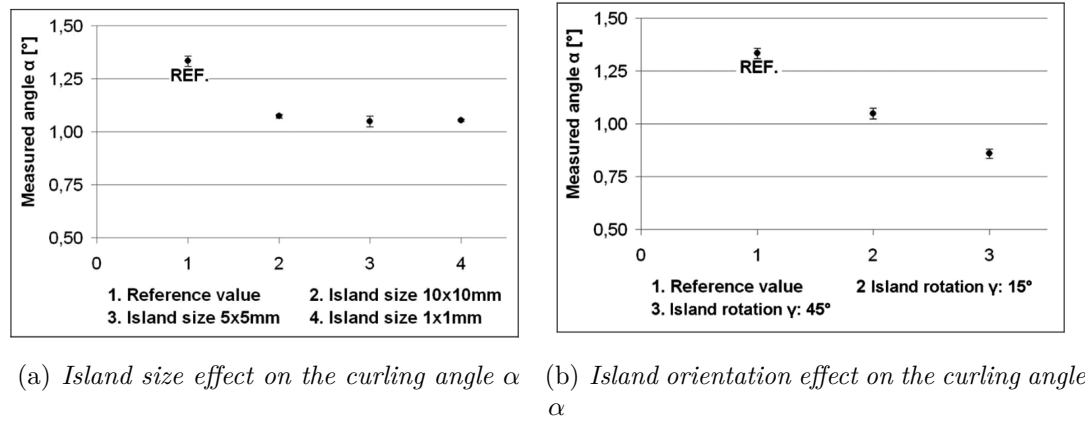


Figure 2.23: Influence of island size and orientation on curling of steel parts; [73].

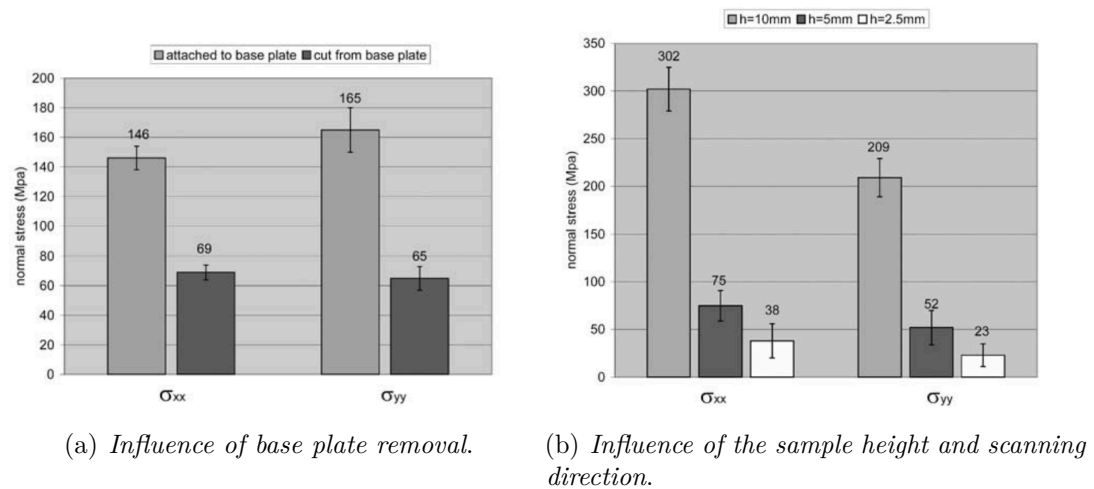
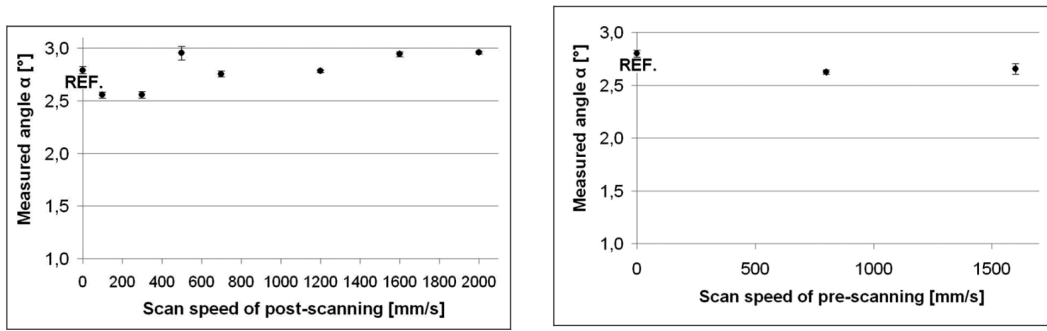


Figure 2.24: Residual stresses on stainless steel 316L sample with: (a) random sector scanning exposure, (b) Y-direction scanning exposure, [88].



(a) Influence of scan speed of post-scanning on curling angle (b) Influence of scan speed of pre-scanning on curling angle

Figure 2.25: Results of post-scanning and pre-scanning with different scan speeds [73].

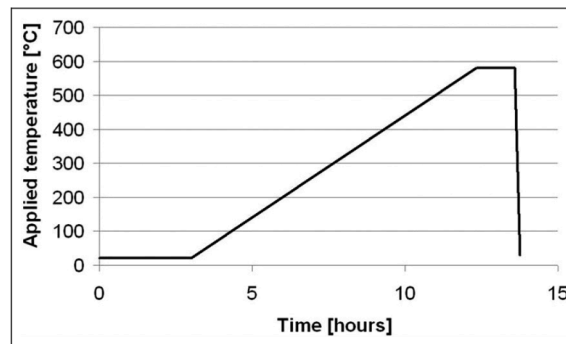


Figure 2.26: Temperature cycle for heat treatment [73].

in the melt pool whereas moving towards the melt pool boundary the grains become coarser. Also a coarse-dendritic microstructure is visible next to keyhole pores because of different thermal conductivity of air in the keyhole and solid material. The keyhole pores contain powder that is not fully melted.

Kruth et al. [72] investigated the effect of scanning velocity on relative density for AISI 316L stainless steel powder bed processed on a Concept Laser M3 Linear SLM machine (Fig. 2.29). At low scanning speed the effect of the layer thickness is negligible and a maximum of 99 % relative density is achievable. At higher scan speed values, a higher layer thickness results in less density. However, the layer thickness can be increased if the scan speed is sufficiently lowered to achieve the same density values.

The effect of three different scanning strategies on relative density for parts produced from Ti6Al4V powder is shown in Fig. 2.30a. The scanning strategies are uni-directional, bi-directional or 'zigzag', and an alternating strategy with bi-directional scan lines in which the scan lines are rotated 90° in each new layer (Fig. 2.30(b)). The latter presents the highest relative density probably due to the reduction of un-melted zones.

Re-melting process is an useful method to obtain full dense parts. Indeed, during SLM little residual porosity can be still problematic for some applications where fatigue loading or excellent strength with high ductility is necessary. Laser re-melting can be applied after scanning each layer or only for the top surface (Surface Re-melting, LSR). The average porosity of parts without re-melting is about 0.77 % whereas for the re-melted parts the porosity is 0.032 % [72]. The re-melting process is also valuable to reduce the surface roughness, e.g. after LSR the average roughness decreases from 12

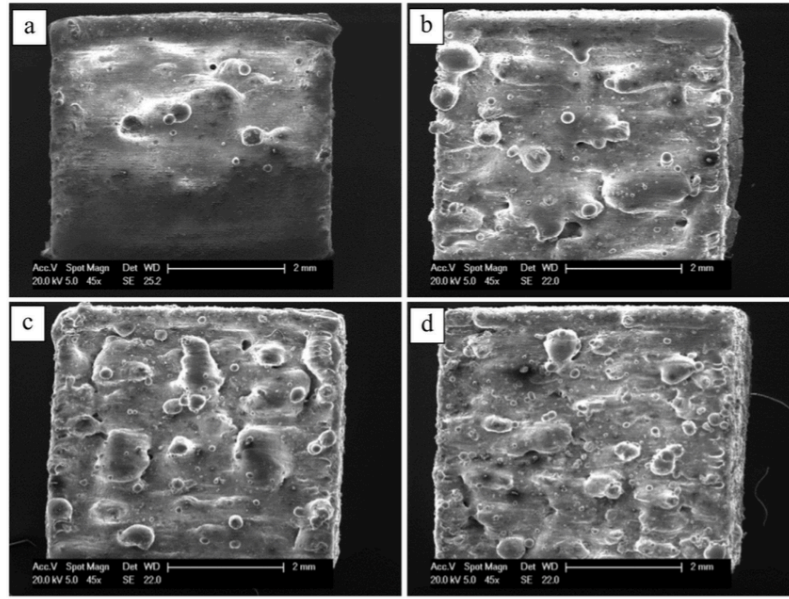


Figure 2.27: Balling increases with higher scanning speed [4].

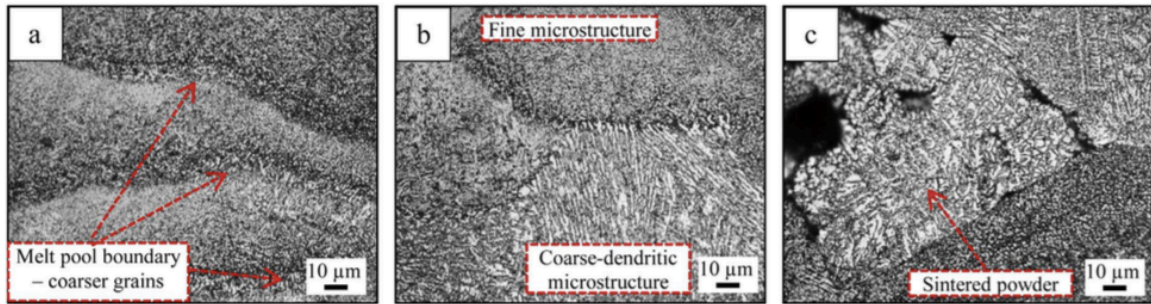


Figure 2.28: Microstructures of etched samples: (a) adjacent melt pool, (b) vicinity of a keyhole pore and (c) keyhole pore enclosing non-molten powders [4].

μm to about $1.5 \mu\text{m}$. LSR procedure can lead to the 'edge effect' when the re-molten material is partially pushed to the contours of the part by the laser beam to form solidified edges. However, the edge effect can be reduced applying appropriate process parameters.

2.3.4 Mechanical properties

The mechanical properties of SLM metals are determined by the micro-structural features in SLM metals, such as grain size, texture and residual porosity. Specific choices of SLM controlling parameters are required in order to obtain optimal mechanical properties. The mechanical properties of SLM components might be different from the properties of bulk materials produced by standard production techniques; indeed the material properties are significantly influenced by the microstructure.

Vrancken et al. [128] studied the effect of several heat treatments on the micro-structures and mechanical properties of Ti6Al4V processed by SLM. In particular they considered the mechanical properties of a extra-low interstitial Ti6Al4V (Grade 23) powder processed by SLM compared to a equiaxed Ti6Al4V (Grade 5) hot forged and mill

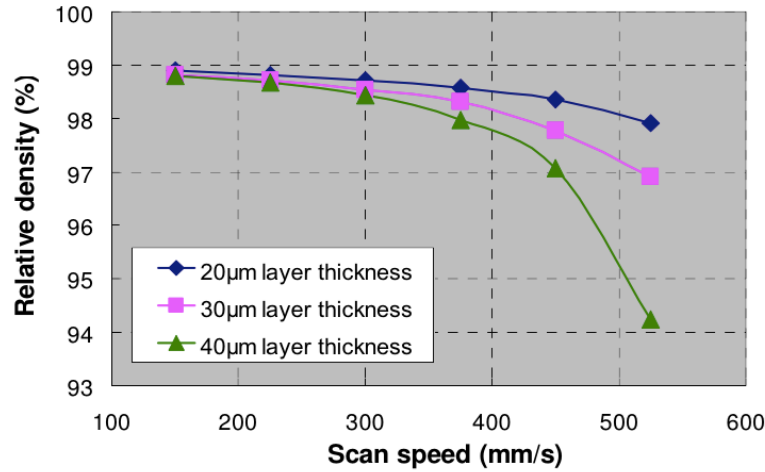


Figure 2.29: Effect of scan speed on the relative density for AISI 316L stainless steel, [72].

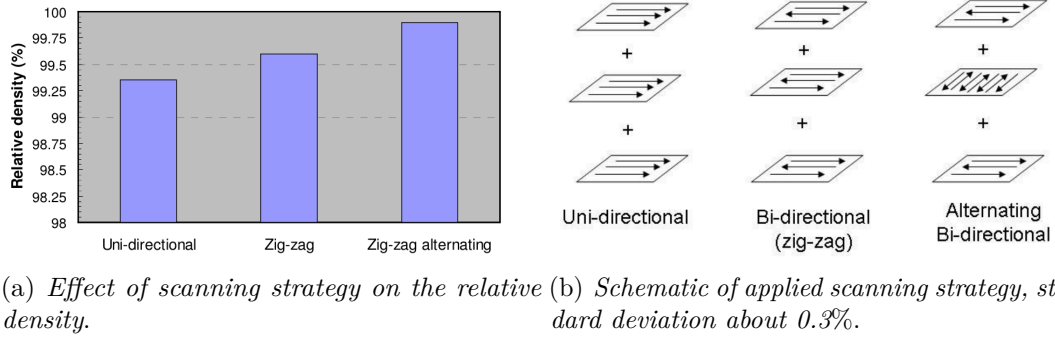


Figure 2.30: Influence of scanning strategy on relative density of Ti6Al4V material, [72].

annealed (reference material). Four tensile test samples of the SLM material were tested perpendicular to the build direction to determine the mechanical properties. The stress-strain responses are presented in Fig. 2.31. The results show that the Young's modulus of the SLM material is slightly lower than that of the reference material due to the texture of the SLM material. Also, the SLM material is much stronger than the reference material because the rapid cooling conditions of SLM always leads to a fine micro-structure. Because of the fine lamellar structure, the fracture strain is much lower compared to the equiaxed reference material. The mechanical properties, Young's modulus, yield stress, ultimate tensile strength and fracture strain, are presented in Tab. 2.1.

Currently the literature presents experimental data for aluminium and titanium alloys,

Table 2.1: Mechanical properties of SLM and reference material.

	E (GPa)	σ_y (MPa)	UTS (MPa)	$\epsilon_{\text{fracture}}$ (%)
SLM	109.2 ± 3.1	1110 ± 9	1267 ± 5	7.28 ± 1.12
Reference	120.2 ± 1.9	960 ± 10	1006 ± 10	18.37 ± 0.88

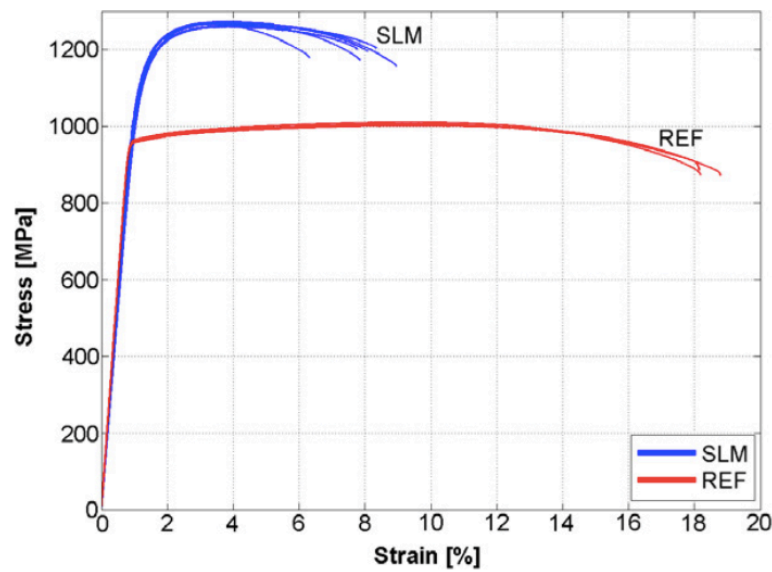


Figure 2.31: Stress-strain curves for SLM material and reference material.

nickel-based alloys, and stainless steels, studying the influence of a limited number of parameters, such as laser power, scan speed, and building direction.

Laser power

Niendorf et al. [93] presented the microstructure and the mechanical behaviour of an highly anisotropic austenitic alloy 316L directly obtained from powder processed by SLM. The loading axis is parallel to the built direction of the tensile specimens. Two Yttrium fiber lasers are employed in the current SLM system, featuring maximum beam energies of 400 W and 1000 W, respectively. The use of a 1000 W high energy laser system for SLM of 316L stainless steel allows for the establishment of a coarse and strongly textured microstructure directly from the powder bed. The stress-strain curves are depicted in Fig. 2.32(a) for 316L samples manufactured by the 400 W and the 1000 W laser systems. The differences in strength and ductility can be explained based on the grain size of either condition. The fine-grained structure of the material processed employing the 400 W system is characterized by high strength according to the Hall–Petch relation [54].

Scan speed

Zhang et al. [148] presented the stress-strain curves at different laser scan speeds for a biomedical Ti-24Nb-4Zr-8Sn alloy, showing changes in ductility, while Young’s modulus and strength do not depend on the scan speed (Fig. 2.32(b)). At the same laser power, the grain size of the SLM material becomes smaller and smaller with the increase of the scanning speed; Song et al. [118] observed that a higher scanning velocity induces a lower cooling rate with resulting small grains. The typical tensile stress-strain curves at different laser scan speeds, with laser power of 100 W, are presented in Fig. 2.33(a). The curve with 0.4 m/s presents an higher Young’s modulus, ultimate tensile strength (UTS) and yield strength ($\sigma_{0.2}$) (Tab. 2.2).

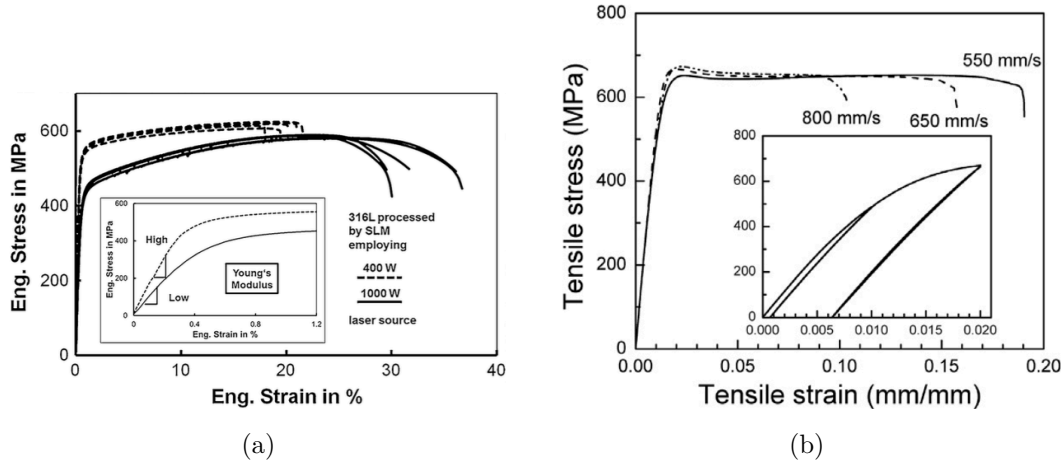


Figure 2.32: (a) Monotonic stress-strain curves for 316L processed by 1000 W (solid lines) and by 400 W (dashed lines), the inset shows the initial response of both conditions upon loading, with significant differences of Young's moduli [93]; (b) Typical stress-strain curves of parts processed at different laser scan speeds[148].

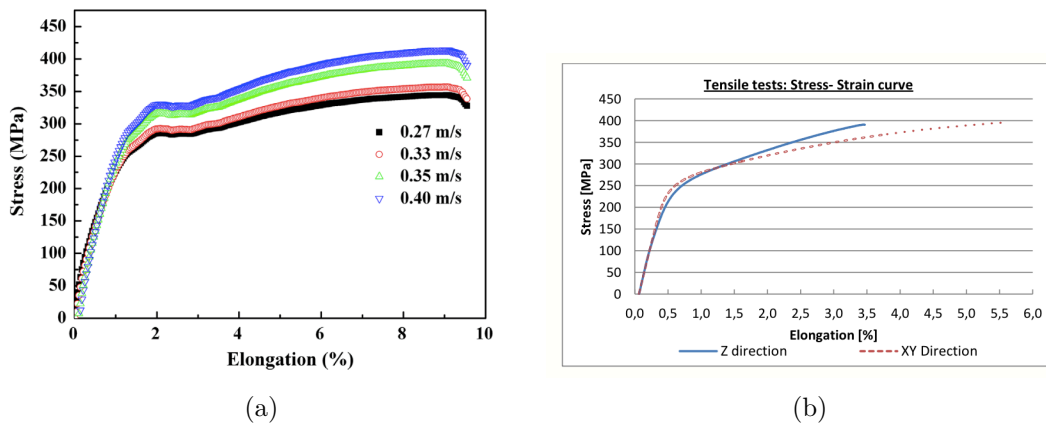


Figure 2.33: (a) Typical stress-strain curves of SLM-processed iron specimens at the laser power of 100 W using different scanning speeds [118]; (b) Stress-strain curves for parts produced with different directions [63].

Table 2.2: Tensile properties of SLM built parts using different laser scanning speeds [118].

V (m/s)	E (GPa)	$\sigma_{0.2}$ (Mpa)	UTS (Mpa)
0.27	205.6 ± 16	245.8 ± 17	354.2 ± 18
0.33	208.7 ± 16	256.5 ± 17	356.6 ± 22
0.35	210.5 ± 20	285.4 ± 20	402.7 ± 24
0.4	215.8 ± 20	305.3 ± 22	411.5 ± 25

Building direction

Building direction is a fundamental process parameter influencing mechanical properties of the produced part and, in fact, SLM samples present anisotropy in their properties (e.g., Tab. 2.3 and Fig. 2.33(b)). Chlebus et al. [28] investigated relationships between layered manufacturing strategy for Ti-6Al-7Nb alloy and its micro-structural and mechanical characteristics. The mechanical properties, as tensile yield, Young's modulus, elongation, ultimate compressive and tensile strengths and Vickers hardness, are shown in Tab. 2.4. Differences in elasticity and in UTS values between horizontal and vertical specimens are related to a different distribution and level of residual stresses. Also the specimens show an higher compression strength than the UTS values, mainly due to the reduction of the dimension of pores during the compression test.

Table 2.3: Mechanical properties of SLM built parts at different building directions [63].

Build direction	E (GPa)	UTS (Mpa)	$\varepsilon_{break}\%$	HV
x-y	68 ± 3	391 ± 6	5.55 ± 0.4	127
z	-	396 ± 8	3.47 ± 0.6	-

Table 2.4: Mechanical properties of SLM built Ti6Al-7Nb alloy at different building directions [28].

Build direction	E (GPa)	$\sigma_{0.2}(MPa)$	UTS (Mpa)	$\varepsilon\%$	HV10	$\sigma_c(MPa)$
A series	88 ± 2	1440 ± 59	1515 ± 60	1.4 ± 0.6	464 ± 14	2002 ± 25
B series	88 ± 3	1360 ± 30	1480 ± 26	3.0 ± 0.7	410 ± 26	-
C series	121 ± 14	-	776 ± 40	-	357 ± 18	1942 ± 64

2.4 Summary

The present chapter presented a description of the main physical phenomena arising during SLM process and an overview of the significant process parameters. Besides the classical heat transfer by conduction, convection and radiation, there exist also very particular physical mechanisms: among these, the undesired 'balling effect' results in a combination of a loss of wetting and capillary instabilities. The control of some input process parameters, such scanning speed and laser power, can significantly affect the success of the final parts. The interest in literature of these effects is justified since there is not a general good selection of input parameters. A significant support to the

comprehension of best parameter choice for a selected material is the introduction of a numerical model of SLM process. The following chapter will describe the governing equations of the physical model.

Chapter 3

Selective Laser Melting modelling

The definition of an efficient model may give a good representation of the real behaviour of the manufactured parts. First of all, this goal can be achieved assuming a multi-scale model able to represent the nature from the melt pool to the macro-structure, and a multi-physics model able to capture the thermo-mechanical behaviour of manufactured parts. To do this a heat conduction model, with or without convection, with the assumed initial and boundary conditions (radiation, laser source, etc.) can clearly represent the problem. A constitutive model must be developed representing the macroscopic behaviour of SLM products. Furthermore phase transformations inside the material with the change of internal energy must be represented in the model to capture the temperature field and the location of solid-liquid interface.

Clearly different choices of physical models can be assumed which can be more or less accurate. In the following chapter an overview of the physical models and its governing equations of heat conduction, phase-field and mechanical models will be presented.

3.1 A description of physical models

SLM modelling is very challenging due to the multi-physics (thermal, mechanical, fluid-dynamic) and multi-scale (micro/meso/macroscale) nature of the process. For a metal alloy space scales range from submicron, associated with the characteristic length of the solid-liquid interface, to the entire process, which can be of order of meters.

During the process new layers of powder are deposited over the domain and the complete process invests many hours; on the other hand a phase change occurs inside the domain with a time scale of microseconds. For this reason a complete model should account the heat transfer and the phase change occurring in an ample range of time and space scales.

In general heat transfer models can be classified into two different approaches: the first based on classical heat conduction equations, neglecting fluid flow, and the second based on Navier-Stokes equations, including fluid flow. The heat transfer model consists of the balance of thermal energy, with the associated boundary and initial conditions. The heat transfer rate is described by the classical Fourier equation:

$$q = -k \nabla T \quad (3.1)$$

where k is the thermal conductivity of the material and T is the temperature.

When convection is considered within the liquid melt, a transport term has to be added to the energy equation; the fluid flow pattern is calculated using the Navier-Stokes equation [22].

Associated with heat transfer, a phase transformation occurs inside the material: during the process the scanned material changes from powder to liquid and from liquid to solid. The phase change can be described using two different approaches: *front tracking models* and *fixed domain models*. The front tracking models use the classical Stefan problem equation and consider two phases (solid and liquid) with distinct governing equations. The condition on the interface between the two regions is described by the Stefan condition:

$$k_s \frac{\partial T_s}{\partial n} - k_l \frac{\partial T_l}{\partial n} = L \rho \frac{ds}{dt} \quad (3.2)$$

where k_s , T_s , k_l , T_l are the thermal conductivities and the temperatures of solid and liquid respectively; L is the latent heat, ρ is the density, and s is solid-liquid interface location.

The fixed domain models consider the solid and liquid phases as a single domain and the Stefan condition is included in the energy equation.

During SLM process multiple heating and cooling cycles in the irradiated parts take place with strong temperature gradients. As cyclic thermal expansions and contractions far exceed the maximum elastic strain of the material, plastic strains are cumulated in the manufactured part generating internal stresses. The internal stresses can reach the strength of the material and cracks may appear during the process or reduce the fatigue life of the part. In particular when laser hits the top surface the expansion of the heated layer is restricted by the surrounding area and compressive stresses are generated on the top surface; as the laser moves away, cooling of the melted parts generates a contraction on the top layer, which is restricted by the surrounding area leading to tensile residual stresses on the top surface (Fig. 3.1). Furthermore, cooling and volumetric shrinkage can generate short top layers and the component is distorted by bending toward the laser beam [46].

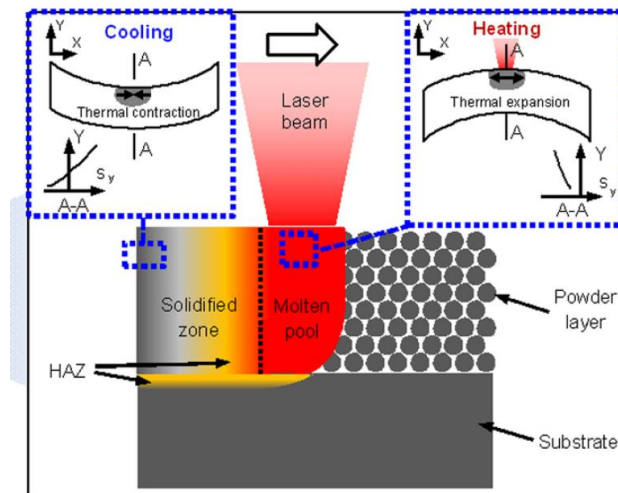


Figure 3.1: SLM process principle [46].

3.1.1 Heat conduction models

The most common formulation considers SLM thermal evolution as a heat transfer process utilizing Fourier heat conduction theory. The following equations describe the governing heat conduction in the moving medium with the initial and boundary conditions on the top and on the bottom of powder bed. The transient spatial temperature distribution $T(x, y, z, t)$ must satisfy the following governing equations:

$$\rho c_p \frac{\partial T}{\partial t} = \nabla \cdot (\mathbf{k} \nabla T) + Q \quad \text{on } \Omega \quad (3.3)$$

$$T(x, y, z, 0) = T_0 \quad \text{on } \Omega \quad (3.4)$$

$$-\mathbf{k} \frac{\partial T}{\partial \mathbf{n}} = \varepsilon \sigma (T^4 - T_e^4) + h(T - T_e) \quad \text{on } \Gamma_g \quad (3.5)$$

$$-\mathbf{k} \frac{\partial T}{\partial \mathbf{n}} = 0 \quad \text{on } \Gamma \quad (3.6)$$

In the heat conduction equation (Eq. 3.3) the laser heat source Q is described

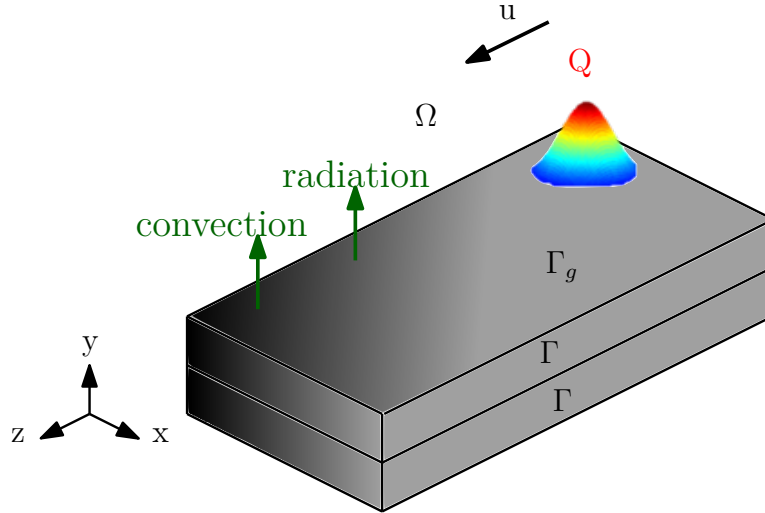


Figure 3.2: Heat conduction problem formulation.

as an internal energy [55]; more common is the definition of the laser heat source as a boundary condition q in Eq. 4.4 [66, 105?]. Hodge et al. [55] and Dai and Shaw [33] used the presented governing equations to investigate the thermal field of a SLM component. Badrossamay and Childs [11] assumed that the major source of heat loss through the powder bed is by conduction and the contributions of convection and radiation can be neglected without any loss of accuracy. Koric and Thomas [67] and Roberts et al. [105] considered only the heat loss by convection and conduction, whereas the radiative contribution is neglected.

Laser beam model

The temperature field distribution of powder bed is strongly influenced by the characteristics of the laser beam, such as laser power, laser beam radius, laser speed, etc. Different choices of laser beam irradiation models can be found in literature but most of them are surface (W/m^2) than volumetric laser beam model (W/m^3) due to the very

small layer thickness of the powder (30-100 μm). The cylindrical model of the laser beam assumes that the laser beam is constant at every point of the spot surface. In this case, the surface heat flux can be written as:

$$q_{cyl} = \frac{P}{\pi R^2} \quad (3.7)$$

where P is the laser power and R is the laser beam radius. Liu et al. [83] adopted the cylindrical model and considered the amount of the laser beam flux absorbed by the powder:

$$q_{cyl} = \frac{\alpha P}{\pi R^2} \quad (3.8)$$

where α is the absorptance of the irradiated material, which is in general temperature dependent.

The Gaussian model is the most widely adopted irradiation model and assumes the symmetrical distribution of the laser irradiation across its field domain. The maximum irradiance (power per unit area) I_0 is in the centre of the beam and it reduces exponentially outwards. The beam irradiance for the Gaussian distribution is [49]:

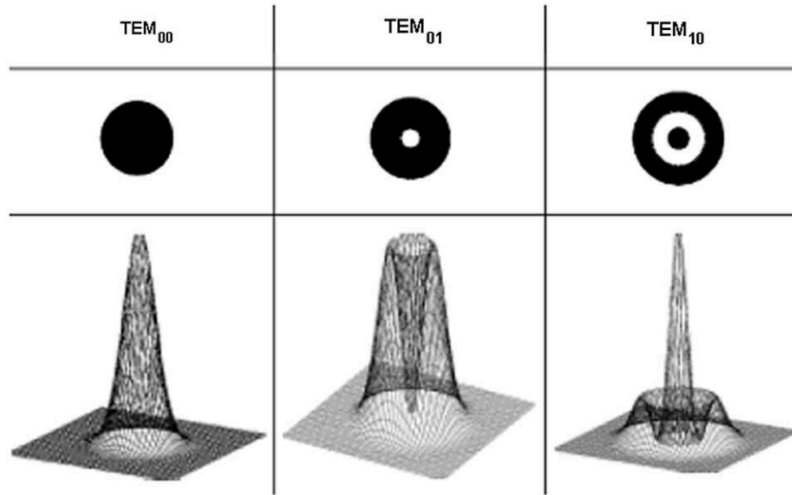


Figure 3.3: Transverse electromagnetic modes of Gaussian profile [106].

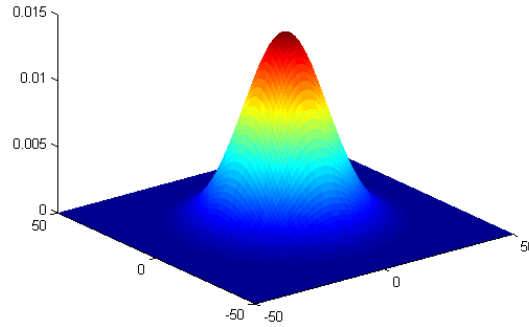
$$I(r) = I_0 e^{-Cr^2} \quad (3.9)$$

where C is the concentration coefficient and $r = \sqrt{(x^2 + y^2)}$ is the radial distance at an instance from the centre of the laser beam and (x, y) are the points belonging to the plane perpendicular to the beam direction. The radius of the laser beam R is the radius corresponding to the point where the laser irradiation is I_0/e^2 . In order to evaluate the concentration coefficient C , the irradiance when $r=R$ is:

$$I(R) = I_0 e^{-CR^2} = I_0 e^{-2} \quad (3.10)$$

Hence,

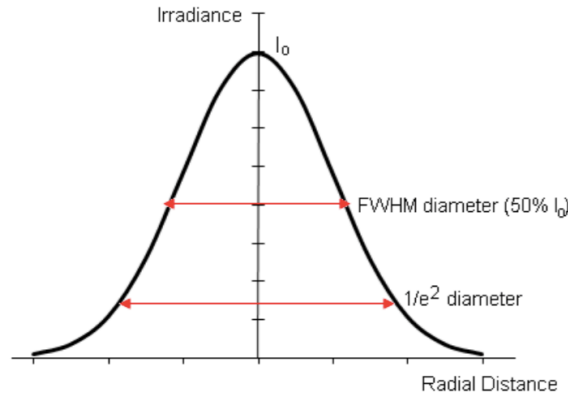
$$C = 2/R^2 \quad (3.11)$$

Figure 3.4: Gaussian heat distribution for $C = 2/R^2$.

and Eq. 3.9 can be re-written:

$$I(r) = I_0 e^{-2r^2/R^2}. \quad (3.12)$$

According with the Full Width at Half Maximum (FWHM), a second definition of the beam radius is where the beam irradiance is reduced to 50 % of its peak (Fig. 3.5). The laser beam power P can be written as:

Figure 3.5: Irradiance profile for Gaussian TEM_{00} mode [106].

$$P = 2\pi \int_0^{+\infty} I(r) r dr. \quad (3.13)$$

The maximum irradiance I_0 can be calculated from the power equation (Eq.3.13):

$$P = 2\pi \int_0^{+\infty} I_0 e^{-2r^2/R^2} r dr \quad (3.14)$$

$$P = 2\pi I_0 \int_0^{+\infty} e^{-2r^2/R^2} r dr \quad (3.15)$$

$$P = -2\pi I_0 \frac{R^2}{4} \int_0^{+\infty} \frac{4r}{R^2} e^{-2r^2/R^2} dr \quad (3.16)$$

$$P = -2\pi I_0 \frac{R^2}{4} \left[e^{-2r^2/R^2} \right]_0^{\infty} \quad (3.17)$$

$$P = 2\pi I_0 \frac{R^2}{4} \quad (3.18)$$

$$I_0 = \frac{2P}{\pi R^2}. \quad (3.19)$$

Toyserkani et al. [123] used a pulsed Gaussian laser beam according with equations 3.9 and 3.19. Yuan and Gu [145] and Dai and Shaw [33] used the Gaussian model considering only the absorbed radiation by the powder material:

$$I(r) = \frac{2\alpha P}{\pi R^2} e^{-2r^2/R^2}. \quad (3.20)$$

Dong et al. [40], Yilbas and Akhtar [143], and Hussein et al. [59] considered the radiation reduced of the loss by reflection if the reflectivity R_e is known:

$$I(r) = (1 - R_e) \frac{2P}{\pi R^2} e^{-2r^2/R^2}. \quad (3.21)$$

Patil and Yadava [100] assumed a different form of the laser irradiance to deduce the temperature distribution in a single metallic powder layer during laser sintering. The equation is given by:

$$I(r) = \frac{4.55P}{\pi R^2} e^{-4.5(r/R)^2}. \quad (3.22)$$

Roberts [106] considered an equivalent form of the cylindrical model computing a numerical average of the Gaussian distribution. The model considers the integration of the Gaussian irradiance (Eq. 3.20) over the circumference of radius R . The equivalent heat flux q results in:

$$\bar{q} = 0.864 \alpha \frac{P}{\pi R^2} = 0.864 \alpha q_{cyl}. \quad (3.23)$$

Goldak et al. [49] considered a Gaussian distribution over an ellipsoid with center at (0,0,0) and semi-axes a , b , and c such that the beam irradiance $I(r)$ (Eq. 3.10) falls to $0.05 I_0$ at ellipsoidal surface. The ellipsoidal heat source is:

$$q(x, y, z) = \frac{6\sqrt{6}\alpha P}{\pi\sqrt{\pi abc}} e^{-3\left(\frac{x^2}{a^2} + \frac{y^2}{b^2} + \frac{z^2}{c^2}\right)} \quad (3.24)$$

and when the depth of the heat source approaches zero (i.e. $b \rightarrow 0$) the ellipsoidal heat source becomes elliptical and is expressed as:

$$q(x, z) = \frac{3\alpha P}{\pi ac} e^{-3\left(\frac{x^2}{a^2} + \frac{z^2}{c^2}\right)}. \quad (3.25)$$

Li et al. [81] assumed a volumetric heating source assuming a mixture of the Gaussian and Doughnut modes:

$$q(x, y, z) = \frac{(1 - R_e)P}{\pi R^2 \gamma} \left[f + (1 - f) \frac{x^2 + y^2}{R^2} \right] \exp \left(-\frac{x^2 + y^2}{R^2} - \frac{|z|}{\gamma} \right) \quad (3.26)$$

where f is the fraction of laser mode structure that contains the Gaussian mode, R_e is the reflectivity and γ is the absorption length of the workpiece material to the incident laser. Tseng and Aoh [124] depicted a tailored TEM_{mixed} mode laser beam composed of TEM₀₀, TEM₀₁, TEM₁₀, TEM₁₁, and TEM₃₃ modes. The heat fluxes of the mixed

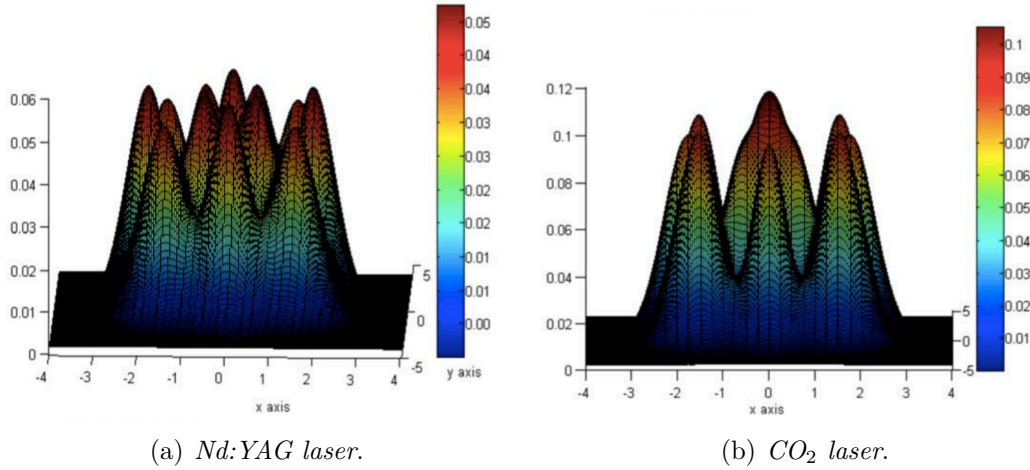


Figure 3.6: Intensity distribution of the tailored TEM_{mixed} mode laser heat sources, [124].

mode q_{mixed} of Nd:YAG and CO₂ lasers are depicted in Fig. 3.6(a)-3.6(b) and are expressed as a combination of the heat flux distribution of the individual TEM_{mn} modes weighted of fraction a_i :

$$q_{mixed} = \sum_{i=1}^n a_i \cdot q_f \quad (3.27)$$

with

$$\sum_{i=1}^n a_i = 1 \quad (3.28)$$

where n is the total number of modes and q_f is the heat flux intensity of the laser beam at the focal point. The laser beam during the SLM process is not static but it moves along the irradiated surface with velocity $\mathbf{u} = (u_x, u_z)$. The radial distance from the centre of the laser beam r can be written as [40]:

$$r = \sqrt{(x - u_x t - x_0)^2 + (z - u_z t - z_0)^2} \quad (3.29)$$

where (x, z) represents the position of the point in the irradiated surface, (u_x, u_z) are the components of the beam velocity vector \mathbf{u} in x and z directions, and (x_0, z_0) are the initial planar coordinate of the center of the laser beam.

3.1.2 Fluid flow models

The physical model of the SLM process is related with the fluid flows of the melted powder which influences the solidification at both the macroscopic and microscopic levels. Convection can be induced by body forces, natural (e.g. gravity associated with a temperature and/or solute gradient) or induced forces (e.g. electromagnetism), and by shear surface stresses at free surfaces which result from surface tension gradients (Marangoni effect) [102]. Modelling convection of non-stationary solidification problem is rather difficult, because the liquid region changes with time. When convection is present within the liquid melt, a transport term has to be added to the heat flow equation (3.3) giving:

$$\rho c_p \frac{\partial T}{\partial t} + \rho c_p \mathbf{u} \cdot \nabla T = \nabla \cdot (k \nabla T) + Q \quad (3.30)$$

where \mathbf{u} is the velocity vector. The continuity and Navier-Stokes equations are introduced to account the motion of the fluid. The continuity, momentum and energy equations which simulate thermo-fluid incompressible transport comprising melting and solidification are given by:

$$\nabla \cdot \mathbf{u} = 0 \quad (3.31)$$

$$\frac{\partial \mathbf{u}}{\partial t} + \mathbf{u} \cdot (\nabla \mathbf{u}) + \frac{1}{\rho} \nabla p = \nu \Delta \mathbf{u} + \mathbf{g} \quad (3.32)$$

$$\frac{\partial}{\partial t}(\rho e) + \nabla \cdot (\rho \mathbf{u} e) = \nabla \cdot (k \nabla T) + r \quad (3.33)$$

where p the pressure, ν the kinematic viscosity, \mathbf{g} the gravity, e is the internal energy and r the rate of heat received by radiation. Zhang and Faghri [151] considered the fluid flow of the liquid phase given by the density change of the material; Chan and Mazumder [22] developed a two-dimensional convective heat transfer and fluid flow analysis which revealed interesting aspects of the surface tension driven fluid flow in the melt pool.

3.2 Phase change models for pure heat conduction equations

Melting and solidification processes of powder material in SLM require the introduction of the concept of *moving-boundary problems*. Problems in which the solution of a differential equation has to satisfy certain conditions on the boundary of a prescribed domain are referred to as *boundary-value problems*. 'Moving boundaries' are associated with time-dependent problems and the position of the boundary has to be determined as a function of time and space. Moving-boundary problems are often called *Stefan problems*, with reference to the early work of J. Stefan who, around 1890, was interested in the melting of the polar ice cap [32].

A detailed description of the phase change problem, along with an overview of the analytical solution for the problem on a one-dimensional domain, can be found in the work of Hu and Argyropoulos [56].

3.2.1 Physical phenomena during phase change

When the solid starts melting it acquires a certain amount of energy to overcome the binding forces that maintain its solid structure. This energy is referred to as the latent heat of fusion L of the material and represents the difference in enthalpy levels between liquid and solid state. The microstructure of the interface between solid and liquid depends on several factors, such as material itself, rate of cooling, temperature gradient in the liquid, surface tension, etc. The thickness of the interface may vary from a few Angstroms to a few centimetres [10].

For most pure materials the phase change is isothermal since occurs at a fixed melting temperature T_m , (Fig. 3.7a). In other cases, typically resulting from supercooling or presence of multiple components (e.g. metal alloy), phase change takes place over a temperature interval, called 'mushy zone', between solid T_s and liquid T_l temperatures; in this case a non-isothermal or mushy phase-change occurs, (Fig. 3.7b). For isothermal case, the interface appears (locally) planar and of negligible thickness; for non-isothermal

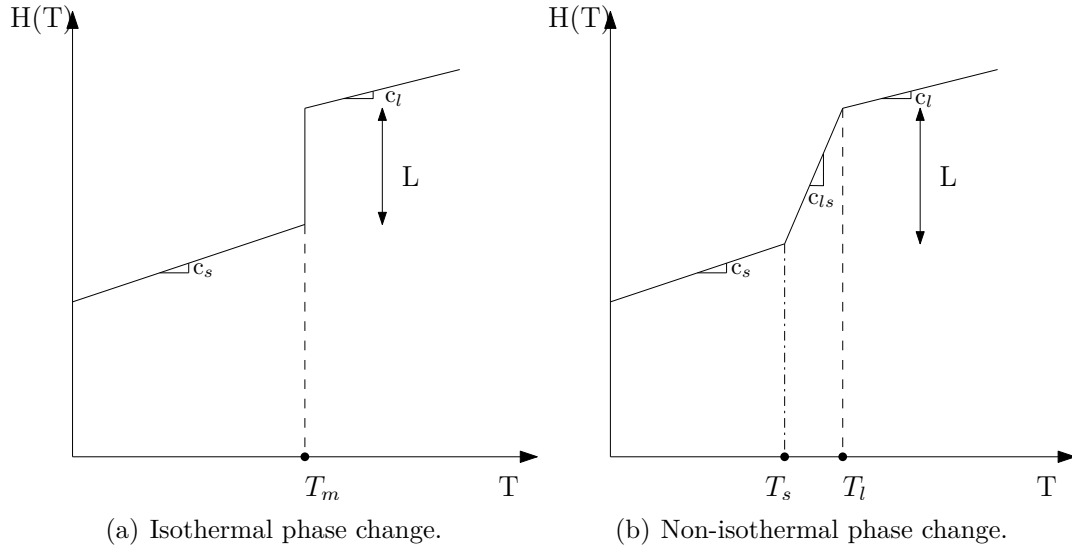


Figure 3.7: Typical enthalpy versus temperature relations: (a) isothermal phase change and non-isothermal phase change.

case the phase transition region may have apparent thickness and its microstructure may appear to be dendritic or columnar, (Fig. 3.8). In this case a sharp solid-liquid interface can be identified only at the microscopic length scale of the “secondary dendrite arm” spacing, $\lambda \approx 10\text{-}100 \mu\text{m}$.

During phase transformation also thermo-physical properties (e.g., thermal conductivity, specific heat, etc.) change with temperature. In particular, density change of material is the most relevant phenomenon which may induce important effects during the transformation: density change results in fluid flow by natural convection in the presence of gravity and also in volume ‘shrinkage’ in porous media.

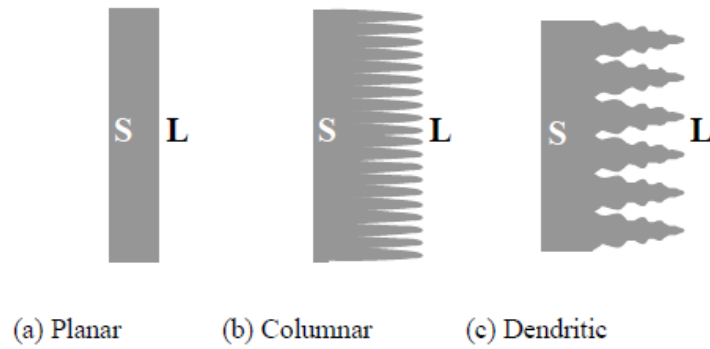


Figure 3.8: Possible solid-liquid interfaces: planar, columnar and dendritic [10].

3.2.2 Front tracking models: the Stefan problem

Single phase

The classical Stefan problem describes the temperature distribution $T(x,t)$ and the evolution of melting interface $s(t)$ in a homogeneous medium undergoing a phase change, for example ice passing to water. For single phase model, suppose to have the ice at

the melting temperature, taken to be zero, and, at time $t=0$, the temperature above zero. Heat flow occurs only in the water region. A boundary surface or interface, on which melting occurs, moves from the surface into the sheet and separates water from ice at zero temperature (Fig. 3.9).

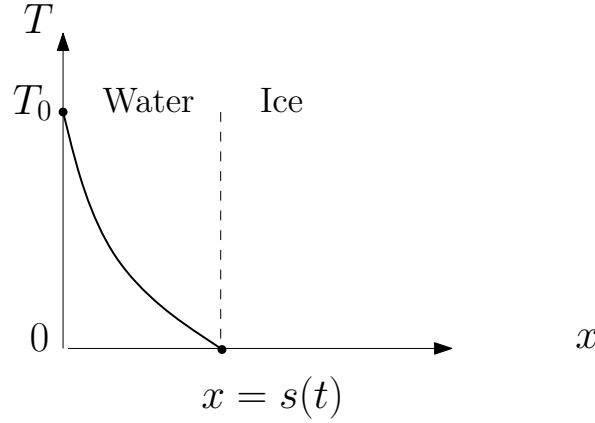


Figure 3.9: Stefan model for a single phase.

The governing equations to obtain the unknowns $T(x,t)$ and $s(t)$ are:

$$c_p \rho \frac{\partial T}{\partial t} = k \frac{\partial^2 T}{\partial x^2}, \quad 0 < x < s(t), \quad t > 0 \quad (3.34)$$

$$T = T_0, \quad x = 0, \quad t > 0 \quad (3.35)$$

$$T = 0, \quad x > 0, \quad t = 0 \quad (3.36)$$

$$s(0) = 0 \quad (3.37)$$

where equation (3.34) is the heat flow equation in the water region; equation (3.35) is the boundary condition, with T_0 the constant surface temperature; equations (3.36) and (3.37) are the initial conditions, respectively on the temperature and on the interface. In equation (3.34) the heat capacity c_p , density ρ and thermal conductivity k are assumed to be constant. Two further conditions are needed to provide the second boundary condition necessary for the solution of the second-order equation (3.34) and to determine the position of the interface itself:

$$T = 0, \quad x = s(t), \quad t > 0 \quad (3.38)$$

$$-k \frac{\partial T}{\partial x} = L \rho \frac{ds}{dt}, \quad x = s(t), \quad t > 0 \quad (3.39)$$

where L is the latent heat required to melt ice. Equation (3.39) is known as 'Stefan condition' and it expresses the heat balance on the interface [32].

Two phases

When the ice is initially at a temperature below the melting temperature, two phases problem occurred and heat flows in both water and ice phases. In this case, the unknowns are $T_l(x, t)$, $T_s(x, t)$ and $s(t)$. For a finite sheet of ice occupying the space $0 \leq s(t) \leq l$, the equations are:

$$c_{pl}\rho_l \frac{\partial T_l}{\partial t} = k_l \frac{\partial^2 T_l}{\partial x^2}, \quad 0 < x < s(t), \quad t > 0 \quad (3.40)$$

$$c_{ps}\rho_s \frac{\partial T_s}{\partial t} = k_s \frac{\partial^2 T_s}{\partial x^2}, \quad s(t) < x < l, \quad t > 0 \quad (3.41)$$

Assuming no volume changes on melting, the Stefan conditions are:

$$T_l = T_s = 0, \quad x = s(t), \quad t > 0 \quad (3.42)$$

$$k_s \frac{\partial T_s}{\partial x} - k_l \frac{\partial T_l}{\partial x} = L\rho \frac{ds}{dt}, \quad x = s(t), \quad t > 0 \quad (3.43)$$

Konrad et al. [66] described the melting and solidification process in a two-component metal powder bed using the Stefan conditions at the interface between liquid and unsintered powder. Also Zhang and Faghri [151] analytically investigated the melting of a subcooled powder bed that contains a mixture of two powders with significantly different melting points using Stefan conditions on the interface.

3.2.3 Numerical methods

The analytical methods used to solve nonlinear phase change problems are very limited: the investigated cases are very simple especially in geometry and the methods does not work for two- or three-dimensional problems, where most real applications of phase change occur. In addition, natural convection in the liquid phase often plays a significant role in the phase-change processes. Therefore, it is necessary to employ numerical methods. The numerical approaches, presented in the literature, may be divided into two classes of methods:

- front-tracking or 2-domain methods
- fixed domain or 1-domain methods

where the main difference is based on the description of the melting front.

Front-tracking methods (Fig. 3.10a) for the melting and solidification process (with fluid flow) in the melt involve treating the solid and the liquid as distinct domains coupled by the boundary conditions at the phase change front. At each time the position of the boundary is explicitly computed. In order to account for its motion, either mesh deformation or a suitable mapping that transforms the problem on a fixed mesh is required. This strategy is suitable for the isothermal phase change of a pure substance and might not be accurate enough when the state transformation happens over a finite temperature interval. Front-tracking methods explicitly evaluate the interface at each time step and consider the temperature gradient across the interface. On the other hand, a starting solution is needed and the description of complex evolutions of the interface is neglected. For multi-phases problems fixed domain methods are used.

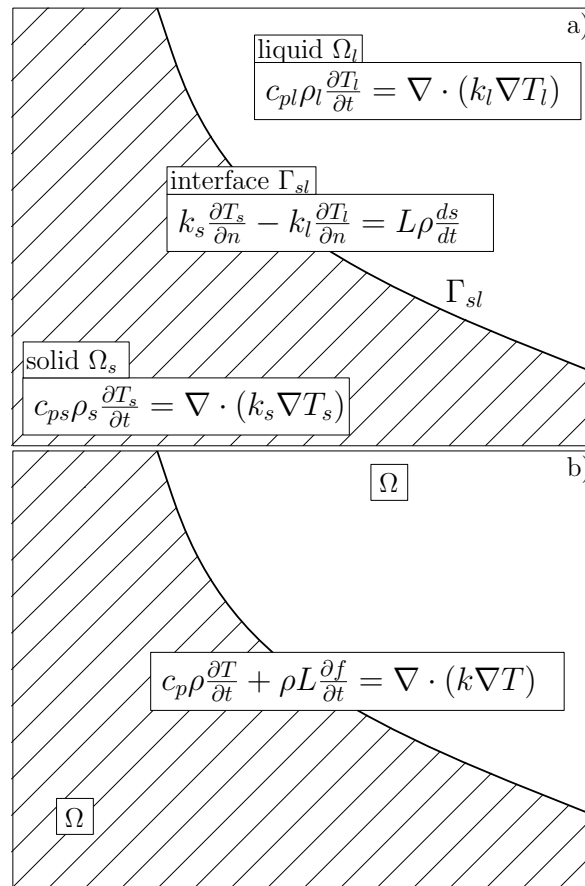


Figure 3.10: Numerical techniques: a) front tracking method; b) fixed domain method

Table 3.1: Main advantages and disadvantages of front tracking and fixed domain methods

Front tracking methods	
<i>Advantages</i>	<i>Disadvantages</i>
Temperature gradients as discontinuous function	Necessary starting solution
Efficient and accurate methods	No mushy phase change
Position of interface explicitly computed	No complex evolutions of interface
	Smooth interface
Fixed domain methods	
<i>Advantages</i>	<i>Disadvantages</i>
Complex evolutions of interface	Temperature gradients as smooth function
Mushy phase change	

Fixed domain methods (Fig. 3.10b) consider the solid and liquid phases as a single domain described by a single governing equation to eliminate the necessity of explicitly satisfying the thermal conditions between the two phases. The location of the solid-liquid interface is determined after the converged temperature distribution is obtained. The three principal important methods in this group are the *enthalpy method* [32, 114], the *equivalent heat capacity method* [12], and the *temperature-transforming model* [17]. A schematic description of the main advantages and disadvantages for front-tracking and fixed domain methods is shown in Tab. 3.1.

3.2.4 Front-tracking methods

Governing equations

In front-tracking methods the governing equations are applied separately to each domain (solid and liquid) and Stefan condition is applied on the interface. Suppose to study a single phase change problem with the following governing equations:

$$c_p \rho \frac{\partial T}{\partial t} = k \frac{\partial^2 T}{\partial x^2}, \quad 0 < x < s(t), \quad t > 0 \quad (3.44)$$

$$T = T_0, \quad x = 0, \quad t > 0 \quad (3.45)$$

$$T = 0, \quad x > 0, \quad t = 0 \quad (3.46)$$

$$s(0) = 0 \quad (3.47)$$

$$\left. \begin{array}{l} T = 0 \\ -k \frac{\partial T}{\partial x} = L \rho \frac{ds}{dt} \end{array} \right\} x = s(t), \quad t > 0. \quad (3.48)$$

When the solution is computed at points on a fixed grid in the space-time domain following the usual methods for obtaining a numerical solution of the simple heat-flow equation, the boundary will in general be between two grid points at any given time. Therefore, special formulae are needed to cope with terms like $\partial T / \partial x$ and ds/dt , as

well as with the partial differential equation itself, in the neighbourhood of the moving boundary. These formulae must allow for unequal space intervals. The difficulty is compounded if implicit finite-difference formulae are used, since the position of the moving boundary is not known at the new time and some iterative procedure is usually inevitable. Alternatively, the grid itself has to be deformed in some way, or some transformation of variables adopted, so that the moving boundary is always on a grid line or is fixed in the transformed domain [32].

3.2.5 Fixed domain methods

Governing equations

In the previous section we have described the front-tracking methods where sometimes is difficult or even impossible to track the moving boundary directly if it does not move smoothly or monotonically with time. The possibility is to reformulate the problem in such a way that the Stefan condition is implicitly bound up in a new form of the equations, over the whole of a fixed domain. The position of the interface is calculated a posteriori as one feature of the solution. Three different fixed domain methods can be distinguished:

- Enthalpy method
- Equivalent heat capacity method
- Temperature-transforming model

Enthalpy Method

In this methodology the governing energy equation is written for the entire region of Phase Change Material (PCM), including solid and liquid phase and the interface. This method has been successfully applied to various phase-change problems [91, 119, 126]. The enthalpy method is introduced by analysing a conduction-controlled, two region melting problem in a finite slab. It is assumed that the density of liquid and solid are identical. The energy equation can be written as:

$$\rho \frac{\partial H}{\partial t} = \frac{\partial}{\partial x} \left(k \frac{\partial T}{\partial x} \right). \quad (3.49)$$

The enthalpy H is a function of temperature T [91]:

$$H(T) = \begin{cases} \int_{T_{ref}}^T c_{p,s}(T) dT, & T \leq T_m \\ \int_{T_{ref}}^{T_m} c_{p,s}(T) dT + L + \int_{T_m}^T c_{p,l}(T) dT, & T > T_m \end{cases} \quad (3.50)$$

where the subscript l is for the liquid region and s for the solid region, L is the latent heat, and T_{ref} is the reference temperature. The variation of enthalpy H with temperature T can be plotted as shown in Fig. 3.7a. At the melting point of the PCM, the enthalpies of solid and liquid phases at the melting point are 0 and L . The thermal conductivity k of the PCM can be expressed as:

$$k(T) = \begin{cases} k_s, & T \leq T_m \\ k_l, & T > T_m \end{cases} \quad (3.51)$$

When the phase change of the material happens over a solid temperature T_s and a liquid temperature T_l (Fig. 3.8b), the enthalpy function can be expressed as [91]:

$$H(T) = \begin{cases} \int_{T_{ref}}^T c_{p,s}(T)dT, & T \leq T_s \\ \int_{T_{ref}}^{T_s} c_{p,s}(T)dT + \int_{T_s}^T \frac{\partial L}{\partial T}dT, & T_s < T \leq T_l \\ \int_{T_{ref}}^{T_s} c_{p,s}(T)dT + L + \int_{T_l}^T c_{p,l}dT, & T > T_l \end{cases} \quad (3.52)$$

Equivalent heat capacity method

During the solid-liquid phase-change process, the PCM can absorb or release heat at a constant temperature T_m . This means that the temperature of the PCM does not change while it absorbs or releases heat, implying that the heat capacity of the PCM at temperature T_m is infinite. In the equivalent heat capacity method, it is assumed that the melting or solidification processes occur over a temperature range ($T_m - \Delta T$, $T_m + \Delta T$) instead of at a single temperature T_m . For a multicomponent system ΔT is chosen based on the range of phase change temperature. For a single-component with well-defined melting point, ΔT should be as small as possible. The latent heat is converted to an equivalent heat capacity of the PCM in the assumed temperature range. Thus the specific heat of the PCM is expressed as:

$$c_p(T) = \begin{cases} c_{ps}, & T < T_m - \Delta T \\ \frac{L}{2\Delta T} + \frac{c_{ps} + c_{pl}}{2}, & T_m - \Delta T < T < T_m + \Delta T \\ c_{pl}, & T > T_m + \Delta T \end{cases} \quad (3.53)$$

which assumes that the temperature of the PCM is changed from $T_m - \Delta T$ to $T_m + \Delta T$ when latent heat is absorbed by the PCM during melting. During the solidification process, the PCM releases the latent heat and its temperature decreases from $T_m + \Delta T$ to $T_m - \Delta T$. The equivalent specific heat in the mushy zone ($T_m - \Delta T < T < T_m + \Delta T$) includes the effect of both latent heat (the first term) and sensible heat (the second term). The relationship between specific heat and temperature in the equivalent heat capacity method is plotted in Fig. 3.11. For a conduction-controlled melting/solidification problem in the Cartesian coordinate system, the energy equation for the entire region of the PCM can be expressed as:

$$\rho c_p \frac{\partial T}{\partial t} = \nabla \cdot (k \nabla T) \quad (3.54)$$

where the thermal conductivity k is a function of temperature T ; for a linear dependence:

$$k(T) = \begin{cases} k_s, & T < T_m - \Delta T \\ k_s + \frac{k_l - k_s}{2\Delta T}, & T_m - \Delta T < T < T_m + \Delta T \\ k_l, & T > T_m + \Delta T \end{cases} \quad (3.55)$$

The advantage of the equivalent heat capacity model is its simplicity. Equation (3.54) is simply the non-linear heat conduction equation, and it appears that a conventional computational methodology for conduction problems is adequate for solving a solid-liquid phase change problem. However, many studies have revealed difficulties in the selection of time step Δt , grid size ($\Delta x, \Delta y, \Delta z$) and the phase change temperature range ΔT .

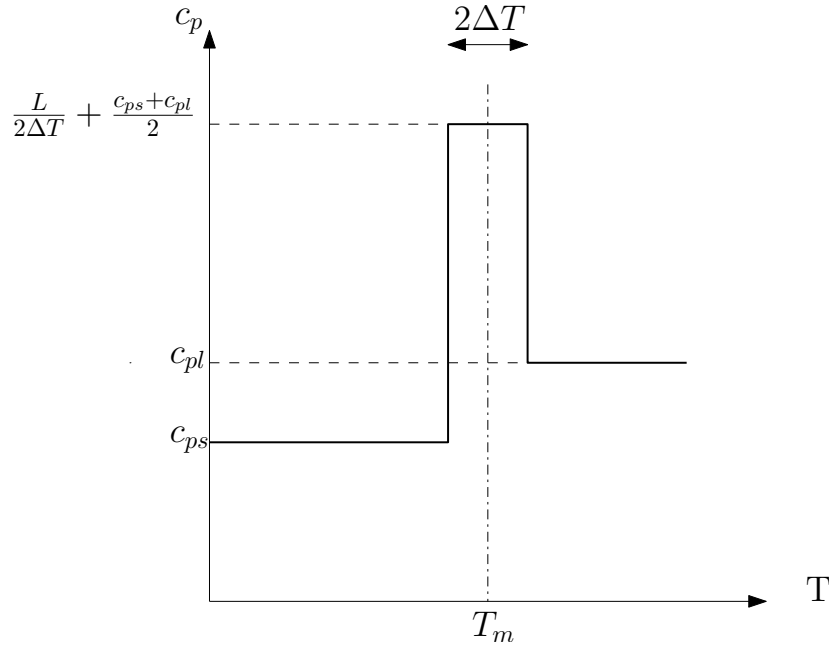


Figure 3.11: Dependence of specific heat to temperature for equivalent heat capacity model.

If these variables cannot be properly selected, the predicted location of the solid-liquid interface and the temperature may include some unrealistic oscillation. Therefore, although the equivalent heat capacity model leads to simple code development, it is not used as widely as the enthalpy model.

Temperature-transforming model

The temperature-transforming model proposed by Cao and Faghri [17] combines the advantages of the enthalpy and equivalent heat capacity models. For a conduction-controlled phase change problem, the governing equation in enthalpy form is:

$$\rho \frac{\partial H}{\partial t} = \nabla \cdot (k \nabla T) \quad (3.56)$$

For a phase change occurring over a temperature range $(T_m - \Delta T, T_m + \Delta T)$ with the specific heats assumed to be constant for each phase, the relationship between enthalpy and temperature can be plotted as in Fig. 3.12. This relationship can be analytically expressed as:

$$H(T) = \begin{cases} c_{ps}(T - T_m) + c_{ps}\Delta T, & T < T_m - \Delta T \\ \left(c_m + \frac{L}{2\Delta T}\right)(T - T_m) + c_m\Delta T + \frac{L}{2}, & T_m - \Delta T < T < T_m + \Delta T \\ c_{pl}(T - T_m) + c_{ps}\Delta T + L, & T > T_m + \Delta T \end{cases} \quad (3.57)$$

with $c_m = \frac{c_{ps} + c_{pl}}{2}$ the specific heat in the mushy zone. Equation (3.57) can be rewritten as:

$$H(T) = c_p(T)(T - T_m) + b(T) \quad (3.58)$$

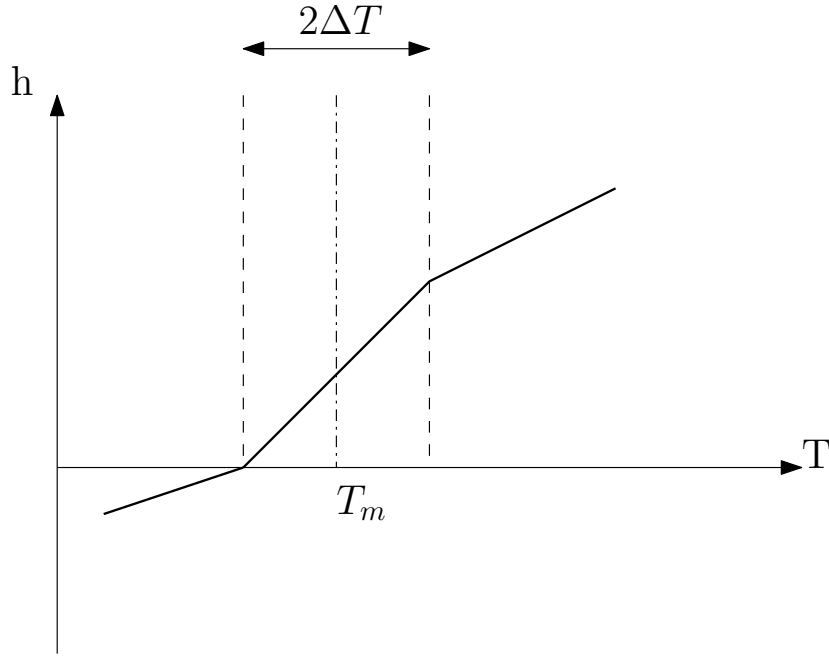


Figure 3.12: Dependence of enthalpy on temperature for phase change occurring over a range of temperature.

where $c_p(T)$ and $b(T)$ are defined as

$$c_p(T) = \begin{cases} c_{ps}, & T < T_m - \Delta T \\ c_m + \frac{L}{2\Delta T}, & T_m - \Delta T < T < T_m + \Delta T \\ c_{pl}, & T > T_m + \Delta T \end{cases} \quad (3.59)$$

$$b(T) = \begin{cases} c_{ps}\Delta T, & T < T_m - \Delta T \\ c_m\Delta T + \frac{L}{2}, & T_m - \Delta T < T < T_m + \Delta T \\ c_{ps}\Delta T + L, & T > T_m + \Delta T \end{cases} \quad (3.60)$$

Substituting Eq. (3.58) into Eq. (3.56) yields:

$$\rho \frac{\partial (c_p T)}{\partial t} = \nabla \cdot (k \nabla T) - \rho \frac{\partial b}{\partial t} \quad (3.61)$$

where the thermal conductivity k is a function of temperature and can be obtained by Eq.3.55. The energy equation has been transformed into a non-linear equation with a single dependent variable T . The temperature-transforming model and the equivalent heat capacity model differ in significant ways. The equivalent heat capacity model is a special case of Eq. 3.61, with $\frac{\partial b}{\partial t} = 0$ and c_p independent of the spatial variables x, y, z and time. This is the underlying reason why many studies using the equivalent heat capacity model have encountered difficulty in selecting the grid size and time step and have often produced physically unrealistic oscillatory results. In order to satisfy $\frac{\partial b}{\partial t} = 0$ and $\frac{\partial (c_p T)}{\partial t} = c_p \frac{\partial T}{\partial t}$, the time step has to be small enough to assure that c_p and b are independent of both time and space variables – a difficult criterion to satisfy. Eq.3.61 can be solved by many numerical methods [25, 26, 138, 150] including the finite volume approach by Chen and Zhang [24]. A very similar formulation is presented by Celentano

et al. [20] where the specific internal energy ω is defined as:

$$\omega = \int_{T_{ref}}^T c_p dT + L f_{pc} \quad (3.62)$$

with f_{pc} the 'phase change function', defined as for isothermal cases:

$$f_{pc} = \begin{cases} 0, & T \leq T_m \\ 1, & T > T_m \end{cases} \quad (3.63)$$

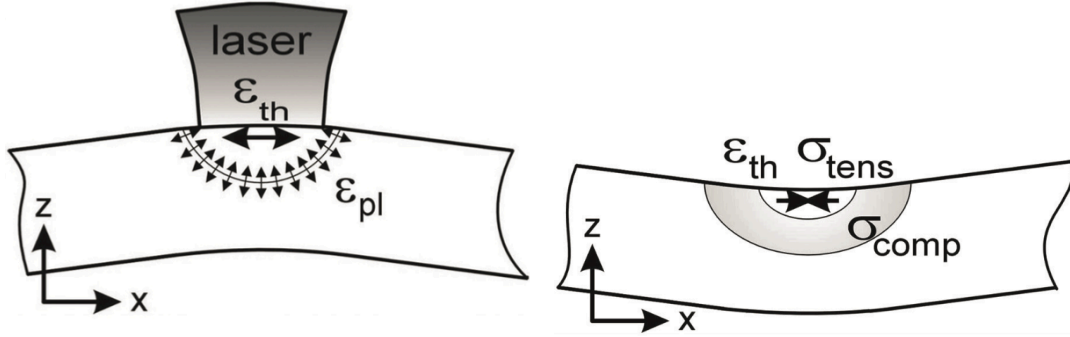
and for non-isothermal cases:

$$f_{pc}(T) = \begin{cases} 0, & T \leq T_s \\ (T - T_s)/(T_l - T_s), & T_s < T \leq T_l \\ 1, & T > T_l \end{cases} \quad (3.64)$$

3.3 Residual stresses: theoretical models

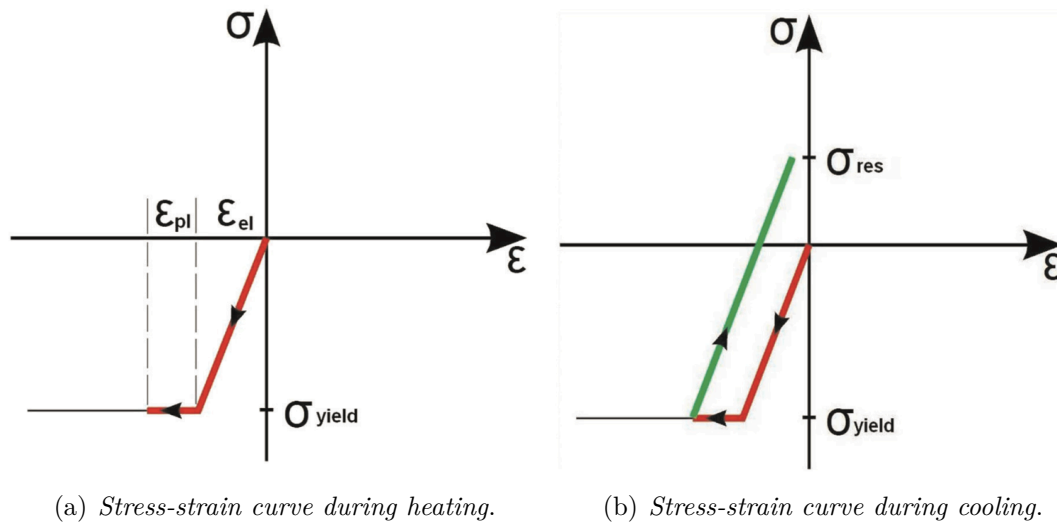
During the SLM process the component experiences large localized temperature fluctuations in short times; this induces high thermal and residual stresses that lead to warpage, crack or reduction of strength of material. As described in the previous section, the residual stresses can be induced by the high thermal gradients and they can be reduced choosing optimal process parameters, e.g. scanning pattern, length of scan vector, and adopting appropriate strategies, for example pre-scanning a deposited powder layer or post-scanning an already scanned layer.

To describe how the residual stresses can arise in SLM part two main mechanisms can be distinguished. The first mechanism is called the Temperature Gradient Mechanism (TGM) [88]. Such mechanism results from the large thermal gradients that occur around the laser spot caused by the rapid heating of the upper surface and the rather slow heat conduction. During heating, the irradiated part expansion is restricted by the underlying material, when the yield strength of the material is reached, the top layer is plastically compressed (Figg. 3.13(a)-3.14(a)). In absence of mechanical constraints also the component assumes a counter bending away from the laser beam. During cooling, the plastically compressed layers start shrinking and a bending angle toward the laser beam develops (Figg. 3.13(b)-3.14(b)). This mechanism does not require the melting of the material, which is described by the second mechanism. The second mechanism is the cool down phase of the molten top layers which tend to shrink to the thermal contraction. This deformation is again inhibited by the underlying material, thus introducing tensile stress in the added top layer and compressive stress below.



(a) Induced stresses and strains during heating. (b) Occurring stresses and strains when the part cools down.

Figure 3.13: Schematic description of the formation of residual stresses during TGM [73].



(a) Stress-strain curve during heating.

(b) Stress-strain curve during cooling.

Figure 3.14: Simplified representation of stress-strain curves during TGM [73].

Mercelis and Kruth [88] and Shiomi et al. [115] defined a similar simplified theoretical model that quantifies the descriptive cool down phase model using the equilibriums of forces and momentum. The model is idealised and limited to constant material properties and assumes the part built on top of the base plate and, due to the continuity of the deformation at the border, the base plate and the part with the same strain profile (Fig. 3.15):

$$\varepsilon_{xx}(z) = az + b. \quad (3.65)$$

Once the layer on the top surface is deposited and scanned by the laser beam, it starts

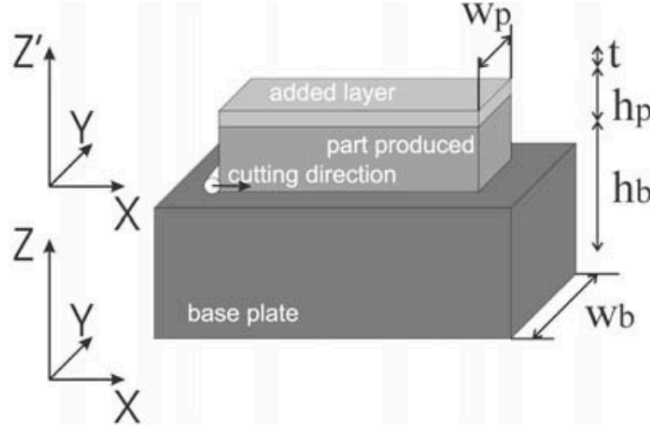


Figure 3.15: Simplified theoretical model of SLM process [88].

to shrink. Such shrinkage ($\alpha\Delta T$) induces a residual stress equal to the yield strength of the material (σ_y). Since there are no external forces acting on the system, the equilibria of force equation (3.66) and moment equation (3.67) can be written:

$$\int_0^{h_b} m(az + b)dz + \int_{h_b}^{h_b+h_p} (az + b)dz + \int_{h_b+h_p}^{h_b+h_p+t} \sigma_y dz = 0 \quad (3.66)$$

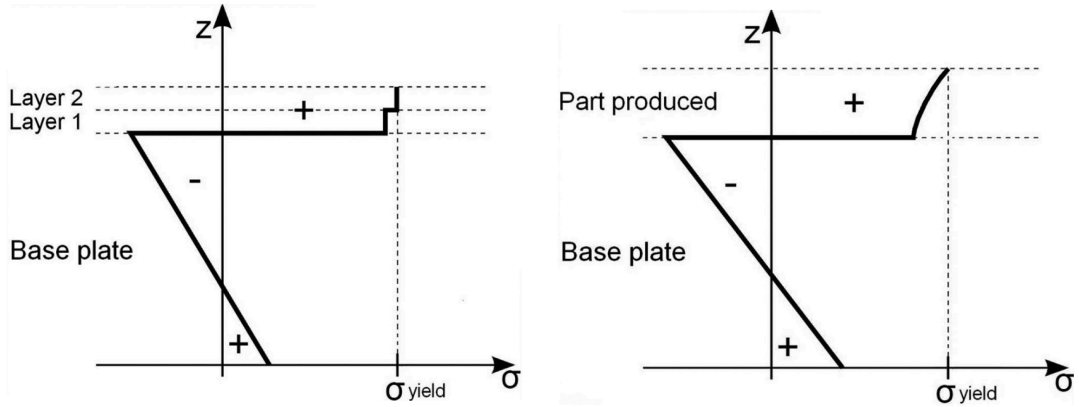
$$\int_0^{h_b} m(az + b)zdz + \int_{h_b}^{h_b+h_p} (az + b)zdz + \int_{h_b+h_p}^{h_b+h_p+t} \sigma_y z dz = 0 \quad (3.67)$$

whit $m = E_{base}/E_{part}$ the ratio of base plate stiffness to the part's stiffness, h_b the base height, h_p the plate height and t the layer thickness. From equations (3.66) and (3.67) the unknown coefficients a and b can be calculated.

The stress profile results in high tensile stresses in the SLM part, compressive stresses in the upper part of the base plate and lower tensile stresses in the lower part of the base plate (Fig. 3.16(a)). When successive layers are added on top each layer induces a certain stress profile in the base plate, but also in the underlying solidified layers, reducing their tensile stress (Fig. 3.16(b)). When the part is removed from the base plate the stress state in the part changes drastically (Fig. 3.17): the high tensile stresses inside the SLM part partially relax. The occurring relaxation consists of a constant term, which effects a uniform shrinkage of the part produced, and a linear term, which produces the bending of the produced part:

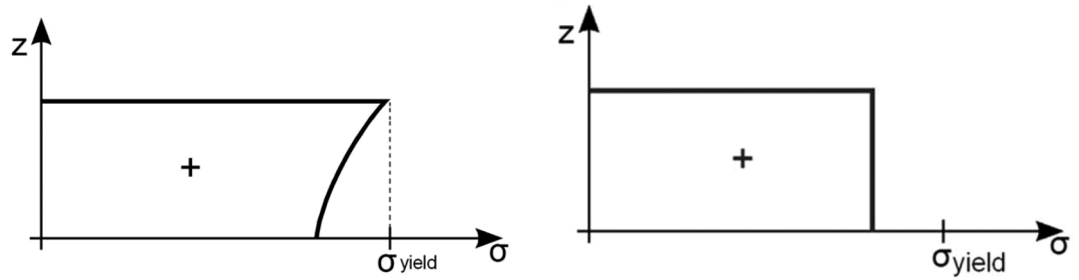
$$\sigma_{relaxation}(z') = cz' + d. \quad (3.68)$$

The coefficients c and d can be determined by recalculating the equilibrium conditions of the part removed from the base plate, considering the new coordinate system X, Y,

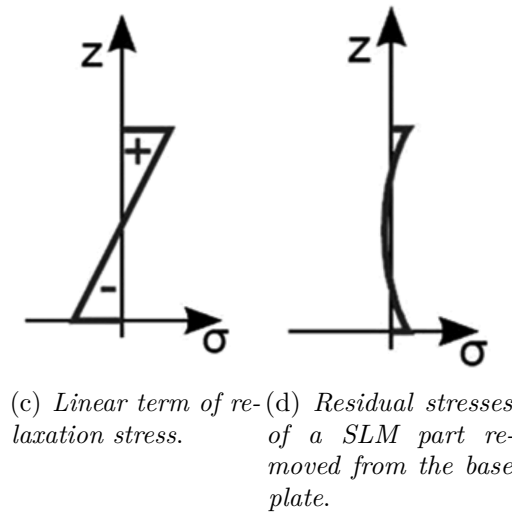


(a) Residual stresses of a SLM part with two layers on a base plate. (b) Residual stresses of a SLM part on a base plate after melting more or all layers forming the part.

Figure 3.16: Residual stress within the SLM part and the base plate (simplified model) [73].

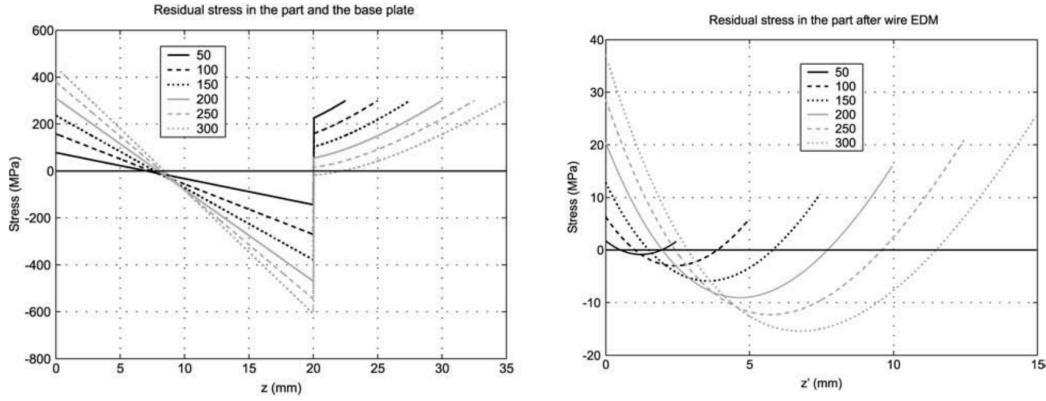


(a) Residual stresses of a SLM part connected to the base plate. (b) Constant term of relaxation stress.



(c) Linear term of relaxation stress. (d) Residual stresses of a SLM part removed from the base plate.

Figure 3.17: Residual stress before and after removing the SLM part from the base plate, [73].



(a) Residual stress profile in SLM part before base removal. (b) Residual stress profile in SLM part after base removal.

Figure 3.18: Influence of number of layers on residual stress profile in SLM part before and after base removal [88].

Z' (Fig. 3.15). The influence of the number of layers on the residual stress profile is investigated considering a base plate of 20 mm height and a SLM part of 50, 100, 150, 200, 250, and 300 layers of 50 μm thickness. If the number of layers increases, compressive stresses occur at the bottom of the part connected to the base plate (Fig. 3.18(a)). After part removal, the stress profile does not change increasing the number of layers (Fig. 3.18(b)). At the top and the bottom of the part, tensile stresses remain with a compressive zone in between. The base plate geometry also affects the residual stress profile of SLM part. According to this model, before part removal, a higher height results in a lower stress level in the base plate itself and a more uniform stress level in the part (Fig. 3.19(a)). Therefore a thick base plate induces smaller deformation due to part removal, compared to a thin base plate. Since almost all stress is released by an uniform shrinkage, only little residual stress remains in the part after removal (Fig. 3.19(b)). An important assumption of the theoretical model is that the part and the base plate are equally wide: $w_{\text{base}} = w_{\text{plate}}$. Usually, this is not true as the base plate is wider than the part. So, the influence of a wider base plate can be simulated by increasing the E modulus of the base plate considering a different m factor: $m = E_{\text{base}}w_{\text{base}}/E_{\text{part}}w_{\text{part}}$. According to the theoretical model an higher yield strength of the material results in higher stress values before and after base removal (Figg. 3.20(a)-3.20(b)). According with Koric and Thomas [67], the thermal strains during solidification are on the order of few percent and an assumption of small displacement gradients can be adopted. The governing equations of the mechanical problem are:

$$\nabla \cdot \boldsymbol{\sigma}(\mathbf{x}) + \mathbf{b} = 0 \quad (3.69)$$

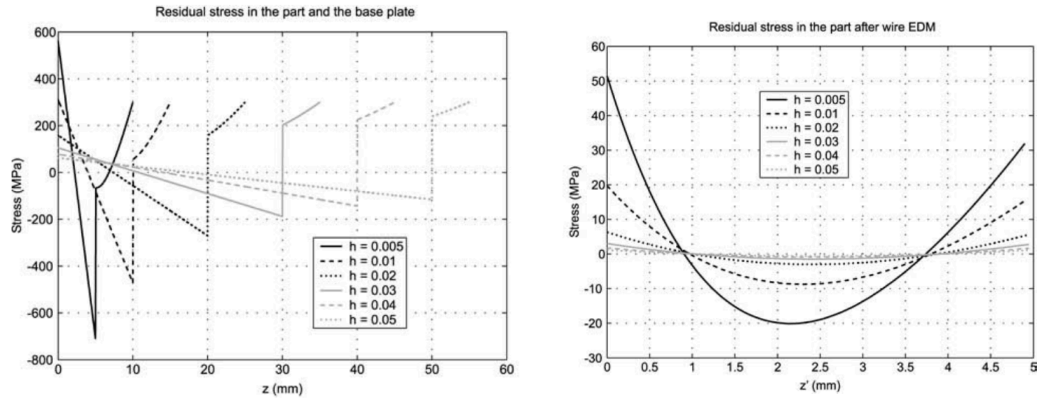
where $\boldsymbol{\sigma}$ is the Cauchy stress tensor, and \mathbf{b} is the body force density with respect to initial configuration. The boundary conditions are:

$$u = \bar{u} \quad \text{on } \Gamma_u \quad (3.70)$$

$$\boldsymbol{\sigma} \cdot \mathbf{n} = \bar{\mathbf{t}} \quad \text{on } \Gamma_t \quad (3.71)$$

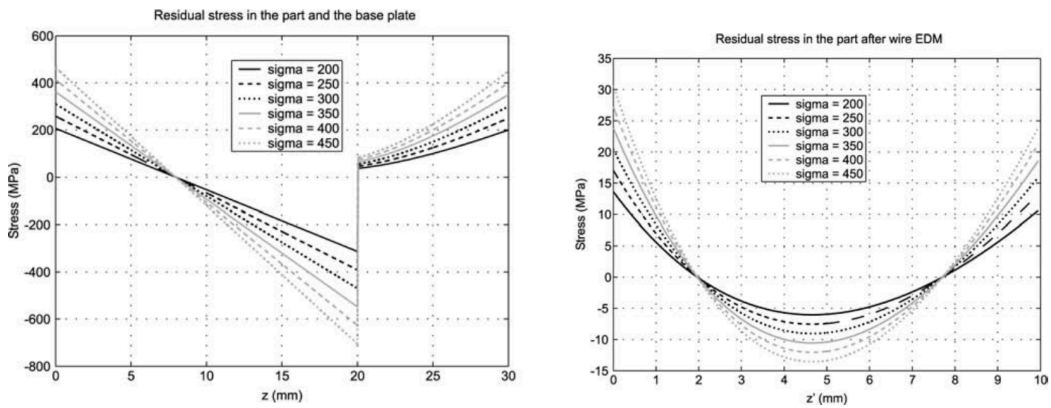
where \bar{u} is the prescribed displacement on the surface Γ_u and $\bar{\mathbf{t}}$ is the prescribed traction on the surface Γ_t . The elastic stress strain relationship is:

$$\boldsymbol{\sigma} = \mathbb{C} \boldsymbol{\varepsilon}_{el} \quad (3.72)$$



(a) Residual stress profile in SLM part before base removal. (b) Residual stress profile in SLM part after base removal.

Figure 3.19: Influence of base plate height on residual stress profile in SLM part before and after base removal [88].



(a) Residual stress profile in SLM part before base removal. (b) Residual stress profile in SLM part after base removal.

Figure 3.20: Influence of materials yield strength on residual stress profile in SLM part before and after base removal [88].

where \mathbb{C} is the fourth-order elasticity tensor and $\boldsymbol{\varepsilon}_{el}$ is the elastic strain. For an isotropic material the elasticity tensor \mathbb{C} is:

$$\mathbb{C} = [\lambda(\mathbf{I} \otimes \mathbf{I}) + 2\mu\mathbb{I}] \quad (3.73)$$

where λ and μ are the first and the second Lamé's constants, \mathbf{I} is the second-order identity tensor and \mathbb{I} is the fourth-order identity tensor ¹:

$$\mathbb{I}^I = \frac{1}{2}[\mathbf{I} \boxtimes \mathbf{I} + \mathbf{I} \hat{\boxtimes} \mathbf{I}]. \quad (3.74)$$

Deng [39] investigated the effects of solid-state phase transformation on welding residual stress and assumed a thermo-mechanical model in which the total strain rate $\dot{\boldsymbol{\varepsilon}}$ is the sum of different strain rate components:

$$\dot{\boldsymbol{\varepsilon}} = \dot{\boldsymbol{\varepsilon}}_{el} + \dot{\boldsymbol{\varepsilon}}_{pl} + \dot{\boldsymbol{\varepsilon}}_{th} + \dot{\boldsymbol{\varepsilon}}_{\Delta v} + \dot{\boldsymbol{\varepsilon}}_{Trp} \quad (3.75)$$

where the components represent respectively strain rate due to elastic, plastic and thermal loading, volumetric change due to the austenite–martensite transformation and transformation plasticity. Liu [82] considered a case in which the solid-state transformation does not occur, so the both components $\dot{\boldsymbol{\varepsilon}}_{\Delta v}$ and $\dot{\boldsymbol{\varepsilon}}_{Trp}$ vanished. He also assumed a rate independent plasticity with Von Mises yield criterion and kinematic hardening. The thermal strain $\boldsymbol{\varepsilon}_{th}$ can be expressed by:

$$\boldsymbol{\varepsilon}_{th} = \beta \Delta T. \quad (3.76)$$

where β is the thermal expansion coefficient.

3.3.1 Shrinkage

The reduction of porosity during solidification is a valuable effect of SLM process which causes a volumetric shrinkage inside the part. Such shrinkage is often non-uniform and anisotropic and affects the presence of residual stresses [73]. The melted material starts solidifying and the shrinkage is partially inhibited by the underlying material producing tensile stresses in the top layers. Many factors and process parameters can influence the volumetric shrinkage, such as the effect of layer thickness, time interval between succeeding layers, laser power, scan spacing and scanning speed on shrinkage (Fig. 3.21).

Ning et al. [94] assumed a general relation between shrinkage S and scan length L (Fig. 3.22):

$$S = 0.20496 + \frac{28.40192}{L} + \frac{1.46881}{L^2}. \quad (3.77)$$

According with this, shorter scan length makes the part denser and consequently leads to a more significant shrinkage. Many authors [33, 85, 149] assume an isotropic shrinkage with a maximum value equal to the porosity ϕ of the material times the layer thickness h (Fig. 3.23). A more realistic assumption is when the volume shrinkage evolves gradually from the powder surface to the maximum depth of $h\phi$. Riedlbauer et al. [104] simulated the volume change introducing a shrinkage strain $\boldsymbol{\varepsilon}_s$ expressed as:

$$\boldsymbol{\varepsilon}_s = \frac{1}{3\omega} \mathbf{I} \quad (3.78)$$

¹ $(\mathbf{A} \boxtimes \mathbf{B})_{ijkl} = A_{ik}B_{jl}$ and $(\mathbf{A} \hat{\boxtimes} \mathbf{B})_{ijkl} = A_{il}B_{kj}$

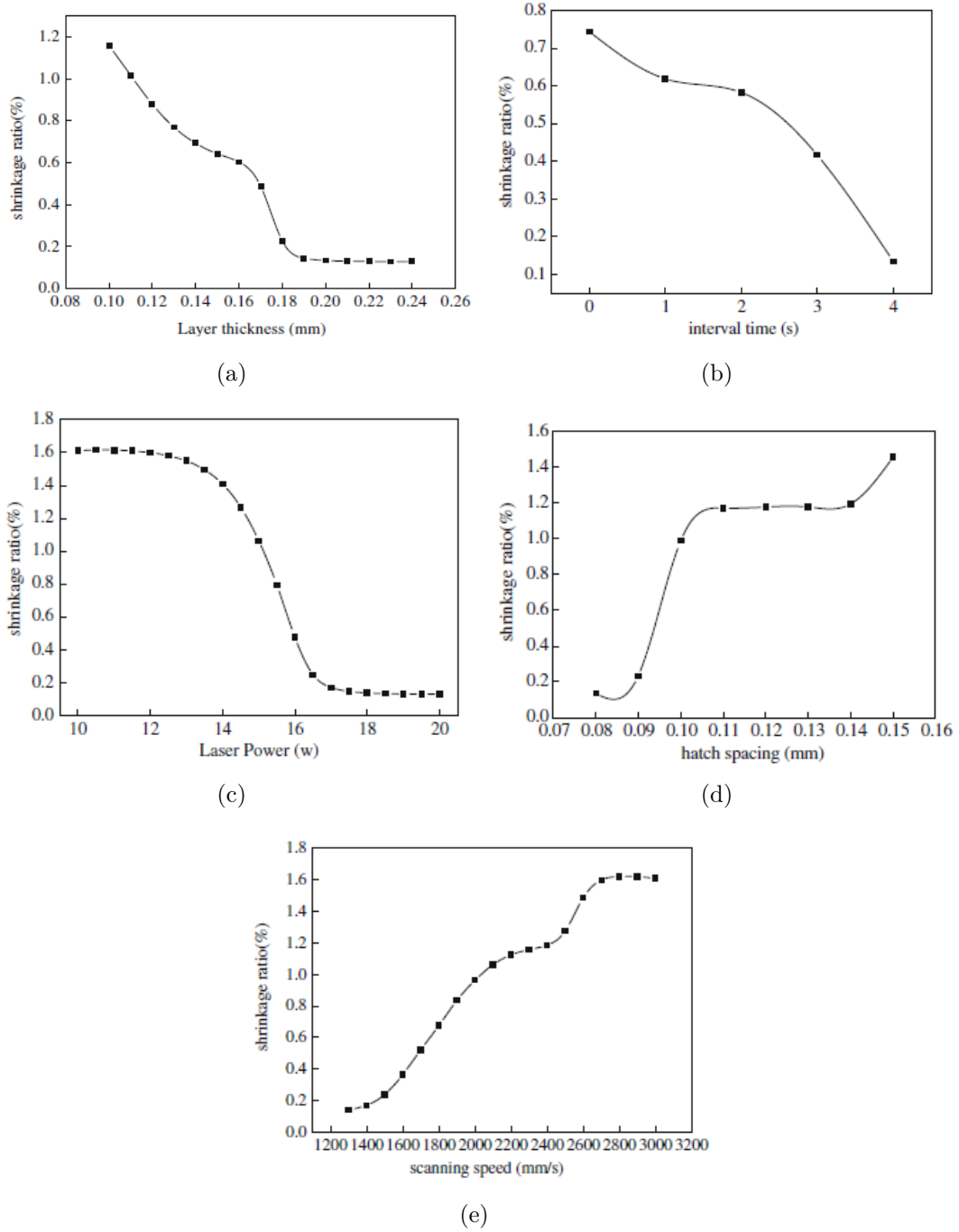


Figure 3.21: Effect of process parameters on shrinkage, Wang et al. [129].

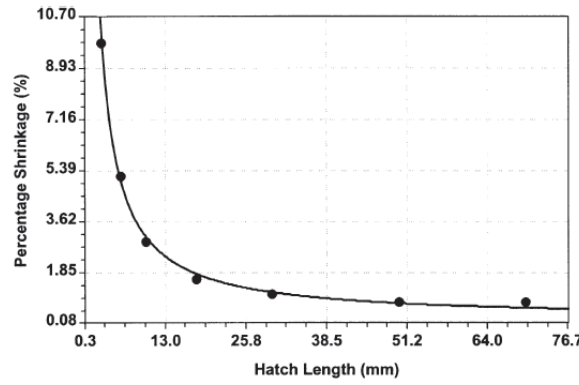


Figure 3.22: Variation of shrinkage with scan length, [94].

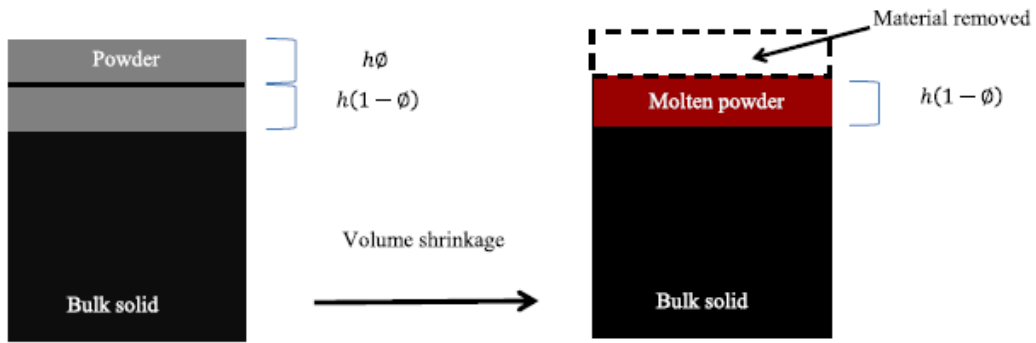


Figure 3.23: Schematic model of volume shrinkage [85].

where \mathbf{I} is the identity matrix and ω is the prescribed temperature dependent volumetric shrinkage which is 0 % when the material is powder and assumes a maximum value of -5 % when the material is liquid-solid.

3.4 Material properties

The nature of material of SLM part clearly influences the thermo-mechanical response affecting the resulting performance. For example, titanium is a material widely used in many application fields, e.g., biomedical [78], aerospace, automotive, etc., for its outstanding mechanical properties. Indeed, titanium exhibits a low density, high strengths, good chemical resistance and excellent bio-compatibility. Furthermore steel materials exhibit a large number of applications, depending on the properties, such as strength, ductility, and biocompatibility. For example, medical and dental applications are based on the idea to generate customized products with fully functional parts.

During the SLM process phase transformations of material from powder to liquid and from liquid to solid can cause changes on material properties. Indeed, the thermal properties of powder material are different from those of corresponding solid (or bulk) material, especially for thermal conductivity. Also the absorptance of the material, which affects the energy efficiency of SLM process, can vary from powder to the corresponding bulk materials. The high absorptance of powder material is due to the multiple reflections of the laser beam in the powder bed, which also result in higher optical penetration depth. Many physicists have studied the absorptivity of different

materials irradiated by distinct wavelengths, although few works interested powder materials. For instance, at $\lambda = 1.06 \mu m$ the absorptance of titanium bulk material is 30 % and that of titanium powder is 77 % [142]. An important parameter is the relative density, which is the ratio of the density attained with SLM and the theoretical density of the bulk material. Iron-based materials processed with SLM show a high relative density above 90 %.

Heat capacity and latent heat are heavily dependent on the material and proportional to the mass to be melted. Many authors consider the same specific heat and latent heat of fusion for powder and solid state.

In the following section a detailed description of physical, thermal and mechanical properties of SLM materials will be presented with a focus on the various models adopted in literature.

3.4.1 Thermo-physical properties

Density

Density is a physical quantity that describes the mass of a unit volume of a substance. Density of powder is strictly related to the porosity ϕ of the material, which can be expressed as:

$$\phi = \frac{\rho_{bulk} - \rho_{powder}}{\rho_{bulk}} \quad (3.79)$$

where ρ_{powder} and ρ_{bulk} are respectively the powder and the bulk material densities.

Hussein et al. [59] assumed that the porosity ϕ varies from 0.4 for powder state to 0 at solid state of single 316L stainless steel layers. Yin et al. [144] considered that the density of solid iron changes linearly with temperature from an initial value $\phi_0 = 0.45$ to the minimum value of $\phi = 0$ corresponding to bulk-like material. In this case the porosity can be expressed as:

$$\rho = \begin{cases} \rho_0(T), & T_0 \leq T \leq T_s \\ \frac{\rho_{bulk}(T_m) - \rho_0(T_s)}{T_m - T_s} (T - T_s) + \rho_0(T_s), & T_s < T < T_m \\ \rho_{bulk}(T), & T \geq T_m \end{cases} \quad (3.80)$$

where ρ_0 is the density corresponding to ϕ_0 , T_s is the solidus temperature and T_m is the melting temperature.

Thermal conductivity

Thermal conductivity is a property of the material which describes the rate at which heat is transferred through the material. The expression of thermal conductivity can considerably affect the conduction within the material and consequently the simulation results. Thermal conductivity depends on the state of material, which can be powder, solid, and liquid. Thermal conductivity of dense material typically ranges from about 8 W/(mK) to 400 W/(mK) and increases with increasing temperature [90].

A typical variation on thermal conductivity with temperature for powder, liquid and solid states is depicted in Fig. 3.24. At initial state the material is powder; the laser beam irradiates the surface and when the temperature of powder reaches the sintering temperature (T_{sint}) the single particles start bonding together. When the temperature is above the liquidus temperature (T_l) the material becomes liquid (Path 1). When

the laser source turns away the liquid material starts cooling since the temperature reaches the solidus temperature (T_s) and the material becomes completely solid (Path 2). Usually, the sintering temperature (T_{sint}) is smaller than the solidus temperature (T_s). The analytical expressions of thermal conductivity for Path 1 and Path 2 can be expressed as:

$$Path\ 1 : k = \begin{cases} k_p(T), & T \leq T_{sint} \\ \frac{\Delta k_{lp}}{T_l - T_{sint}}(T - T_{sint}) + k_p(T_{sint}), & T_{sint} < T < T_l \\ k_l(T), & T \geq T_l \end{cases} \quad (3.81)$$

$$Path\ 2 : k = \begin{cases} k_s(T), & T \leq T_s \\ \frac{\Delta k_{ls}}{T_l - T_s}(T - T_s) + k_s(T_s), & T_s < T < T_l \\ k_l(T), & T \geq T_l \end{cases} \quad (3.82)$$

with:

$$\Delta k_{lp} = k_l(T_l) - k_p(T_{sint}) \quad (3.83)$$

$$\Delta k_{ls} = k_l(T_l) - k_s(T_s) \quad (3.84)$$

where $k_p(T)$, $k_s(T)$, $k_l(T)$ are respectively the thermal conductivities of powder, solid and liquid material.

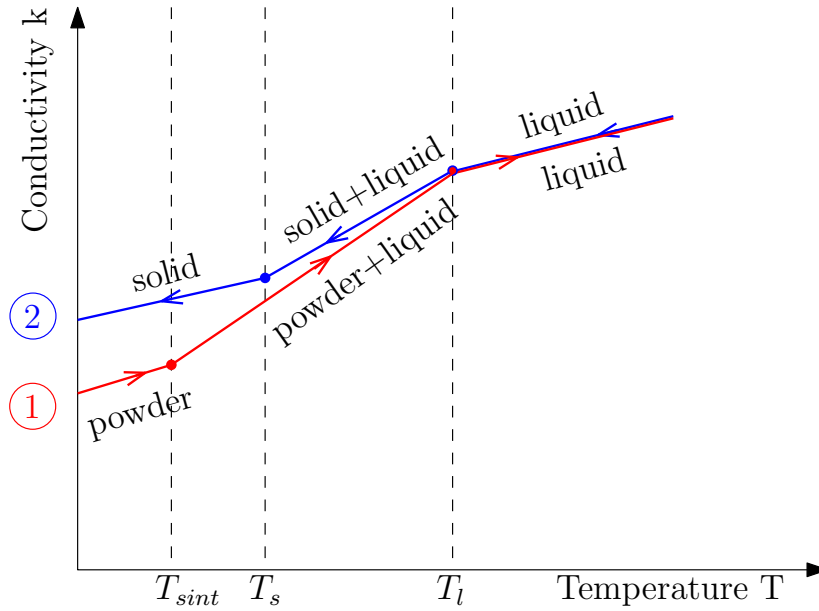


Figure 3.24: Typical pattern powder-liquid-solid of thermal conductivity versus temperature.

Many authors consider the thermal conductivity of the powder bed from the thermal conductivity of the bulk material affected of the porosity of loose powder. An example is given by Yin et al. [144] where the conductivity of powder bed is:

$$k_{powder} = k_{bulk}(1 - \phi)^n \quad (3.85)$$

where n is an empirical parameter. Thermal conductivity of the powder bed is strongly dependent on the linear contact distance between the particles and an effective conductivity of a packed bed have been developed by Bugeda et al. [15], which considered the

effects of conduction, convection and radiation:

$$k_e = \frac{\mu k_s}{1 + \Phi \frac{k_s}{k_g}} \quad (3.86)$$

where k_s is the conductivity of the solid material, k_g is the conductivity of air, μ is the solid fraction $\mu = \frac{\rho}{\rho_s}$, and Φ is an empirical coefficient normally taken as $\Phi = 0.02 \cdot 10^{2(0.7-\mu)}$.

Gusarov et al. [51] and Tolochko et al. [121] studied the effect of the powder bed packing style on powder bed density and thermal conductivity during 'Solid State Sintering' (SSS). Such phenomenon involves the formation of contact areas ('necks') between neighbouring particles.

The powder particles may have a symmetric arrangement in the powder bed (Fig. 3.25) such as diamond, simple cubic (SC), body centered cubic (BCC), face centered cubic (FCC), or more possibly, a combination of these packing styles that presents a random thermal conduction behaviour. The thermal conductivity of any symmetric packing

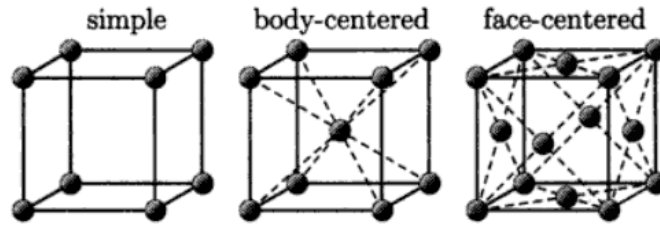


Figure 3.25: Cubic unit cell: simple cubic (SC), body centered cubic (BCC), and face centered cubic (FCC), [21].

styles as well as the random packing style depends on three parameters including the relative density, the symmetric packing style coordination number, and the powder particles contact size. In this case, the effective thermal conductivity can be written as the contribution of the effect of heat loss by conduction, radiation, and convection:

$$k_e = k_{CD} + k_{RD} + k_{CV} \quad (3.87)$$

where k_{CD} , k_{RD} , and k_{CV} are the conductive, radiative, and convective heat transfer coefficients, respectively. If the process happens in a vacuum, the effect of heat transfer by convection can be neglected ($k_{CV} \approx 0$). The radiation term can be written as:

$$k_{RD} = \frac{16}{3} l_{ph} \sigma T^3 = \frac{16}{3} \frac{\sigma T^3}{\beta} \quad (3.88)$$

where σ is the Stefan-Boltzmann constant, l_{ph} is the mean photon path between the powder particles and β is the effective extinction coefficient. The parameter l_{ph} is about pore sizes and is estimated to be equal to the solid powder particle size. Rombouts [107] experimentally measured the effective extinction coefficient β which varies from 232 mm^{-1} to 21 mm^{-1} . Furthermore, in that study the corresponding radiative conductivity k_{RD} was calculated (Fig. 3.26): the radiative conductivity is negligible at low temperature compared to the thermal conductivity of powder beds at

room temperature, which is of the order of 0.1-0.2 W/(mK), Tab. 3.2. The conduction term of Eq. 3.87 can be written as:

$$k_{CD} = \Lambda k_0 r_c \quad (3.89)$$

Table 3.2: Values of thermal conductivity of powder beds measured at room temperature in air atmosphere [107].

Material	Size Range $d_{10} - d_{50} - d_{90}$ (μm)	Shape	Relative density ϕ	Thermal conductivity (W/(mK))
1. Stainless steel 316L	22-26-34	spherical	0.54	0.156 ± 0.004
2. Stainless steel 316L	30-36-58	spherical	0.60	0.186 ± 0.002
3. Stainless steel 316L	37 - 42 - 61	spherical	0.59	0.186 ± 0.003
4. Stainless steel 316L	51 - 57 - 85	spherical	0.6	0.157 ± 0.002
5. Iron	27 - 44 - 63	irregular	0.33	0.1135 ± 0.0007
6. Iron	27 - 58 - 72	irregular	0.47	0.166 ± 0.003
			0.34	0.111 ± 0.005
7. Copper	5 - 10.5 - 21	spherical	0.37	0.078 ± 0.006
8. Copper	11 - 30 - 52	spherical	0.52	0.19 ± 0.02

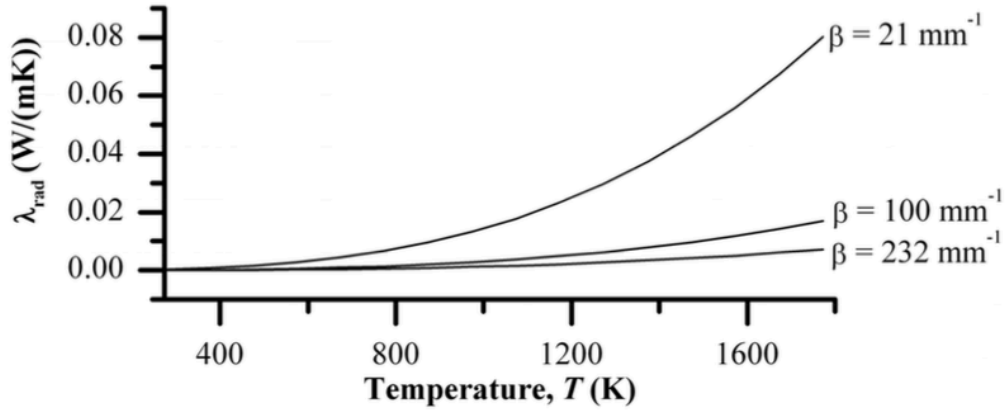


Figure 3.26: Radiative thermal conductivity as a function of the temperature T and the extinction coefficient β , [107].

where Λ is the normalized contact conductivity, k_0 is the temperature dependent thermal conductivity of the solid, and $r_c = b/r$ is the contact size ratio, where $2b$ is the powder particles contact length and r is the powder radius (Fig. 3.27). The normalized contact conductivity values Λ for the four diamond, SC, BCC, and FCC powder bed packing styles are respectively 0.433, 1, 1.732, and 2.828 corresponded to the relative densities of 34 %, 52.4 %, 68 %, and 74 % (Tab. 3.3).

Jamshidinia et al. [61] presented a non-linear regression equation to relate powder bed density to the corresponding normalized contact conductivity:

$$\Lambda = \frac{\rho - 6.639531965}{-0.02694964737 \cdot 10\rho^2 + 2.368512196\rho - 3.534958904}. \quad (3.90)$$

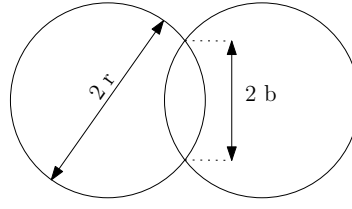


Figure 3.27: Two solid powder particles sintering zone.

Table 3.3: Relative densities, coordination number and normalised contact conductivity for diamond, SC, BCC and FC unit cell, [51].

Structure	Relative density p	Coordination number n	Λ
FCC	$\pi\sqrt{2}/6 = 0.740$	12	$2\sqrt{2}=2.828$
BCC	$\pi\sqrt{3}/8 = 0.680$	8	$\sqrt{3}=1.732$
SC	$\pi/6 = 0.524$	6	1
Diamond	$\pi\sqrt{3}/16 = 0.340$	4	$\sqrt{3}/4=0.433$

The effect of the increase of thermal conductivity of powder due to solid state sintering on temperature profile is illustrated in Fig. 3.28 [107]. When the temperature of the

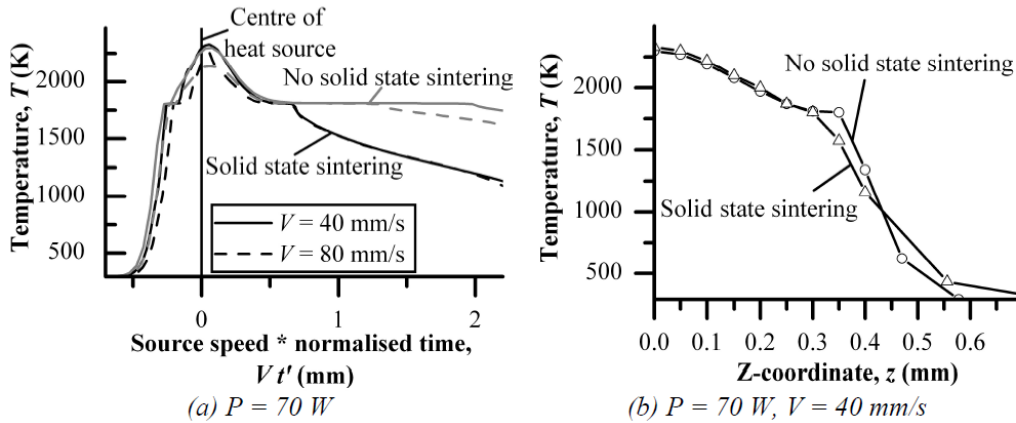


Figure 3.28: Effect of increase of thermal conductivity on temperature profile [107].

powder bed exceeds the melting point T_m , the particles melt and join together. In this case the effective thermal conductivity is equal to that of dense material:

$$k_e = k_0. \quad (3.91)$$

Liu [82] considered an increased thermal conductivity since it is influenced by the 'Marangoni effect':

$$k_m(T) = \begin{cases} k(T), & T \leq T_l \\ 2.5 k(T), & T > T_l \end{cases} \quad (3.92)$$

where T_l is the liquidus temperature.

Absorptance

Absorptance is defined as the ratio between the absorbed radiation (I_a) to the incident radiation (I):

$$\alpha = \frac{I_a}{I}. \quad (3.93)$$

In general, absorptance of powder materials is greater than dense material. Indeed, part of the incident radiation is absorbed by the particles, and another part penetrates through the pores and reaches the underlying particles. The absorption of pores of powder approaches the absorption of the blackbody. The higher absorptance and the lower thermal conductivity of powder material than dense material lead to a decrease of laser power density required to melt the material.

According with Tolochko et al. [122] the absorptance of a material depends on many factors, such as laser wavelength, nature of materials, surface geometry, ambient gas, temperature, etc., but it does not really depend on particle size distribution. In particular, absorptance of metals and carbides decreases with increasing wavelength of laser, meanwhile absorptance of oxides and polymers increases with the wavelength of laser.

In Fig. 3.29 is shown the absorptance profile of Ni-alloy I metal powder during laser processing (laser wavelength of $\lambda = 1.06\mu m$). When the laser beam heats the powder material, absorptance starts to increase for the changes on thermo-physical properties. If the power density of laser is rather low, sintering between the particles occurs since the absorptance reaches its maximum value (3.29(a)). For higher power density, melting of particles occurs with a drastic reduction in porosity leading to a decrease of absorptance (3.29(b)).

In order to simplify laser energy absorption modelling, many authors [46, 82, 144] assume a constant value for the laser absorptance of the material. This assumption is unrealistic because attenuation of the absorbed laser energy occurs as a result of powder cloud formation, scattering and changes to the surface and state of the material, [106]. Fu and Guo [46] assumed a realistic value of absorptance for titanium powder equal to 0.77. Roberts [106] considered a more conservative value of absorptance for titanium powder which is equal to 0.3. Rombouts [107] showed that the temperature distribution over the scanned part is mostly influenced by the product of the laser power P and the absorptance α above the liquidus temperature. Indeed, as it is shown in Fig. 3.30, the curves with power $P=70$ W and a constant absorptance $\alpha=76.5\%$ (circles) and with $P=130$ W and a variable absorptance α (crosses) exhibit the same αP product and a similar distribution.

Latent heat of fusion

Enthalpy H is a thermodynamic function consisting of the internal energy e and the product of the pressure p and the volume V :

$$H = e + pV. \quad (3.94)$$

A change in temperature in the system causes a change in the enthalpy of the system. The thermodynamic processes considered in the following cases are assumed to be at constant pressure. When a phase change occurs the latent heat of fusion L represents

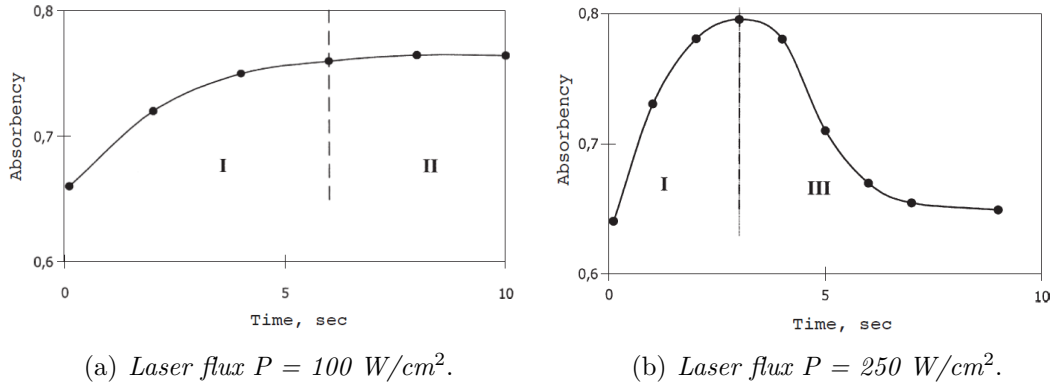


Figure 3.29: Absorptance profile of Ni-alloy I metal powder during laser processing (laser wavelength of $\lambda = 1.06\mu\text{m}$), [122].

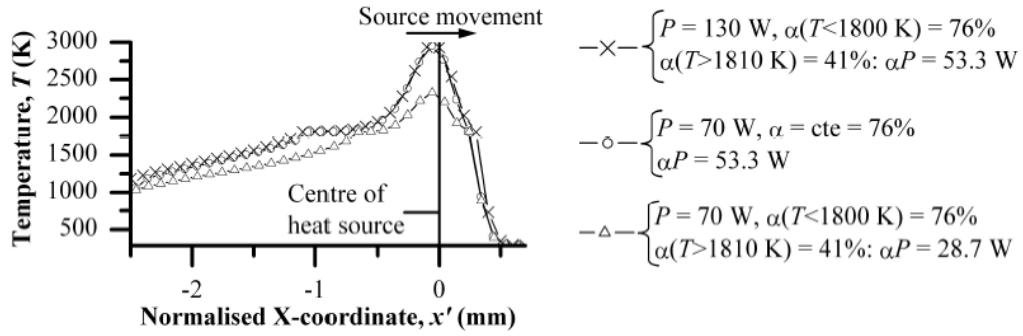


Figure 3.30: Temperature profile on an iron powder bed for different values of laser absorptance α and laser power P , [107].

the energy released or absorbed during a constant-temperature process. In this case the enthalpy H (or the specific internal energy e) can be expressed as:

$$H(T) = \int_{T_{ref}}^T c_p dT + Lf \quad (3.95)$$

where the coefficient f is the volumetric liquid function defined as:

$$f = \begin{cases} 0, & T < T_s \\ \frac{T - T_s}{T_l - T_s}, & T_l \leq T \leq T_s \\ 1, & T > T_l \end{cases} \quad (3.96)$$

In many cases the effect of the latent heat of fusion L is not considered inside the enthalpy formulation (Eq. 3.95) but it is accounted defining an equivalent specific heat c_p^e between the solidus and the liquid temperatures (Fig. 3.31):

$$c_p^e(T) = \frac{L}{T_l - T_s} + c_p(T), \quad T_l \leq T \leq T_s \quad (3.97)$$

Rombouts [107] and [82] adopted the equivalent heat capacity method in Abaqus to simulate the effect of latent heat of fusion.

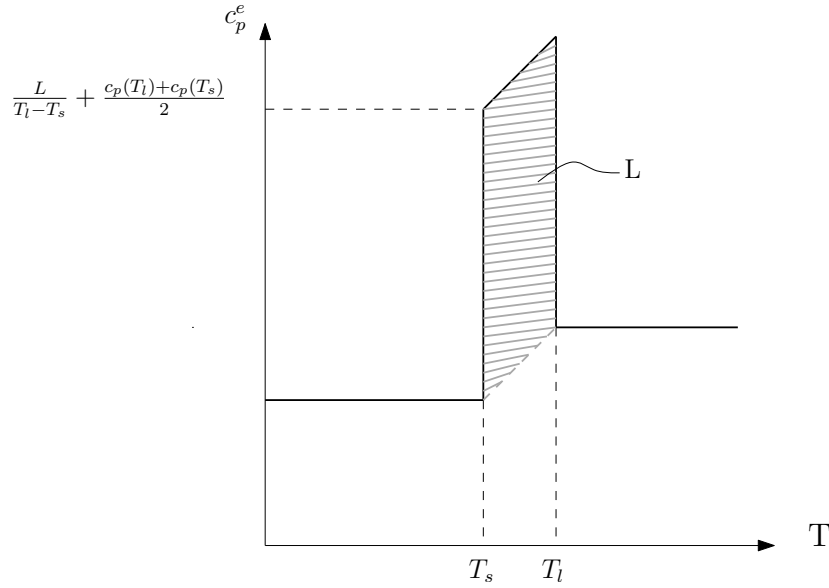


Figure 3.31: Dependence of specific heat to temperature for equivalent heat capacity model.

3.4.2 Thermo-mechanical properties

The mechanical properties of the material also should depend on the temperature T during the simulation. In general, the Young's modulus, Poisson's ratio, yield stress and thermal expansion coefficient vary with temperature. In general Young's modulus and yield stress decreases with temperature. The thermal expansion coefficient of metals generally increases with temperature. In Fig. 3.32 is shown a typical variation of Young's modulus with temperature for Ti-6Al-4V.

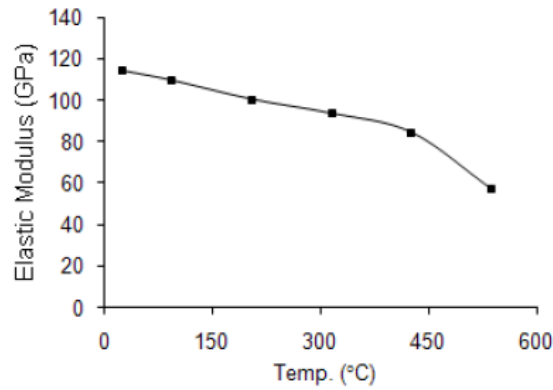


Figure 3.32: Variation of Young's modulus with temperature for Ti-6Al-4V material, [106].

3.5 Summary

In the present chapter an overview of various physical models of SLM process has been presented showing the importance to make an accurate choice of hypothesis and assumptions. For example an efficient model should take into account the phase transformation of the material and the change of material properties, such thermal conductivity, density and absorptance which gravely depend on the temperature field. In the following chapter we will present a simulation model of SLM making some hypothesis and assumptions, which will be justified by the author.

Chapter 4

Finite Element simulation of SLM process

Finite Element Analysis (FEA) is a reliable and efficient numerical technique widely used to simulate the physical behaviour of different geometries. In the last decades such technique has been employed to predict the temperature and stress field of SLM manufactured parts when complex geometries are involved and analytical models fail. The solution of temperature field inside the material for a stationary or moving heat flux is crucial to determine micro-structure, heat affected zone (HAZ), residual stresses and deformation of the part. The temperature distribution for a moving heat source is rather complicate, presenting an unsymmetrical shape over the surface, with a typical 'comet tail', and over the depth [5]: in Fig. 4.1 is depicted a typical temperature distribution for a 2D problem on time and on the spatial coordinate along the moving Gaussian heat flux. According with Powar et al. [101] the time temperature field can be divided in three different stages: a stationary/initiation stage, where the temperature starts to increase; a quasi-stationary stage, where the temperature is stationary; an ending-stage, where the temperature decreases.

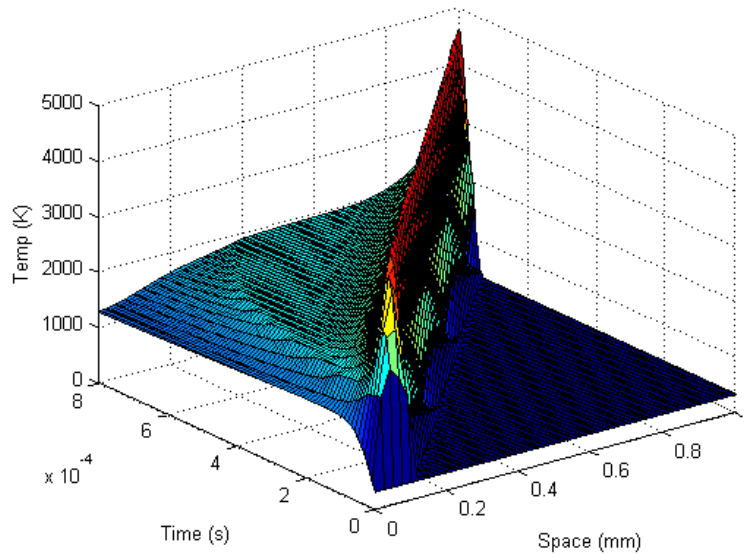


Figure 4.1: Temperature distribution $T(x,t)$ for 2D problem.

Various FE models has been presented in literature able to capture such variability, especially for non-linear problems. In particular the nonlinearity is given by the temperature dependent material properties and by the introduction of latent heat of fusion, which drastically changes the temperature profile.

In the following chapter we will present the potential of FE models to describe the temperature and the mechanical field of SLM components with some numerical examples implemented in Abaqus [36] with a highlight over the advantages and the limitations of the numerical model.

4.1 State of art

In recent years a large number of analytical and numerical models have been developed to assess the thermal field of SLM parts, which is essential to predict the residual stresses, expansions and deflections. In particular, temperature distribution of moving heat flux has been largely investigated in literature in many fields of engineering, such as welding, laser treatments, surface hardening, etc.

Analytical solutions of temperature have been introduced using Rosenthal's equation for instant, line and surface heat fluxes [109], Green function [41] and Duhamel's integral [70] for moving heat sources. For example Fachinotti et al. [41] introduced the solution of temperature field in a semi-infinite body by a welding moving heat source with Gaussian distribution inside a double-ellipsoidal volume. The introduced analytical solution respect to the previous work of Nguyen et al. [92] accounts for differences between the front and rear contributions of the double-ellipsoidal heat source. The authors also observed that the analytical solution fitted very well the FE numerical solution. Kumar [75] analytically predicted the temperature distribution, the peak temperature, the cooling rate and the thermal cycles in a solid work piece welded by laser welding. For these cases no phase transformation occurred and the material properties are assumed constant.

In order to capture the nonlinearity of the problem many authors introduce the implementation of a numerical model. For example, Darmadi [35] investigated the temperature field via a FE model in ANSYS of a stainless steel 316L 120 x 180 x 17 mm domain with temperature-dependent material properties.

The use of analytical solutions for SLM application is far less common. A semi-analytical modelling approach is presented in the work of Knol [64], where the temperature solution is equal to the superposition of a known analytical solution of point sources in a semi-infinite space, plus an additional boundary-correction field. The analytical results of melt pool width are compared with the experimental results obtaining a maximum error of 10 %. Clearly the assumption of the superposition needs that the equations are linear and phase transformation is neglected.

The use of FE models for SLM components gives a reliable alternative to analytical models, able to simulate 2D and 3D complex geometries with material nonlinearities. Fu and Guo [46] implemented a 3D FE model in Abaqus to predict the temperature field and the dimension of the melt pool in a multilayer Ti-6Al-4V material. They assumed a moving Gaussian heat flux and temperature-dependent material properties, except for density and absorptance. Liu [82] developed a 3D FE thermo-mechanical analysis in Abaqus of a AISI 304 Stainless Steel domain processed by Direct Metal Deposition (DMD) and they compared the results with experimental tests. Roberts [106] developed

a 3D FE model in ANSYS to investigate the development of thermal and residual stresses in SLM of Ti-6Al-4V powders on a steel platform. The results revealed that the scanned tracks experienced similar temperature cycles, thermal stresses and residual stress distributions with the exception of the edge locations. The numerical solutions were in good agreement with the experimental results and a parametric study on the residual stresses was also developed: stresses increase with the number of layers and decrease increasing the platform thickness.

Rombouts [107] implemented a FE thermo-mechanical analysis in Abaqus of iron powder processed by SLM/SLS. For thermal analysis the author introduced temperature dependent properties with FORTRAN subroutines in Abaqus; for the mechanical problem a linear elastic constitutive model is assumed. The author investigated the effect on temperature considering Solid State Sintering (SSS) of powder particles, which enables the formation of contact 'necks'. A phase transformation is included in the model, assuming an increase on the specific heat between the liquidus and solidus temperatures. Foroozmehr et al. [45] introduces a 3D FEM of a single layer of 316L stainless steel over a powder bed. They adopted the Optical Penetration Depth (OPD) of the laser source, which takes into account the multiple reflections through the powder layers. The heat source is volumetric and it is assumed to be constant.

The assumption of a constant energy source is followed by different authors [34, 79, 87] due to the high computational costs interesting large FE models. The main advantage of these models is the reduction of the number of time steps and the numerical resolution can be coarse due to the limited thermal gradient. In these models an estimation of residual stresses and deformation is given, although the information of the scanning path is lost. Experimental tests reveal a strong dependence between the scan path and residual stresses [88], so the numerical model should account for the scanning pattern of the heat source.

4.2 Problem definition

Within the described background we present the development of a Finite Element (FE) numerical model of SLM process able to reproduce the thermo-mechanical behaviour of metal parts. In particular, starting from some scientific papers we developed some numerical simulations of SLM process of different geometries using the commercial software Abaqus [36]. The numerical simulation model wants to predict the main features of SLM process, such as temperature time history, melt pool dimensions, residual stresses, deformation, etc. This goal will be achieved through the definition of a laser beam model which can represent the intensity radiation of the laser and its movement along the surface; an evolving domain with a layer build-up process; a thermo-physical material model able to represent the different phases of material (powder, solid, liquid) during the process, including porosity-dependent powder material properties; a material state change model from powder to liquid and from liquid to solid and a mechanical constitutive model which can predict the deformations and residual stresses arising from temperature gradients. The scheme depicted in Fig. 4.2 shows the steps used in the numerical procedures which will be implemented with some modelling assumptions:

- the whole media is considered to be homogeneous and continuous;

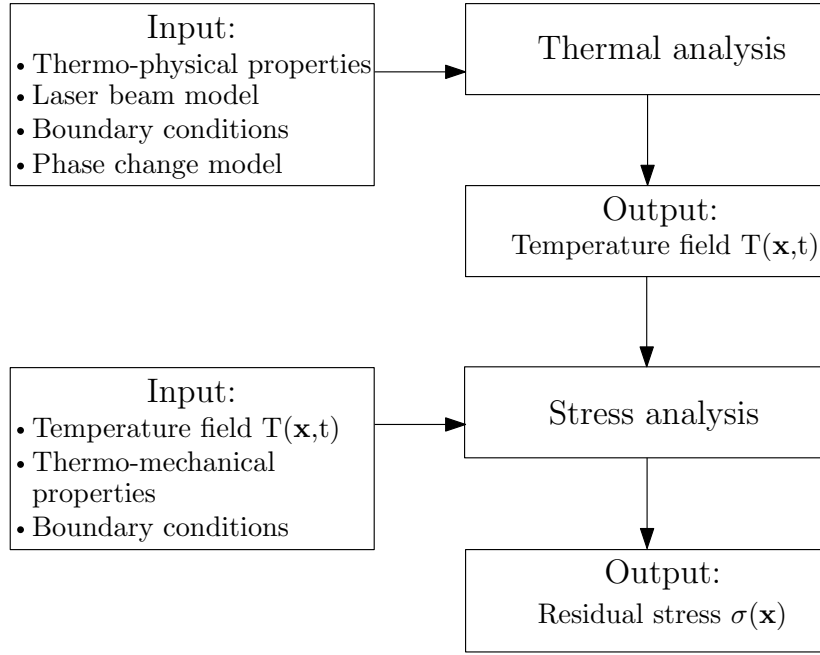


Figure 4.2: Flow chart of numerical model in Abaqus

- stress and displacement are considered to be dependent on temperature field but there is no inverse dependency; for this reason a sequentially coupled thermal-stress analysis is conducted;
- the moving heat source for thermal analysis is developed using an user subroutine DFLUX in FORTRAN. The input parameters of laser beam, i.e. laser power, scan velocity, beam radius, absorptance, and the scanning path are defined in the subroutine;
- the temperature field is obtained by the only effects of conduction and convection (where it is assumed) with a constant convection coefficient; meanwhile radiative effect is neglected;
- chemical reaction and fluid flow of melt pool are neglected during the thermal analysis;
- where a transformation on porosity is assumed, the density change from powder to solid material is expressed assuming a field variable by the user subroutine USDFLD in FORTRAN. The subroutine also calls the subroutine GETVRM to access the solution of temperature at each material point and at each increment.
- thermo-physical properties (e.g. thermal conductivity, specific heat, density, etc.) and mechanical properties (e.g., Young modulus, yield stress, etc.) of materials are temperature-dependent;
- where a powder-liquid-solid phase change is assumed, the variations on material properties, i.e. thermal conductivity and specific heat, and total energy are implemented using user subroutine UMATHT in FORTRAN. In particular subroutine UMATHT is called at the start of each increment and for each material point reading the current temperature and updating the material state. Indeed

4.3. Finite Element formulation

assuming an INDEX as state variable the subroutine updates the change on thermal conductivity: at initial state (powder) INDEX is set to 0 and when the temperature is above the melting temperature INDEX changes to 1 (solid). The subroutine also modifies the specific heat and the enthalpy including the effects of latent heat of fusion. The subroutine is called after the user subroutine USDFLD, which passes all the defined state variables (STATEV); a flow chart describing the implemented subroutines is given in Fig. 4.3.

- an equivalent heat capacity method is used to simulate the phase transformation, with an increase of the specific heat between solidus and liquidus temperatures;
- volume shrinkage during solidification is not considered in the stress analysis.

4.3 Finite Element formulation

The strong form of the heat conduction equation for transient problems is to find $T : \bar{\Omega} \times [0, \mathcal{T}]$ such that [57]:

$$\rho c_p \frac{\partial T}{\partial t} = \nabla \cdot (\mathbf{k} \nabla T) + Q \quad \text{on } \Omega \times]0, \mathcal{T}[\quad (4.1)$$

$$-\mathbf{k} \frac{\partial T}{\partial \mathbf{n}} = g \quad \text{on } \Gamma_g \times]0, \mathcal{T}[\quad (4.2)$$

$$T(\mathbf{x}, 0) = T_0(\mathbf{x}) \quad \mathbf{x} \in \Omega \quad (4.3)$$

where with $\bar{\Omega}$ we denote the closure of Ω , with g the prescribed heat flux, which can include the heat loss for convection and radiation (Eq. 4.4):

$$g = \varepsilon_\theta \sigma (T^4 - T_e^4) + h(T - T_e) \quad \text{on } \Gamma_g \times]0, \mathcal{T}[. \quad (4.4)$$

If we denote with \mathcal{S} the space of trial solutions and with \mathcal{V} the variation space, we can multiply the strong formulation (4.1) with $w \in \mathcal{V}$, integrate on Ω and obtain the following weak form:

$$\int_{\Omega} w \rho c_p \frac{\partial T}{\partial t} \partial \Omega + \int_{\Omega} \nabla w \cdot \mathbf{k} \cdot \nabla T \partial \Omega = \int_{\Omega} w Q \partial \Omega + \int_{\Gamma_g} w g \partial \Gamma_g. \quad (4.5)$$

$$\int_{\Omega} w \rho c_p T(0) \partial \Omega = \int_{\Omega} w \rho c_p T_0 \partial \Omega \quad (4.6)$$

To develop the Galerkin formulation we define the approximate weighting functions space \mathcal{V}^h with $w^h \in \mathcal{V}^h$ and the function $T^h \in \mathcal{S}^h$ are determined by:

$$\int_{\Omega} w^h \rho c_p \frac{\partial T^h}{\partial t} \partial \Omega + \int_{\Omega} \nabla w^h \cdot \mathbf{k} \cdot \nabla T^h \partial \Omega = \int_{\Omega} w^h Q \partial \Omega + \int_{\Gamma_g} w^h g \partial \Gamma_g. \quad (4.7)$$

$$\int_{\Omega} w^h \rho c_p T^h(0) \partial \Omega = \int_{\Omega} w^h \rho c_p T_0 \partial \Omega \quad (4.8)$$

The function w^h and T^h can be expressed in terms of shape functions N as follows:

$$w^h(\mathbf{x}, t) = \sum_{i=1}^{\mathcal{N}} N_i(\mathbf{x}) \hat{w}(t) \quad (4.9)$$

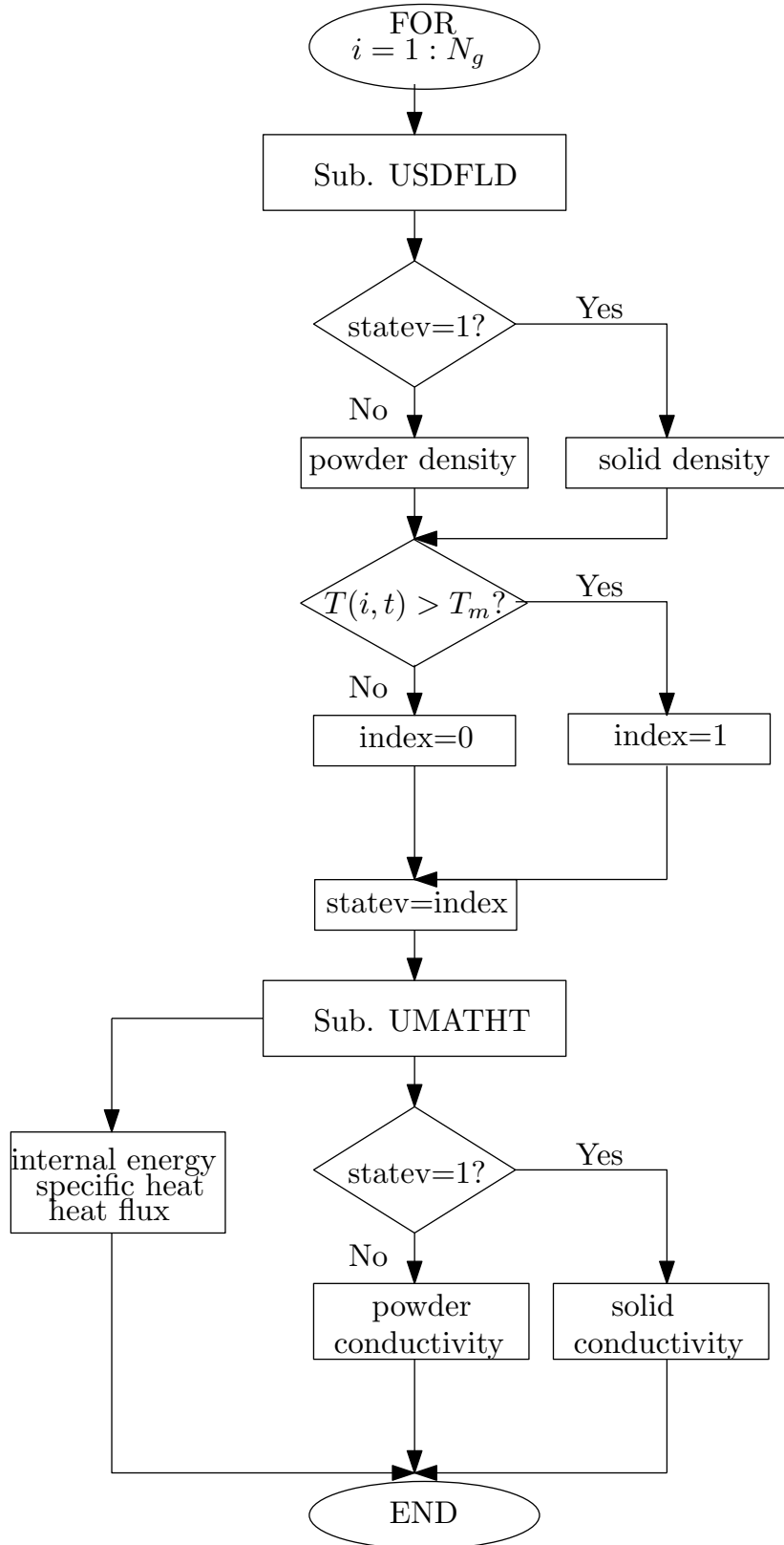


Figure 4.3: Flow chart of user subroutine USDFLD and UMATHT called for i -th Gauss point ($i = 1, \dots, N_g$) at a specific time increment t

4.4. Numerical examples

$$T^h(\mathbf{x}, t) = \sum_{j=1}^{\mathcal{N}} N_j(\mathbf{x}) \hat{T}(t) \quad (4.10)$$

where \mathcal{N} is the total number of nodes, N_i and N_j are the shape functions associated respectively with node i and j and \hat{T} are the unknown temperatures on the nodes. Substituting Eq. 4.9 and 4.10 in Eq. 4.7 and 4.8 we obtain the following matrix problem:

$$\mathbf{M}\dot{\mathbf{T}} + \mathbf{K}\mathbf{T} = \mathbf{F} \quad t \in]0, \mathcal{T}[\quad (4.11)$$

$$\mathbf{T}(0) = \mathbf{T}_0 \quad (4.12)$$

where \mathbf{M} and \mathbf{K} are the assembled capacity and stiffness matrices, and \mathbf{F} is the assembled force vector over all the elements:

$$\mathbf{M} = \mathbf{A}_{e=1}^{nel} \mathbf{m}^e \quad (4.13)$$

$$\mathbf{K} = \mathbf{A}_{e=1}^{nel} \mathbf{k}^e \quad (4.14)$$

$$\mathbf{F}(t) = \mathbf{F}_{nodal}(t) + \mathbf{A}_{e=1}^{nel} \mathbf{f}^e(t) \quad (4.15)$$

with nel the total number of finite elements. The components of the element matrices are defined as:

$$(\mathbf{M})_{ij} = \int_{\Omega} N_i \rho c_p N_j \partial \Omega \quad (4.16)$$

$$(\mathbf{K})_{ij} = \int_{\Omega} \nabla N_i k \nabla N_j \partial \Omega \quad (4.17)$$

$$(\mathbf{F})_i = \int_{\Omega} N_i Q \partial \Omega + \int_{\Gamma_g} N_i g \partial \Gamma_g. \quad (4.18)$$

4.4 Numerical examples

The first goal is the development of an efficient thermal model able to estimate the temperature distribution over the material due to the laser scanning. For this reason we need to validate the FE model: first we evaluate and compare the linear temperature distribution of a semi-infinite body with an analytical solution of temperature field.

Afterwards we simulate the SLM process evaluating the temperature distribution and the melt pool size of a multi-layer Ti64 powder bed. In this example the solidification of the scanned material is neglected considering a powder-liquid-powder phase change; obviously this assumption is quite far to the reality and the temperature distribution is clearly affected to the choice of material model.

In the last example we investigate the thermal and mechanical behaviour of a single layer of titanium alloy over a steel base plate. Finally we assume a powder-liquid-solid phase transformation for the thermal problem and afterwards we conduct a stress analysis with an elasto-plastic constitutive model. We comment the resulted numerical solutions and we conclude with some considerations about the limits of the presented numerical model.

4.4.1 Effect of material model selection

We investigate the temperature profile of a single track assuming for the material three different phase transformations: (i) powder-liquid-powder ('p-l-p'); (ii) solid-liquid-solid ('s-l-s'); (iii) powder-liquid-solid ('p-l-s'); clearly 'p-l-s' is the case which best represents the physics of SLM process and we expect it results to a temperature profile which is between 'p-l-p' and 's-l-s'.

In Fig. 4.4 we show the temperature distributions over a $1 \times 1 \text{ mm}^2$ Ti64 single layer for the mentioned phase transformations. The layer is meshed by $0.1 \times 0.1 \times 0.1 \text{ mm}^3$ and scanned by an elliptical heat source with velocity $v = 1.2 \text{ m/s}$ and laser power $P=195 \text{ W}$ [49]. The presence in the model of powder material leads to an increase of the temperatures in the rear side of the laser due to the lower thermal conductivity of powder ($\approx 10^{-1} \text{ W/(m K)}$) than the solid material ($\approx 10 \text{ W/(m K)}$); for example the maximum temperature at the center point of the scan path for 'p-l-p' is 4613.6 K against the values of 4067.2 K for 's-l-s' and of 4271.2 K for 'p-l-s'. After the center point reaches the maximum temperature it starts cooling and the rate of cooling is depicted in Fig. 4.5. The material model with powder material ('p-l-p') cools down more slowly than the case with only solid ('s-l-s'); this fact is related to the conductivity of the surrounding material, which in case of powder, confines and limits the heat loss. We deduce that the choice of material model for the thermal analysis greatly affects the temperature and consequently the residual stress profiles; a rough simplification of the material model can give solutions distant from the reality.

4.4.2 Comparison with analytical model

In order to validate the numerical model a comparison with the analytical solution of temperature field proposed by Fachinotti et al. [41] is compared with the corresponding numerical solution for a 3D linear problem.

The analytical solution of the temperature field proposed by Fachinotti et al. [41] is obtained in a semi-infinite body with an initial homogeneous temperature and constant material properties. The heat source moves along z -direction with velocity v and it is a double-ellipsoidal heat source. Indeed, the heat source has two semi-ellipsoidal volumes, corresponding to the front and the rear parts of the moving source. The heat source has a Gaussian distribution and the expression is:

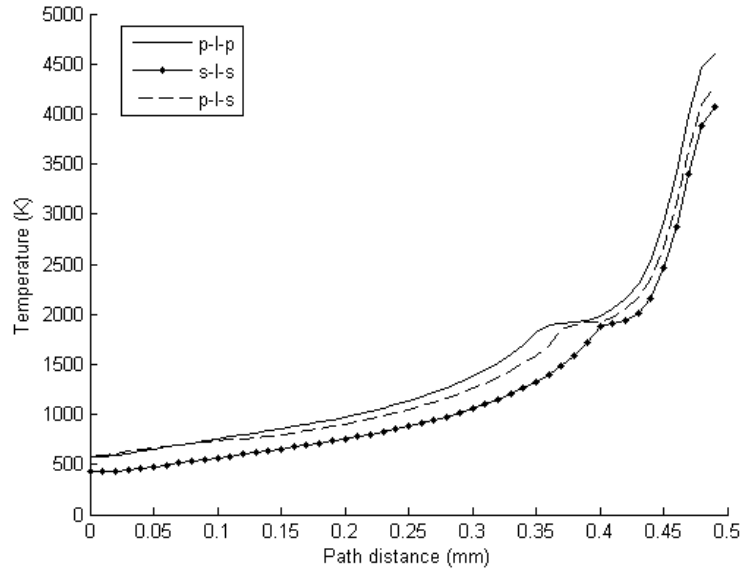
$$q(x, y, z, t) = \frac{6\sqrt{6}P}{\pi\sqrt{\pi}ab} \begin{cases} \frac{f_f}{c_f} \exp[-3\frac{x^2}{a^2} - 3\frac{y^2}{b^2} - 3\frac{(z-vt)^2}{c_f^2}], & \text{for } z > vt \\ \frac{f_r}{c_r} \exp[-3\frac{x^2}{a^2} - 3\frac{y^2}{b^2} - 3\frac{(z-vt)^2}{c_r^2}], & \text{for } z < vt \end{cases} \quad (4.19)$$

where P is the laser power, a , b , c_r , and c_f are the semi-axes parallel to x , y , and z (the rear and front semi-axes of ellipsoid) (Fig. 4.6); f_r and f_f are the portion of the heat deposited. When the depth of the heat source approaches zero (i.e. $b \rightarrow 0$) the double-ellipsoidal source becomes a surface or double-elliptical heat source and the expression is:

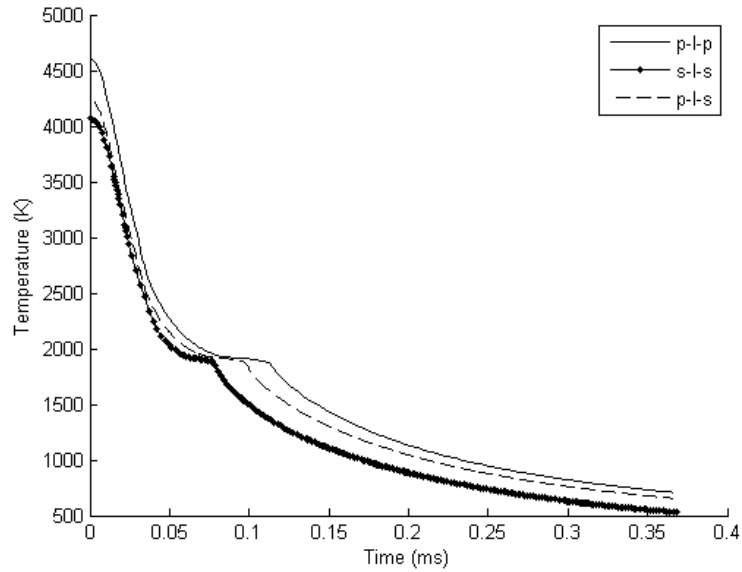
$$q(x, z, t) = \frac{3P}{\pi a} \begin{cases} \frac{f_f}{c_f} \exp[-3\frac{x^2}{a^2} - 3\frac{(z-vt)^2}{c_f^2}], & \text{for } z > vt \\ \frac{f_r}{c_r} \exp[-3\frac{x^2}{a^2} - 3\frac{(z-vt)^2}{c_r^2}], & \text{for } z < vt \end{cases} \quad (4.20)$$

We are interested in studying the cases where the two semi-ellipsoids and semi-ellipses are equal, i.e., substituting $c_f=c_r=c$ and $f_f=f_r=1$ in double-ellipsoidal heat source

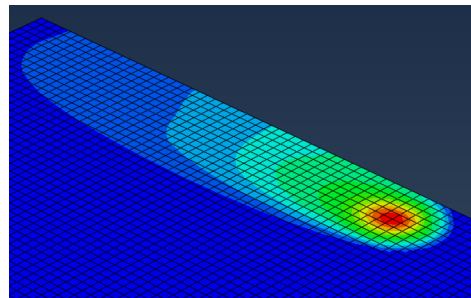
4.4. Numerical examples



(a) Temperature profile along scanning path at $t=3.75$ ms.



(b) Temperature history at the center point of the scan path.



(c) Temperature profile of Ti64 layer at 0.375 ms ('p-l-s')

Figure 4.4: Temperature distribution of a single scanning track over a Ti64 layer with an elliptical heat source: powder-liquid-powder ('p-l-p'); solid-liquid-solid ('s-l-s'); powder-liquid-solid ('p-l-s' case).

4.4. Numerical examples

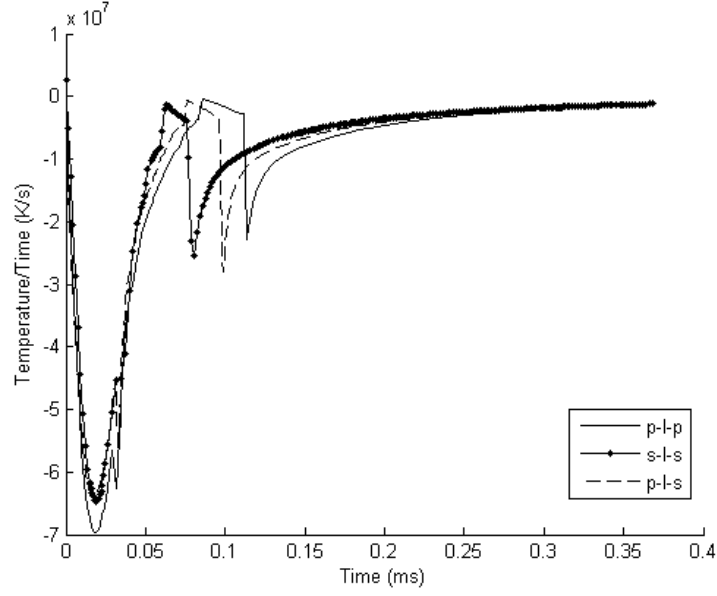


Figure 4.5: Time derivative of temperature at the center point of the scan path: powder-liquid-powder ('p-l-p'); solid-liquid-solid ('s-l-s'); powder-liquid-solid ('p-l-s' case).

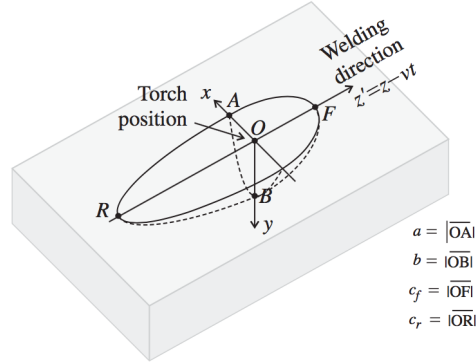


Figure 4.6: Double ellipsoidal heat source, [41].

equation (Eq. 4.19) and in double-elliptical heat source equation (Eq. 4.20). Therefore the heat sources are ellipsoidal and elliptical and can be described by the following expressions:

$$q(x, y, z, t) = \frac{6\sqrt{6}P}{\pi\sqrt{\pi}abc} \exp \left[-3\frac{x^2}{a^2} - 3\frac{y^2}{b^2} - 3\frac{(z-vt)^2}{c^2} \right], \quad (4.21)$$

$$q(x, z, t) = \frac{3P}{\pi ac} \exp \left[-3\frac{x^2}{a^2} - 3\frac{(z-vt)^2}{c^2} \right]. \quad (4.22)$$

The analytical solutions of temperature field at the position (x, y, z) and time t due to an ellipsoidal and elliptical heat sources applied at time t' are respectively:

$$T(x, y, z, t) = T_0 + \frac{3\sqrt{3}}{\pi\sqrt{\pi}} P / \rho c_p \int_0^t \frac{\exp \left[-3\frac{x^2}{12k(t-t') + a^2} - 3\frac{y^2}{12k(t-t') + b^2} \right]}{\sqrt{12k(t-t') + a^2} \sqrt{12k(t-t') + b^2}} [A(1-B) + A(1+B)] dt' \quad (4.23)$$

4.4. Numerical examples

$$T(x, z, t) = T_0 + \frac{3\sqrt{3}}{\pi\sqrt{\pi}} P / \rho c_p \int_0^t \frac{\exp[-3\frac{x^2}{12k(t-t') + a^2}]}{\sqrt{12k(t-t') + a^2} \sqrt{12k(t-t')}} [A(1-B) + A(1+B)] dt' \quad (4.24)$$

with:

$$A = A(z, t, t', c) = \frac{\exp[-3\frac{(z-vt')^2}{12k(t-t') + c^2}]}{\sqrt{12k(t-t') + c^2}} \quad (4.25)$$

$$B = B(z, t, t', c) = \operatorname{erf} \left[\frac{c}{2} \frac{z - vt'}{\sqrt{k(t-t')} \sqrt{12k(t-t') + c^2}} \right]. \quad (4.26)$$

The dimensions of the infinite layer are 200 mm (length) x 100 mm (width) x 100 mm (thickness). The moving heat source starts at point O (0,0,0) at time t=0 and moves along the pattern OF (Fig. 4.7). Four different typologies of mesh size are defined and shown; 'Mesh size 1' is the finest mesh with elements 1x1x1 mm³ over the scanning path (Fig. 4.8). A time step of 0.1 s is kept constant during the analysis. During the

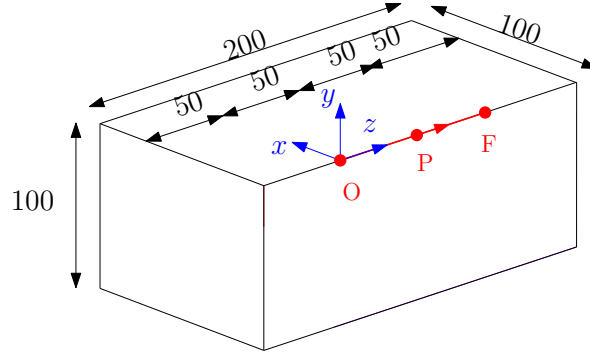


Figure 4.7: Dimensions of infinite layer (mm).

thermal analysis we want to evaluate the temperature history of point P (0, 0, 50 mm) and the temperature profile of the path OF when the laser beam is located on the point P. We consider two different laser heat sources: ellipsoidal and elliptical heat sources (Eq. 4.21 and 4.22). The initial temperature is set to 293.15 K (20 °C). The material

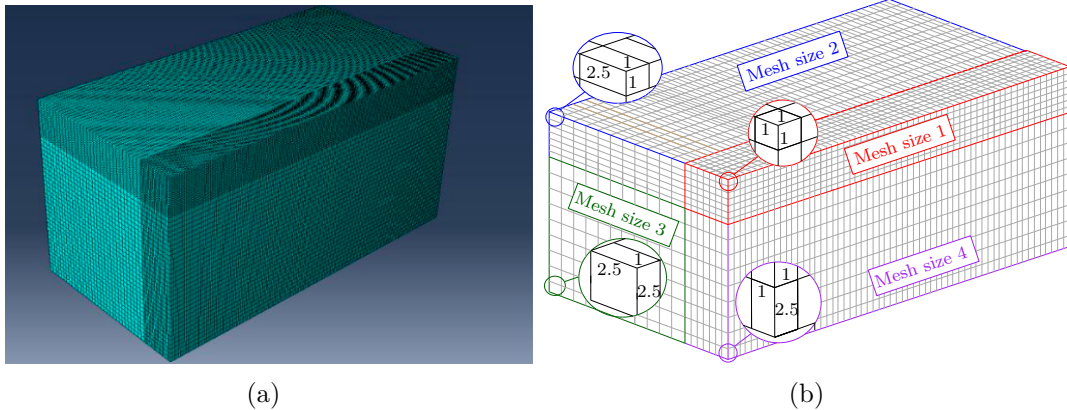


Figure 4.8: Mesh size used in numerical model (mm).

4.4. Numerical examples

properties of the infinite layer are constant and are listed in Table 4.1 with the laser input parameters.

Table 4.1: Input parameters used in analytical solution and numerical model [41]

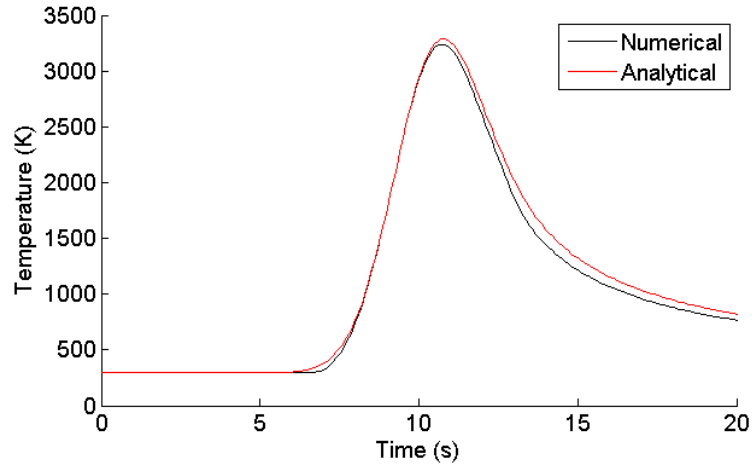
Semi-axis along x (a)	10 mm
Semi-axis along y (b)	2 mm
Semi-axis along z (c)	15 mm
Density (ρ)	7820 kg/m ³
Specific heat (c_p)	600 J/(kg °C)
Thermal conductivity (k)	29 W/(m °C)
Laser power (P)	5083 W
Scanning velocity (v)	5 mm/s

Numerical Results

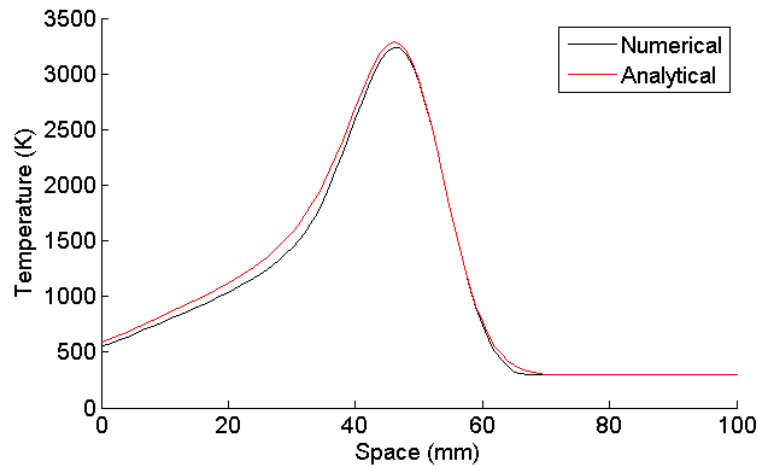
A comparison between numerical and analytical solutions of temperature profile for both ellipsoidal and elliptical heat sources is given in Fig. 4.9 and 4.10. In particular, Fig. 4.9(a) and 4.10(a) show the temperature history of point P (0, 0, 50 mm) and Fig. 4.9(b) and 4.10(b) show the temperature profile along the path OF at t=10 s for the ellipsoidal and elliptical sources respectively.

We can see that the solution of numerical model fits very well the analytical curves. The numerical model can be used to simulate the temperature distribution also for more complex cases.

4.4. Numerical examples



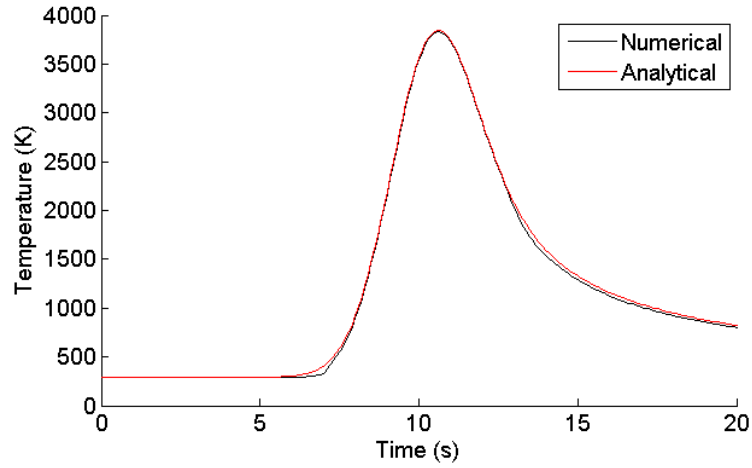
(a) Numerical and analytical solutions of temperature history of point P $(0, 0, 50 \text{ mm})$.



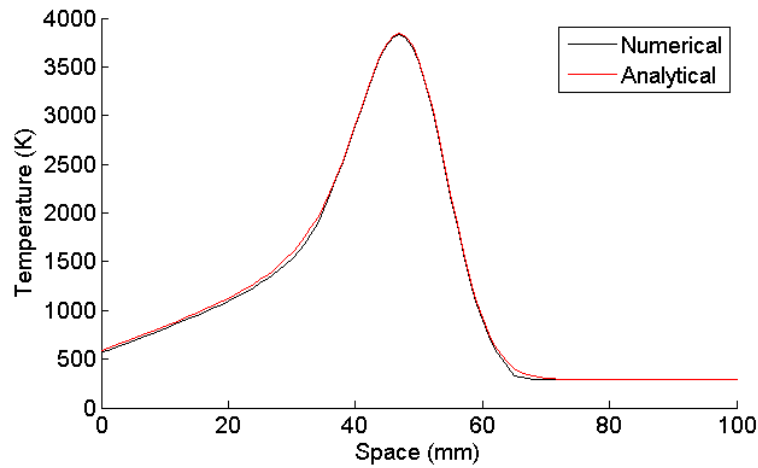
(b) Numerical and analytical solutions of temperature profile along the path OF for $t=10 \text{ s}$.

Figure 4.9: Ellipsoidal heat source: temperature distribution.

4.4. Numerical examples



(a) Numerical and analytical solutions of temperature history of point P $(0, 0, 50 \text{ mm})$.



(b) Numerical and analytical solutions of temperature profile along the path OF for $t=10 \text{ s}$.

Figure 4.10: Elliptical heat source: temperature distribution.

4.4.3 Titanium alloy: Ti-6Al-4V

Titanium is a material with great mechanical properties, low density and good bio-compatibility. Despite the use of titanium with standard methods is very difficult due to the high melting temperature and the extreme reactivity of liquid titanium with atmospheric gases, there is a large production of pure titanium [9, 128] and titanium alloys [84, 89] for SLM applications. In particular Ti-6Al-4V alloy is widely used for biomedical applications, as an implant material due to the relatively low modulus, good bio-compatibility, and corrosion resistance compared to other conventional alloys [9]. The thermal properties of Ti-6Al-4V alloy adopted in the following numerical examples are summarized in Tab. 4.3, 4.4, 4.5. The density of powder material is calculated considering a porosity ϕ equal to 0.4 by the bulk material density:

$$\rho_p = (1 - \phi)\rho_{bulk}. \quad (4.27)$$

According with [108] the temperature distribution is influenced only by the absorptance when the material is liquid; for this reason, when it is not specified, we can assume for powder a value equal to the absorptance of liquid material (≈ 0.1).

Table 4.2: Thermal properties of Ti-6Al-4V alloy [106].

Solidus Temperature	1878.15 K
Liquidus Temperature	1923.15 K
Latent heat of fusion	282000 J/kg

Table 4.3: Specific heat of Ti-6Al-4V alloy [90].

<i>Powder and solid</i> Ti-6Al-4V	
Temperature (K)	Specific heat J/(K kg)
293.15	546
373.15	562
773.15	651
1273.15	641
1873.15	750
1923.15	759
1933.15	831
2173.15	831
3073.15	831

Table 4.4: Thermal conductivity and density of solid Ti-6Al-4V alloy [90].

<i>Solid Ti-6Al-4V</i>		
Temperature (K)	Thermal conductivity (W/m K)	Density (kg/m ³)
293.15	7	4420
373.15	7.45	4406
773.15	12.60	4350
1273.15	19.30	4282
1873.15	27	4198
1923.15	28.40	4189
1933.15	33.40	3920
2173.15	34.60	3750
3073.15	34.60	3138

Table 4.5: Thermal conductivity and density of powder Ti-6Al-4V alloy [46].

<i>Powder Ti-6Al-4V</i>		
Temperature (K)	Thermal conductivity (W/m K)	Density (kg/m ³)
293.15	0.2	2652
1878.15	19.4	4189
1923.15	28.3	4189

4.4.4 Melt pool analysis

The prediction of melt pool during the fusion of powder material is crucial to the outcomes of the SLM component, such as microstructure and mechanical properties. The following numerical example is performed in order to obtain a good estimation of the melt pool, starting from the work of Fu and Guo [46] and simulating a multilayer Ti-6Al-4V part scanned by a moving heat flux.

In order to reduce the computational costs a reduced geometry from the original study [46] is depicted in Fig. 4.11(a). The dimensions of the part are 1 mm (length) x 0.2 mm (width) x 0.09 mm (thickness). The thickness of the layer is 0.03 mm and three layers are built-up during the simulation. The part is symmetric with respect to Y-Z plane. In order to simulate the presence of a solid substrate, an infinite convection coefficient is assumed on the bottom of the first layer. The initial temperature is set to the room temperature and it is equal to 293.15 K (20 °C). The Gaussian heat source moves along the z direction over each layer (Fig. 4.11(b)) with the following expression:

$$q(r) = \frac{\alpha P}{\pi R^2} \exp\left(-2r^2/R^2\right) \quad (4.28)$$

where r is the radial distance and R the beam radius. The laser beam parameters are listed in Table 4.6. At initial state the titanium alloy material is powder and a powder-liquid-powder material model is assumed. The thermal conductivity and the specific heat are temperature-dependent while absorptance α and density ρ are assumed constant ($\alpha_p = 0.77$, $\rho_s = 4428$ kg/m³).

The numerical model is discretized with a mesh of 8-node brick elements (DC3D8). A constant mesh size of 0.01 x 0.01 x 0.01 mm³ is adopted (Fig. 4.12). The modelling of the layer build-up process is simulated using the MODEL CHANGE option in Abaqus: the whole geometry is created with the powder mesh; then the second and the third

4.4. Numerical examples

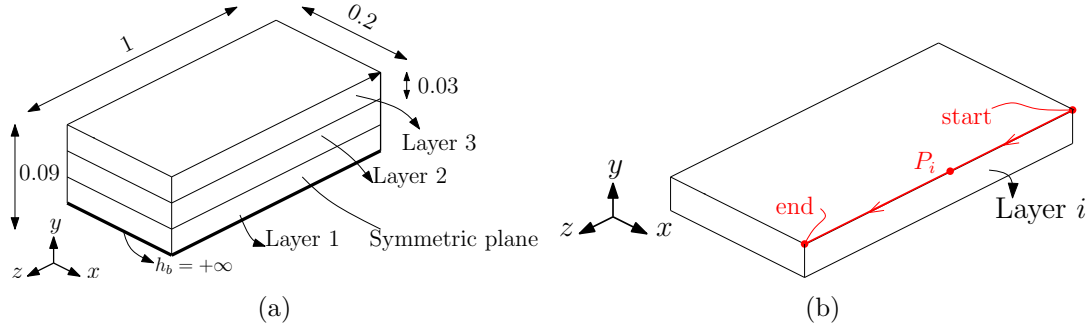


Figure 4.11: Geometry of melt pool analysis. a) Dimensions of geometry (mm); b) Scanning path along layer i (with $i=1,2,3$) with middle point $P_i = (x_P, y_{P_i}, z_P)$.

layers are deactivated at the beginning of the analysis; after each layer is activated followed by the laser scanning.

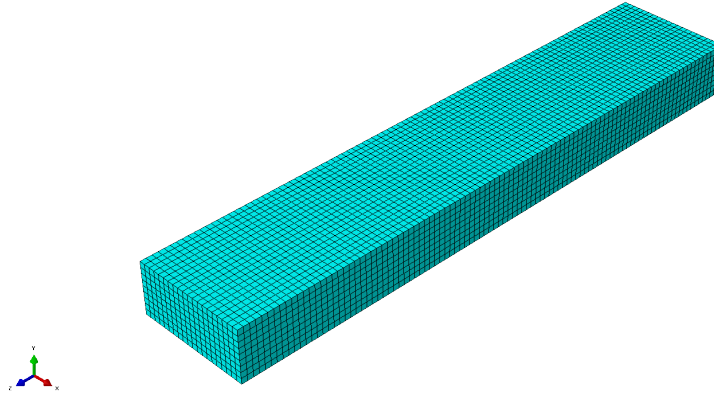


Figure 4.12: FE mesh of multiple layers.

Table 4.6: Laser beam parameters [46].

Laser power (P)	20 W
Scanning velocity (v)	200 mm/s
Laser beam radius (R)	0.026 mm

Numerical results

The temperature distribution of i st layer (with $i=1,2,3$) when the laser beam center is placed on the middle point $P_i = (x_P, y_{P_i}, z_P)$ is shown in Fig. 4.13. The temperature distribution exhibits the common 'comet tail', which derives from the higher thermal conductivity of liquid than powder material. This phenomenon is also widely reported by many authors [59, 106]. The last layer shows an higher temperature in the powder due to the heated previous layers when a re-coating time of powder is not assumed. The region depicted in gray is the melt pool, where the temperature is greater than liquidus temperature ($T_l = 1928.15$ K). The dimensions of the melt pool region for the three layers are very close and agree with the simulation data for powder material

4.4. Numerical examples

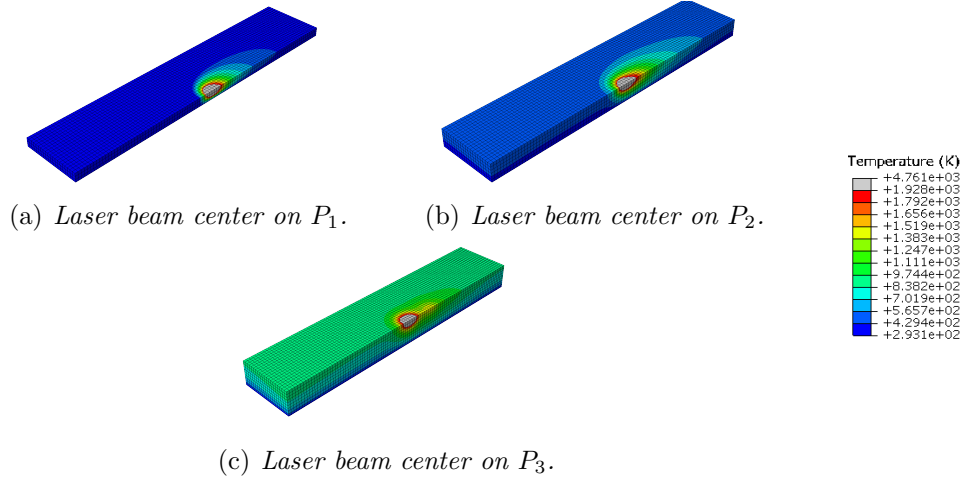


Figure 4.13: Temperature field (K) and melt pool (gray region) in Layer 1, 2, 3.

obtained by Fu and Guo [46]. A representative figure of half melt pool region in the first layer with the respective dimensions is shown in Fig. 4.14. In particular, for the selected laser power (20 W), the melting depth D is about 0.02 mm, less than the layer thickness, therefore no remelting of the underlying layers occurs. The melting width W and length L are about 0.06 mm and 0.07 mm respectively; the length to diameter ratio (L/W) of the melt pool is less than the critical value π , therefore the 'balling effect' does not occur.

The temperature profiles from the point P_3 along the depth, the width and the scanning directions are shown in Fig. 4.15. The curves exhibit a temperature gradient in good agreement with the numerical results obtained by Fu and Guo [46].

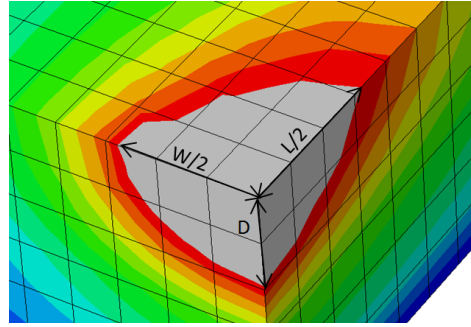


Figure 4.14: Half melt pool in the first layer; dimensions: depth (D), width ($W/2$), and length ($L/2$).

4.4. Numerical examples

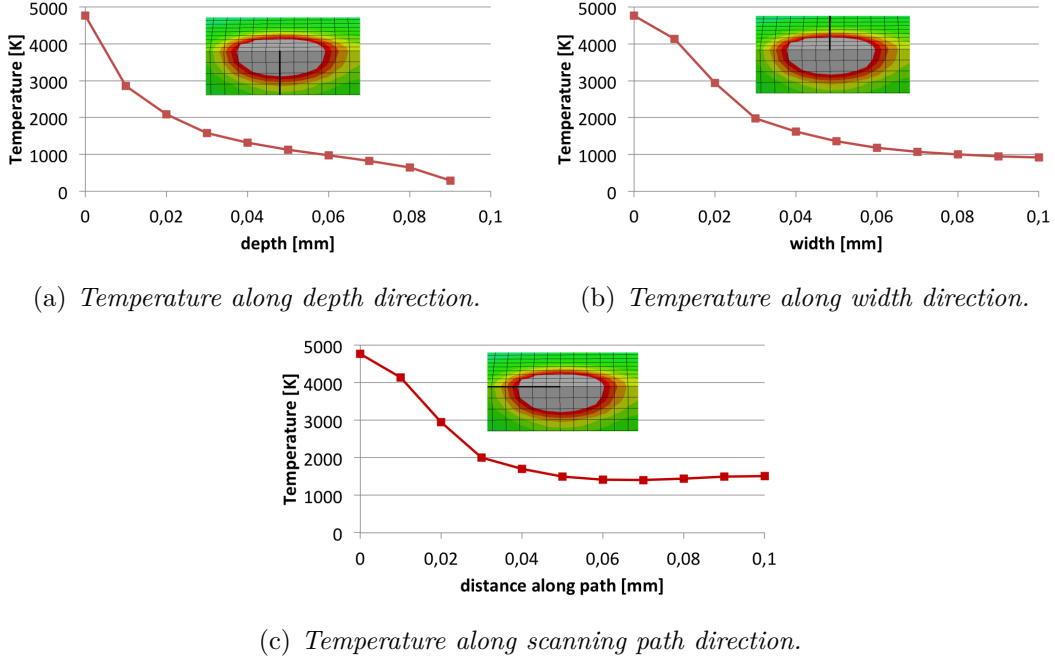


Figure 4.15: Temperature field (Kelvin) along the depth, width and scanning direction.

4.4.5 Thermo-mechanical analysis

The prediction of the temperature distribution during the laser scanning is essential for the prediction of the residual stresses in the final part. The following example is presented to investigate the distribution of the internal stresses profile on a single titanium-alloy powder layer placed over a steel base plate.

The geometry of the investigated part is depicted in Fig. 4.16. The dimensions of the single layer are 1 mm (length) x 1 mm (width) x 0.03 mm (thickness) while the dimensions of the base plate are 3 mm (length) x 3 mm (width) x 1 mm (thickness). The initial temperature is set equal to the chamber temperature (≈ 313.15 K) and the

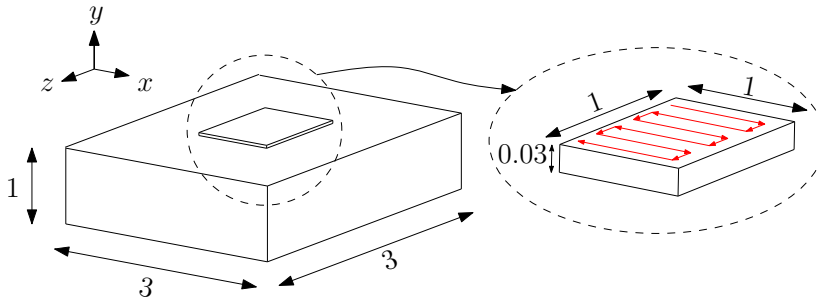


Figure 4.16: Dimensions of Ti64 layer on steel base plate (mm).

upper surface can loose heat by convection, with a constant coefficient $h=20$ W/m² K, while radiation is neglected.

The laser beam moves over the single layer following the scanning path in Fig. 4.17: the whole laser scanning takes 8 ms, after this the laser beam is moved away and the temperature is cooled down for 600 s. The heat flux is cylindrical to reduce the computational effort and it is obtained from a numerical average of the Gaussian

4.4. Numerical examples

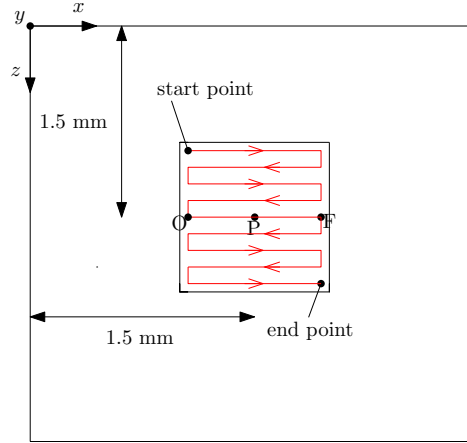


Figure 4.17: Scanning strategy of laser beam

distribution [106]:

$$\bar{q} = 0.864 \alpha \frac{P}{\pi R^2} \quad (4.29)$$

with the laser beam parameters listed in Tab. 4.7. The scanned region is modelled as a square with dimensions equivalent to the beam diameter.

Table 4.7: Laser beam parameters [106]

Laser power (P)	195 W
Scanning velocity (v)	1200 mm/s
Laser beam radius (R)	0.05 mm

The Ti-6Al-4V layer is initially powder; when the laser beam moves over the powder bed the material reaches the melting temperature and becomes liquid; after the material cools down it becomes solid; the phase transformation is implemented by the user subroutines UMATHT and USDFLD (Fig. 4.3), which are also reported in Appendix A. The thermo-physical material properties of the Ti64 and AISI 1015 are respectively summarized in Tab. 4.4, 4.5 and Tab. 4.8-4.10.

Table 4.8: Thermal properties of AISI 1015 [106].

Solidus Temperature	1753.15 K
Liquidus Temperature	1773.15 K
Latent heat of fusion	247000 J/kg

The thermal and stress analyses are conducted separately: first the temperature distribution in space and in time is computed and after it is projected in the stress analysis as a predefined field. The mesh size is the same for thermal and stress analyses (element size $0.01 \div 0.2$ mm) with the only difference on the element type (Fig. 4.18).

The boundary conditions on the mechanical analysis represent the experimental tests carried out by Roberts [106]: one side of the base plate is fixed (Fig. 4.19(a)), therefore a clamped boundary condition is imposed on the extreme side (Fig. 4.19(b)). The constitutive model is an elasto-plastic model; according with Roberts [106] the assumption of a kinematic hardening model gives more accurate displacement results than the

4.4. Numerical examples

<i>Solid</i> AISI 1015		
Temperature (K)	Thermal conductivity (W/m K)	Density (kg/m^3)
298.15	51.9	7950
673.15	49	7785
1073.15	29.3	7575
1753.15	30	7260
1773.15	30	6880
1923.15	30	6725
2373.15	30	6300
3073.15	30	5630

Table 4.9: Thermal conductivity and density of AISI 1015 [106].

Table 4.10: Specific heat of AISI 1015 [106].

<i>Solid</i> AISI 1015	
Temperature (K)	Specific heat J/(K kg)
298.15	630
673.15	630
1073.15	687
1923.15	770
2373.15	770
3073.15	770

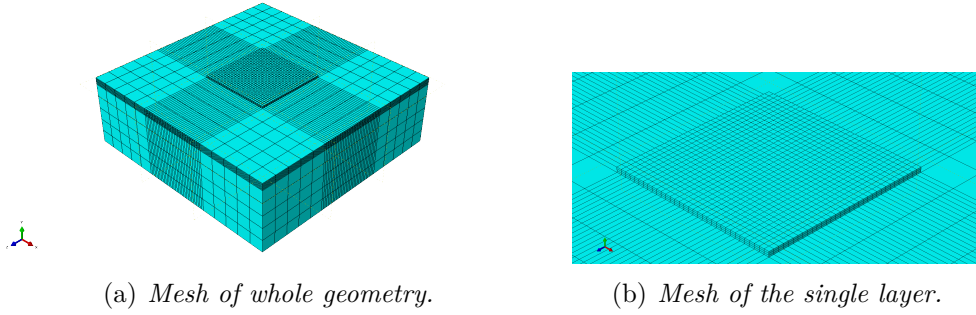


Figure 4.18: FE Mesh size of Example 2.

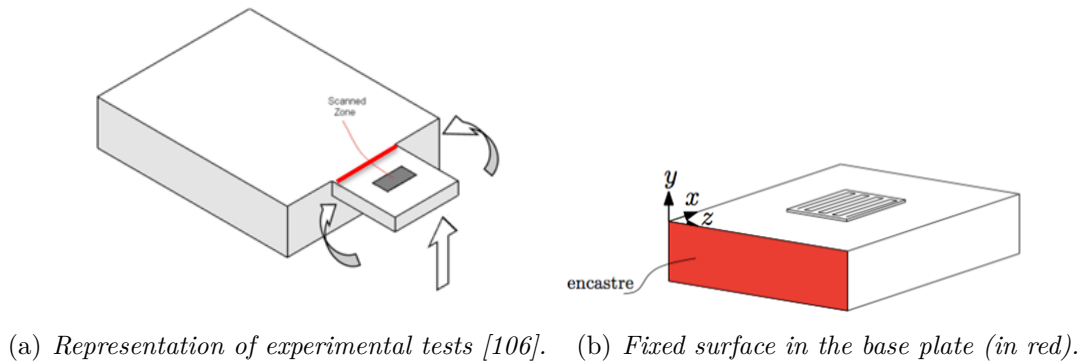


Figure 4.19: Boundary condition in the base plate for stress analysis.

4.4. Numerical examples

Table 4.11: Mechanical properties of Ti64 [106].

Ti-6Al-4V			
Temperature (K)	Young modulus (GPa)	Yield stress (MPa)	Expansion coefficient 10^{-6} (1/°C)
298.15	114	1061	8.2
373.15	109	933.7	9.2
473.15	100	742.7	9.9
588.15	93	668.4	1.05
703.15	84	615.4	1.1
813.15	57	477.5	1.14
1923.15	0.1	1	2.01
3073.15	0.1	1	2.01

Table 4.12: Mechanical properties of AISI 1015 [106].

AISI 1015			
Temperature (K)	Young modulus (GPa)	Yield stress (MPa)	Expansion coefficient 10^{-5} (1/°C)
298.15	200	255	1.07
373.15	196	247.4	1.24
473.15	190	224.4	1.37
588.15	180	204	1.48
703.15	166	178.5	1.56
813.15	140	112.2	1.62
923.15	100	61.2	1.64
1073.15	0.1	1	1.65
3073.15	0.1	1	2.81

isotropic model. Anyway, the final residual stresses are not significantly affected by the choice of strain-hardening model; for this reason we adopt an isotropic hardening model. In particular, the total strain can be generally represented by:

$$\varepsilon = \varepsilon_{el} + \varepsilon_{pl} + \varepsilon_{th} \quad (4.30)$$

where ε_{el} , ε_{pl} , ε_{th} are respectively the elastic, plastic and thermal strain components. The thermal component ε_{th} is calculated by:

$$\varepsilon_{th} = \beta \Delta T \quad (4.31)$$

where β is the thermal expansion coefficient [1/°C].

The mechanical properties of Ti-6Al-4V and AISI 1015 (i.e., Young modulus, yield stress, thermal expansion coefficient) are also temperature dependent and are depicted in Tab.4.11 and 4.12 respectively.

4.4.6 Results and discussions

Thermal analysis

The temperature distribution in the single layer of Ti-6Al-4V is depicted in Fig. 4.20 for different time steps: 0.4, 0.8, 3, 5.5 ms. The maximum temperature on the surface is about 2946 K and the contour plots of the temperature field are very similar during the simulation time. Along a single track and after few time increments the temperature field reveals a similar pattern.

The evolution of temperature profile along the first scanning track is depicted in Fig. 4.21: at the initial time increment the temperature increases from 313 K to about 1000 K over a length which is equal to the laser diameter; at successive time increments, when the laser moves, the temperature profile skews towards the rear of the laser due to the higher thermal conductivity of melted material and after few time increments it reaches a 'steady-state' profile.

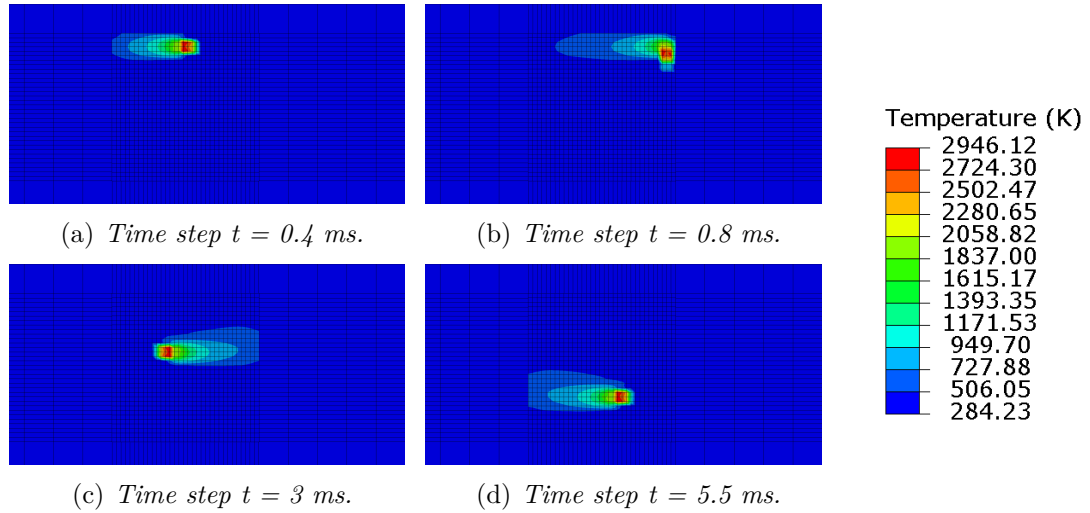


Figure 4.20: Temperature distribution (K) of the layer for different time steps.

The single track is independent from the adjacent scan tracks since when the laser moves along a new pattern, the previous track is just cooled. In Fig. 4.22 the temperature history of point P ($x=1.5$ mm, $z=1.5$ mm) is depicted for three adjacent scan tracks; the increments of temperature over the chamber temperature due to the previous and successive scans are respectively of 100 K and 300 K.

The melt pool region is preserved constant during the simulation and in Fig. 4.23(a) the grey region represents the region where the temperature is higher than the melting temperature ($T_m = 1923.15$ K). The length (L) and the width (W) of the melt pool are about 1.5 mm and 1.2 mm and the ratio (L/W) is less than the critical balling value π . The melt pool depth (D) is about 0.018 mm which is less than the height of the powder layer: this fact is due to the low value of powder thermal conductivity respect to the liquid (Fig. 4.23(b)).

During the time simulation whenever the value of temperature in the integration point exceeds the melting temperature, the material model is switched from powder to solid: in Fig. 4.23(c) the red part represents the solidified part while the blue part represents the unmelted powder. This information is very useful to select the best choice of process parameters to obtain a good connection between the layers and prevent delamination; in

4.4. Numerical examples

particular the solidified part depends on the intensity of laser power and laser velocity.

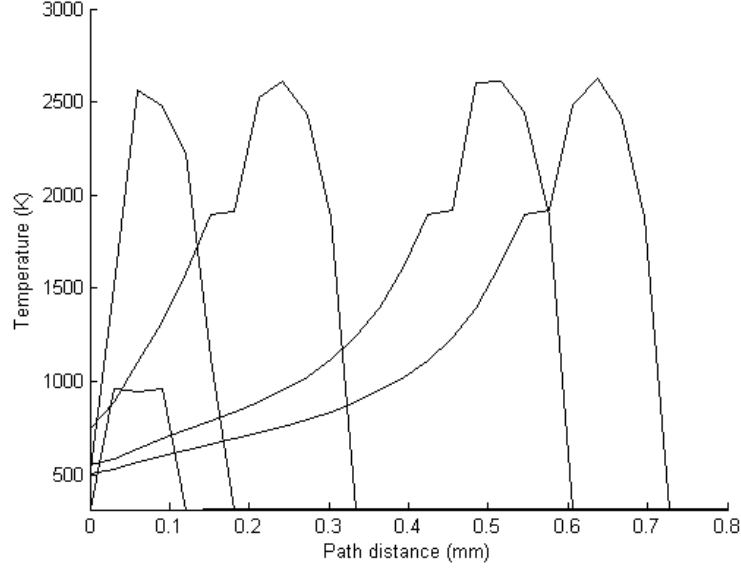


Figure 4.21: Temperature profiles along the first scan track for different time steps.

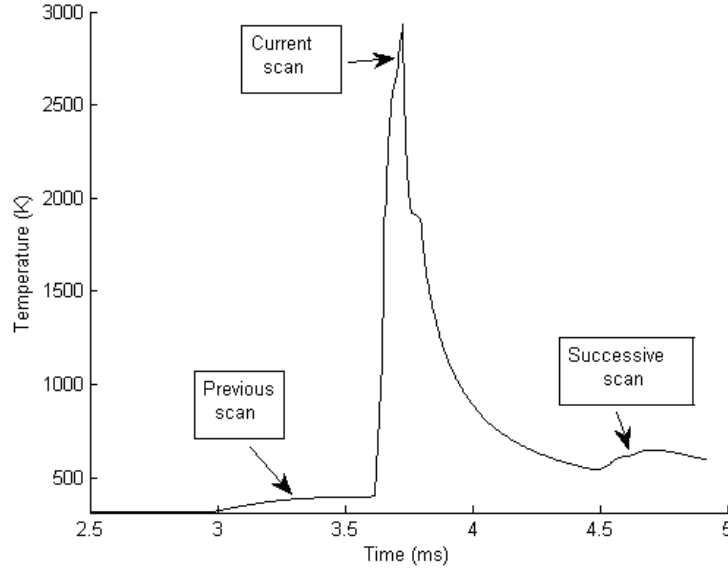


Figure 4.22: Temperature history of point P ($x=1.5$ mm, $z=1.5$ mm).

The temperature profile along depth when the laser center is placed on P is given in Fig. 4.26. The powder layer observes a steeper temperature gradient respect to the base plate ($30 \mu\text{m}$ depth) where the temperature is about 450 K, much lower the melting temperature of the AISI 1015 (≈ 1773.15 K), which is in contrast with the observations of Roberts [106]. This discrepancy on results is probably related to the different solidification criterion: according with Dai and Shaw [33] the criterion to judge whether an element is powder or solid greatly affects the resulted temperature solution

4.4. Numerical examples

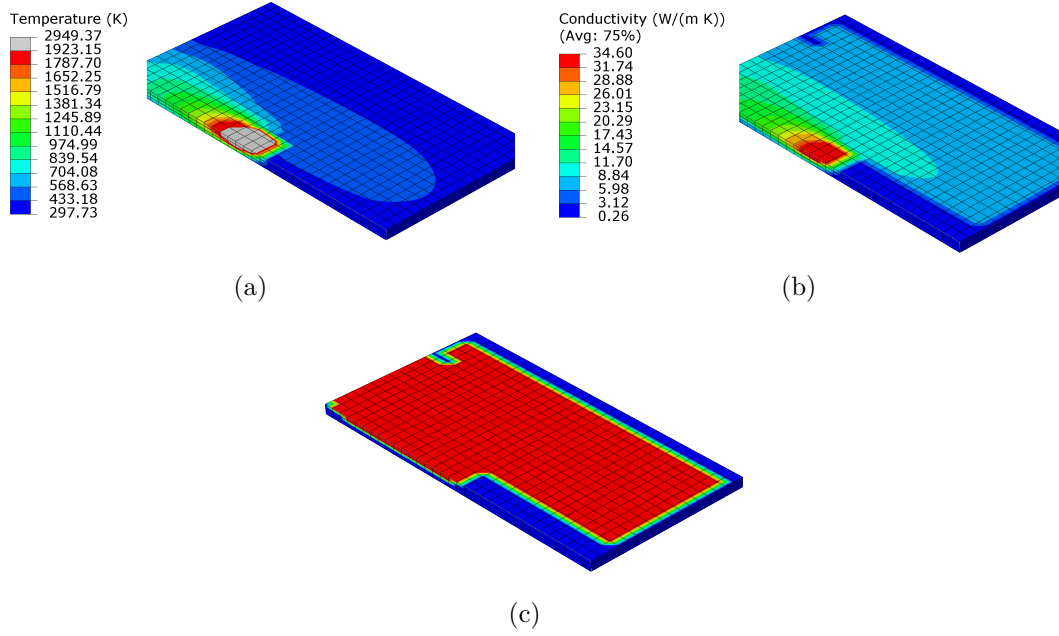


Figure 4.23: Solution and material properties at 3.675 ms: (a) Temperature solution (K); (b) Temperature dependent thermal conductivity (W/(m K)); (c) Solidified material (red part).

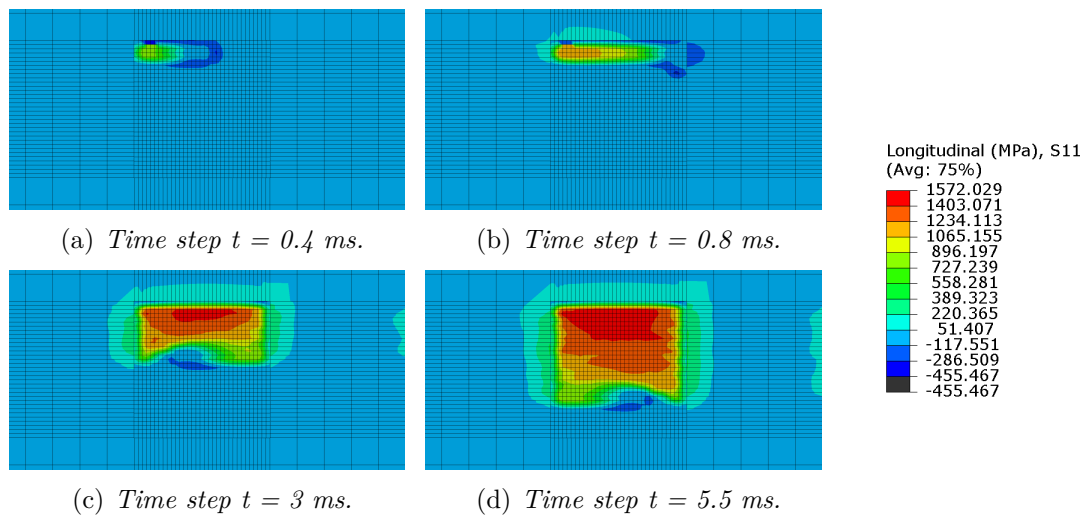


Figure 4.24: Longitudinal transient stresses σ_{xx} (MPa) for different time steps.

4.4. Numerical examples

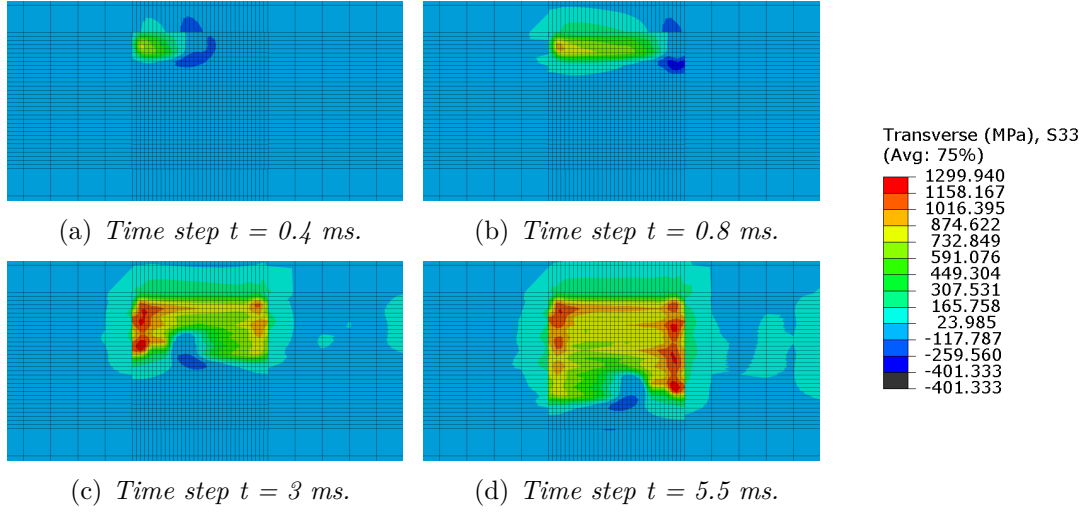


Figure 4.25: Transverse transient stresses σ_{zz} (MPa) for different time steps.

and also the solid profile. Roberts [106] converted an element from powder to solid if the lowest nodal temperature on each element exceeds the melting point; if we also assume such criterion we should obtain a lower temperature value on the top surface of the layer and an higher value on the top of the base plate, obtaining comparable results.

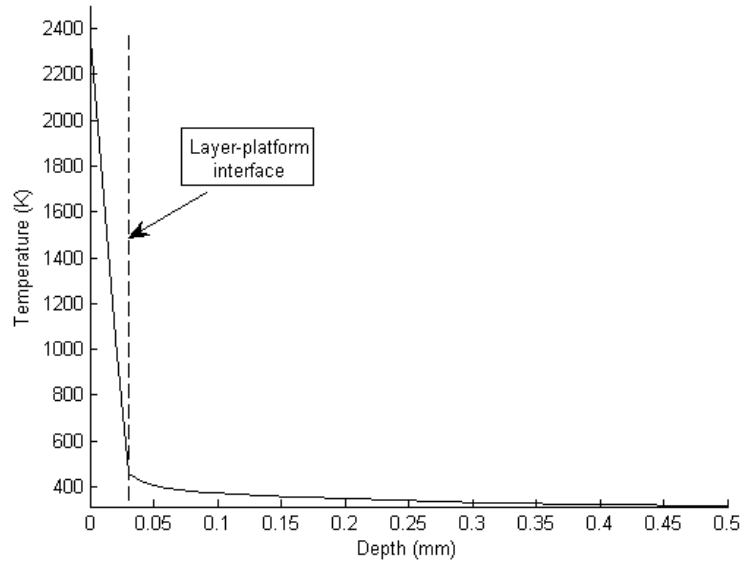


Figure 4.26: Temperature profile along depth at 3.675 ms.

Stress analysis

During the analysis transient thermal stresses are visible during the laser transition; in particular when the laser beam heats the surface the thermal stresses are compressive (negative values) due to the thermal expansion of the upper part of the layer and during

4.4. Numerical examples

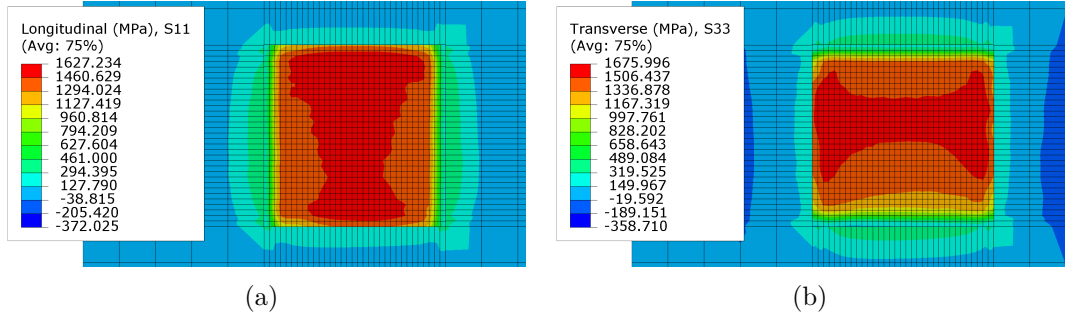


Figure 4.27: Residual stresses profile at 600 s: (a) longitudinal stresses (b) transverse stresses.

cooling the thermal stresses becomes tensile (positive values) due to the shrinkage of the upper part.

In general the normal stress component (σ_{yy}) are very small compared to the longitudinal (σ_{xx}) and transverse (σ_{zz}) stress components; for this reason we show the numerical results of longitudinal and transverse transient stresses when the laser is moving over the surface (Fig. 4.24, 4.25). The longitudinal thermal stresses are higher than the transient stresses and in this case the maximum values during the time history are 1572 MPa for the longitudinal direction and 1299 MPa for the transverse direction.

After a time of 600 s the part is completely cold and the residual stresses arise inside the part. The distribution of residual longitudinal and transverse stresses on the Ti64 layer are concentrated along the scanning directions (Fig. 4.27). Tensile residual stresses for both directions have maximum values above the yield stress (≈ 1061 MPa). The distribution along the OF path is depicted in Fig. 4.28: the longitudinal stresses are uniformly distributed along the path while the transverse stresses are concentrated along the edges; this is because the residual stresses are much greater along the scanning direction. The maximum longitudinal stress value along OF is 1491.8 MPa and the transverse stress is 1623.4 MPa.

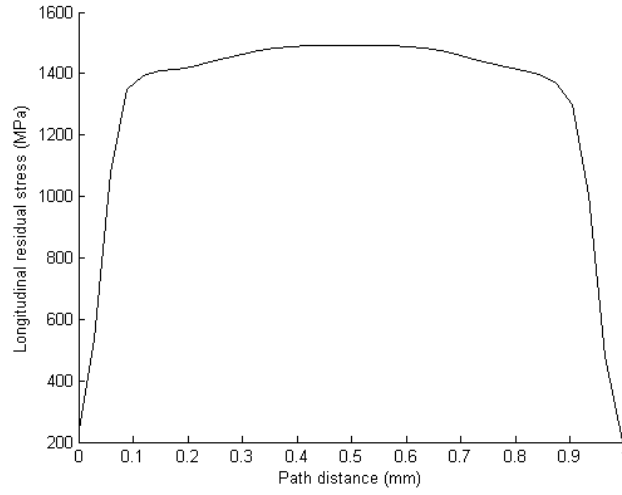
The longitudinal (σ_{xx}) stress profile along depth drastically changes from the layer to the platform: the residual stresses in the single layer are tensile and decrease with depth transforming in compressive stresses at about 0.13 mm depth (Fig. 4.29). A very similar distribution is obtained by Roberts [106] for isotropic hardening model (Fig. 4.29(c)).

Deformation of the base plate

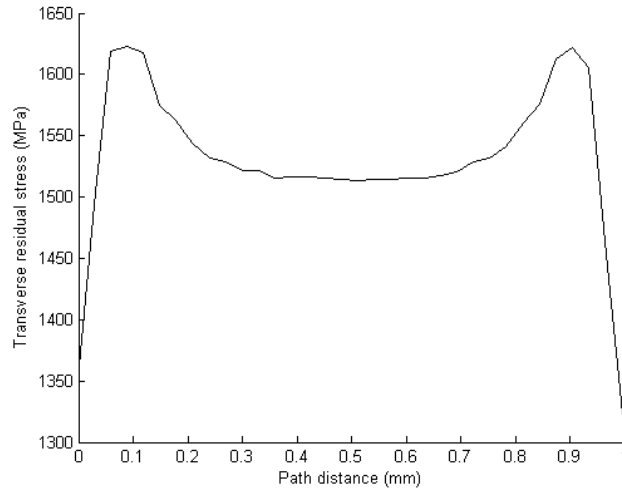
The role of the base plate to the outcomes of SLM parts is also crucial; for example a thicker platform can reduce the residual stresses and the bending deformation. For this reason is essential to implement and assess the mechanical behaviour of the base plate. In particular the base plate experiences an outright bending during the process. During heating ($t < 8$ ms) the top surface expands while the bottom part shrinks (Fig. 4.30); after cooling ($t > 600$ s) the upper part starts to shrink and the bottom part enlarges (Fig. 4.31).

We show the vertical displacements of the base plate along the cross sections A-A' and B-B' in Fig. 4.32. Along section A-A' the point on the free edge experiences a deflection with maximum magnitude of $-0.753 \mu\text{m}$ (Fig. 4.33a) and of $+0.893 \mu\text{m}$ during

4.4. Numerical examples



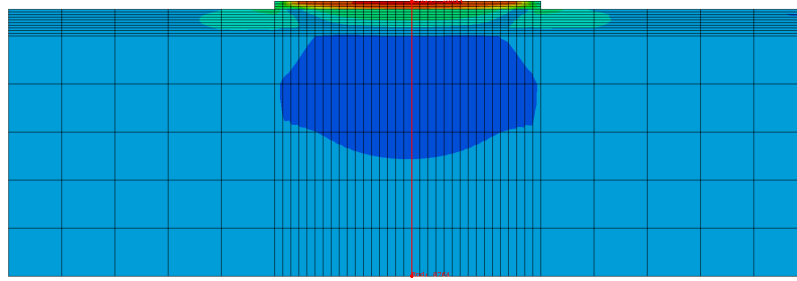
(a)



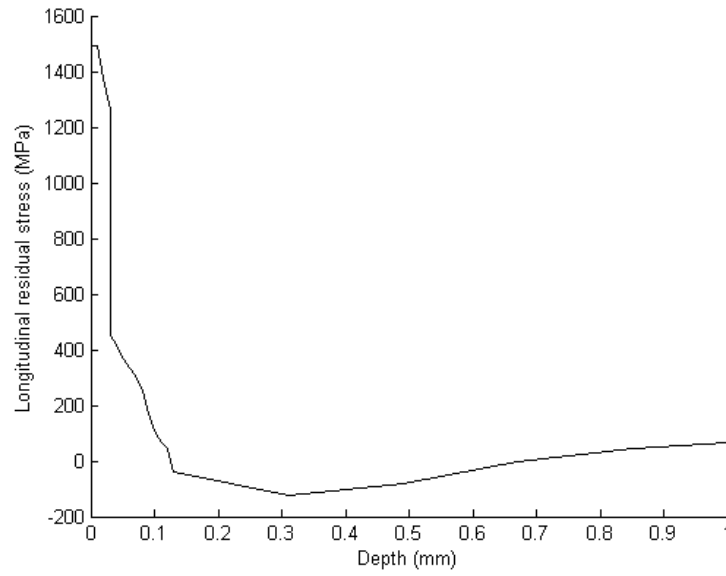
(b)

Figure 4.28: Residual stresses profile along path OF: (a)longitudinal stresses; (b)transverse stresses.

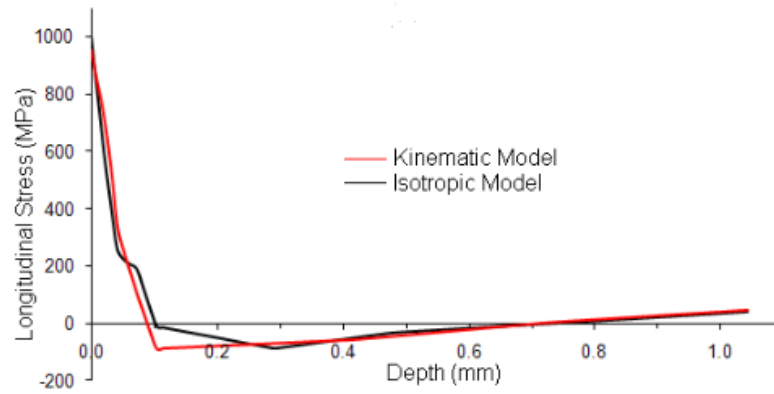
4.4. Numerical examples



(a)



(b)



(c)

Figure 4.29: (b) Longitudinal residual stresses (σ_{xx}) along depth (black line); (c) Longitudinal residual stresses along depth obtained by Roberts [106].

4.4. Numerical examples

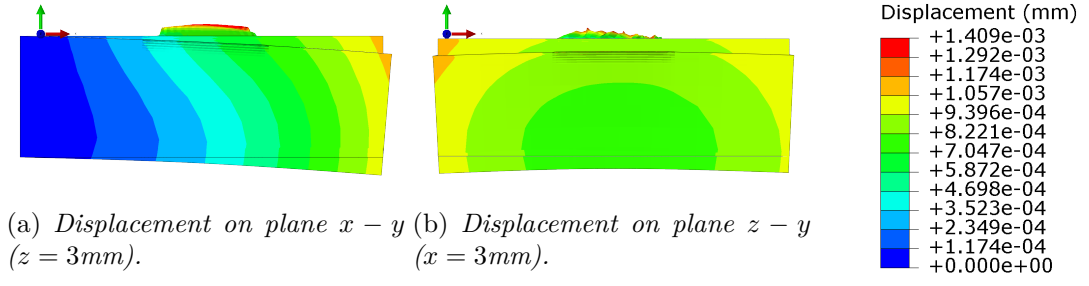


Figure 4.30: Displacement (magnitude) of base plate at 8 ms (deformation scale factor: 150).

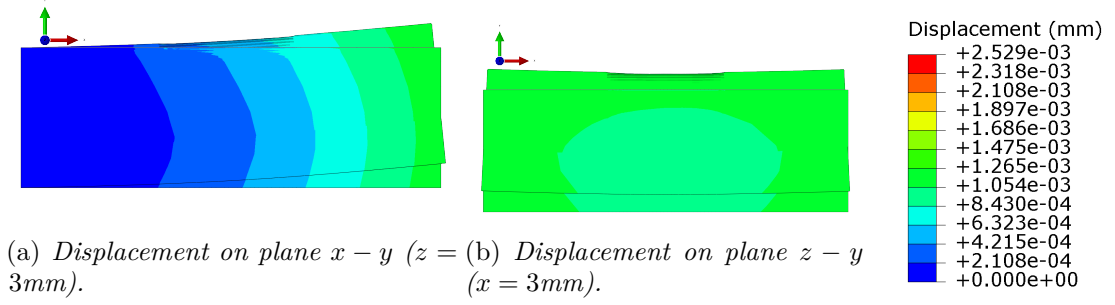


Figure 4.31: Displacement (magnitude) of base plate at 600 s (deformation scale factor: 150).

heating (Fig. 4.34a). The vertical displacement on the extreme points along section B-B' is about $-0.37\ \mu\text{m}$ (Fig. 4.33b) during heating and about $+0.3\ \mu\text{m}$ during cooling (Fig. 4.34b). Therefore we can deduce from results that the nodes of the base plate, quite far from the scanned region, observe comparable vertical displacement during heating-cooling period.

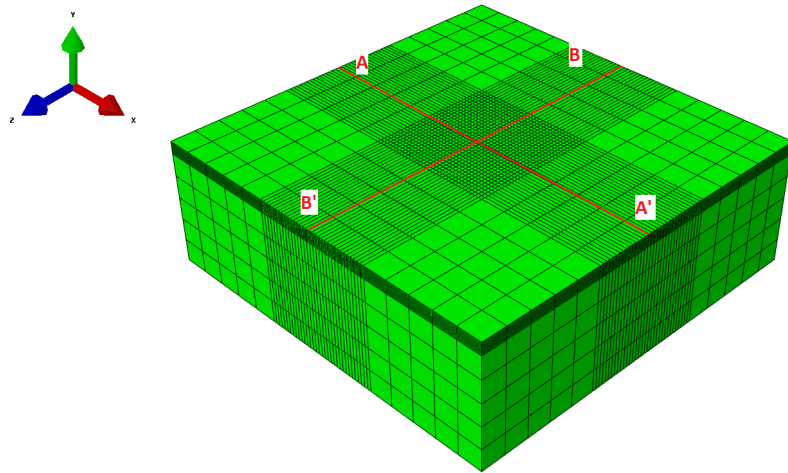


Figure 4.32: View of base plate and cross sections.

4.4. Numerical examples

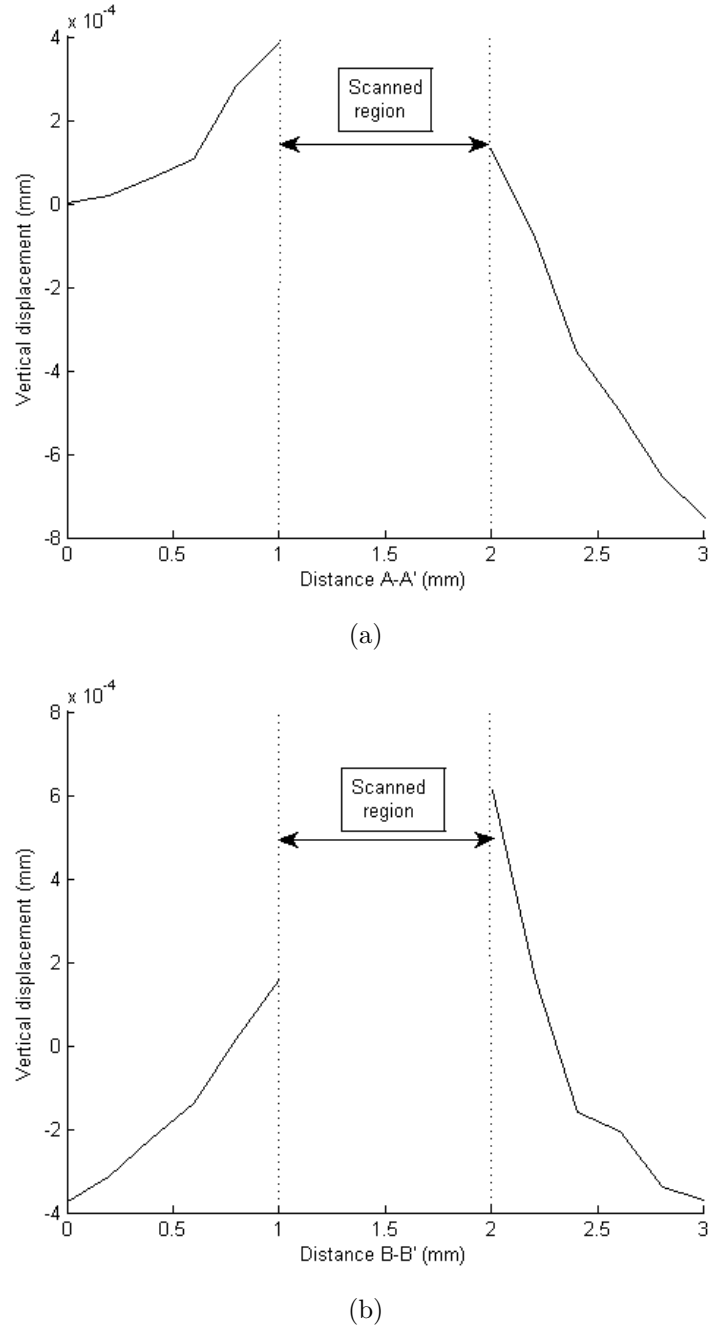


Figure 4.33: Vertical displacement (mm) of base plate along cross sections A-A' and B-B' at 8 ms.

4.4.7 Computational times and limitations

The computational time is a measure of efficiency and reliability of the numerical method which can have a great impact in terms of cost and material waste, especially for AM applications. Abaqus/Standard uses the Newton-Raphson method to solve nonlinear heat transfer problems and the time integration in transient problems is done with the backward Euler method, which is unconditionally stable for linear problems. For the investigated numerical examples the computational times are summarized in Tab. 4.13. The thermal model presented in Sec. 4.4.4 has 21210 dofs and it is

4.4. Numerical examples

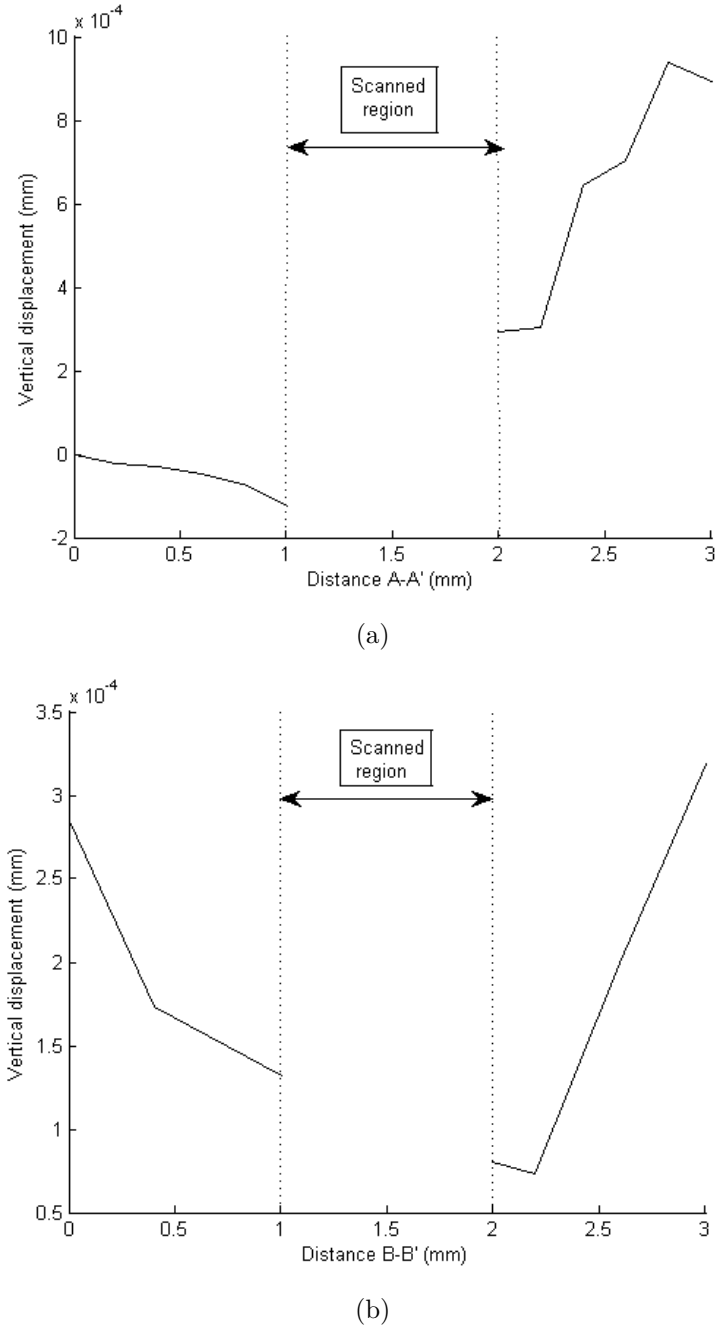


Figure 4.34: Vertical displacement (mm) of base plate along cross sections A-A' and B-B' at 600 s.

performed with 1 CPU, with a total wallclock time of 32 min. The thermal and stress analyses of the numerical model presented in Sec. 4.4.5 with 34444 dofs are performed with 6 CPU; the wallclock time for the thermal analysis is 26 hours and 42 min, and for the stress analysis is 3 hours and 4 min.

From the reported results it is evident that the thermal analysis requires much computational effort due to the strong nonlinearity came from the phase transformation (with latent heat) and the presence of two material states inside the element (solid and liquid). Furthermore the presence of powder material leads to high thermal gradients with the

4.4. Numerical examples

necessity of using small time increments to reach stable solution. This fact is confirmed if we compute the same thermal analysis but assuming a solid-liquid-solid phase change and a powder-liquid-powder phase change: in these cases the computational times are respectively 8 hours and 14 hours.

Table 4.13: Computational times of three-dimensional SLM simulation.

Model	Numerical analysis	DOFs	Analysis time
Sec. 4.4.4	Thermal analysis	21210	32 min
Sec. 4.4.5	Thermal analysis	34444	26 hours and 42 min
	Stress analysis	34444	3 hours and 4 min

Due to the necessity to enhance the speed of computation time, especially for thermal analysis, in the following section we introduce a simplified model where we assume a simplified source model with an imposed temperature distribution. The temperature distribution comes from a 'steady-state' temperature solution of a single track of laser beam. Afterwards we impose such solution along consecutive scanning tracks with width equal to the laser beam diameter (0.1 mm).

4.5 Improvements of numerical model

From the numerical results of the previous section (Sec. 4.4.5) we can deduce that most of the elements of the base plate remain 'linear' during the thermal analysis.

The variation of temperature during the laser scanning interests the nodes of the base plate within 0.1 mm depth (Fig. 4.35(a)). For this reason in the following section we re-define the mesh of the numerical model in Sec.4.4.5 assuming a non-conforming mesh between the two parts (Fig. 4.35(b)); a fine mesh is assumed equal to $0.03 \times 0.03 \times 0.01 \text{ mm}^3$ and a coarse mesh is $0.1 \times 0.1 \times 0.1 \text{ mm}^3$. The two parts are connected assuming a surface-surface tie constraint, which allows to fuse two regions even though with dissimilar meshes. The temperature distribution on the powder layer is comparable with the solution obtained with the old mesh, as it is shown in Fig. 4.36.

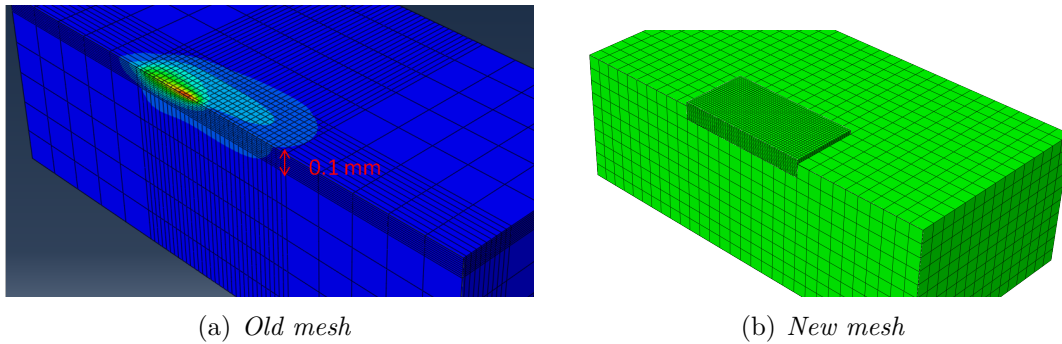


Figure 4.35: New mesh for the thermal problem.

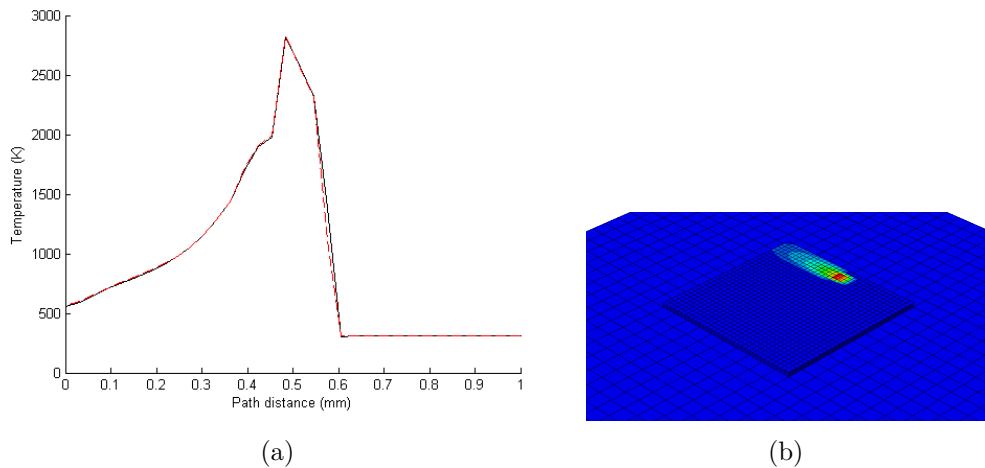


Figure 4.36: Temperature profile on the powder layer at 4 ms.

4.5.1 Simplified source model

In order to speed up the thermal analysis, with a view in future perspectives of simulating multiple layers, we would find a suitable temperature solution which can be projected during the multiple laser tracks. Indeed, we showed how the temperature profiles for consecutive scanning tracks are very similar and almost independent from each

others, except along the edges. For this reason, we evaluate the temperature profiles for different time steps of a single track and we select the solution in a 'steady' condition. The temperature distributions at different time steps along the first scan track are depicted in Fig. 4.37: after an initiation stage where the temperature starts increasing, a quasi-stationary stage is reached after few time steps. At the initial time increment (first curve in Fig. 4.37(a)) the maximum temperature is about 1909 K and after few time steps the maximum temperature starts increasing to a maximum value of 2837 K.

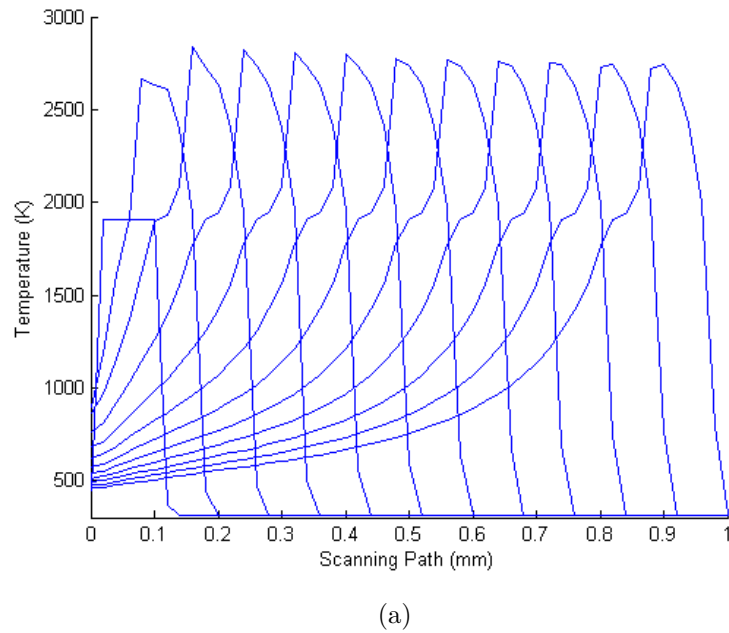


Figure 4.37: Temperature distributions at different time steps along the first scanning track.

We select a temperature distribution $T(x, y, z)$ at a single time step and we impose such solution as a moving boundary condition for each scanning track, using the user subroutine DISP in Abaqus. The temperature solution $T(x, y, z)$ at a specified time t is imposed over the single layer with a width equal to the laser beam diameter (0.1 mm) and a depth equal to the layer thickness (0.03 mm), (Fig. 4.38). The movement of the laser beam over the different scanning regions is simulated activating and deactivating the boundary condition. Such activation and deactivation allows the diffusion of heat by conduction to the vicinity of the part.

The simplification of assuming a moving boundary condition over the powder layer has benefits on the computational time; indeed the analysis time for the thermal analysis is drastically reduced as shown in Tab. 4.14.

Table 4.14: Comparison of computational times between the three-dimensional models with the old and new meshes.

Model	Numerical analysis	DOFs	Analysis time
Sec. 4.4.5	Thermal analysis	34444	26 hours and 42 min
Simplified heat source	Thermal analysis	46904	1 hour

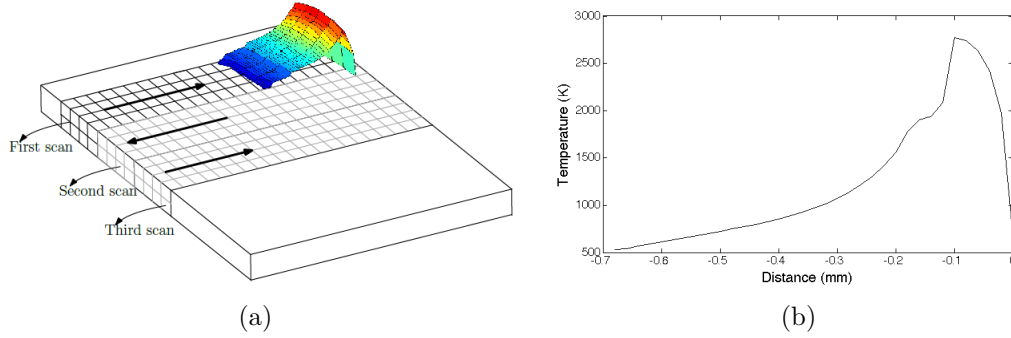


Figure 4.38: Temperature solution imposed as boundary condition on the powder layer.

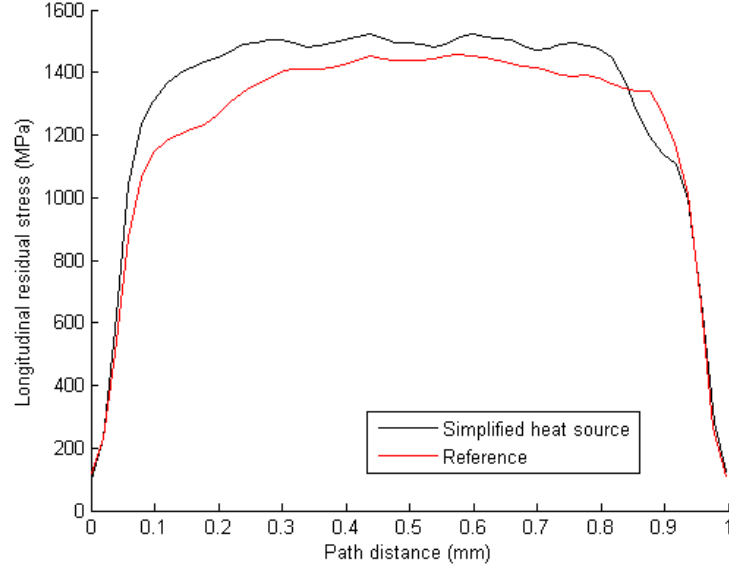
The effect of the imposition of the temperature distribution on the final residual stresses over the powder layer are depicted in Fig. 4.39, the reference solution is the solution obtained considering the real moving heat flux with Gaussian distribution.

The use of the simplified heat source results in a good approximation of the residual stresses: in particular along the longitudinal direction the stresses are overestimated, while along the transverse direction are underestimated. Experimental evidence shows that higher temperature values produce higher residual stresses [127]; indeed along the longitudinal direction the imposed temperature solution is greater than the average temperature history distribution, while, along the transverse direction, the temperature is higher for the reference solution.

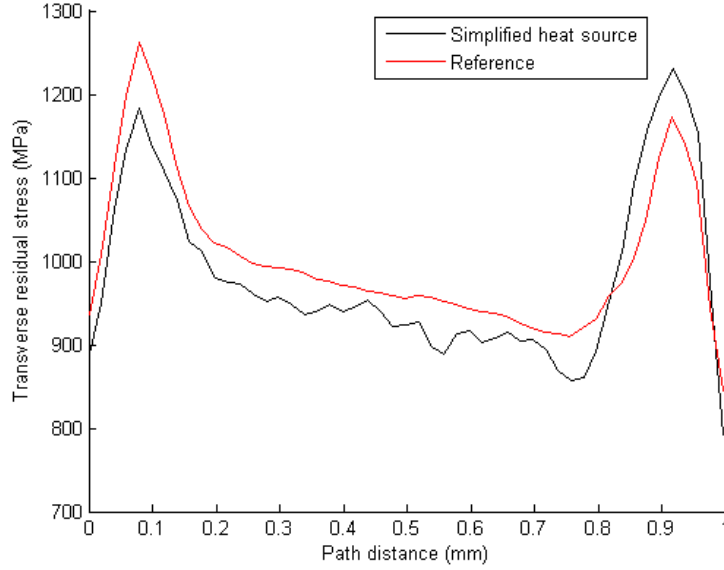
The root mean square (RMS) error is calculated by the following formula:

$$Error_{RMS}\% = \sqrt{\frac{\sum_{i=1}^n (T_{ref,i} - T_i)^2}{\sum_{j=1}^n T_{ref,i}^2}} \times 100 \quad (4.32)$$

and for longitudinal residual stresses is 8.18%, while for transverse residual stresses is 4.82%. The encouraging results, in terms of computational time and residual stress solutions, allow the use of the simplified model to further analyses.



(a)



(b)

Figure 4.39: Residual stresses profile along path OF: (a)longitudinal stresses; (b)transverse stresses. *Simplified heat source*: model with imposed temperature solution; *Reference solution*: model with Gaussian moving heat flux.

4.6 Summary

In the present study we developed a three-dimensional finite element model of SLM process using the software Abaqus.

We showed the modelling assumptions and the modelling procedures to develop an accurate FE model, which includes the presence of several user subroutines to assess the moving of the laser beam, the phase transformation and the temperature dependent material properties. The thermal and stress analyses of a titanium alloy powder layer

4.6. *Summary*

are conducted separately and the numerical results agreed with the numerical and experimental results given by [106].

The high computational effort of the thermal analysis, due to the strong nonlinearity, requires the necessity of developing a simplified heat source model. The temperature history of a one track laser scanning is obtained and a 'steady-state' solution is selected and after imposed as a moving Dirichlet boundary condition. The computational times with the simplified model are drastically reduced and the results, in terms of residual stresses, are still accurate.

Chapter 5

Substructuring and model order reduction techniques

In the previous chapter we showed how the prediction of temperature evolution in SLM components during the laser scanning is a costly challenge from a computational point of view. The high temperature gradients localized between the melted region and the surrounded powder material increase the solution times. For this reason many authors investigate small parts of SLM problems with fine mesh [106] or single layers with coarse mesh and fitted mesh over the scanning region [59, 65, 145], while the solid platform is not considered. Despite the high number of elements and degrees of freedom (DOFs) the presence of the base plate in the numerical model can considerably affect the global temperature distribution and the resulted residual stresses [106].

Dynamic Substructuring (DS) is a well recognized approach to reduce computational burden where individual components of a geometry are computed separately and then combined to predict the behaviour of the built-up structure. Such approach gives good advantages when similar parts compose the geometry and the substructure matrices can be computed once.

In such scenario different DS methods can be mentioned and an extended overview is given by de Klerk et al. [38]. For example, Component-Mode Synthesis (CMS) method is based to find reduced models for several substructures independently and to use compatibility conditions to connect the substructures to the whole structure. A very famous CMS method with fixed interfaces is proposed by Craig and Bampton in 1968 [31] which expanded the work of Hurty in 1964 [58]. In this method the substructure

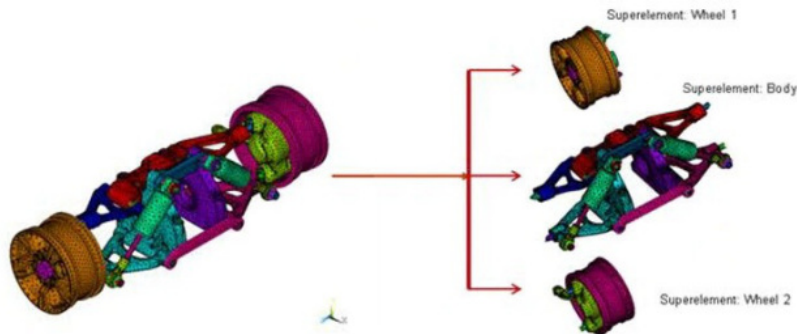


Figure 5.1: Representation of substructuring for a FE model [3]

is composed of boundary (*b*) and interior (*i*) degrees of freedom which are accurately

reduced.

The reduced basis is composed of two types of modes: constrain modes, which derive from the static condensation [53]; and normal modes, which are the eigenvectors of the constrained structure. Therefore such method requires to solve an eigenvalue problem for each substructure which can be very intensive. For this reason it is preferable to use some special vectors, called Ritz vectors [133], that give an approximation to some of the eigenvectors. In such scenario, the Lanczos algorithm can be used to construct a set of orthogonal vectors known as Lanczos vectors [76]. The use of Lanczos vectors as reduced basis is especially applied for linear transient thermal problems [6, 18, 96]; this basis is able to capture the development of temperature gradients giving better results than with the same number of eigenvectors [18, 95].

For large-scale nonlinear problems Model Order Reduction (MOR) is still a ongoing topic: for example Proper Orthogonal Decomposition (POD) is a method to solve linear and nonlinear problems with some extensions, e.g. POD-DEIM [23], POD-GFEM [7] and V-GFEM [16] have recent applications. In POD a set of randomly-distributed sample points (or snapshots) of the true solution at a given parameter value is generated to construct the parameter space. A two-dimensional model using POD for linear transient heat conduction analysis with moving heat source is presented by [14]; an application of POD to SLM for the solution of three-dimensional non-linear transient heat conduction problems is given by [19]. Despite the method is able to give accurate solutions, the limit of POD lies to the necessity of pre-processing the full analysis for different choices of parameters to construct the parameter space; according with [19], POD can be used as optimization method.

Modal Derivatives (MDs) is an approach introduced by Idelsohn and Cardona [60] with particular application in nonlinear structural mechanics and dynamics [130, 136, 137] because of its preservation of nonlinear eigenfrequencies. Modal derivatives are new vectors added to the reduction basis to consider the nonlinear effects. Cardona and Idelsohn [18] introduced a similar concept for the derivatives of Lanczos vectors to construct a suitable reduction basis for nonlinear heat conduction problems.

In the present chapter first we describe a suitable reduction basis for linear transient problems which uses eigenmodes; then the Craig-Bampton method is described to subdivide the large FE model in substructures and to reduce the degrees of freedom. Afterwards we present the Lanczos algorithm to generate an efficient alternative to the eigenmodes and we use the Lanczos vectors as a basis for the Craig-Bampton method. For nonlinear transient thermal problems we describe the basis of MDs and similarly we introduce some derivatives of Lanczos vectors as nonlinear extension of Craig-Bampton method. Furthermore we verify the potential of using Lanczos vectors and the derivatives of these vectors as reduction basis with some numerical examples implemented in Matlab [1].

5.1 Linear transient problems

The linear FE system for transient heat conduction problem is:

$$\mathbf{M}\dot{\mathbf{T}}(t) + \mathbf{K}\mathbf{T}(t) = \mathbf{F}(t) \quad (5.1)$$

where the matrices \mathbf{M} and \mathbf{K} have dimension $n \times n$.

The Craig-Bampton method is able to subdivide the thermal system in single substructures which are accurately reduced by the definition of a (modal) reduction basis. Since the resolution of an eigenvalue problem is quite computationally expensive, especially for transient thermal problems many authors use Lanczos vectors as reduction basis which reveals a more accurate solution than with the same number of eigenvectors [6, 18, 96].

5.1.1 Eigenmodes and linear modal truncation

The symmetric linear eigenvalue problem of the linear FE equation in Eq. 5.1 is:

$$\lambda_i \mathbf{M} \boldsymbol{\phi}_i = \mathbf{K} \boldsymbol{\phi}_i \text{ for } i = 1, \dots, n \quad (5.2)$$

where $(\lambda_i, \boldsymbol{\phi}_i)$ are the eigenpairs of the system with $i = 1 \dots n$. The eigenvalues are ordered by magnitude, i.e. $\lambda_1 \leq \lambda_2 \leq \dots \leq \lambda_n$, and the eigenvectors constitute a orthonormal basis:

$$\boldsymbol{\phi}_i^T \mathbf{M} \boldsymbol{\phi}_j = \delta_{ij}, \quad \boldsymbol{\phi}_i^T \mathbf{K} \boldsymbol{\phi}_j = \delta_{ij} \lambda_i \quad (5.3)$$

The eigenmodes can be used as projection basis of temperature \mathbf{T} as:

$$\mathbf{T} = \boldsymbol{\Phi} \mathbf{d} = \sum_{i=1}^n \boldsymbol{\phi}_i d_i \quad (5.4)$$

where \mathbf{d} is the vector of modal coordinates. Such choice of basis permits the diagonalization of linear static and dynamic problems and can be used for reduction of large-scale linear systems [132]. Therefore we assume a reduced or truncated basis of eigenmodes $\boldsymbol{\Phi}^k \in \mathbb{R}^{n \times k}$, with $n_k \ll n$:

$$\mathbf{T}^k = \boldsymbol{\Phi}^k \mathbf{d}^k = \sum_{i=1}^{n_k} \boldsymbol{\phi}_i d_i \quad (5.5)$$

This method is widely spread in engineering applications and it is called *modal truncation* or *modal reduction* [37].

5.1.2 Craig-Bampton Method

The Craig-Bampton method (CBM) is set to subdivide the large FE model (Eq. 5.1) into smaller components and to reduce the single parts. The DOFs of each substructure where we are interested to preserve the information of the solution are called *boundary degrees of freedom* ($T^b \in \mathbb{R}^b$); on the contrary the DOFs where we can loose some informations are the *internal degrees of freedom* ($T^i \in \mathbb{R}^i$). For example in a thermal system with a large number of DOFs we can identify some regions where we are not interested on the solution and decide to condense the internal DOFs keeping as boundary DOFs the interface nodes with the rest of the part (Fig. 5.2).

At this point we can re-write Eq. 5.1 considering the separated contribution of internal and boundary degrees of freedom:

$$\begin{bmatrix} \mathbf{M}^{bb} & \mathbf{M}^{bi} \\ \mathbf{M}^{ib} & \mathbf{M}^{ii} \end{bmatrix} \begin{bmatrix} \dot{\mathbf{T}}^b \\ \dot{\mathbf{T}}^i \end{bmatrix} + \begin{bmatrix} \mathbf{K}^{bb} & \mathbf{K}^{bi} \\ \mathbf{K}^{ib} & \mathbf{K}^{ii} \end{bmatrix} \begin{bmatrix} \mathbf{T}^b \\ \mathbf{T}^i \end{bmatrix} = \begin{bmatrix} \mathbf{F}^b \\ \mathbf{F}^i \end{bmatrix} \quad (5.6)$$

where the superscripts b and i refer to the boundary and internal degrees of freedom

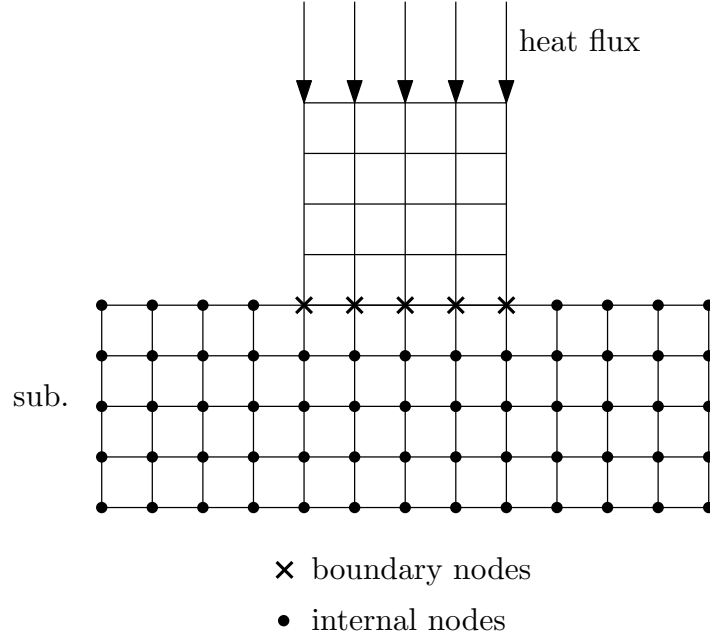


Figure 5.2: Thermal system composed by one substructure

respectively.

The reduced basis for CBM is composed by two modes: the *constraint modes* and the *normal modes*. The constraint modes can be determined applying a successive unit displacement on a boundary node, when the left over are totally constrained (Fig. 6.5(a)); in order to derive the constraint modes for the static problem of 5.6 the forces at all internal DOFs are set equal to zero yielding:

$$\mathbf{K}^{ib}\mathbf{T}^b + \mathbf{K}^{ii}\mathbf{T}^i = \mathbf{0} \quad (5.7)$$

and obtaining the following relation between internal and boundary DOFs:

$$\mathbf{T}^i = -\mathbf{K}^{ii-1}\mathbf{K}^{ib}\mathbf{T}^b = \mathbf{\Psi}\mathbf{T}^b \quad (5.8)$$

where $\mathbf{\Psi}$ has dimension $n_i \times n_b$ and is called the matrix of constrained modes.

The normal or fixed interface modes are the normal modes of the substructure when the boundary is totally constrained, i.e. $\mathbf{T}^b = \mathbf{0}$ (Fig. 5.4(b)) and they can be derived solving the following *generalized eigenvalue problem*:

$$(\mathbf{K}^{ii} - \lambda_j \mathbf{M}^{ii})\phi_j = \mathbf{0} \text{ for } j = 1, \dots, n_i \quad (5.9)$$

where we assume:

$$\mathbf{T}^i = \phi_j e^{\lambda_j t}. \quad (5.10)$$

The matrix of eigenvectors $\mathbf{\Phi}$ of 5.9 has dimension $n_i \times n_i$ and contains the normal modes of the constrained substructure.

$$\mathbf{\Phi} = [\phi_1 \quad \phi_2 \quad \dots \quad \phi_{n_i}]. \quad (5.11)$$

We assume a n_k reduced set of eigenvectors $\mathbf{\Phi}^k$, with $n_k \subset \{1, \dots, n_i\}$:

$$\mathbf{\Phi}^k = [\phi_1 \quad \phi_2 \quad \dots \quad \phi_{n_k}]. \quad (5.12)$$

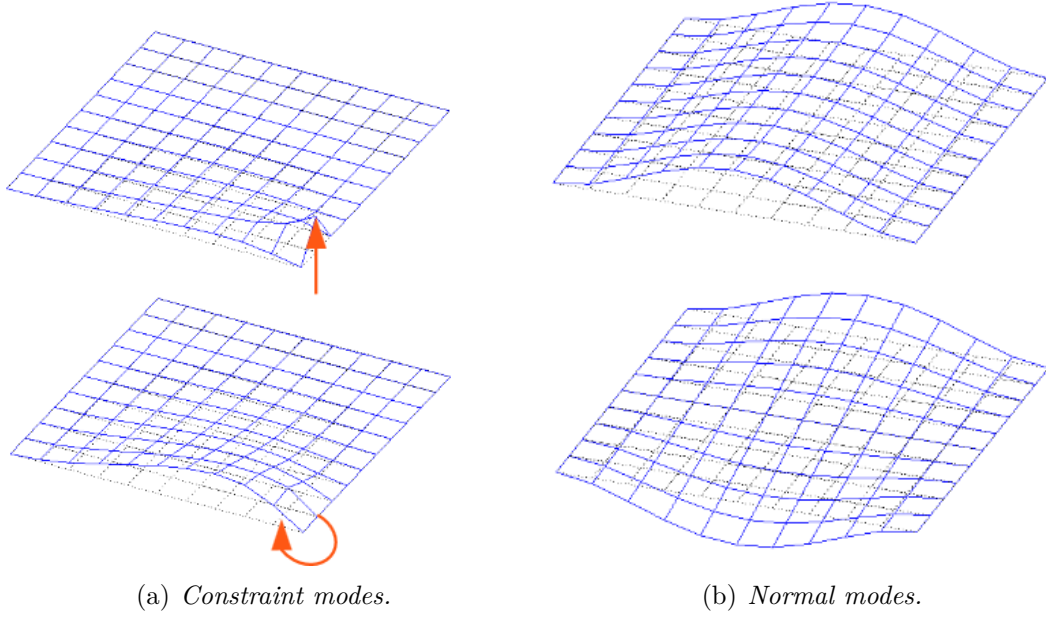


Figure 5.3: Component modes for CBM [2].

At this point the solution vector $\mathbf{T} \in \mathbb{R}^n$ is projected to the reduced coordinate vector $\mathbf{d} \in \mathbb{R}^{(b+k)}$:

$$\mathbf{T} = \mathbf{Q}\mathbf{d} \Leftrightarrow \begin{bmatrix} \mathbf{T}^b \\ \mathbf{T}^i \end{bmatrix} = \begin{bmatrix} \mathbf{I} & \mathbf{0} \\ \mathbf{\Psi} & \mathbf{\Phi}^k \end{bmatrix} \begin{bmatrix} \mathbf{T}^b \\ \mathbf{d}^k \end{bmatrix} \quad (5.13)$$

Therefore the internal degrees of freedom \mathbf{T}_i are connected to the boundary nodes \mathbf{T}_b and the modal amplitudes $\mathbf{d}^k \in \mathbb{R}^k$ by:

$$\mathbf{T}^i = \mathbf{\Psi}\mathbf{T}^b + \mathbf{\Phi}^k \mathbf{d}^k. \quad (5.14)$$

The matrix $\mathbf{Q} \in \mathbb{R}^{n \times (b+k)}$ is the projection matrix defined as:

$$\mathbf{Q} = \begin{bmatrix} \mathbf{I} & \mathbf{0} \\ \mathbf{\Psi} & \mathbf{\Phi}^k \end{bmatrix} \quad (5.15)$$

Substituting the reduction basis (Eq. 5.13) in the semi-discrete heat equation (Eq. 5.6) we obtain:

$$\begin{aligned} & \begin{bmatrix} \mathbf{I} & \mathbf{\Psi}^T \\ \mathbf{0} & \mathbf{\Phi}^T \end{bmatrix} \begin{bmatrix} \mathbf{M}^{bb} & \mathbf{M}^{bi} \\ \mathbf{M}^{ib} & \mathbf{M}^{ii} \end{bmatrix} \begin{bmatrix} \mathbf{I} & \mathbf{0} \\ \mathbf{\Psi} & \mathbf{\Phi}^k \end{bmatrix} \begin{bmatrix} \dot{\mathbf{T}}^b \\ \dot{\mathbf{d}}^k \end{bmatrix} + \\ & + \begin{bmatrix} \mathbf{I} & \mathbf{\Psi}^T \\ \mathbf{0} & (\mathbf{\Phi}^k)^T \end{bmatrix} \begin{bmatrix} \mathbf{K}^{bb} & \mathbf{K}^{bi} \\ \mathbf{K}^{ib} & \mathbf{K}^{ii} \end{bmatrix} \begin{bmatrix} \mathbf{I} & \mathbf{0} \\ \mathbf{\Psi} & \mathbf{\Phi}^k \end{bmatrix} \begin{bmatrix} \mathbf{T}^b \\ \mathbf{d}^k \end{bmatrix} = \begin{bmatrix} \mathbf{I} & \mathbf{\Psi}^T \\ \mathbf{0} & (\mathbf{\Phi}^k)^T \end{bmatrix} \begin{bmatrix} \mathbf{F}^b \\ \mathbf{F}^i \end{bmatrix}. \end{aligned} \quad (5.16)$$

Solving the matrix product yields:

$$\begin{aligned} & \begin{bmatrix} (\mathbf{I}\mathbf{M}^{bb} + \mathbf{\Psi}^T\mathbf{M}^{ib})\mathbf{I} + (\mathbf{I}\mathbf{M}^{bi} + \mathbf{\Psi}^T\mathbf{M}^{ii})\mathbf{\Psi} & (\mathbf{I}\mathbf{M}^{bi} + \mathbf{\Psi}^T\mathbf{M}^{ii})\mathbf{\Phi}^k \\ \mathbf{\Phi}^k\mathbf{M}^{ib}\mathbf{I} + (\mathbf{\Phi}^k)^T\mathbf{M}^{ii}\mathbf{\Psi} & (\mathbf{\Phi}^k)^T\mathbf{M}^{ii}\mathbf{\Phi}^k \end{bmatrix} \begin{bmatrix} \dot{\mathbf{T}}^b \\ \dot{\mathbf{d}}^k \end{bmatrix} + \\ & \begin{bmatrix} (\mathbf{I}\mathbf{K}^{bb} + \mathbf{\Psi}^T\mathbf{K}^{ib})\mathbf{I} + (\mathbf{I}\mathbf{K}^{bi} + \mathbf{\Psi}^T\mathbf{K}^{ii})\mathbf{\Psi} & (\mathbf{I}\mathbf{K}^{bi} + \mathbf{\Psi}^T\mathbf{K}^{ii})\mathbf{\Phi}^k \\ (\mathbf{\Phi}^k)^T\mathbf{K}^{ib}\mathbf{I} + (\mathbf{\Phi}^k)^T\mathbf{K}^{ii}\mathbf{\Psi} & (\mathbf{\Phi}^k)^T\mathbf{K}^{ii}\mathbf{\Phi}^k \end{bmatrix} \begin{bmatrix} \mathbf{T}^b \\ \mathbf{d}^k \end{bmatrix} = \end{aligned} \quad (5.17)$$

$$\begin{bmatrix} \mathbf{I}\mathbf{F}^b + \boldsymbol{\Psi}^T \mathbf{F}^i \\ (\boldsymbol{\Phi}^k)^T \mathbf{F}^i \end{bmatrix}$$

Assuming zero forces on the internal DOFs ($\mathbf{F}^i = \mathbf{0}$) and using the definition of $\boldsymbol{\Psi}$ in Eq. (5.8), finally we obtain:

$$\begin{bmatrix} \hat{\mathbf{M}}^{bb} & \hat{\mathbf{M}}^{bk} \\ \hat{\mathbf{M}}^{kb} & \mathbf{I}^{kk} \end{bmatrix} \begin{bmatrix} \dot{\mathbf{T}}^b \\ \dot{\mathbf{d}}^k \end{bmatrix} + \begin{bmatrix} \hat{\mathbf{K}}^{bb} & \mathbf{0} \\ \mathbf{0} & \boldsymbol{\Lambda}^{kk} \end{bmatrix} \begin{bmatrix} \mathbf{T}_b \\ \mathbf{d}^k \end{bmatrix} = \begin{bmatrix} \mathbf{F}_b \\ \mathbf{0} \end{bmatrix} \quad (5.18)$$

where the eigenvector $\boldsymbol{\phi}_j$ (with $j = 1, \dots, k$) is normalized respect to the capacity matrix \mathbf{M}^{ii} :

$$\mathbf{I}^{kk} = (\boldsymbol{\Phi}^k)^T \mathbf{M}^{ii} \boldsymbol{\Phi}^k \quad (5.19)$$

$$\boldsymbol{\Lambda}^{kk} = (\boldsymbol{\Phi}^k)^T \mathbf{K}^{ii} \boldsymbol{\Phi}^k \quad (5.20)$$

where \mathbf{I}^{kk} is the identity matrix and $\boldsymbol{\Lambda}^{kk}$ the eigenvalue matrix of dimension $n_k \times n_k$.

5.1.3 Rayleigh-Ritz Approximation

The Rayleigh-Ritz approximation [57] is a method for computing approximate solutions of a generalized eigenvalue problem 5.9. Assume $(\tilde{\lambda}, \tilde{\boldsymbol{\phi}})$ being an approximating Ritz pair to some of the eigenvalues and eigenvectors $(\lambda, \boldsymbol{\phi})$ we can define the residual \mathbf{r} as:

$$\mathbf{r} = \mathbf{K}\tilde{\boldsymbol{\phi}} - \tilde{\lambda}\mathbf{M}\tilde{\boldsymbol{\phi}} \quad (5.21)$$

where the approximating eigenvectors can be expressed as the combination of *trial vectors* $\mathbf{X}_m = [\mathbf{x}_1, \mathbf{x}_2, \dots, \mathbf{x}_m]$ and some coefficients $\mathbf{s} = [s_1, s_2, \dots, s_m]$:

$$\tilde{\boldsymbol{\phi}} = \mathbf{X}_m \mathbf{s} = \sum_{i=1}^m \mathbf{x}_i s_i. \quad (5.22)$$

The method assumes that the residual \mathbf{r} is orthogonal to the trail vectors \mathbf{X}_m :

$$\mathbf{X}_m^T \mathbf{r} = \mathbf{X}_m^T \mathbf{K}\tilde{\boldsymbol{\phi}} - \mathbf{X}_m^T \tilde{\lambda} \mathbf{M}\tilde{\boldsymbol{\phi}} = \mathbf{0} \quad (5.23)$$

by the definition 5.22 we obtain:

$$\mathbf{X}_m^T \mathbf{K} \mathbf{X}_m \mathbf{s} - \mathbf{X}_m^T \tilde{\lambda} \mathbf{M} \mathbf{X}_m \mathbf{s} = \mathbf{0} \quad (5.24)$$

with the following reduced eigenvalue problem:

$$\mathbf{K}^m \mathbf{s} - \tilde{\lambda} \mathbf{M}^m \mathbf{s} = \mathbf{0}. \quad (5.25)$$

After solving the reduced problem 5.25 for \mathbf{s}^i and $\tilde{\lambda}_i$ we can compute the real eigenvectors of 5.9 through the trail vectors \mathbf{X}_m .

5.1.4 Lanczos vectors

The Lanczos algorithm was initially developed for reducing a symmetric matrix to tridiagonal form [76], but it is viewed as a very efficient tool to compute a few of the extreme eigenvalues and corresponding eigenvector of a symmetric matrix of the following *standard eigenvalue problem*:

$$(\mathbf{K} - \lambda_j \mathbf{M}) \boldsymbol{\phi}_j = \mathbf{0} \text{ for } j = 1, \dots, n \quad (5.26)$$

To obtain the standard eigenvalue problem of 5.9, we perform a shift σ of the origin:

$$(\mathbf{K}_\sigma - (\lambda_j - \sigma)\mathbf{M})\phi_j = \mathbf{0} \text{ for } j = 1, \dots, n \quad (5.27)$$

$$(\mathbf{K}_\sigma - \nu_j\mathbf{M})\phi_j = \mathbf{0} \text{ for } j = 1, \dots, n \quad (5.28)$$

where $\mathbf{K}_\sigma = \mathbf{K} - \sigma\mathbf{M}$. The standard formulation 5.28 has the same eigenvectors of the generalized formulation 5.9 while the eigenvalues ν_j are related to the original spectrum through:

$$\nu_j = \frac{1}{\lambda_j - \sigma}. \quad (5.29)$$

The Lanczos algorithm is closely related to the inverse iteration and power methods and it is able to extract a set of \mathbf{M} -orthonormal vectors referred to the Krylov sequence $\{\mathbf{r}, \mathbf{K}_\sigma^{-1}\mathbf{M}\mathbf{r}, (\mathbf{K}_\sigma^{-1}\mathbf{M})^2\mathbf{r}, \dots, (\mathbf{K}_\sigma^{-1}\mathbf{M})^j\mathbf{r}\}$ which converges (as $j \rightarrow \infty$) to the eigenvector corresponding to the eigenvalue λ closest to the shift σ .

The Lanczos vectors can be used in the Rayleigh-Ritz approximation as trial vectors to construct an approximation of eigenvectors of 5.28. The process starts initializing \mathbf{q}_0 to the zero vector and the initial vector \mathbf{r}_0 accurately. At a typical step j the Lanczos algorithm computes α_j , β_{j+1} and the new Lanczos vector \mathbf{q}_{j+1} , where β_{j+1} is the normalizing factor (Algorithm 1). The final set of Lanczos vectors is given by:

$$\mathbf{Q}_m = [\mathbf{q}_1, \mathbf{q}_2, \dots, \mathbf{q}_{m+1}] \text{ with } m \ll n \quad (5.30)$$

which are orthogonal respect to \mathbf{M} :

$$\mathbf{q}_i^T \mathbf{M} \mathbf{q}_j = \delta_{ij} \quad (5.31)$$

with δ_{ij} the Kronecker delta. The algorithm can start from the three-term relation:

$$\mathbf{r}_j \equiv \mathbf{q}_{j+1}\beta_{j+1} = \bar{\mathbf{r}}_j - \mathbf{q}_j\alpha_j - \mathbf{q}_{j-1}\beta_j \quad (5.32)$$

with:

$$\bar{\mathbf{r}}_j = \mathbf{K}_\sigma^{-1}\mathbf{M}\mathbf{q}_j. \quad (5.33)$$

The coefficients α_j can be determined multiplying Eq. 5.32 by $\mathbf{q}_j^T \mathbf{M}$ obtaining:

$$\mathbf{q}_j^T \mathbf{M} \mathbf{r}_j = \mathbf{q}_j^T \mathbf{M} \mathbf{K}_\sigma^{-1} \mathbf{M} \mathbf{q}_j - \mathbf{q}_j^T \mathbf{M} \mathbf{q}_j \alpha_j - \mathbf{q}_j^T \mathbf{M} \mathbf{q}_{j-1} \beta_j \quad (5.34)$$

The term on the left side and the last term of the right side vanish due to the orthogonality condition of the Lanczos vectors (Eq. 5.31) yielding:

$$\alpha_j = \mathbf{q}_j^T \mathbf{M} \mathbf{K}_\sigma^{-1} \mathbf{M} \mathbf{q}_j. \quad (5.35)$$

In structural dynamics the choice of the initial vector \mathbf{r}_0 is related to the spatial distribution of the load which remains constant and only the load amplitude varies with time $\mathbf{F} = \mathbf{b}\varepsilon(t)$ [95]:

$$\mathbf{r}_0 = \mathbf{K}^{-1}\mathbf{b}. \quad (5.36)$$

For heat conduction problems Cardona and Idelsohn [18] give as starting vector \mathbf{r}_0 the increment of nodal temperatures evaluated at the first time increment Δt :

$$\mathbf{r}_0 = [\mathbf{K}_\sigma + (1/\Delta t)\mathbf{M}]^{-1}[\mathbf{F} - (1/\Delta t)\mathbf{M}\mathbf{T}_0] \quad (5.37)$$

Algorithm 1 Lanczos algorithm

```

1:  $\mathbf{q}_0 = \mathbf{0}$ 
2:  $\mathbf{r}_0 = [\mathbf{K}_\sigma + (1/\Delta t)\mathbf{M}]^{-1}[\mathbf{F} - (1/\Delta t)\mathbf{M}\mathbf{T}_0]$ 
3:  $\beta_1 = (\mathbf{r}_0^T \mathbf{M} \mathbf{r}_0)^{1/2}$ 
4:  $\mathbf{q}_1 = \mathbf{r}_0 / \beta_1$ 
5: for  $j = 1, \dots, m$  do
6:    $\bar{\mathbf{r}} = \mathbf{K}_\sigma^{-1} \mathbf{M} \mathbf{q}_j$ 
7:    $\hat{\mathbf{r}}_j = \bar{\mathbf{r}} - \mathbf{q}_{j-1} \beta_j$ 
8:    $\alpha_j = \mathbf{q}_j^T \mathbf{M} \hat{\mathbf{r}}_j$ 
9:    $\mathbf{r}_j = \hat{\mathbf{r}}_j - \mathbf{q}_j \alpha_j$ 
10:   $\beta_{j+1} = (\mathbf{r}_j^T \mathbf{M} \mathbf{r}_j)^{1/2}$ 
11:   $\mathbf{q}_{j+1} = \mathbf{r}_j / \beta_{j+1}$ 
12: end for

```

where \mathbf{T}_0 is the vector of the initial temperatures. After m Lanczos steps Eq. 5.32 can be arranged as a matrix equation:

$$[\mathbf{K}_\sigma^{-1} \mathbf{M}] [\mathbf{Q}_m] - [\mathbf{Q}_m] [\mathbf{T}_m] = \mathbf{r} \mathbf{e}_m^T \quad (5.38)$$

where \mathbf{Q}_m is the $n \times m$ matrix composed by the Lanczos vectors \mathbf{q}_i ($i = 1, \dots, m$), $\mathbf{e}_m = [0, 0, \dots, 0, 1]$ and \mathbf{T}_m is the *tridiagonal matrix*, expressed as:

$$\mathbf{T}_m = \begin{bmatrix} \alpha_1 & \beta_2 & & & & \\ \beta_1 & \alpha_2 & \beta_3 & & & \\ & \beta_3 & \cdot & \cdot & & \\ & & \cdot & \cdot & \cdot & \\ & & & \cdot & \cdot & \beta_m \\ & & & & \beta_m & \alpha_m \end{bmatrix} \quad (5.39)$$

We multiply the matrix equation 5.38 by $\mathbf{Q}_m^T \mathbf{M}$ and we obtain the expression for \mathbf{T}_m :

$$\mathbf{T}_m = \mathbf{Q}_m^T \mathbf{M} \mathbf{K}_\sigma^{-1} \mathbf{M} \mathbf{Q}_m \quad (5.40)$$

which is the projection of $\mathbf{M} \mathbf{K}_\sigma^{-1} \mathbf{M}$ on the subspace with basis \mathbf{Q}_m .

The matrix \mathbf{Q}_m composed by the Lanczos vectors can be used as a set of trial vectors for the Rayleigh-Ritz procedure to obtain the best approximation of the eigenvectors in 5.21:

$$\tilde{\phi}_i^m = \mathbf{Q}_m \mathbf{s}_i^m \quad \text{with } i = 1, \dots, m \quad (5.41)$$

The residual vector associated with the approximating Ritz pair $\{\tilde{\lambda}_i^m, \tilde{\phi}_i^m\}$ is \mathbf{M} -orthogonal to the Lanczos vectors and we can write:

$$\mathbf{Q}_m^T \mathbf{M} (\mathbf{K}_\sigma^{-1} \mathbf{M} \tilde{\phi}_i^m - \tilde{\lambda}_i^m \tilde{\phi}_i^m) = \mathbf{0} \quad \text{with } i = 1, \dots, m \quad (5.42)$$

Substituting Eq. 5.41 in Eq. 5.42 and considering the definition of the tridiagonal matrix \mathbf{T}_m (Eq. 5.40) and the orthogonality condition of the Lanczos vectors (Eq. 5.31) we obtain the following reduced *tridiagonal eigenproblem*:

$$\mathbf{T}_m \mathbf{s}_i^m - \tilde{\lambda}_i^m \mathbf{s}_i^m = \mathbf{0} \quad (5.43)$$

Finally $\{\tilde{\lambda}_i^m, \mathbf{s}_i^m\}$ is the eigenpair of the tridiagonal matrix \mathbf{T}_m .

Increasing the number m of Lanczos vectors, the eigenvalue $\tilde{\lambda}_i^m$ converges to the eigenvalue $1/(\lambda_i - \sigma)$ of Eq. 5.28, and the eigenvector $\tilde{\Phi}_i^m$, calculated from Eq. 5.41, converges to the eigenvectors Φ_i of Eq. 5.28.

5.1.5 Convergence criterion and loss of orthogonality

The norm of the residual vector respect to the capacity matrix \mathbf{M} ($\|\mathbf{r}_m\|_M$) is used to verify the convergence of the eigenvalue $\tilde{\lambda}$ to ν [57]:

$$|\nu_i - \tilde{\lambda}_i^m| < \|\mathbf{r}_m\|_M \quad (5.44)$$

where the residual vector is:

$$\mathbf{r}_m = \mathbf{K}_\sigma^{-1} \mathbf{M} \tilde{\Phi}_i^m - \tilde{\lambda}_i^m \tilde{\Phi}_i^m. \quad (5.45)$$

The norm of the residual vector can be deduced multiplying Eq. 5.38 by \mathbf{s}_i^m and recalling Eq. 5.41 we obtain:

$$\mathbf{K}_\sigma^{-1} \mathbf{M} \tilde{\Phi}_i^m - \tilde{\lambda}_i^m \tilde{\Phi}_i^m = \mathbf{r}_m \mathbf{e}_m^T \mathbf{s}_i^m \quad (5.46)$$

taking the norms respect to the capacity matrix yields:

$$\begin{aligned} \|\mathbf{K}_\sigma^{-1} \mathbf{M} \tilde{\Phi}_i^m - \tilde{\lambda}_i^m \tilde{\Phi}_i^m\|_{\mathbf{M}} &= \|\mathbf{r}_m \mathbf{e}_m^T \mathbf{s}_i^m\|_{\mathbf{M}} \\ &= \|\mathbf{r}_m\|_{\mathbf{M}} |\mathbf{e}_m^T \mathbf{s}_i^m| \\ &= \beta_{m+1} |\zeta_i|. \end{aligned} \quad (5.47)$$

where ζ_i is the bottom element of \mathbf{s}_i^m which is the eigenvector of \mathbf{T}_m ; β_{m+1} is a scalar quantity. Therefore the quantity $\beta_{m+1} |\zeta_i|$ is calculated after the computed Lanczos vector and the algorithm converges when this quantity is less than a specified tolerance:

$$\beta_{m+1} |\zeta_i| < \text{tol}. \quad (5.48)$$

In exact arithmetic the above governing equations are satisfied and the Lanczos vectors are \mathbf{M} -orthogonal. In finite precision, after few steps of the algorithm the Lanczos vectors loose their orthogonality and also become linearly dependent, depending on the roundoff error ϵ which measures the accuracy of the arithmetic.

Paige [97] expressed the level of non-orthogonality with the inner product of each Ritz vector $\tilde{\Phi}_i^m$, through Eq. 5.41, and the Lanczos vectors \mathbf{q}_{j+1} ;

$$\tilde{\Phi}_i^j \mathbf{M} \mathbf{q}_{j+1} = \frac{\gamma_{ji} \epsilon \|\mathbf{T}_j\|}{\beta_{j+1} |\zeta_i|} \quad (5.49)$$

where γ_{ji} is a scalar quantity close to unity; so when β_{j+1} decreases results in a loss of orthogonality. According with the convergence criterion in Eq. 5.48, the convergence of the Ritz value $\tilde{\lambda}_i^j$ results in a loss of orthogonality of the vector \mathbf{q}_{j+1} .

To restore the orthogonality condition there exist different approaches: full re-orthogonalization (FRO) is used at each step of orthogonality but it is computationally expensive; cheaper approaches are selective re-orthogonalization (SO), introduced by Parlett and Scott [99] where the orthogonalization of the Lanczos vector is made against the Ritz vector, and partial re-orthogonalization (PRO) introduced by Simon [116] where the level of orthogonality is satisfied orthogonalizing the Lanczos vectors with each others.

In the present work we adopt the full orthogonalization method since, as we will show in the following, the investigated cases require a small number of steps of Lanczos algorithm to achieve an accurate solution.

5.1.6 Lanczos vectors as reduced basis

The use of Lanczos vectors as reduction basis is an approach widely used to reduce linear systems, especially for heat conduction problems [6, 18, 96]. The matrix $\mathbf{Q}_m \in \mathbb{R}^{n \times m}$ is the projection matrix, composed by the Lanczos vectors $(\mathbf{q}_1, \dots, \mathbf{q}_m, \text{ with } m \ll n)$. The temperature solution vector $\mathbf{T} \in \mathbb{R}^n$ is expressed in reduced representation by the reduced coordinate vector $\mathbf{p}^m \in \mathbb{R}^m$:

$$\mathbf{T} = \mathbf{T}_0 + \mathbf{Q}_m \mathbf{p}^m = \sum_{i=1}^m \mathbf{q}_i p_i \quad (5.50)$$

where \mathbf{T}_0 is the vector of the initial temperatures; in the following we assume that is equal to zero.

If we substitute the relation in Eq. 5.50 to the linear system in Eq. 5.1 we can compute the reduced coordinate vector \mathbf{p}^m by:

$$\mathbf{Q}_m^T \mathbf{M} \mathbf{Q}_m \dot{\mathbf{p}}^m + \mathbf{Q}_m^T \mathbf{K} \mathbf{Q}_m \mathbf{p}^m = \mathbf{Q}_m^T \mathbf{F} \quad (5.51)$$

$$\hat{\mathbf{M}} \dot{\mathbf{p}}^m + \hat{\mathbf{K}} \mathbf{p}^m = \hat{\mathbf{F}}. \quad (5.52)$$

The matrix \mathbf{Q}_m of Lanczos vectors can be introduced also in the Craig-Bampton method to reduce the vector \mathbf{T}_i of the internal degrees of freedom. In this case the projection matrix $\mathbf{Q} \in \mathbb{R}^{n \times (b+m)}$ is expressed as:

$$\mathbf{T} = \mathbf{Q} \mathbf{p} \Leftrightarrow \begin{bmatrix} \mathbf{T}^b \\ \mathbf{T}^i \end{bmatrix} = \begin{bmatrix} \mathbf{I} & \mathbf{0} \\ \mathbf{\Psi} & \mathbf{Q}_m \end{bmatrix} \begin{bmatrix} \mathbf{T}^b \\ \mathbf{p}^m \end{bmatrix} \quad (5.53)$$

where $\mathbf{p} \in \mathbb{R}^{b+m}$ is the coordinate reduced vector.

5.2 Nonlinear Transient problems

The nonlinear FE equation for transient heat conduction problem is:

$$\mathbf{M}(\mathbf{T}(t)) \dot{\mathbf{T}}(t) + \mathbf{g}(\mathbf{T}(t)) = \mathbf{F}(t) \quad (5.54)$$

where \mathbf{g} is the nonlinear internal force vector, which can be linearised to:

$$\mathbf{g}(\mathbf{T}(t)) = \mathbf{K} \mathbf{T}(t) \quad (5.55)$$

with \mathbf{K} the linear conductivity matrix.

For nonlinear structural dynamics there are two extensions of the linear eigenmodes [130]: tangent modes and nonlinear normal modes (NNM). The nonlinear normal modes give accurate solution in nonlinear frequency analysis in terms of self-excited vibrations but they require a computational effort to be computed.

Tangent modes are the eigenmodes computed from the eigenvalue problem with the tangent stiffness matrix \mathbf{K}_T for a current deformation state:

$$\lambda_j \mathbf{M} \phi_j = \mathbf{K}_T(\phi_j) \phi_j. \quad (5.56)$$

Therefore tangent modes are computed to construct a suitable modal basis for each time step. We will see that using the so-called Modal Derivatives (MDs) of eigenmodes for nonlinear problems we do not need to update the reduction basis for each configuration.

5.2.1 Modal derivatives

Modal Derivatives (MDs) are an approach introduced in 80s by [60] to compute a reduction basis for nonlinear systems, especially applied for nonlinear structural mechanics and dynamics [130, 131, 136, 137]. For linear structural dynamics the eigenmodes are determined from the following eigenvalue problem [117]:

$$\mathbf{\Lambda} \mathbf{M} \mathbf{\Phi} = \mathbf{K} \mathbf{\Phi} \quad (5.57)$$

where $\mathbf{\Lambda} = \text{diag}(\lambda_i)_{i=1,\dots,n}$ is the matrix of the eigenvalues with $\lambda_i = \omega_i^2$ and $\mathbf{\Phi} = (\phi_i)_{i=1,\dots,n}$ the matrix of eigenmodes which constitutes a suitable projection basis for the linear problem:

$$\mathbf{u} - \mathbf{u}_0 = \Delta \mathbf{u} = \mathbf{\Phi} \mathbf{d} = \sum_{i=1}^n \phi_i d_i \quad (5.58)$$

where \mathbf{u}_0 is the initial displacement vector.

For nonlinear cases the tangent stiffness matrix depends on the solution \mathbf{u} and so also the (tangent) modes $\mathbf{\Phi}$ depend on it:

$$\mathbf{u} - \mathbf{u}_0 = \Delta \mathbf{u} = \mathbf{\Phi} \mathbf{d} = \sum_{i=1}^n \phi_i(\mathbf{u}) d_i. \quad (5.59)$$

We now develop $\Delta \mathbf{u}$ around its starting configuration $\Delta \mathbf{u} = \mathbf{0}$ (i.e. $\mathbf{d} = \mathbf{0}$) into a second order Taylor series:

$$\Delta \mathbf{u} = \sum_{i=1}^n \left(\frac{\partial \Delta \mathbf{u}}{\partial d_i}(\mathbf{d} = \mathbf{0}) d_i + \sum_{j=1}^n \left(\frac{\partial^2 \Delta \mathbf{u}}{\partial d_i \partial d_j}(\mathbf{d} = \mathbf{0}) \frac{d_j}{2} \right) d_i \right). \quad (5.60)$$

The first and second derivatives of the nodal displacement can be computed differentiating Eq. 5.70 respect to the modal coordinates d_i :

$$\frac{\partial \Delta \mathbf{u}}{\partial d_i} = \sum_{k=1}^n \left(\frac{\partial \phi_k(\mathbf{u})}{\partial d_i} d_k + \phi_i(\mathbf{u}) \right) \quad (5.61)$$

$$\frac{\partial^2 \Delta \mathbf{u}}{\partial d_i \partial d_j} = \sum_{k=1}^n \left(\frac{\partial^2 \phi_k(\mathbf{u})}{\partial d_i \partial d_j} d_k + \frac{\partial \phi_j(\mathbf{u})}{\partial d_i} + \frac{\partial \phi_i(\mathbf{u})}{\partial d_j} \right) \quad (5.62)$$

and then calculated both equations 5.61 and 5.62 at $\mathbf{d} = \mathbf{0}$:

$$\frac{\partial \Delta \mathbf{u}}{\partial d_i}(\phi = \mathbf{0}) = \phi_i(\mathbf{0}) \quad (5.63)$$

$$\frac{\partial^2 \Delta \mathbf{u}}{\partial d_i \partial d_j}(\mathbf{d} = \mathbf{0}) = \frac{\partial \phi_j(\mathbf{0})}{\partial d_i} + \frac{\partial \phi_i(\mathbf{0})}{\partial d_j}. \quad (5.64)$$

Therefore, from Eq. 5.63 and 5.64 we deduce that the first derivatives of the nodal solution are the linear eigenmodes and the second derivatives of the nodal solution are the modal derivatives.

Modal derivatives can be calculated differentiating the nonlinear eigenvalue problem respect to the modal coordinate d_j , obtaining:

$$(\mathbf{K} - \lambda_i \mathbf{M}) \frac{\partial \phi_i}{\partial d_j} + \left(\frac{\partial \mathbf{K}}{\partial d_j} - \frac{\partial \lambda_i}{\partial d_j} \mathbf{M} \right) \phi_i = \mathbf{0} \quad (5.65)$$

According with [117] a way to compute the modal derivatives is excluding the 'mass consideration'; for this reason we neglect the terms with the mass matrix \mathbf{M} from Eq. 5.65 and we obtain the definition of *modal derivative*:

$$\frac{\partial \phi_i}{\partial d_j} = -\mathbf{K}^{-1} \frac{\partial \mathbf{K}}{\partial d_j} \phi_i. \quad (5.66)$$

The derivative of the (tangent) stiffness matrix can be approximated and computed with the following finite difference [132]:

$$\frac{\partial \mathbf{K}}{\partial d_j} \approx \frac{\mathbf{K}(\mathbf{u}_0 + \varepsilon \phi_j) - \mathbf{K}(\mathbf{u}_0)}{\varepsilon} \quad (5.67)$$

where $\mathbf{K}(\mathbf{u}_0)$ is the linear stiffness matrix at the initial configuration. The modal derivatives are symmetric, i.e.:

$$\frac{\partial \phi_i}{\partial d_j} = \frac{\partial \phi_j}{\partial d_i}, \quad \text{with } i, j = 1, \dots, n \quad (5.68)$$

A proof of simmetry property is given by Weeger et al. [132]. For the simmetry property the number of the computed MDs is reduced; if we construct a reduced set of 'linear' eigenmodes Φ_k as described in Sec. 5.1.1 after we compute n_k derivatives of the (tangent) stiffness matrix through Eq. 5.67 and finally a set of $s = k(k+1)/2$ MDs are computed.

Therefore the calculation of the modal derivatives grows quadratically with the number k and it might be not desirable to compute all the modal derivatives; a criterion for the selection of modal derivatives is given by Tiso [120].

5.2.2 Derivatives of Lanczos vectors

In Sec. 5.1.6 we have seen that for linear heat conduction problems we can express the temperature solution vector \mathbf{T} in terms of a reduced set m of Lanczos vector \mathbf{q}_i and a reduced coordinates p_i :

$$\mathbf{T} - \mathbf{T}_0 = \Delta \mathbf{T} = \mathbf{Q}_m \mathbf{p}^m = \sum_{i=1}^m \mathbf{q}_i p_i \quad (5.69)$$

with \mathbf{T}_0 the initial vector.

The nonlinear solution of temperature \mathbf{T} can be written in terms of the Lanczos vector $\mathbf{q}_i(\mathbf{T})$, which is now dependent on the nodal solution, and the reduced coordinates p_i :

$$\mathbf{T} - \mathbf{T}_0 = \Delta \mathbf{T} = \mathbf{Q}_m \mathbf{p}^m = \sum_{i=1}^m \mathbf{q}_i(\mathbf{T}) p_i. \quad (5.70)$$

Similarly as we have done for structural problems, we develop $\Delta \mathbf{T}$ around its starting configuration $\Delta \mathbf{T} = \mathbf{0}$ (i.e. $\mathbf{p}^m = \mathbf{0}$) into a second order Taylor series:

$$\Delta \mathbf{T} = \sum_{i=1}^m \left(\frac{\partial \Delta \mathbf{T}}{\partial p_i} (\mathbf{p}^m = \mathbf{0}) p_i + \sum_{j=1}^m \left(\frac{\partial^2 \Delta \mathbf{T}}{\partial p_i \partial p_j} (\mathbf{p}^m = \mathbf{0}) \frac{p_j}{2} \right) p_i \right). \quad (5.71)$$

The first and second derivatives of the nodal temperature in Eq. 5.71 can be computed differentiating Eq. 5.70 respect to the coordinates p_i :

$$\frac{\partial \Delta \mathbf{T}}{\partial p_i} = \sum_{k=1}^m \left(\frac{\partial \mathbf{q}_k(\mathbf{T})}{\partial p_i} p_k + \mathbf{q}_i(\mathbf{T}) \right) \quad (5.72)$$

$$\frac{\partial^2 \Delta \mathbf{T}}{\partial p_i \partial p_j} = \sum_{k=1}^m \left(\frac{\partial^2 \mathbf{q}_k(\mathbf{T})}{\partial p_i \partial p_j} p_k + \frac{\partial \mathbf{q}_j(\mathbf{T})}{\partial p_i} + \frac{\partial \mathbf{q}_i(\mathbf{T})}{\partial p_j} \right) \quad (5.73)$$

and then calculated both equations 5.72 and 5.73 at $\mathbf{p}^m = \mathbf{0}$:

$$\frac{\partial \Delta \mathbf{T}}{\partial p_i}(\mathbf{p}^m = \mathbf{0}) = \mathbf{q}_i(\mathbf{0}) \quad (5.74)$$

$$\frac{\partial^2 \Delta \mathbf{T}}{\partial p_i \partial p_j}(\mathbf{p}^m = \mathbf{0}) = \frac{\partial \mathbf{q}_j(\mathbf{0})}{\partial p_i} + \frac{\partial \mathbf{q}_i(\mathbf{0})}{\partial p_j}. \quad (5.75)$$

Similarly as we have seen for structural dynamics, the first derivatives of the nodal temperature solution are the linear Lanczos vectors and the second derivatives are derivative of the Lanczos vectors.

To compute the first derivative of the Lanczos vectors we remember the definition of $\bar{\mathbf{r}}_j$ in Eq. 5.33 and we re-write as follows:

$$\mathbf{K}_\sigma \bar{\mathbf{r}}_j = \mathbf{M} \mathbf{q}_j \quad (5.76)$$

We differentiate Eq. 5.76 respect to the coordinates p_i and afterwards we \mathbf{M} -orthogonalize $\bar{\mathbf{r}}$ obtaining:

$$\mathbf{K}_\sigma \frac{\partial \bar{\mathbf{r}}_j}{\partial p_i} + \frac{\partial \mathbf{K}_\sigma}{\partial p_i} \bar{\mathbf{r}}_j = \frac{\partial \mathbf{M}}{\partial p_i} \mathbf{q}_j + \mathbf{M} \frac{\partial \mathbf{q}_j}{\partial p_i} \quad (5.77)$$

$$\mathbf{K}_\sigma \frac{\partial \mathbf{q}_{j+1}}{\partial p_i} + \frac{\partial \mathbf{K}_\sigma}{\partial p_i} \mathbf{q}_{j+1} = \frac{\partial \mathbf{M}}{\partial p_i} \mathbf{q}_j + \mathbf{M} \frac{\partial \mathbf{q}_j}{\partial p_i} \quad (5.78)$$

where have used:

$$\mathbf{q}_{j+1} = \left(\frac{1}{\bar{\mathbf{r}}^T \mathbf{M} \bar{\mathbf{r}}} \right) \bar{\mathbf{r}}_j. \quad (5.79)$$

similarly we neglect the terms associated with the capacity matrix \mathbf{M} in Eq. 5.78, obtaining the following *derivative of Lanczos vector*:

$$\frac{\partial \mathbf{q}_{j+1}}{\partial p_i} = -\mathbf{K}_\sigma^{-1} \frac{\partial \mathbf{K}_\sigma}{\partial p_i} \mathbf{q}_{j+1}. \quad (5.80)$$

The derivative of the (tangent) stiffness matrix in Eq. 5.80 can be approximated and computed with the following finite difference:

$$\frac{\partial \mathbf{K}_\sigma}{\partial p_i} \approx \frac{\mathbf{K}_\sigma(\mathbf{T}_0 + \varepsilon \mathbf{q}_i) - \mathbf{K}_\sigma(\mathbf{T}_0)}{\varepsilon} \quad (5.81)$$

where $\mathbf{K}_\sigma(\mathbf{T}_0)$ is the linear stiffness matrix at the initial configuration; the term $\mathbf{K}_\sigma(\mathbf{T}_0 + \varepsilon \mathbf{q}_i)$ is computed m -times along the variation $\varepsilon \mathbf{q}_j$, with $j = 1 \dots m$. Also in this case for the simmetry property of the Lanczos derivatives we need to compute $r = m(m+1)/2$ derivatives.

In Algorithm 2 are summarized the procedures to calculate the derivatives of the Lanczos vectors.

Algorithm 2 Algorithm for Lanczos vectors derivatives

-
- 1: Calculate $\mathbf{K}_\sigma(\mathbf{T}_0) = \mathbf{K}(\mathbf{T}_0) - \sigma\mathbf{M}(\mathbf{T}_0)$
 - 2: Compute Lanczos vectors with 1 $\mathbf{Q}_m = \{\mathbf{q}_1, \dots, \mathbf{q}_m\}$
 - 3: **for** $i = 1, \dots, m$ **do**
 - 4: Calculate $\mathbf{K}_\sigma(\mathbf{T}_0 + \varepsilon\mathbf{q}_i)$
 - 5: Compute $\frac{\partial \mathbf{K}_\sigma}{\partial p_i} \approx \frac{\mathbf{K}_\sigma(\mathbf{T}_0 + \varepsilon\mathbf{q}_i) - \mathbf{K}_\sigma(\mathbf{T}_0)}{\varepsilon}$
 - 6: **for** $j = i, \dots, m$ **do**
 - 7: Solve $\boldsymbol{\theta}_{ij} = \frac{\partial \mathbf{q}_j}{\partial p_i} = -\mathbf{K}_\sigma^{-1} \frac{\partial \mathbf{K}_\sigma}{\partial p_i} \mathbf{q}_j$
 - 8: **end for**
 - 9: **end for**
-

5.2.3 Derivatives of Lanczos vectors as reduced basis

We found that the derivative of the Lanczos vectors θ_{ij} is:

$$\boldsymbol{\theta}_{ij} = \frac{\partial \mathbf{q}_i}{\partial p_j} = -\mathbf{K}_\sigma^{-1} \frac{\partial \mathbf{K}_\sigma}{\partial p_j} \mathbf{q}_i \quad \text{with } i, j = 1, \dots, m \quad (5.82)$$

and the temperature increments can be written as a linear combination of the derivatives $\boldsymbol{\theta}_{ij}$ plus the Lanczos vectors \mathbf{q}_i at the initial configuration:

$$\Delta \mathbf{T} = L \left\{ \mathbf{q}_i(\mathbf{T}_0), \dots, \boldsymbol{\theta}_{ij} \right\} \quad \text{with } i = 1, \dots, m, \quad j \geq i \quad (5.83)$$

The derivatives can be also introduced in the Craig-Bampton method as an extension of nonlinear cases. In this cases the vector \mathbf{T}_i of the internal degrees of freedom is projected through the matrix $\mathbf{Q} \in \mathbb{R}^{n \times (b+m+r)}$ yielding:

$$\mathbf{T} = \mathbf{Q}\mathbf{p} \Leftrightarrow \begin{bmatrix} \mathbf{T}^b \\ \mathbf{T}^i \end{bmatrix} = \begin{bmatrix} \mathbf{I} & \mathbf{0} & \mathbf{0} \\ \boldsymbol{\Psi} & \mathbf{Q}_m & \boldsymbol{\Theta} \end{bmatrix} \begin{bmatrix} \mathbf{T}^b \\ \mathbf{p}^m \\ \boldsymbol{\xi} \end{bmatrix} \quad (5.84)$$

where we assume that \mathbf{T}_0 is equal to the zero vector.

Once the reduction basis (Eq. 5.84) has been derived, the nonlinear FE problem (Eq. 5.54) can be evaluated and projected to obtain a model of greatly reduced dimensions.

5.2.4 Numerical example using Matlab

The following numerical example, implemented in Matlab, is a simple case to show how the use of Lanczos vectors and their derivatives can give accurate solutions respectively for linear and nonlinear heat conduction problems, against the use of eigenmodes and modal derivatives. In the example we show the linear and nonlinear heat conduction problem of a two-dimensional bar exposed on the left side to a time-dependent heat flux (Fig. 5.4). The thermal material properties for linear case are summarized in Tab. 5.1. For the nonlinear case we assume a temperature dependent conductivity and specific heat, while the density is 1800 kg/m^3 (Fig. 5.5). The 2D bar is discretize with 20 linear quadrilateral elements with a total of 42 dofs.

The temperature distribution and the heat flux along the bar for the linear case are depicted in Fig. 5.6 for three different time steps: 5, 10, 40 s. We compare the solutions assuming 5 eigenmodes, i.e. (ϕ_1, \dots, ϕ_5) , and 5 Lanczos vectors, i.e. (q_1, \dots, q_5) , as

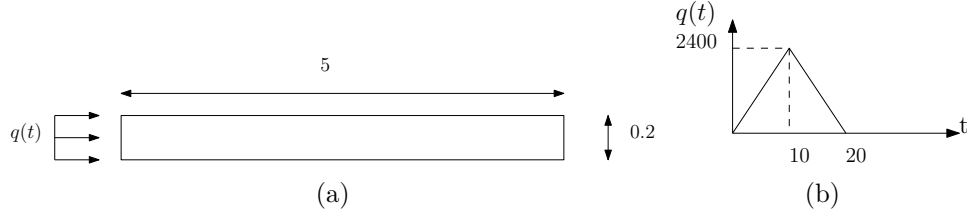


Figure 5.4: 2D bar exposed to a time dependent heat flux.

Table 5.1: Linear case: Input parameters for 2D bar [60].

Density (ρ)	1800 kg/m ³
Specific heat (c_p)	0.2 J/(kg °C)
Thermal conductivity (k)	40 W/(m °C)

reduced basis. The figures show how the use of Lanczos vectors can give more accurate solutions comparing with the same number of eigenmodes. In particular we observe that the eigenmodes well approximate only the solution at time $t = 40$ s, i.e. when the external flux is zero ($q(t) = 0$) and the system has free motion.

For the nonlinear case we compare the solution with the first 5 eigenmodes, i.e. (ϕ_1, \dots, ϕ_5) , the first 5 Lanczos vectors, i.e. (q_1, \dots, q_5) , (Fig. 5.8), and the first 3 Lanczos vectors plus 2 derivatives of the Lanczos vectors in Fig. 5.9, i.e. $(q_1, \dots, q_3, \psi_{11}, \frac{1}{2}(\psi_{12} + \psi_{21}))$. The temperature and heat flux at $t=10$ s are depicted in Fig 5.7; even if the use of 5 Lanczos vectors give good solutions, the enhancement of Lanczos derivatives on the reduction basis results into more accurate solutions with the same number of degree of freedoms. This fact is also evident in Fig. 5.10 where the root mean square (RMS) error is calculated for the temperature solution at $t=10$ s for increasing size of the projection basis. The RMS error is calculated by the following formula:

$$Error_{RMS}\% = \sqrt{\frac{\sum_{i=1}^n (T_{ref,i} - T_i)^2}{\sum_{j=1}^n T_{ref,i}^2}} \times 100 \quad (5.85)$$

where n is the total of degrees of freedom (42 dofs) and the reference solution is the solution of the full system. The RMS error corresponding to 5 DOFs is 38.2 % with eigenvector solution, 20.84 % with Lanczos vector solutions and 3.85 % with Lanczos vectors and derivatives (3+2) solution.

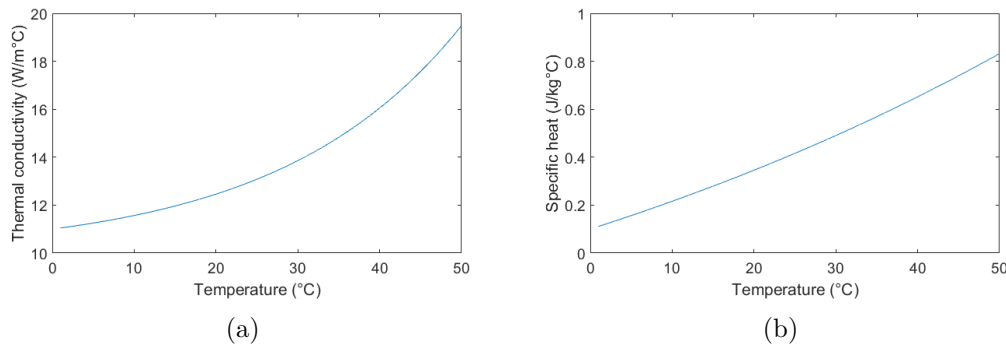


Figure 5.5: Nonlinear case: Input parameters for 2D bar.

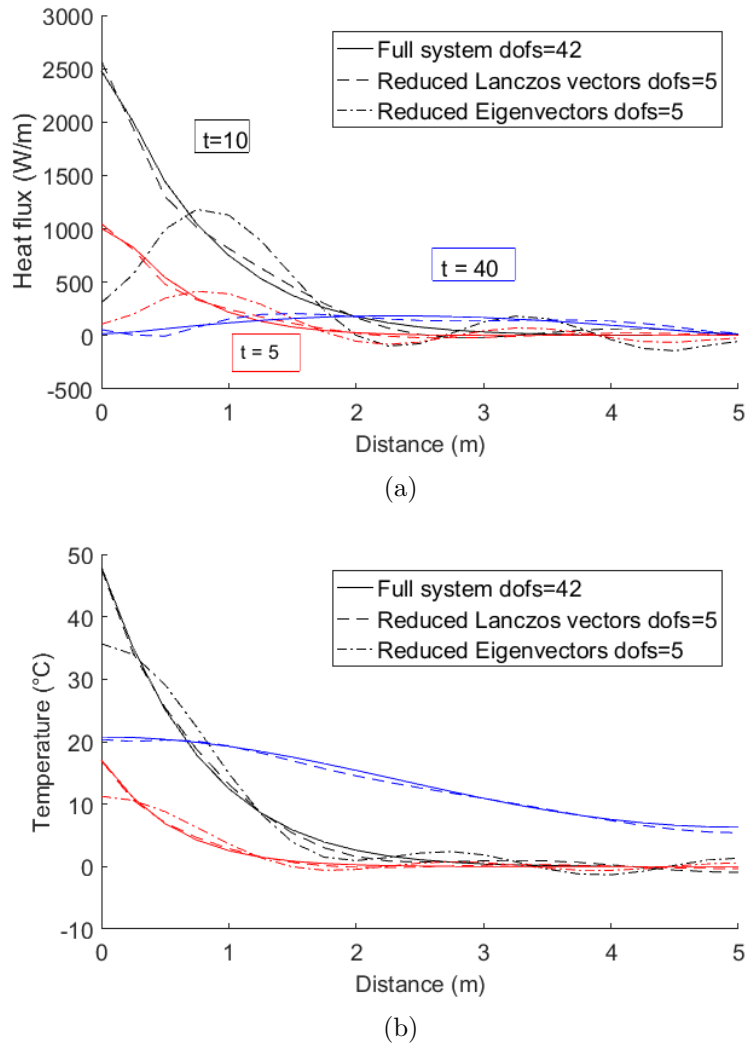
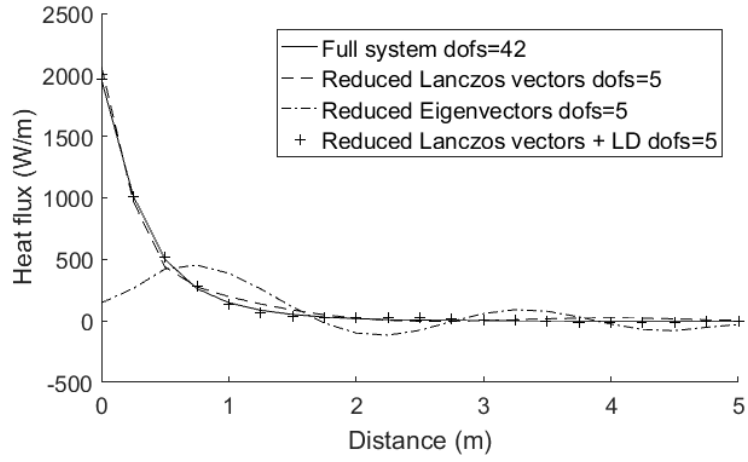
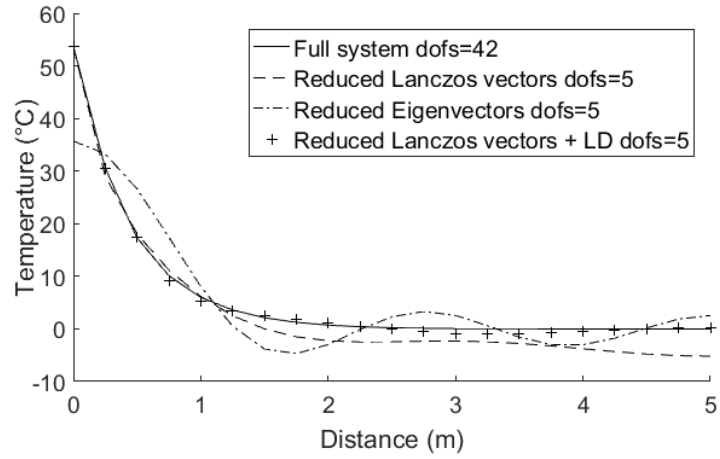


Figure 5.6: Linear case: Temperature distribution and heat flux along the 2D bar for three different time steps: 5, 10, 40 s.



(a)



(b)

Figure 5.7: Nonlinear case: Temperature distribution and heat flux along the 2D bar for $t=10$ s.

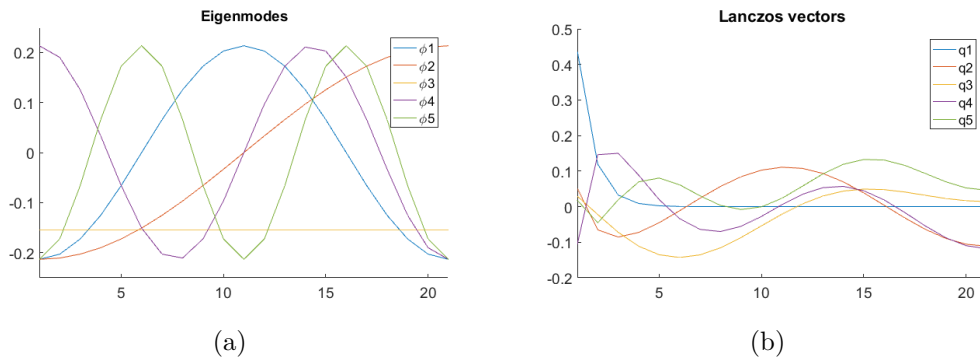


Figure 5.8: Nonlinear case: (a) Eigenmodes, (b) Lanczos vectors

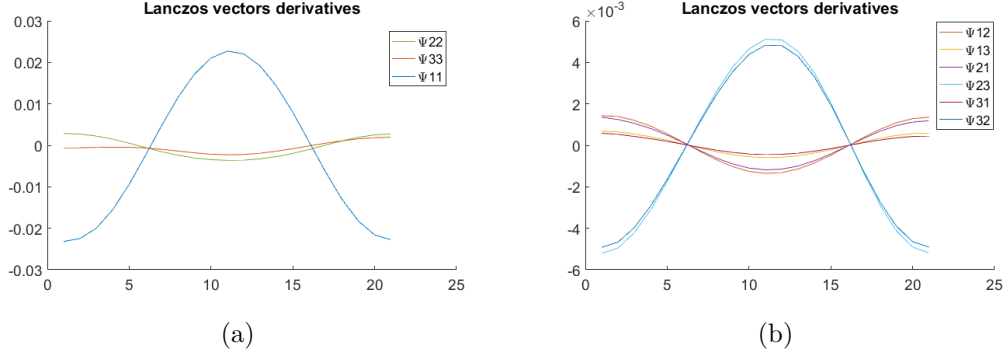
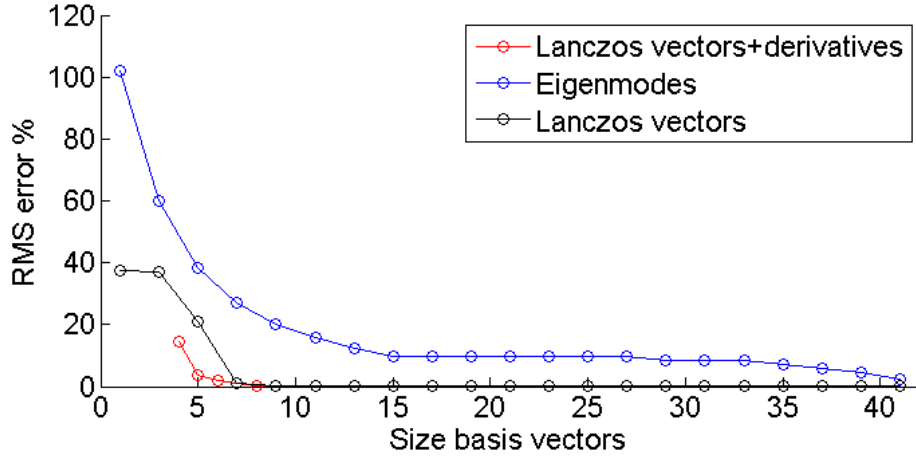


Figure 5.9: Nonlinear case: Lanczos vectors derivatives

Figure 5.10: Root mean square (RMS) error of temperature solution for: Eigenmodes solution, Lanczos vectors solution and Lanczos vectors (3)+ Lanczos derivatives (*Reference solution: full system*).

5.2.5 Summary

In the described chapter we have introduced some model order reduction (MOR) techniques to reduce large-scale linear and nonlinear problems. In particular, for linear problems the use of modal truncation technique is based on the selection of a reduction set of eigenmodes as projection basis; this technique is widely used for structural dynamics and can give accurate solutions. The Craig-Bampton method (CBM) belongs to the substructuring methods and uses a modal truncation technique to reduce some (internal) degrees of freedom, where the information on the solution is not essential.

A more accurate method to generate a reduction basis is using the Lanczos algorithm, a very efficient tool to generate a set of \mathbf{M} -orthonormal vectors called Lanczos vectors. After each iteration of the algorithm, the Lanczos vectors loses their orthogonality condition and a full orthogonalization against the previous set of vectors can be adopted. The Lanczos vectors are a suitable basis especially for linear heat conduction problems, and a modification of the CBM with these vectors is presented.

For nonlinear systems the introduction of some special vectors, called Modal derivatives (MDs) is very powerful, especially for structural dynamics. A similar approach is given for thermal problems, when an enrichment of the projection basis with some Lanczos

derivatives is able to give accurate solutions. The new basis, composed by Lanczos vectors and their derivatives, can be used also in CBM to reduce the internal degrees of freedom as an extension to nonlinearity.

In conclusion we compare the accuracy of the solution for a heat conduction problem assuming the eigenmodes and the Lanczos vectors as reduction basis. We investigated a simple numerical example in Matlab of a two-dimensional bar exposed to a time dependent heat flux. For both linear and nonlinear problems we found that Lanczos vectors give more accurate solution than the use of eigenmodes. The introduction of Lanczos derivatives to the set of Lanczos vectors is also able to capture the nonlinearity of the system.

Chapter 6

A new user subroutine implementation for model order reduction in Abaqus

The development of a suitable projection basis composed by a set of \mathbf{M} -orthonormal vectors called Lanczos vectors and their derivatives, can be used to reduce linear and nonlinear heat conduction problems. In particular the use of substructures through the Craig-Bampton method can be applied for linear portions of the thermal analysis.

Commercial software Abaqus develops itself the use of linear substructuring to static and dynamic mechanical problems with a particular extension for large rotations and translations of the substructure. On the contrary, in Abaqus no automatic implementation of substructuring is available for thermal problems. For this reason, in order to enable substructuring also for thermal analysis we use the user subroutine UEL, which permits to define a user element with precomputed reduced thermal matrices.

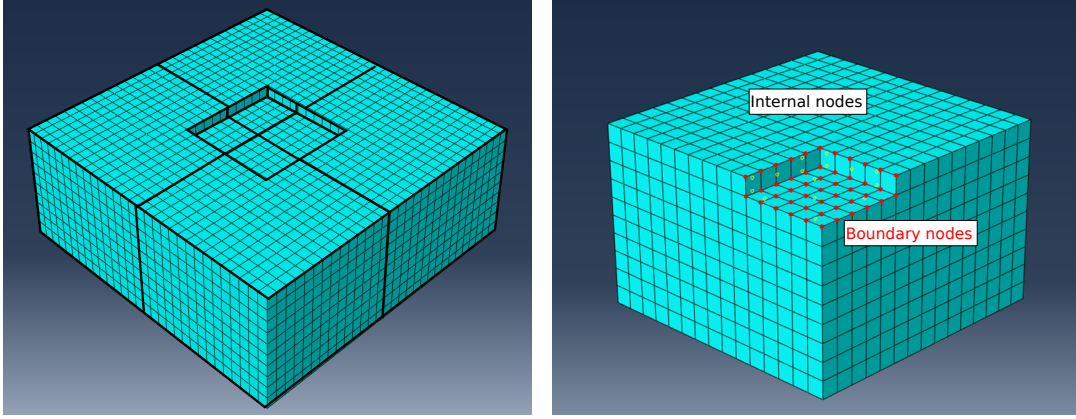
The reduction of large-scale nonlinear thermal systems is introduced in the software Abaqus by the development of a new in-house user subroutine to compute the nonlinear (tangent) matrices and directly apply the reduction technique.

In literature, model order reduction techniques applied to commercial softwares are not very common, only few papers concern the MOR to the software Abaqus [29]; while other authors apply MOR to the software Ansys [110], for weak nonlinearity in material properties of semiconductor devices [44].

6.1 Substructuring applied to FE model of SLM process

As we have described in Chapter 5, substructuring is clearly adopted to reduce the computational burden especially for linear cases; anyway substructuring can be also applied to 'linear' portions of nonlinear systems and compute them separately. In this case the element matrices of the single substructures can be calculated separately and assembled after to the rest of the model.

The advantages of using substructuring is evident especially for the cases where a single component is repeated multiple times inside the model; in this case the FE matrices can be calculated only once and the substructure itself can be used many times, with significant savings of computational effort.



(a) Model with four substructures.

(b) Single substructure with internal and boundary nodes (in red).

Figure 6.1: Substructuring of thermal model in Abaqus.

During the thermal analysis, presented in Sec. 4.5, a large portion of the base plate remains 'linear', i.e. the temperature solution does not change a lot from the chamber temperature (≈ 313.15 K), while the rest of the model, directly scanned by the laser beam, experiences a strong nonlinear behaviour. The finite elements of the base plate can be clearly condensed and assumed as a linear component, repeated inside the model four times (Fig. 6.1(a)).

For the single component we can identify some boundary nodes \mathbf{T}_b , which are connected with the rest of the model, and some internal nodes \mathbf{T}_i (Fig. 6.1(b)).

The definition of the single substructure within the software Abaqus is made by the user subroutine UEL, which is used to define a user element with precomputed reduced stiffness \mathbf{K} and capacity matrices \mathbf{M} .

The flow chart in Fig. 6.2 describes the path to generate substructures in the thermal problem: at the initial state we compute the assembled stiffness and capacity matrices from Abaqus; after we generate in Matlab a suitable reduction basis composed by a set of Lanczos vectors and we use this basis to reduce the stiffness and capacity matrices; finally the UEL is performed with the reduced matrices and assembled with the rest of the model.

The number of boundary nodes for the single substructure are 47, while the number of internal nodes are 2744 (Fig. 6.1(b)).

A set $m=2$ of Lanczos vectors, i.e. $\mathbf{Q}_m = \{\mathbf{q}_1, \dots, \mathbf{q}_m\}$, is generated in Matlab following the Lanczos algorithm in Alg. 1 (Sec. 5) and is used to project the solution to the reduced coordinates \mathbf{p} :

$$\mathbf{T} = \mathbf{Q}\mathbf{p} \Leftrightarrow \begin{bmatrix} \mathbf{T}^b \\ \mathbf{T}^i \end{bmatrix} = \begin{bmatrix} \mathbf{I} & \mathbf{0} \\ \mathbf{\Psi} & \mathbf{Q}_m \end{bmatrix} \begin{bmatrix} \mathbf{T}^b \\ \mathbf{p}^m \end{bmatrix} \quad (6.1)$$

with:

$$\begin{matrix} \mathbf{T}^i \\ (2744 \times 1) \end{matrix} = \begin{matrix} \mathbf{\Psi} \\ (2744 \times 47) \end{matrix} \times \begin{matrix} \mathbf{T}^b \\ (47 \times 1) \end{matrix} + \begin{matrix} \mathbf{Q}_m \\ (2744 \times 2) \end{matrix} \times \begin{matrix} \mathbf{p}^m \\ (2 \times 1) \end{matrix} \quad (6.2)$$

The stiffness and the capacity matrices and the force vector are projected to the reduced coordinate system by the projection matrix \mathbf{Q} :

$$\begin{matrix} \hat{\mathbf{K}} \\ (49 \times 49) \end{matrix} = \begin{matrix} \mathbf{Q}^T \\ (2791 \times 49) \end{matrix} \times \begin{matrix} \mathbf{K} \\ (2791 \times 2791) \end{matrix} \times \begin{matrix} \mathbf{Q} \\ (2791 \times 49) \end{matrix} \quad (6.3)$$

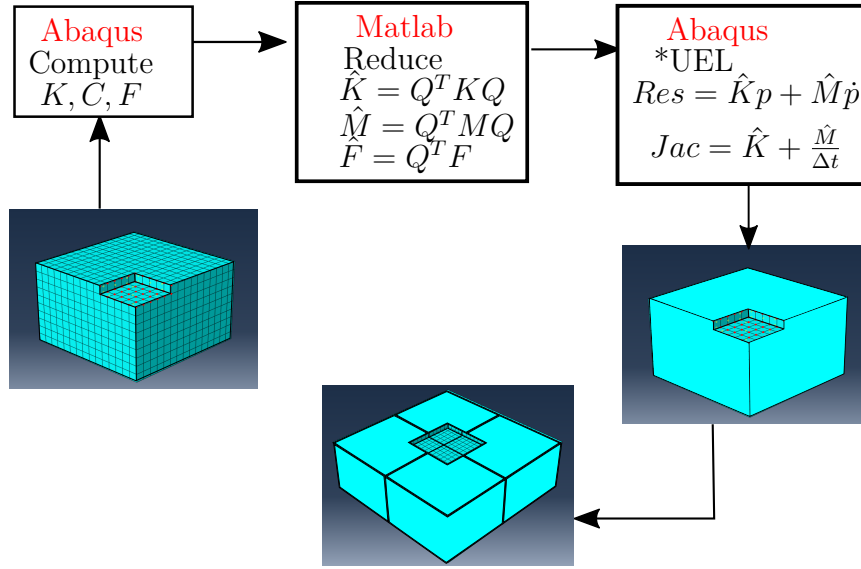


Figure 6.2: Generation of substructuring using User Element (UEL).

$$\hat{\mathbf{M}}_{(49 \times 49)} = \mathbf{Q}_{(2791 \times 49)}^T \times \mathbf{M}_{(2791 \times 2791)} \times \mathbf{Q}_{(2791 \times 49)} \quad (6.4)$$

$$\hat{\mathbf{F}}_{(49 \times 1)} = \mathbf{Q}_{(2791 \times 49)}^T \times \mathbf{F}_{(2791 \times 1)} \quad (6.5)$$

In the present case, the single substructure has zero external force, i.e. $\mathbf{F} = \mathbf{0}$. The sparsity pattern of stiffness and capacity matrices before and after reduction are depicted in Fig. 6.3; before reduction the matrices are more sparse while after reduction the matrices appear denser but much smaller.

The number of DOFs and the computational times before and after substructuring are summarized in Tab. 6.1. The benefit on analysis time is not so significant, indeed the reduction of degrees of freedom after the substructuring is about 20 %, but the introduced method can be also used to condense also more complex geometries of SLM models. Now we want to extend the concept of substructuring to the nonlinear case,

Table 6.1: Comparison between computation times before and after linear substructuring.

Model	Numerical analysis	DOFs	Analysis time
Before substructuring	Thermal analysis	46904	1 hour and 2 min
After substructuring	Thermal analysis	36610	49 min and 22 s

introducing in the software Abaqus a user subroutine in Fortran to compute and reduce the nonlinear thermal system.

6.2 Model order reduction subroutine

The commercial software Abaqus provides a user interface though a wide range of user subroutines which can be compiled to perform customized applications. In the previous chapters we have used some of these useful subroutines; for example, UEL can

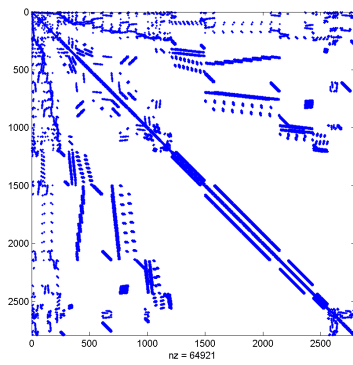
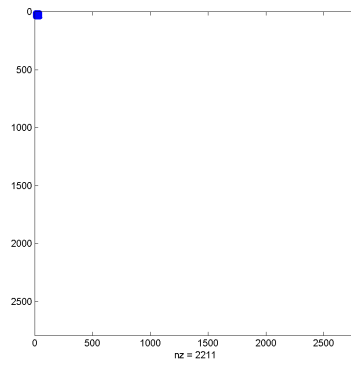
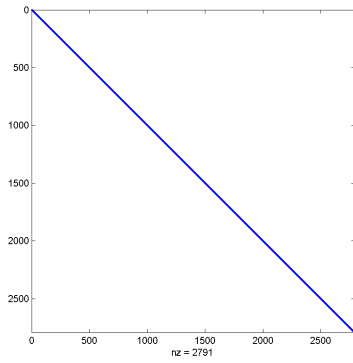
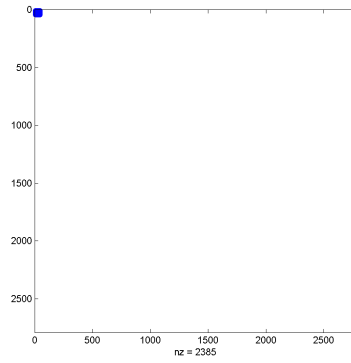
(a) *Unreduced stiffness matrix.*(b) *Reduced stiffness matrix.*(c) *Unreduced capacity matrix.*(d) *Reduced capacity matrix.*

Figure 6.3: Sparsity pattern of stiffness and capacity matrices of the system before and after projection.

be used to define complex user elements, which are not present in the Abaqus library; also UMATHT is a powerful subroutine for heat conduction problems used to define customized material models. On the contrary, the use of a commercial software do not permit a complete freedom and a control over some parameters and procedures, such as the modification of FE matrices.

Anyway, the idea of operating on the FE matrices seems to be very useful, especially for high nonlinear problems as SLM simulations, in order to reduce the size of the system. To reach the objective we would define the following procedures for each time increment:

1. Computing the finite element matrices at the current nodal temperature T :

$$(\mathbf{m}^e)_{ij} = \int_{\Omega} N_i \rho(T) c_p(T) N_j \partial \Omega^e$$

$$(\mathbf{k}^e)_{ij} = \int_{\Omega} \nabla N_i k(T) \nabla N_j \partial \Omega^e$$

$$(\mathbf{f}^e)_i = \int_{\Omega} N_i q \partial \Omega + \int_{\Gamma_g} N_i g \partial \Gamma_g.$$

2. Assembling the finite element matrices to global matrices:

$$\mathbf{M} = \mathbf{A}_{e=1}^{nel} \mathbf{m}^e$$

$$\mathbf{K} = \mathbf{A}_{e=1}^{nel} \mathbf{k}^e$$

$$\mathbf{F}(t) = \mathbf{F}_{nodal}(t) + \mathbf{A}_{e=1}^{nel} \mathbf{f}^e(t)$$

3. Reduce the global matrices by the projection matrix \mathbf{Q} :

$$\hat{\mathbf{M}} = \mathbf{Q}^T \mathbf{M} \mathbf{Q}$$

$$\hat{\mathbf{K}} = \mathbf{Q}^T \mathbf{K} \mathbf{Q}$$

$$\hat{\mathbf{F}} = \mathbf{Q}^T \mathbf{F}$$

4. Solve the reduced system:

$$\hat{\mathbf{K}} \mathbf{p}(t) + \hat{\mathbf{M}} \dot{\mathbf{p}}(t) = \hat{\mathbf{F}}$$

5. Update the nodal temperature solution:

$$\mathbf{T}(t) = \mathbf{Q} \mathbf{p}(t)$$

6. Repeat from 1.

Since it does not exist in Abaqus a unique user subroutine providing the described procedures, we proceed in a tricky way by using the user subroutines UEL and URDFIL. The subroutine UEL is used as for the linear case (Sec. 6.1) to define the substructure inside the model; the user subroutine URDFIL is introduced to access the temperature solution at the end of any increment of the analysis which is read from a result file. The temperature solution is used to update the nonlinear material properties at each time increment.

In Fig. 6.4 we show a schematic description of the implemented tool: the software Abaqus calls the user subroutine UEL, which is used to define the single substructure with the reduced degrees of freedom; for the first increment of the time step we import the precomputed reduced matrices, i.e. $\hat{\mathbf{K}}_1, \hat{\mathbf{M}}_1, \hat{\mathbf{F}}_1$, by an external text file (1). The software solves the reduced system and update the reduced nodal coordinates; afterwards the software calls the subroutine URDFIL which reads the updated nodal coordinates and computes the nodal temperature by the projection matrix \mathbf{Q} , which is imported in the subroutine from Matlab (3). Afterwards we compute the tangent element matrices for the current nodal temperatures and we assemble the global matrices, $\hat{\mathbf{K}}_2, \hat{\mathbf{M}}_2, \hat{\mathbf{F}}_2$ (4). Then we reduce the assembled matrices and the force vector by the projection matrix \mathbf{Q} to obtain the reduced matrices. The reduced matrices and vector are called again by the UEL subroutine (though a *common block*) and the software Abaqus solves the reduced system: $\hat{\mathbf{K}}_2 \mathbf{p}_2 + \hat{\mathbf{M}}_2 \dot{\mathbf{p}}_2 = \hat{\mathbf{F}}_2$ (5). Afterwards the procedure is repeated for the successive time increments until the end of the step.

The projection matrix \mathbf{Q} is computed in Matlab with the Lanczos algorithm; the described algorithm is written in Fortran; to reduce the memory allocation the sparse matrices are constructed using the Compressed Row Storage (CRS) format which puts the subsequent nonzeros of the matrices rows in contiguous memory locations. A description of CRS format for sparse matrices is given in Appendix B.

The developed user subroutines inside the software Abaqus calculate directly the assembled finite element matrices and after reduce the system without the necessity of using additional programs during the analysis. The only input variables needed to be pre-computed (in Matlab) are:

- the reduced stiffness and capacity matrices at the initial state: $\hat{\mathbf{K}}(\mathbf{T}_0)$ and $\hat{\mathbf{M}}(\mathbf{T}_0)$;
- the projection matrix \mathbf{Q} in full and sparse (CSR) format.

6.2.1 Application examples

In the following we present the numerical text of a [1,1] two-dimensional square subject to a time dependent heat flux (Fig. 6.5). For the 2D square we investigate the validity and the efficiency of the presented algorithm in terms of time reduction for a linear and nonlinear case. The nonlinearity is introduced considering temperature dependent conductivity (Tab. 6.2). The 2D square is discretized with 100x100 linear elements (DC2D4).

The temperature profile for linear and nonlinear cases along the square vertical is depicted in Fig. 6.6 and 6.7 for two different time steps: 10 s and 15 s.

In Tab. 6.3 we report the RMS error for the temperature solution obtained with the reduction respect to the reference solution of the full model, obtained from Abaqus. We observe that the reduced models for linear case with 4 DOFs and for nonlinear case with

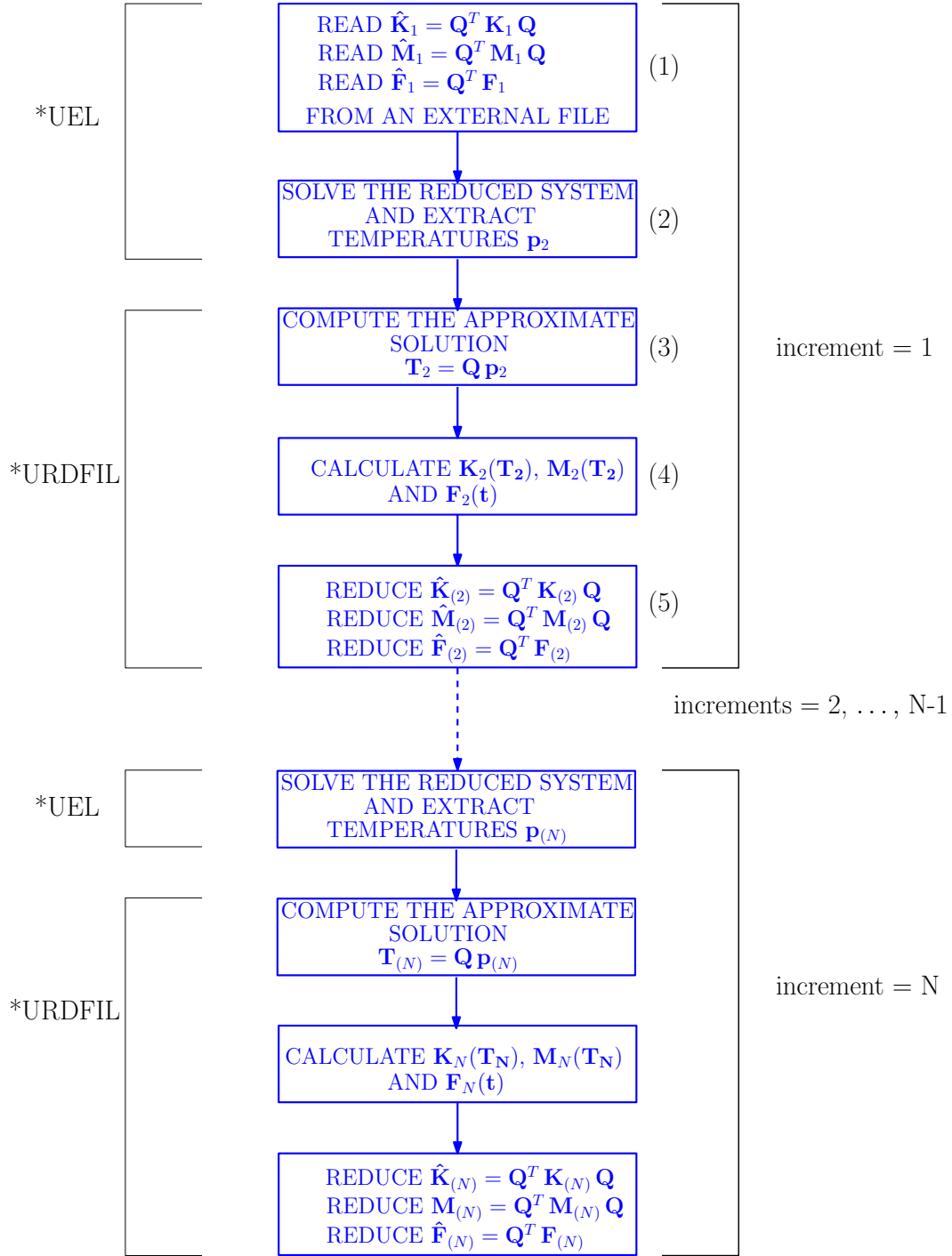


Figure 6.4: Algorithm to reduce the nonlinear matrices in Abaqus.

5 DOFs fit well the solution of the full system with 10201 DOFs. The computational time with the present algorithm is reduced for both the cases: in particular from Tab. 6.3 we observe that the reduction of analysis time is about 46 % for the linear case and 17 % for the nonlinear case.

In Appendix C the input file and the computed user subroutines are presented.

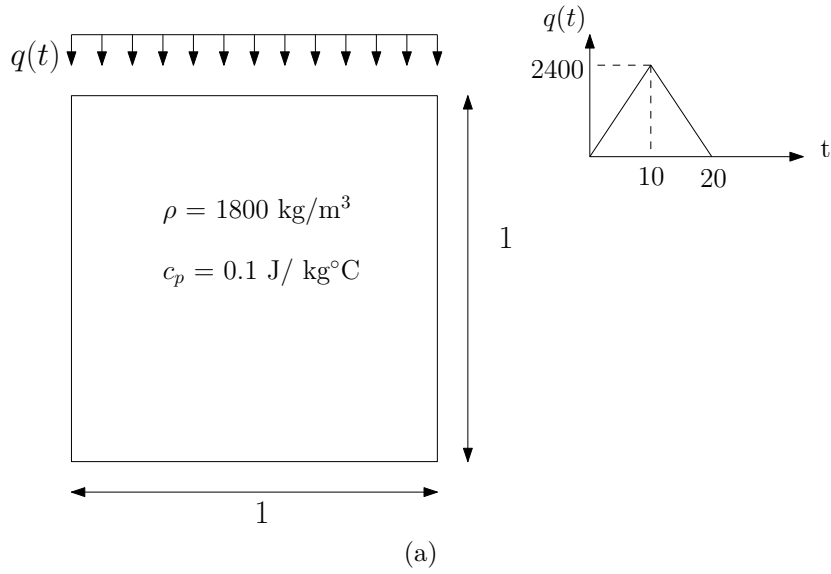
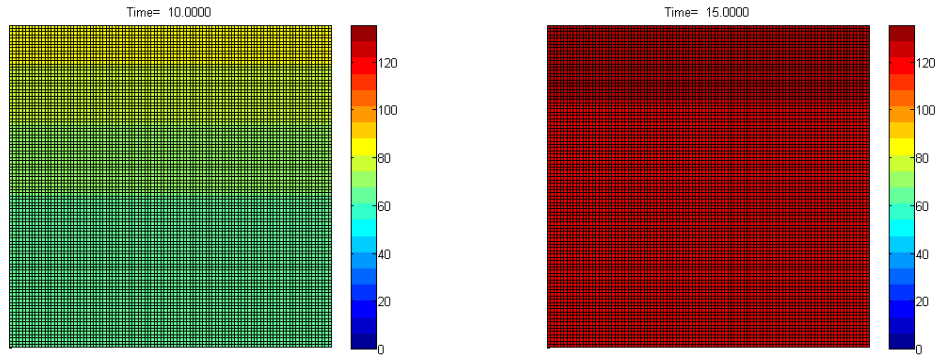
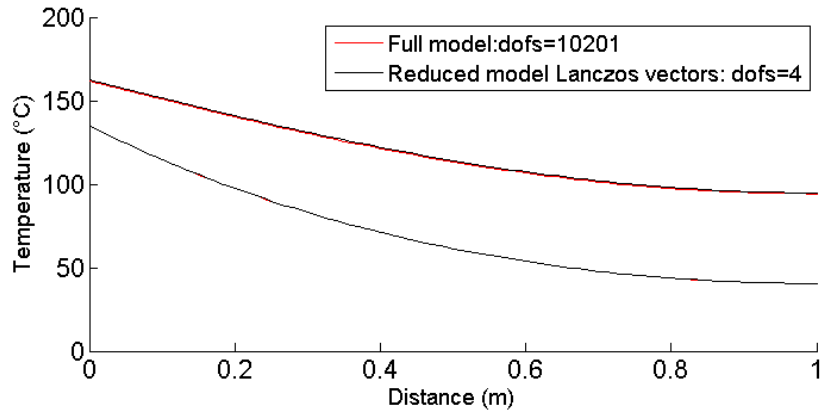


Figure 6.5: 2D square exposed to a time dependent heat flux.



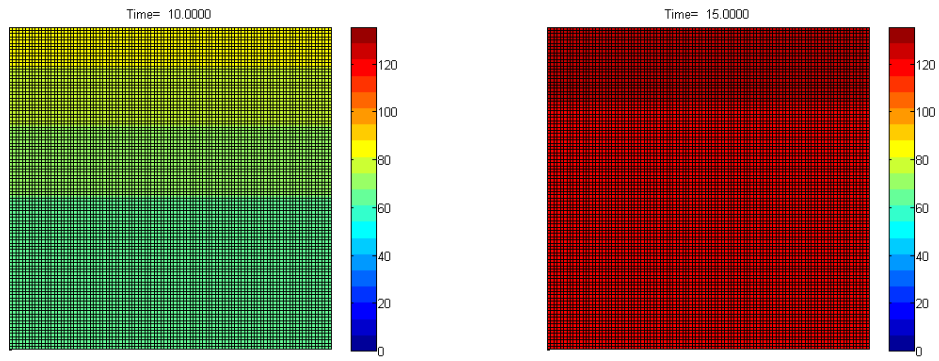
(a) Temperature field (°C) at 10 s.

(b) Temperature field (°C) at 15 s.



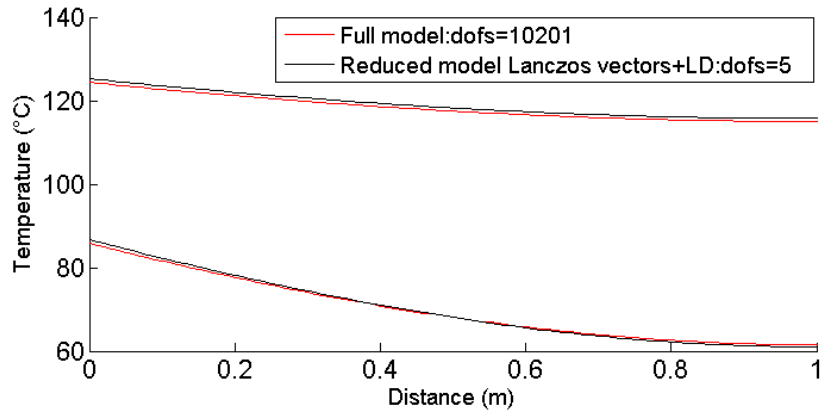
(c) Temperature profile (°C) along the square vertical.

Figure 6.6: Linear case: temperature field (°C).



(a) *Temperature field (°C) at 10 s.*

(b) *Temperature field (°C) at 15 s.*



(c) *Temperature profile (°C) along the square vertical.*

Figure 6.7: Nonlinear case: temperature field (°C).

Table 6.2: Nonlinear case: Input parameters for 2D square.

Temperature (°C)	Thermal conductivity (W/(m °C)) (W/(m °C))
10	11
20	25
50	40
200	100

Table 6.3: Comparison between the solutions obtained with the full model and with the reduced model by the reduction tool in Fig. 6.4.

Case	Full model		Reduced model		RMS error (%)	
	Dofs	Time (s)	Dofs	Time (s)	t = 10 s	t = 15 s
Linear	10201	37.17	4	20	0.0303	0.5952
Nonlinear	10201	65.04	5	53.77	0.6254	0.6529

Chapter 7

Final remarks

The present thesis deals with a topic which is most current and it is developed from a general necessity of a standard procedure of selective laser melting process. Clearly the SLM process is rather complex and includes many challenges: the lack of process credibility and design rules, the generation of a large number of measurements, the low part quality and productivity, size limitations and imperfections, etc. The role of scientific community is giving a properly evaluation of the real behaviour of SLM parts, making experimental tests or developing numerical simulations.

The second chapter presented a detailed overview of the main physical phenomena arising during the process. Many experimental tests are conducted in literature to highlight the effect of some process parameters over the physical behaviour: for example, decreasing the laser speed and increasing the laser power we obtain deeper melt pool regions, preventing delamination.

SLM process includes multi-physics and multi-scale phenomena; in the third chapter we defined the physical models and governing equations for heat conduction problem, with and without convection, material models, phase transformation with the classical Stefan problem definition.

Indeed, the modelling of SLM is becoming always more attractive and essential to understand and select a standard printing procedure which is able to build-up competitive and optimized products. Many numerical techniques are developed to predict the multi-scale and multi-physics behaviour of welded parts, which experience similar temperature distributions. More recent numerical models are focused directly on the simulation of SLM parts and most used commercial software are introducing some additive manufacturing packages; anyway the missing of a efficient computational tool able to be fast and cost-effective is still a current issue.

For this reason the present thesis developed a three-dimensional FE model with the attempt of reducing the computational burden. To reach the objective, we decided to use the finite element commercial software Abaqus, which is able to simulate a multitude of physical phenomena with high accuracy.

In chapter 4 we first developed thermal and stress analysis for different cases with the use of customized user subroutines, written in Fortran. The thermal and stress analyses for the experimental setup conducted by [106] gave accurate results.

In order to speed-up the computational model, we adopted a simplified heat input for the thermal analysis, replacing the moving heat source. The simplified heat input is obtained from the steady-state temperature solution of a single laser track and it is imposed as a Dirichlet boundary condition.

Model order techniques for heat conduction problems are introduced in chapter 5 for both linear and nonlinear cases. In particular a set of \mathbf{M} -orthonormal vectors (Lanczos vectors) and their derivatives are chosen to construct the projection basis.

In chapter 6 the model order reduction is applied to reduce the computational effort. Linear substructuring with the Craig-Bampton method is performed to condense linear portions of the thermal model: a large part of the base plate remained linear and is condensed pre-computing the reduced thermal matrices. The extension of model order reduction to nonlinear thermal problems was possible by the definition of a in-house user subroutine, written in Fortran, which directly performs the reduction of (tangent) thermal matrices at each time increment.

7.1 Future developments

The results obtained from the present thesis provide the basis of developing more complex models of SLM modelling. In particular we present possible future developments in the following:

- The introduction of a simplified heat input has positive impacts to the reduction of computational burden of thermal analysis. Furthermore this equivalent model gives accurate results, in terms of residual stresses, and for this reason can be used for larger domains with multiple layers and more complex scanning strategies;
- The development of linear Craig-Bampton method for transient heat conduction problems can be easily implemented in Abaqus. This procedure can be applied to condense linear portions of the SLM model: in particular for multiple-layer geometries the linear substructures can be applied to the underlying layers when the effect of the laser input on temperature distribution is below a given tolerance.
- The implementation of model reduction technique by the definition of a new user subroutine in Abaqus is useful to reduce directly the nonlinear thermal matrices, without using additional programs. The Fortran code can be used to sequentially reduce single layers of the SLM model during the build-up process. One possibility is to define two components, one linear with constant reduced thermal matrices and one nonlinear with the corresponding projection basis \mathbf{Q} ; the layers with a temperature field which is affected by the laser input can be condensed using the nonlinear substructure, when the laser is far away and the temperature field is quite constant the layer switches to the linear substructure (Fig. 7.1). The nonlinear substructure can not be defined directly to the scanned layers because the implemented subroutine does not provide the possibility of taking storage of the temperature history at the integration points.

Clearly the described procedure has some limitations that must be considered and mentioned. The application of substructures must be applied to proper geometries, where the number of boundary nodes is not too high and the reduction is considerable. Furthermore, the memory allocation related to user subroutines is limited, since they share memory sources with Abaqus. Allocate the memory dynamically could be an answer, so the memory is allocated from the heap and not the stack [36]. In the end, Fortran is not a very high-level language and coding the user subroutines can be very complex and time-consuming.

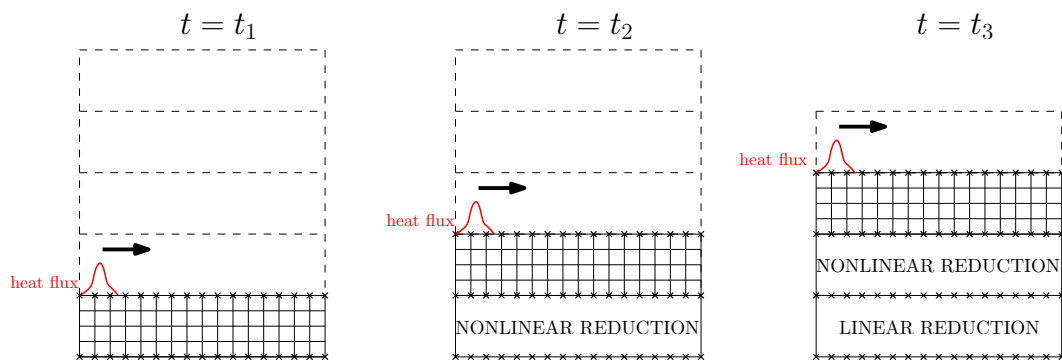


Figure 7.1: Future developments: sequentially substructuring.

Appendices

Appendix A

User subroutines for FE thermal model of SLM process

The following appendix is presented to show the user subroutines, written in Fortran, for the FE three-dimensional model presented in Sec. 4.4.5. In detail we present the subroutine DFLUX for the moving heat flux and the subroutines USDFLD and UMATHT for the phase transformation and the dependence of material properties (i.e., conductivity, specific heat and density) with temperature.

A.1 User subroutines

```
c *****SUBROUTINE USDFLD*****
SUBROUTINE USDFLD(FIELD,STATEV,PNEWDT,DIRECT,T,CELENT,
TIME,DTIME,CMNAME,ORNAME,NFIELD,NSTATV,NOEL,NPT,LAYER,
KSPT,KSTEP,KINC,NDI,NSHR,COORD,JMAC,JMATYP,MATLAYO,
LACCFLA)
C
INCLUDE 'ABA_PARAM.INC'
C
CHARACTER*80 CMNAME,ORNAME
CHARACTER*3 FLGRAY(15)
DIMENSION FIELD(NFIELD),STATEV(NSTATV),DIRECT(3,3),
T(3,3),TIME(2)
DIMENSION ARRAY(15),JARRAY(15),JMAC(*),JMATYP(*),
COORD(*)

CALL GETVRM('TEMP',ARRAY,JARRAY,FLGRAY,JRCD,JMAC,JMATYP,MATLAYO,LACCFLA)
TEMP=ARRAY(1)
INDEX=STATEV(4)
IF (TEMP.GE.1923.15) THEN
INDEX=1
ENDIF

FIELD(1)=INDEX
STATEV(4)=FIELD(1)
```

```

C If error , write comment to .DAT file :
IF(JRCD.NE.0)THEN
WRITE(6,*) 'REQUEST ERROR IN USDFLD FOR ELEMENT NUMBER ',
NOEL, 'INTEGRATION POINT NUMBER ',NPT
ENDIF
C
RETURN
END

c*****SUBROUTINE UMATH*****
SUBROUTINE UMATH(U,DUDT,DUDG,FLUX,DFDT,DFDG,
STATEV,TEMP,DTEMP,DTEM DX,TIME,DTIME,PRED,DPRED,
CMNAME,NTGRD,NSTATV,PROPS,NPROPS,COORDS,PNEWDT,
NOEL,NPT,LAYER,KSPT,KSTEP,KINC)
C
IMPLICIT REAL*8(A-M,O-Z)
C
CHARACTER*80 CMNAME
DIMENSION DUDG(NTGRD),FLUX(NTGRD),DFDT(NTGRD),
DFDG(NTGRD,NTGRD),STATEV(NSTATV),DTEM DX(NTGRD),
TIME(2),PRED(1),DPRED(1),PROPS(NPROPS),COORDS(3),
TABLE_K(2,9),TABLE_C(2,9),TABLE_KP(2,3)

C solidus temperature
TSOL=PROPS(1)
C liquidus temperature
TLIQ=PROPS(2)
C latent heat of fusion
LH=PROPS(3)

TEMPDT= TEMP+DTEMP

C conductivity of solid Ti-64
DATA TABLE_K/7.D0,298.15,7.45,373.15,12.6,773.15,19.3,1273.15,27,
1873.15,28.4,1923.15,33.4,1933.15,34.6,2173.15,34.6,3073.15/
C conductivity of powder Ti-64
DATA TABLE_KP/0.2,293.15,19.4,1878.15,28.3,1923.15/
C specific heat of Ti-64
DATA TABLE_C/5.46E8,298.15,5.62E8,373.15,6.51E8,773.15,6.41E8,
1273.15,7.5E8,1873.15,7.59E8,1923.15,8.31E8,1933.15,8.31E8,2173.15,
8.31E8,3073.15/

INC1=0
INC2=0
INC=0

C conductivity of powder Ti-64
IF(STATEV(4).EQ.0)THEN

```

```

IF (TEMPDT.LE.TABLE_KP(2,1)) THEN
COND=TABLE_KP(1,1)
DCOND=0.d0
ELSEIF (TEMPDT.GE.TABLE_KP(2,3)) THEN
COND=TABLE_KP(1,3)
DCOND=0.d0
ELSEIF (TEMPDT.GT.TABLE_KP(2,1).AND.TEMPDT.LT.TABLE_KP(2,3)) THEN
DO K1=1,2
TL1=TABLE_KP(2,K1+1)
IF (TEMPDT.LT.TL1.AND.INC.EQ.0) THEN
TL0=TABLE_KP(2,K1)
DT=TL1-TL0
C0=TABLE_KP(1,K1)
C1=TABLE_KP(1,K1+1)
DC=C1-C0
DCOND=DC/DT
COND=DCOND*(TEMPDT-TL0)+C0
INC=1
ENDIF
END DO
END IF

```

C conductivity of solid Ti-64

```
ELSEIF (STATEV(4).EQ.1) THEN
```

```

IF (TEMPDT.LE.TABLE_K(2,1)) THEN
COND=TABLE_K(1,1)
DCOND=0.d0
ELSEIF (TEMPDT.GE.TABLE_K(2,9)) THEN
COND=TABLE_K(1,9)
DCOND=0.d0
ELSEIF (TEMPDT.GT.TABLE_K(2,1).AND.TEMPDT.LT.TABLE_K(2,9)) THEN
DO K1=1,8
TL1=TABLE_K(2,K1+1)
IF (TEMPDT.LT.TL1.AND.INC1.EQ.0) THEN
TL0=TABLE_K(2,K1)
DT=TL1-TL0
C0=TABLE_K(1,K1)
C1=TABLE_K(1,K1+1)
DC=C1-C0
DCOND=DC/DT
COND=DCOND*(TEMPDT-TL0)+C0
INC1=1
ENDIF
END DO
END IF
END IF

```

```

C  specific heat
IF (TEMPDT.LE.TABLE_C(2,1)) THEN
SPECHT=TABLE_C(1,1)
ELSEIF (TEMPDT.GE.TABLE_C(2,9)) THEN
SPECHT=TABLE_C(1,9)
ELSEIF (TEMPDT.GT.TABLE_C(2,1).AND.TEMPDT.LT.TABLE_C(2,9)) THEN
DO K1=1,8
TL1=TABLE_C(2,K1+1)
  IF (TEMPDT.LT.TL1.AND.INC2.EQ.0) THEN
    TL0=TABLE_C(2,K1)
    DT=TL1-TL0
    C2=TABLE_C(1,K1)
    C3=TABLE_C(1,K1+1)
    DCC=C3-C2
    SPECHT=(DCC/DT)*(TEMPDT-TL0)+C2
    INC2=1
  ENDIF
END DO
END IF

```

```

DUDT = SPECHT      ! specific heat
DU = DUDT*DTEMP    ! increment of energy input

```

```

IF (TEMP.LE.TSOL)THEN
  IF (TEMPDT.LE.TSOL)THEN
    DF=0.D0
  ELSEIF (TEMPDT.GT.TSOL.AND.TEMPDT.LE.TLIQ)THEN
    DF=(TEMPDT-TSOL)/(TLIQ-TSOL)
  ELSEIF (TEMPDT.GT.TLIQ)THEN
    DF=1.D0
  ENDIF
ELSEIF (TEMP.GT.TSOL.AND.TEMP.LE.TLIQ)THEN
  IF (TEMPDT.LE.TSOL)THEN
    DF=-(TEMP-TSOL)/(TLIQ-TSOL)
  ELSEIF (TEMPDT.GT.TSOL.AND.TEMPDT.LE.TLIQ)THEN
    DF=(TEMPDT-TSOL)/(TLIQ-TSOL)-(TEMP-TSOL)/(TLIQ-TSOL)
  ELSEIF (TEMPDT.GT.TLIQ)THEN
    DF=1.D0-(TEMP-TSOL)/(TLIQ-TSOL)
  ENDIF
ELSEIF (TEMP.GT.TLIQ)THEN
  IF (TEMPDT.LE.TSOL)THEN
    DF=-1.D0
  ELSEIF (TEMPDT.GT.TSOL.AND.TEMPDT.LE.TLIQ)THEN
    DF=(TEMPDT-TSOL)/(TLIQ-TSOL)-1.D0
  ELSEIF (TEMPDT.GT.TLIQ)THEN
    DF=0.D0
  ENDIF

```

```

ENDIF

C equivalent heat capacity method
IF (TEMPDT.GT.TSOL.AND.TEMPDT.LE.TLIQ)THEN
SLOPE=LH/(TLIQ-TSOL)
ELSE
SLOPE=0.D0
ENDIF

DUDT=DUDT+SLOPE
DU = DU+LH*DF

U = U+DU

C heat flux
DO I=1, NTGRD
FLUX(I)=-COND*DTEM DX(I)
DFDG(I,I)=-COND
DFDT(I)=-DCOND*DTEM DX(I)
END DO

RETURN

END

c*****SUBROUTINE DFLUX*****
SUBROUTINE DFLUX(FLUX,SOL,KSTEP,KINC,TIME,NOEL,NPT,
COORDS,JLTYP,TEMP,PRESS,SNAME)

IMPLICIT REAL*8(A-M,O-Z)

DIMENSION FLUX(2),TIME(2),COORDS(3)
CHARACTER*80 SNAME

V=1200      ! Travel speed [mm/s]
RBEAM=0.05  ! Radius of laser beam [mm]
DBEAM=0.1   ! Diameter of laser beam [mm]
P=195000    ! Laser power [mJ/s]
L=1         ! Length of geometry [mm]
A=1         ! Width of geometry [mm]
XA = A+RBEAM
ZA = L+2*RBEAM
XB = XA+0.9
TEMPT=SOL
ALPHA = 0.1  ! Absorptance

! path 1
IF (TIME(1).GE.0.d0.AND.TIME(1).LE.0.00075)THEN
ZM=COORDS(3)-ZA

```

```

XM=COORDS(1)-V*(TIME(1)-0.d0)-XA

! path 2
ELSEIF (TIME(1).GT.0.00075.AND.TIME(1).LE.0.0008) THEN
ZM=COORDS(3)-V*(TIME(1)-0.00075)-ZA
XM=COORDS(1)-XB

! path 3
ELSEIF (TIME(1).GT.0.0008.AND.TIME(1).LE.0.0015) THEN
ZM=COORDS(3)-ZA -DBEAM
XM=COORDS(1)+V*(TIME(1)-0.0008)-XB
ENDIF

IF (XM.GE.-RBEAM.AND.XM.LE.RBEAM.AND.ZM.GE.-RBEAM.AND.ZM.LE.RBEAM) THEN
FLUX(1) =0.864*ALPHA*P/(3.14*RBEAM**2)
ELSE
FLUX(1)=0.d0
ENDIF

10 RETURN
20 CONTINUE
END

```


Appendix B

Compressed Row Storage format for sparse matrices

Compressed Row Storage (CRS) useful formats to represent a non-symmetric matrix \mathbf{A} with dimension $n \times m$ in sparse way by defining three one-dimensional arrays: \mathbf{a} , \mathbf{ja} , and \mathbf{ia} .

The first one \mathbf{a} is for floating-point numbers and stores the non-zero values of the matrix \mathbf{A} as they are counted in a row-wise manner; the dimension of this vector is equal to the total non-zero values (nnz) of the matrix, i.e.:

$$\mathbf{a}(k) = A_{ij} \quad \text{with } k = 1, \dots, nnz$$

The vector \mathbf{ja} also has nnz dimension and contains the column indexes of the non-zeros values of the vector \mathbf{a} , i.e. if $\mathbf{a}(k) = A_{ij}$:

$$\mathbf{ja}(k) = j \quad \text{with } k = 1, \dots, nnz$$

The last vector \mathbf{ia} has dimension $n + 1$ and stores the location of the non-zero value which starts a row, i.e. if $\mathbf{a}(k) = A_{ij}$:

$$\mathbf{ia}(i) < k < \mathbf{ia}(i + 1).$$

The first and the last values of the vector \mathbf{ia} are equal to:

$$\mathbf{ia}(1) = 1, \quad \mathbf{ia}(n + 1) = nnz + 1.$$

For example for a non-symmetric matrix \mathbf{A} :

$$\mathbf{A} = \begin{bmatrix} 5 & 0 & 10 & 12 & 22 \\ 1 & 0 & 0 & 0 & 9 \\ 4 & 8 & 0 & 2 & 0 \\ 6 & 6 & 18 & 3 & 0 \end{bmatrix}$$

the CRS format is given by the following three vectors:

$$\mathbf{a} = [5, 10, 12, 22, 1, 9, 4, 8, 2, 6, 6, 18, 3]$$

$$\mathbf{ja} = [1, 3, 4, 5, 1, 5, 1, 2, 4, 1, 2, 3, 4]$$

$$\mathbf{ia} = [1, 5, 7, 10, 14]$$

Appendix C

New user subroutine for nonlinear model order reduction in Abaqus

The present appendix gives the input file and the in-house user subroutines, written in Fortran language, for the nonlinear numerical example of a 2D square presented in Sec. 6.2.1. The following code is used to develop the nonlinear model order reduction technique inside the software Abaqus; in particular the following subroutines will be presented:

- UEL: defines the user-defined element;
- URDFIL: computes the nonlinear (tangent) thermal matrices and reduce the global system;
- GSPT: defines the coordinates of the Gauss points;
- GSWT: defines the weights of Gauss points;
- DER: defines the shape functions and the shape function gradients;
- UCAP: defines the temperature dependent specific heat;
- UCOND: defines the temperature dependent thermal conductivity;
- QSORTI and ORDINA: sort an array in ascending order;
- AMUB: performs the matrix product $C=A*B$ in CSR format;
- AMUX: multiplies a CSR matrix times a vector.

Most of the code is written by the author, while some subroutines, i.e. AMUX, AMUB, QSORTI, are taken from some libraries [111] to improve and speed up the code.

C.1 Input file

```
*HEADING:TRANSIENT HEAT TRANSFER ANALYSIS
TEMPERATURE DEPENDENT THERMAL CONDUCTIVITY
COMPARISON OF DC2D4 ELEMENTS AND 4 NODED UEL ELEMENTS
*****
```

```

*****  DC2D4 ELEMENT DEFINITION
*****
**
** PARTS
**
*Part , name=Part-1
*Node
  1, 0., 0.
  2, 0.009999999978, 0.
  ....
  ....
  ....
  10201, 1., 1.
*Nset , nset=Set-15, generate
  1, 10201, 1
*****  UEL ELEMENT DEFINITION
*USER ELEMENT,NODES=4,TYPE=U1,PROP=4,COORDINATES=2,VAR=1
  11,
*ELEMENT,TYPE=U1,ELSET=UEL
  10001, 1, 2, 3, 4
*UEL PROPERTY,ELSET=UEL
  1.,1800.,0.1,11.
*End Part
**
** ASSEMBLY
**
*Assembly , name=Assembly
**
*Instance , name=Part-1-1, part=Part-1
*End Instance
**
*Nset , nset=Set-15, instance=Part-1-1, generate
  1, 10201, 1
*Nset , nset=Set-1, instance=Part-1-1, generate
  1, 4, 1
*Nset , nset=Set-2, instance=Part-1-1, generate
  1, 4, 1
*Elset , elset=Set-2, instance=Part-1-1
  10001
*Elset , elset=Set-4, instance=Part-1-1
  10001
*End Assembly
**
**
*MATERIAL,NAME=ALUM
*CONDUCTIVITY
  11,
*DENSITY
  1800,

```

```

*SPECIFIC HEAT
0.1 ,
*****
*****
*INITIAL CONDITIONS,TYPE=TEMP
Set -2,0
*Step , name=Step -1, nlgeom=NO, inc=10000
*Heat Transfer , end=PERIOD
0.5 , 25 , , ,
**NODE PRINT,FREQ=1
**NT,
*OUTPUT, FIELD ,FREQ=1
*NODE OUTPUT
NT,
**
**
*ELEMENT MATRIX OUTPUT, ELSET=Set -2, FREQUENCY=1, STIFFNESS=YES,
OUTPUT FILE=RESULTS FILE
**
**
*NODE FILE , NSET=Set -2,FREQUENCY=1
NT
**
**
**NODE PRINT, NSET=Set -2,FREQUENCY=1
**NT
*END STEP

```

C.2 User subroutines

```

c*****SUBROUTINE UEL*****
C      Input:  KR=reduced tangent stiffness matrix
C              MATRIX=reduced tangent capacity matrix
C              F=reduced force vector
C      Output: RHS=residual vector
C              AMATRX=Jacobian matrix
SUBROUTINE UEL(RHS,AMATRX,SVARS,ENERGY,NDOFEL,NRHS,NSVARS,PROPS,
NPROPS,COORDS,MCRD,NNODE,U,DU,V,A,JTYPE,TIME,DTIME,
KSTEP,KINC,JELEM,PARAMS,NDLOAD,JDLTYP,
ADLMAG,PREDEF,NPREDF,LFLAGS,MLVARX,DDL MAG,
MDLOAD,PNEWDT,JPROPS,NJPROP,PERIOD)

INCLUDE 'aba_param.inc'
INCLUDE 'common.txt'  ! input parameter size

DIMENSION RHS(MLVARX,*),AMATRX(NDOFEL,NDOFEL),SVARS(NSVARS),
ENERGY(8),PROPS(*),COORDS(MCRD,NNODE),U(NDOFEL),
DU(MLVARX,*),V(NDOFEL),A(NDOFEL),TIME(2),PARAMS(*),
JDLTYP(MDLOAD,*),ADLMAG(MDLOAD,*),DDL MAG(MDLOAD,*),
PREDEF(2,NPREDF,NNODE), LFLAGS(*),JPROPS(*)

```

```

REAL*8 KR(NDOFEL,NDOFEL) , CT(NDOFEL) , KT(NDOFEL) , F(NDOFEL)
REAL*8 CGL(NDOFEL,NDOFEL) ,KGLR(RED,RED) ,CGLR(RED,RED) ,
FR(RED) ,FGLR(RED)
PARAMETER (ZERO=0.D0, ONE=1.D0)
PARAMETER (NDIM=2, NDOF=1)

COMMON/CMN/KGLR,CGLR,FGLR
C reduced thermal matrices at initial state
OPEN(UNIT=1, FILE='/home/Temp/K0.txt ') !reduced stiffness matrix
OPEN(UNIT=2, FILE='/home/Temp/C0.txt ') !reduced capacity matrix
OPEN(UNIT=3, FILE='/home/Temp/F0.txt ') !reduced force vector

C Initialize thermal matrices
DO I=1,NDOFEL
  F(I) =ZERO
  DO J=1,NDOFEL
    KR(I,J) = ZERO
    MATRIX(I,J)=ZERO
  END DO
END DO

C Initialize residual vector and Jacobian matrix
DO K1=1,NDOFEL
  RHS(K1,NRHS)=ZERO
  DO K2=1,NDOFEL
    AMATRIX(K2,K1)=ZERO
  END DO
END DO

C Increment equal to 1
IF (KINC.LE.1) THEN
  DO I=1,NDOFEL
    READ(1,*) KR(I,:)
    READ(2,*) MATRIX(I,:)
  END DO
  READ(3,*) (F(I),I=1,NDOFEL)
C Increment greater than 1
ELSEIF (KINC.GT.1) THEN
  DO I=1,NDOFEL
    F(I) =FGLR(I)
    DO J=1,NDOFEL
      KR(I,J) = KGLR(I,J)
      MATRIX(I,J)=CGLR(I,J)
    END DO
  END DO

END IF

CLOSE(1)
CLOSE(2)
CLOSE(3)

```

```

C   Transient analysis
      IF (LFLAGS(1).EQ.32.OR.LFLAGS(1).EQ.33) THEN
C   Update residual vector
      DO I=1,NDOFEL
      DO J=1,NDOFEL
      RHS(I,1)=-(MATRIX(I,J)*(U(J)-(U(J)-DU(J,1)))/DTIME+
      KR(I,J)*U(J))+RHS(I,1)
      END DO
      END DO

      DO I=1,NDOFEL
      RHS(I,1) = RHS(I,1)+F(I)
      END DO
C   Update Jacobian matrix
      DO K1=1, NDOFEL
      DO K2=1, NDOFEL
      AMATRIX(K1,K2) =KR(K1,K2) + MATRIX(K1,K2)/DTIME
      END DO
      END DO

      ELSE

      WRITE(*,*) 'Abaqus does not have the right procedure'
      WRITE(*,*) 'go back and check the procedure type'
      WRITE(*,*) 'lflags(1)=',lflags(1)
      CALL xit

      END IF

      RETURN
      END

c*****SUBROUTINE URDFIL*****
C      Input:  ELEMENTS.TXT=connectivity matrix (N1,N2,N3,N4)
C              NODES.TXT=nodes (N, x, y)
C              Q.TXT=projection matrix (from Matlab)
C              NODCODE.TXT=boundary information list:
C      nodcode(i) = 0 —> node i is internal
C      nodcode(i) = 1 —> node i is a boundary but not a corner point
C      nodcode(i) = 2 —> node i is a corner point (corner points)
C      B,IB,JB = Q in CSR sparse format (from Matlab)
C      BT,IBT,JBT = transpose of Q in CRS format (from Matlab)
C      OUTPUT: KGLR=reduced tangent stiffness matrix
C              CGLR=reduced tangent capacity matrix
C              FGLR=reduced force vector
C      TEMP.TXT=reduce coordinate vector
C      TEMPERATURE_SOL.TXT=solution of temperature at nodes

SUBROUTINE URDFIL(LSTOP,LOVRWRT,KSTEP,KINC,DTIME,TIME)
INCLUDE 'aba_param.inc'
INCLUDE 'common.txt' ! input parameter size

```

```

C A,IA,JA = KGL in CRS sparse format
C CG,ICG,JCG = CGL_LUMPED in CRS sparse format
C B,IB,JB = Q in CRS sparse format (from Matlab)
C BT,IBT,JBT = QT in CRS sparse format (from Matlab)
C C,IC,JC = KGL*Q
C G,IG,JG = QT*KGL*Q
C H,IH,JH = CGL_LUMPED*Q
C O,IO,JO = QT*CGL_LUMPED*Q
DIMENSION ARRAY(513),JRRAY(NPRECD,513),TIME(2),KO(1,4)

REAL*8KEL(4,4),CEL(4,4),UU(RED2),M(4),COORD(NO3),COORDI(2,4),
GPX(4),GPY(4),PHI(4),PHIX(4),PHIY(4),PHIC(4),PHIE(4),GWEI(4),
GWE(2),Q(NO,RED),QT(RED,NO),QKGL(RED,NO),QCGL(RED,NO),
TEMP(NO),FF(4),IFACE(6),KGLR(RED,RED),CGLR(RED,RED),FR(RED),
A(NNZ),ASORTED(NNZ),B(NNZ2),CSORTED(NZMAX),C(NZMAX),
BT(NNZ2),G(NZMAX2),FGL(NO),CG(NO),H(NZMAX),O(NZMAX2),
FGLR(RED),TEMPP(RED)

INTEGER IA(N1),W(NO),NODCODE(NO),IWK(NO),JWK(NO),JA(NNZ),
JASORTED(NNZ),START,STOPP,SIZEA,N,JB(NNZ2),IB(N1),JC(NZMAX),
IC(N1),JCSORTED(NZMAX),IW(RED),IERR,JBT(NNZ2),IBT(RED1),
JG(NZMAX2),IG(RED1),POT(SIZEMAX),ORD(SIZEMAX)

INTEGER ICG(N1),JCG(NO),JH(NZMAX),IH(N1),IO(RED1),JO(NZMAX2)

c NO: number of nodes , NL: number of elements ,RED: reduced order

EQUIVALENCE (ARRAY(1),JRRAY(1,1))
PARAMETER(TOL=2.09D8,THICK=1,RHO=1800,
CP=0.1,CONDUCT=0.D0,ZERO=0.d0,TOLL = 1E-04,DT=0.5,T0=0)

DATA IFACE/1,2,3,4,1,4/

COMMON/CMN/KGLR,CGLR,FGLR
N=NO

OPEN(UNIT=1, FILE='/home/Temp/elements.txt ')
OPEN(UNIT=3, FILE='/home/Temp/nodes.txt ')
OPEN(UNIT=5, FILE='/home/Temp/Q.txt ')
OPEN(UNIT=6, FILE='/home/Temp/nodcode.txt ')

OPEN(UNIT=10, FILE='/home/Temp/jb2.txt ')
OPEN(UNIT=11, FILE='/home/Temp/ib2.txt ')
OPEN(UNIT=12, FILE='/home/Temp/b2.txt ')

OPEN(UNIT=13, FILE='/home/Temp/jbT2.txt ')
OPEN(UNIT=14, FILE='/home/Temp/ibT2.txt ')
OPEN(UNIT=15, FILE='/home/Temp/bT2.txt ')

```

```
OPEN(UNIT=20,file = '/home/Temp/temperature_sol.txt',status='UNKNOWN',
  action='write',form='formatted',position="append")
```

```
READ(6,*) nodcode
READ(10,*) jb
READ(11,*) ib
READ(12,*) b
READ(13,*) jbT
READ(14,*) ibT
READ(15,*) bT
```

```
CLOSE(6)
CLOSE(10)
CLOSE(11)
CLOSE(12)
CLOSE(13)
CLOSE(14)
CLOSE(15)
```

```
C boundary heat flux
IF (TIME(2).LE.10)THEN
TD = 240*(TIME(2)+DT)
ELSE IF (TIME(2).GT.10.AND.TIME(2).LE.20)THEN
TD = -240*(TIME(2)+DT) + 4800
ELSEIF (TIME(2).GT.20)THEN
TD = 0.D0
END IF
```

```
C Initialize global stiffness matrix in CRS format
```

```
IA(1)=1
DO 5 I=1,NO
  IF (NODCODE(I).EQ.0)THEN
    W(I)=9
  ELSEIF (NODCODE(I).EQ.1)THEN
    W(I)=6
  ELSEIF (NODCODE(I).EQ.2)THEN
    W(I)=4
  END IF
5 CONTINUE

DO 6 I=2,NO+1
  IA(I) = IA(I-1) + W(I-1)
6 CONTINUE

DO 14 I=1,NO
  IWK(I)=IA(I)-1
  JWK(I)=0
14 CONTINUE
```



```

      DO 15 I=1,NNZ
      A(I)=0.D0
      JA(I)=0
15  CONTINUE
C Initialize global capacity matrix in CRS format
      ICG(1)=1
      ICG(N1)= NO+1

      DO 88 I=2,NO
      ICG(I)=ICG(I-1)+1
88  CONTINUE

      DO 89 I=1,NO
      CG(I)=0.D0
      JCG(I)=0
89  CONTINUE
C      read projection matrix
      DO I=1,RED
      READ(5,*) Q(:,I)
      END DO
      CLOSE(5)
C      initialize reduced thermal matrices
      DO I=1,RED
      FGLR(I) = ZERO
      DO J=1,RED
      KGLR(I,J)=ZERO
      CGLR(I,J)=ZERO
      END DO
      END DO
C initialize nodal temperature
      DO I=1,NO
      TEMP(I) = ZERO+T0
      END DO
C start reading result file
      CALL POSFIL(KSTEP,KINC,ARRAY,JRCD)
C initialize global force vector
      DO I =1,NO
      FGL(I) = 0.D0
      END DO

      CONTA=0
      DO K1=1,999999
      CALL DBFILE(0,ARRAY,JRCD)
      IF (JRCD .NE. 0) GO TO 110
      KEY=JRRAY(1,2)
C read values in the reduced coordinate vector
      IF (KEY.EQ.201) THEN

```

```

      NN= JRRAY(1,3)    ! NODE NUMBER
      U = ARRAY(4)      ! NODAL VALUE
      CONTA = CONTA+1
      TEMPP(CONTA) = U

      ELSEIF (KEY.EQ.1001) THEN
C read global node coordinates
      REWIND 3
      DO I=1,NO
      READ(3,*) COORD(I,:)
      END DO
C update global temperature
      DO I=1,NO
      DO J=1,RED
      TEMP(I) = TEMP(I)+Q(I,J)*TEMPP(J)
      END DO
C write nodal temperature
      WRITE(20,*) KINC, I,TEMP(I) SOLUTION
      END DO
C loop over the elements
      REWIND 1
      DO LL = 1,NL
C connectivity matrix
      DO I = 1,4
      KO(1,I) = ZERO
      END DO
      READ(1,*) KO(1,:)
C initialize element matrices
      DO I=1,4
      FF(I)=ZERO
      DO J=1,4
      KEL(I,J)=ZERO
      CEL(I,J)=ZERO
      END DO
      END DO
C temperature at nodes of the element
      DO I = 1,4
      P = KO(1,I)
      M(I) = TEMP(P)
      END DO
C coordinates of nodes of element
      DO J=1,4
      WW = KO(1,J)
      COORDI(1,J) = COORD(WW,2)    !coord x
      COORDI(2,J) = COORD(WW,3)    !coord y
      END DO
C determine Gauss points
      CALL GSPT(GPX,GPY)

```

```

C  determine Gauss weights
      CALL GSWT(GWEI,GWE)
      DO 300 K=1,4
C  loop through Gauss points
      C=GPX(K)
      E=GPY(K)
      CALL DER(C,E,GPX,GPY,GWEI,PHI,PHIC,PHIE,DXDC,DXDE,
      DYDC,DYDE,JEL,COORDI,AJACOB,PHIX,PHIY)
      T=ZERO
      DO I=1,4
      T=M(I)*PHI(I)+T
      END DO
C  check dependence thermal conductivity on temperature
      IF (CONDUCT.NE.0.d0) THEN
      COND=CONDUCT
      ELSE
      CALL UCOND(T,COND)
      END IF
C  check dependence specific heat on temperature
      IF (CP.NE.0.d0) THEN
      SPEC=CP
      ELSE
      CALL UCAP(T,SPEC)
      END IF
C  update element matrices
      WE=GWEI(K)*AJACOB
      DO KI=1,4
      DO KJ=1,4
      KEL(KI,KJ)=KEL(KI,KJ)+
      THICK*WE*COND*(PHIX(KI)*PHIX(KJ) + PHIY(KI)*PHIY(KJ))

      CEL(KI,KJ)=CEL(KI,KJ)+
      THICK*WE*PHI(KI)*PHI(KJ)*RHO*SPEC
      END DO
      END DO
300    CONTINUE
C  apply Neumann boundary condition
      IF (COORDI(2,3).EQ.1) THEN ! if coord y=1
      E=1.
      DO KI=3,4
C  loop through Gauss points
      C=GPX(KI)
      CALL DER(C,E,GPX,GPY,GWEI,PHI,PHIC,PHIE,DXDC,DXDE,
      DYDC,DYDE,JEL,COORDI,
1    AJACOB,PHIX,PHIY)
      DS=SQRT(DXDE*DXDE + DYDE*DYDE)
      DO KJ=3,4
      FF(IFACE(KJ))= FF(IFACE(KJ))+GWEI(KI)*DS*PHI(IFACE(KJ))*TD

```

```

        END DO
        END DO
        END IF
C calculate global matrices
        DO 120 KA=1,4
            II = KO(1,ka)
            IF (FF(KA).GT.TOLL)THEN
                FGL(ii) = FGL(II) + FF(KA)
            END IF
            IROWST = IA(II)
            IROWST2 = ICG(II)
            ILAST = IWK(II)
            DO 109 K=IROWST,ILAST
                JWK(JA(K)) = K
109          CONTINUE
            DO 108 KB=1,4
                JJ = KO(1,KB)
                K = JWK(JJ)
                IF (CEL(KA,KB).GT.TOLL)THEN
                    JCG(IROWST2)=II
                    CG(IROWST2)=CG(IROWST2)+CEL(KA,KB)
                END IF
                IF (K.EQ.0) THEN
                    ILAST=ILAST+1
                    JWK(JJ) = ILAST
                    JA(ILAST) = JJ
                    A(ILAST) = KEL(KA,KB)
                ELSE
                    A(K) = A(K) + KEL(KA,KB)
                END IF
108          CONTINUE
C refresh JWK
            DO 119 K=IROWST,ILAST
                JWK(JA(K)) = 0
119          CONTINUE
            IWK(II) = ILAST
120          CONTINUE
        END DO !CLOSE LOOP OVER THE ELEMENTS
C calculate reduced force vector
        CALL AMUX(RED, FGL, FGLR, bT,jbT,ibT,NO,NNZ2,RED,RED1)
C sort JA,A
        DO 19 L=1,NNZ
            JASORTED(L)= 0
            ASORTED(L)=0
19          CONTINUE
        DO 11 K=1,NO
            START=IA(K)
            STOPP=IA(K+1)

```

```

      SIZEA=STOPP-START
      DO KK=1,SIZEMAX
      POT(KK)=0
      ORD(KK)=0
      END DO
      IF (SIZEA.GT.SIZEMAX) STOP 'too large passed array '
      CALL ORDINA(JASORTED,ASORTED,JA,IA,A,POT,SIZEA,NX,
      NNZ,N1,START,ORD,STOPP)
11      CONTINUE
C   calculate K_GL*Q
      IERR = 0
      CALL AMUB(NO,NO,1,ASORTED,JASORTED,IA,B,JB,IB,C,JC,IC,NZMAX,
      IW,IERR,NNZ,NNZ2)

C   calculate CGL_LUMPED*Q
      CALL AMUB(NO,NO,1,CG,JCG,ICG,B,JB,IB,H,JH,IH,NZMAX,
      IW,IERR,NO,NNZ2)

C   calculate Q'*K_GL*Q
      CALL AMUB(RED,NO,1,BT,JBT,IBT,C,JC,IC,G,JG,IG,NZMAX2,IW,I
      ERR,NNZ2,NNZ2)

C   calculate Q'*CGL_LUMPED*Q
      CALL AMUB(RED,NO,1,BT,JBT,IBT,H,JH,IH,O,JO,IO,NZMAX2,IW,
      IERR,NNZ2,NNZ2)

      DO I=1,RED
      KK =(IG(I+1)-IG(I))
      KK2 =(IO(I+1)-IO(I))
      DO J=1,KK
      KGLR(I,J)=KGLR(I,J)+G(J+KK*(I-1))
      END DO
      DO J=1,KK2
      CGLR(I,J)=CGLR(I,J)+O(J+KK2*(I-1))
      END DO
      END DO
END IF

      END DO
110      CONTINUE
      CLOSE(1)
      CLOSE(2)
      CLOSE(3)
      CLOSE(20)
      RETURN
      END

c*****SUBROUTINE GSPT*****
SUBROUTINE GSPT(GPX,GPY)
INCLUDE 'aba_param.inc'

```

```

DIMENSION AR(2),GPX(4),GPY(4)
      PARAMETER(ZERO=0.D0,ONENEG=-1.D0,ONE=1.D0,THREE=3.D0,TEN=10.D0)
C C      GPX: x coordinate of Gauss pt
C C      GPY: y coordinate of Gauss pt
      R=SQRT(ONE/THREE)
      AR(1)=ONENEG
      AR(2)=ONE
      GPX(1)=AR(1)*R
      GPX(2)=AR(2)*R
      GPX(3)=AR(2)*R
      GPX(4)=AR(1)*R
      GPY(1)=AR(1)*R
      GPY(2)=AR(1)*R
      GPY(3)=AR(2)*R
      GPY(4)=AR(2)*R
10      CONTINUE
      RETURN
      END

c*****SUBROUTINE GSWT*****
SUBROUTINE GSWT(GWEI,GWE)
INCLUDE 'aba_param.inc'
DIMENSION GWEI(4), GWE(2)
PARAMETER(FIVE=5.D0,EIGHT=8.D0,NINE=9.D0)
C C      GWEI : Gauss weight
      GWE(1)=1
      GWE(2)=1
      DO 10 I=1,2
      DO 10 J=1,2
      NUMGP=(I-1)*2+J
      GWEI(NUMGP)=GWE(I)*GWE(J)
10      CONTINUE
      RETURN
      END

c*****SUBROUTINE DER*****
SUBROUTINE DER(C,E,GPX,GPY,GWEI,PHI,PHIC,PHIE,DXDC,DXDE,
DYDC,DYDE,JEL,COORDI,AJACOB,PHIX,PHIY)
INCLUDE 'aba_param.inc'

REAL*8 COORDI(2,4), PHI(4),PHIX(4),PHIY(4),PHIC(4),PHIE(4)

PARAMETER(ZERO=0.D0,FOURTH=0.25D0,HALF=0.5D0,ONE=1.D0,
TWO=2.D0)
C      interpolation functions
      PHI(1) = FOURTH*(ONE-C)*(ONE-E)
      PHI(2) = FOURTH*(ONE+C)*(ONE-E)
      PHI(3) = FOURTH*(ONE+C)*(ONE+E)
      PHI(4) = FOURTH*(ONE-C)*(ONE+E)
C C      derivates wrt to C

```

```

      PHIC(1) = -FOURTH*(ONE-E)
      PHIC(2) = FOURTH*(ONE-E)
      PHIC(3) = FOURTH*(ONE+E)
      PHIC(4) = -FOURTH*(ONE+E)
C C   derivates wrt to E
      PHIE(1) = -FOURTH*(ONE-C)
      PHIE(2) = -FOURTH*(ONE+C)
      PHIE(3) = FOURTH*(ONE+C)
      PHIE(4) = FOURTH*(ONE-C)
C
      DXDC=ZERO
      DXDE=ZERO
      DYDC=ZERO
      DYDE=ZERO
C
      DO 3 I=1,4
      DXDC=DXDC+COORDI(1,I)*PHIC(I)
      DXDE=DXDE+COORDI(1,I)*PHIE(I)
      DYDC=DYDC+COORDI(2,I)*PHIC(I)
      DYDE=DYDE+COORDI(2,I)*PHIE(I)
3   CONTINUE
C calculation of jacobian
      AJACOB=(DXDC*DYDE-DXDE*DYDC)
C derivates wrt to x and y
      DO 5 I=1,4
      PHIX(I)=(PHIC(I)*DYDE-PHIE(I)*DYDC)/AJACOB
      PHIY(I)=(PHIE(I)*DXDC-PHIC(I)*DXDE)/AJACOB
5   CONTINUE
      RETURN
      END
c*****SUBROUTINE UCAP*****
SUBROUTINE UCAP(T,P)
  INCLUDE 'aba_param.inc'
  DIMENSION TABLE(2,5)
C
  PARAMETER(ZERO=0.D0)
  DATA TABLE/0.1,10.D0,0.5,20.D0,0.7,50.D0,1,100.D0,1.5,200.D0/
C
C   TABLE(1,N): specific heat (N DATA PAIRS)
C   TABLE(2,N): temperature (N DATA PAIRS)
C
  INC=0

  IF (T.LT.TABLE(2,1)) THEN
    P=TABLE(1,1)
    DPDT=ZERO
    RETURN
  END IF

```

```

IF (T.GT.TABLE(2,5)) THEN
P=TABLE(1,5)
DPDT=ZERO
RETURN
END IF

DO 10 K1=1,4
    TL1=TABLE(2,K1+1)
    IF (T.LT.TL1.AND.INC.EQ.0) THEN
    TL0=TABLE(2,K1)
    DT=TL1-TL0
    P0=TABLE(1,K1)
    P1=TABLE(1,K1+1)
    DP=P1-P0
    DPDT=DP/DT
    P=DPDT*(T-TL0)+P0
    INC=1
    ENDIF
10 CONTINUE
RETURN
END

c*****SUBROUTINE UCOND*****
SUBROUTINE UCOND(T,C)
INCLUDE 'aba_param.inc'
DIMENSION TABLE(2,5)
C
PARAMETER(ZERO=0.D0)
DATA TABLE/11.D0,10.D0,25.D0,20.D0,40.D0,50.D0,60.D0,100.D0,
100.D0,200.D0/
C
C    TABLE(1,N): conductivity (N DATA PAIRS)
C    TABLE(2,N): temperature (N DATA PAIRS)
C
INC=0

IF (T.LT.TABLE(2,1)) THEN
C=TABLE(1,1)
DCDT=ZERO
RETURN
END IF

IF (T.GT.TABLE(2,5)) THEN
C=TABLE(1,5)
DCDT=ZERO
RETURN
END IF
DO 10 K1=1,4

```



```

TL1=TABLE(2,K1+1)
IF (T.LT.TL1.AND.INC.EQ.0) THEN
TL0=TABLE(2,K1)
  DT=TL1-TL0
C0=TABLE(1,K1)
  C1=TABLE(1,K1+1)
  DC=C1-C0
  DCDT=DC/DT
  C=DCDT*(T-TL0)+C0
  INC=1
ENDIF
10 CONTINUE
  RETURN
END

```

```

c*****SUBROUTINE QSORTI*****

```

```

SUBROUTINE QSORTI (ORD,N,A)

```

```

C=====SORTS THE ARRAY A(I), I=1,2,...,N BY PUTTING THE
C  ASCENDING ORDER VECTOR IN ORD.  THAT IS ASCENDING ORDERED A
C  IS A(ORD(I)), I=1,2,...,N; DESCENDING ORDER A IS A(ORD(N-I+1)),
C  I=1,2,...,N.  THIS SORT RUNS IN TIME PROPORTIONAL TO N LOG N.
C
C

```

```

C  ACM QUICKSORT - ALGORITHM #402 - IMPLEMENTED IN FORTRAN 66 BY
C  WILLIAM H. VERITY, WHV@PSUVM.PSU.EDU
C  CENTER FOR ACADEMIC COMPUTING
C  THE PENNSYLVANIA STATE UNIVERSITY
C  UNIVERSITY PARK, PA. 16802
C

```

```

  IMPLICIT INTEGER (A-Z)

```

```

C
  DIMENSION ORD(N),POPLST(2,20)
  INTEGER X,XX,Z,ZZ,Y

```

```

  INTEGER A(N),SORTED(N)

```

```

C
  NDEEP=0
  U1=N
  L1=1
  DO 1 I=1,N
1 ORD(I)=I
2 IF (U1.LE.L1) RETURN
C
3 L=L1
  U=U1
C
C PART
C
4 P=L

```

```

Q=U

X=A(ORD(P))
Z=A(ORD(Q))
IF (X.LE.Z) GO TO 5
Y=X
X=Z
Z=Y
YP=ORD(P)
ORD(P)=ORD(Q)
ORD(Q)=YP
5 IF (U-L.LE.1) GO TO 15
XX=X
IX=P
ZZ=Z
IZ=Q
C
C LEFT
C
6 P=P+1
  IF (P.GE.Q) GO TO 7
  X=A(ORD(P))
  IF (X.GE.XX) GO TO 8
  GO TO 6
7 P=Q-1
  GO TO 13
C
C RIGHT
C
8 Q=Q-1
  IF (Q.LE.P) GO TO 9
  Z=A(ORD(Q))
  IF (Z.LE.ZZ) GO TO 10
  GO TO 8
9 Q=P
  P=P-1
  Z=X
  X=A(ORD(P))
C
C DIST
C
10 IF (X.LE.Z) GO TO 11
  Y=X
  X=Z
  Z=Y
  IP=ORD(P)
  ORD(P)=ORD(Q)
  ORD(Q)=IP

```

```

11 IF (X.LE.XX) GO TO 12
   XX=X
   IX=P
12 IF (Z.GE.ZZ) GO TO 6
   ZZ=Z
   IZ=Q
   GO TO 6
C
C OUT
C
13 CONTINUE
   IF (.NOT.(P.NE.IX.AND.X.NE.XX)) GO TO 14
   IP=ORD(P)
   ORD(P)=ORD(IX)
   ORD(IX)=IP
14 CONTINUE
   IF (.NOT.(Q.NE.IZ.AND.Z.NE.ZZ)) GO TO 15
   IQ=ORD(Q)
   ORD(Q)=ORD(IZ)
   ORD(IZ)=IQ
15 CONTINUE
   IF (U-Q.LE.P-L) GO TO 16
   L1=L
   U1=P-1
   L=Q+1
   GO TO 17
16 U1=U
   L1=Q+1
   U=P-1
17 CONTINUE

   IF (U1.LE.L1) GO TO 18
C
C start recursive call
C
   NDEEP=NDEEP+1
   POPLST(1,NDEEP)=U
   POPLST(2,NDEEP)=L
   GO TO 3
18 IF (U.GT.L) GO TO 4
C
C pop back up in the recursion list
C
   IF (NDEEP.EQ.0) GO TO 2
   U=POPLST(1,NDEEP)
   L=POPLST(2,NDEEP)
   NDEEP=NDEEP-1
   GO TO 18

```

```

C
C END SORT
C END QSORT
END
c*****SUBROUTINE AMUB*****
SUBROUTINE AMUB(NROW,NCOL,JOB,A,JA,IA,B,JB,IB,C,JC,IC,
NZMAX,IW,IERR,NNZ,NNZ2)
C*****
DOUBLE PRECISION A(NNZ), B(NNZ2), C(NZMAX)
INTEGER JA(NNZ),JB(NNZ2),JC(NZMAX),IA(NROW+1),IB(NCOL+1),IC(NCOL+1),
1 IW(NCOL),NROW,NCOL,JOB,NZMAX,IERR
DOUBLE PRECISION SCAL
LOGICAL VALUES
VALUES = (JOB.NE.0)
LEN = 0
IC(1) = 1
IERR = 0
C Initialize array iw.
C
      do 15 J=1,NCOL
        IW(J) = 0
15      continue

      DO 500 II=1,NROW
C      row i
        DO 200 KA=IA(II),IA(II+1)-1
          IF (VALUES) SCAL=A(KA)
          JJ = JA(KA)
          DO 100 KB=IB(JJ),IB(JJ+1)-1
            JCOL = JB(KB)
            JPOS = IW(JCOL)
            IF (JPOS .EQ. 0) THEN
              LEN = LEN+1
              IF (LEN.GT.NZMAX) THEN
                IERR=II
                RETURN
              END IF
              JC(LEN) = JCOL
              IW(JCOL)= LEN
              IF (VALUES) C(LEN) = SCAL*B(KB)
            ELSE
              IF (VALUES) C(JPOS) = C(JPOS) + SCAL*B(KB)
            END IF
          100      CONTINUE
        200      CONTINUE
        DO 201 K=IC(II),LEN
          IW(JC(K)) = 0
        201      CONTINUE

```

```

      IC(II+1) = LEN+1
500    CONTINUE

```

```

      RETURN
      END

```

```

c *****SUBROUTINE ORDINA*****
SUBROUTINE ORDINA(JASORTED,ASORTED,JA,IA,A,POT,S,NX,
NNZ,N1,START,ORD,STOPP)
DOUBLE PRECISION A(NNZ),ASORTED(NNZ)
INTEGER S,NX,JA(NNZ),JASORTED(NNZ),IA(N1),N1,NNZ,START,STOPP
INTEGER POT(S),ORD(S)

```

```

      DO 12 L=1,S
      POT(L)=JA(START+L-1)
12     CONTINUE
C     SORT NUMBERS
      CALL QSORTI (ORD,S,POT)
      CONT = 0
      DO 13 U=START,STOPP-1
      CONT=CONT+1
      JASORTED(U)=POT(ORD(CONT))
      ASORTED(U)=A(START-1+ORD(CONT))
13     CONTINUE

```

```

      RETURN
      END

```

```

c *****SUBROUTINE AMUX*****
SUBROUTINE AMUX(N,X,Y,A,JA,IA,NO,NNZ2,RED,RED1)
C*****
DOUBLE PRECISION X(NO),Y(N),A(NNZ2),T
INTEGER N,JA(NNZ2),IA(RED1)
INTEGER I,K

```

```

      DO 100 I=1,N
c
c      compute the inner product of row i with vector x
c
      T=0.0
      DO 99 K=IA(I),IA(I+1)-1
      T= T + A(K)*x(JA(K))
99     CONTINUE
c
c      store result in y(i)
c
      Y(I)=T
100    CONTINUE

```

RETURN
END

Bibliography

- [1] *The Mathworks Inc. Natick, MA, USA.*
- [2] *Salome-Meca version 2015.2.*
- [3] (2013). *Ansys Manual.*
- [4] Aboulkhair, N. T., N. M. Everitt, I. Ashcroft, and C. Tuck (2014). Reducing porosity in AlSi10Mg parts processed by selective laser melting. *Additive Manufacturing vol. 1-4*, pp. 77–86.
- [5] Akbari, M., D. Sinton, and M. Bahrami (2009). Moving heat sources in a half space: Effect of source geometry. In *ASME. Heat Transfer Summer Conference*, Volume 3, pp. 685–694.
- [6] Alvaro, L. G., A. Coutinho, L. Landau, L. C. Wrobel, and N. F. Ebecken (1989). Modal solution of transient heat conduction utilizing Lanczos algorithm. *International Journal for Numerical Methods in Engineering vol. 28*, pp. 13–25.
- [7] Aquino, W., J. Brigham, C. Earls, and N. Sukumar (2009). Generalized finite element method using proper orthogonal decomposition. *Numerical Methods in Engineering vol. 79, no. 7*, pp. 887–906.
- [8] Attar, E. (2011). *Simulation of Selective Electron Beam Melting Processes*. Ph. D. thesis, Universität Erlangen-Nürnberg.
- [9] Attar, H., M. Calin, L. Zhang, S. Scudino, and J. Eckert (2014). Manufacture by selective laser melting and mechanical behavior of commercially pure titanium. *Materials Science & Engineering A vol. 593*, pp. 170–177.
- [10] Ayasoufi, A. (2004). *Numerical Simulation of heat conduction with melting and/or freezing by space-time conservation element and solution element method*. Ph. D. thesis, The University of Toledo.
- [11] Badrossamay, M. and T. Childs (2007). Further studies in selective laser melting of stainless and tool steel powders. *International Journal of Machine Tools and Manufacture vol. 47, no. 5*, pp. 779–784.
- [12] Bonacina, C., G. Comini, A. Fasano, and M. Primicerio (1973). Numerical solutions of phase-change problems. *International Journal of Heat and Mass Transfer vol. 16, no. 10*, pp. 1825–1832.
- [13] Botello, O. E. L. (2016). *Simulation of Microstructural Evolution of Selective Laser Melting of Metal Powders*. Ph. D. thesis, University of Sheffield.

- [14] Brands, B., J. Mergheim, and P. Steinmann (2016). Reduced-order modelling for linear heat conduction with parametrised moving heat sources. *GAMM-Mitteilungen* vol. 39, no. 2, pp. 170–188.
- [15] Bugada, G., M. Cervera, and G. Lombera (1999). Numerical prediction of temperature and density distributions in laser sintering processes. *Rapid Prototyping Journal* vol. 5, no. 1, pp. 21–26.
- [16] Canales, D., A. Leygue, F. Chinesta, D. Gonzalez, E. Cueto, E. Feulvarch, J.-M. Bergheau, and A. Huerta (2016). Vademecum-based GFEM (V-GFEM): optimal enrichment for transient problems. *Numerical Methods in Engineering* vol. 108, no. 9, pp. 971–989.
- [17] Cao, Y. and A. Faghri (1990). A numerical analysis of phase-change problems including natural convection. *Journal of Heat Transfer* vol. 112, no.3, pp. 812–816.
- [18] Cardona, A. and S. Idelsohn (1986). Solution of non-linear thermal transient problems by a reduction method. *Internal Journal for Numerical Methods in Engineering* vol. 23, no. 6, pp. 1023–1042.
- [19] Carraturo, M. (2016). Reduced order method for selective laser melting processes using the finite cell method. Master’s thesis, Technische Universität München.
- [20] Celentano, D., E. Onate, and S. Oller (1994). A temperature-based formulation for finite element analysis of generalized phase-change problems. *Int. J. For numerical methods in Engineering* vol. 37, no. 20, pp. 3441–3465.
- [21] Chaikin, P. M. and T. C. Lubensky (2000). *Principles of Condensed Matter Physics*. Cambridge University Press.
- [22] Chan, C. and J. Mazumder (1984). A two-dimensional transient model for convection in laser melting pool. *Metallurgical Transactions A* vol. 15, no. 12, pp.1984–2175.
- [23] Chaturantabut, S. and D. C. Sorensen (2010). Nonlinear model reduction via discrete empirical interpolation. *SIAM J. Sci. Comput.* vol. 32, no. 5, pp. 2737–2764.
- [24] Chen, T. and Y. Zhang (2005). Thermal modeling of metal powder-based selective laser sintering. In *Solid Freeform Fabrication Symposium*.
- [25] Chen, T. and Y. Zhang (2006). Three-dimensional modeling of selective laser sintering of two-component metal powder layers. *Journal of Manufacturing Science and Engineering* vol. 128, no. 1, pp. 299–306.
- [26] Chen, T. and Y. Zhang (2007). Three-dimensional modeling of laser sintering of a two-component metal powder layer on top of sintered layers. *Journal of Manufacturing Science and Engineering* vol. 129, no. 3, pp. 575–582.
- [27] Childs, T. H. C., C. Hauser, and M. Badrossamay (2005). Selective laser sintering (melting) of stainless and tool steel powders: experiments and modelling. *Proceedings of the Institution of Mechanical Engineers. Part B: Journal of Engineering Manufacture* vol. 129, no. 4, pp. 339–357.

- [28] Chlebus, E., B. Kuznicka, T. Kurzynowski, and B. Dybala (2011). Microstructure and mechanical behaviour of Ti-6Al-7Nb alloy produced by selective laser melting. *Materials Characterization* vol. 62, no. 5, pp. 488–495.
- [29] Cobanoglu, A. C., S. Mossner, M. Hojjat, and F. Duddeck (2016). Model order reduction methods for explicit FEM. In *2016 Science in the Age of Experience*.
- [30] Contuzzi, N., S. L. Campanelli, and A. D. Ludovico (2011). 3D finite element analysis in the selective laser melting process. *International Journal of Simulation Modelling* vol. 10, no. 3, pp. 113–121.
- [31] Craig Jr., R. R. and M. C. C. Bampton (1968). Coupling of substructures for dynamic analyses. *AIAA Journal* vol. 6, no. 7, pp. 1313–1319.
- [32] Crank, J. (1984). *Free and moving boundary problems*. Clarendon press-Oxford.
- [33] Dai, K. and L. Shaw (2005). Finite element analysis of the effect of volume shrinkage during laser densification. *Acta Materialia* vol. 53, no. 18, pp. 4743–4754.
- [34] Dai, K. and L. Shaw (2006). Parametric studies of multi-material laser densification. *Materials Science & Engineering: A* vol. 430, no. 1-2, pp. 221–229.
- [35] Darmadi, D. B. (2001). Validating the accuracy of heat source model via temperature histories and temperature field in bead-on-plate welding. *International Journal of Engineering & Technology IJET-IJENS* vol. 11, no. 5, pp. 12–20.
- [36] Dassault Systems Simulia Corp. (2014). *Abaqus Manual, version 6.14*.
- [37] Davison, E. J. (1966). A method for simplifying linear dynamic systems. *IEEE Transaction on Automated Control* vol. 11, no. 1, pp. 93–101.
- [38] de Klerk, D., D. Rixen, and S. N. Voormeeren (2008). General framework for dynamic substructuring: History, review, and classification of techniques. *AIAA journal* vol. 46, no.5(5), pp. 1169–1181.
- [39] Deng, D. (2009). FEM prediction of welding residual stress and distortion in carbon steel considering phase transformation effects. *Materials and Design* vol. 30, pp. 359–366.
- [40] Dong, L., A. Makradi, S. Ahzi, and Y. Remond (2009). Three-dimensional transient finite element analysis of the selective laser sintering process. *Journal of Materials Processing Technology* vol. 209, no. 2, pp. 700–706.
- [41] Fachinotti, V. D., A. A. Anca, and A. Cardona. (2009). Analytical solutions of the thermal field induced by moving double-ellipsoidal and double-elliptical heat sources in a semi-infinite body. *International Journal for Numerical Methods in Biomedical Engineering* vol. 27, no. 4, pp. 595, 607.
- [42] Fan, Z. and F. Liou (2012). Numerical modeling of the additive manufacturing (AM) processes of titanium alloy. *Titanium Alloys - Towards Achieving Enhanced Properties for Diversified Applications, Edited by Dr. A.K.M. Nurul Amin, ISBN 978-953-51-0354-7*.

- [43] Faure, S. P., L. Mercier, P. Didier, R. Roux, J. F. Coulon, and S. Garel (2012). Laser sintering process analysis: Application to Chromium-Cobalt alloys for dental prosthesis production. In *ASME 2012 11th Biennial Conference on Engineering Systems Design and Analysis*.
- [44] Feng, L., E. B. Rudnyi, J. G. Korvink, C. Bohm, and T. Hauck (2005). Compact electro-thermal model of semiconductor device with nonlinear convection coefficient. In *Proceedings of EuroSimE*.
- [45] Foroozmehr, A., M. Badrossamay, E. Foroozmehr, and S. Golabi (2016). Finite element simulation of selective laser melting process considering optical penetration depth of laser in powder bed. *Materials and Design* vol. 89, no. 5(89), pp. 255–263.
- [46] Fu, C. H. and Y. B. Guo (2014). Three-dimensional temperature gradient mechanism in selective laser melting of Ti-6Al-4V. *Journal of Manufacturing Science and Engineering* vol. 136, no. 6.
- [47] Gebhardt, A. (2011). *Understanding Additive Manufacturing*. Hanser Publishers.
- [48] Gibson, I., D. Rosen, and B. Stucker (2015). *Additive Manufacturing Technologies. 3D Printing, Rapid Prototyping, and Direct Digital Manufacturing. Second Edition*. Springer.
- [49] Goldak, J., A. Chakravarti, and M. Bibby (1984). A new finite element model for welding heat sources. *Transport Phenomena Metallurgical Transactions B* vol. 15, no. 2, pp. 299–305.
- [50] Gürtler, F.-J., M. Karg, K.-H. Leitz, and M. Schmidt (2013). Simulation of laser beam melting of steel powders using the three-dimensional volume of fluid method. *Physics Procedia* vol. 41, pp. 881–886.
- [51] Gusarov, A., T. Laoui, L. Froyen, and V. Titov (2003). Contact thermal conductivity of a powder bed in selective laser sintering. *International Journal of Heat and Mass Transfer* vol. 46, no. 6, pp. 1103–1109.
- [52] Gusarov, A., I. Yadroitsev, P. Bertrand, and I. Smurov (2007). Heat transfer modelling and stability analysis of selective laser melting. *Applied Surface Science* vol. 254, no. 4, pp. 975–979.
- [53] Guyan, R. J. (1965). Reduction of stiffness and mass matrices. *AIAA Journal* vol. 3, no. 2, pp. 380–380.
- [54] Hansen, N. (2004). Hall-Petch relation and boundary strengthening. *Scripta Materialia* vol. 51, no. 8, pp. 801–806.
- [55] Hodge, N. E., R. M. Ferencz, and J. M. Solberg (2014). Implementation of a thermomechanical model for the simulation of selective laser melting. *Computational Mechanics* vol. 54, no. 1, pp. 33–51.
- [56] Hu, H. and S. A. Argyropoulos (1996). Mathematical modelling of solidification and melting: a review. *Modelling and Simulation in Materials Science and Engineering* vol. 4, no. 4, pp. 371–396.

- [57] Hughes, T. J. R. (2000). *The Finite Element Method: Linear Static and Dynamic Finite Element Analysis*. Dover publications, inc.
- [58] Hurty, W. C. (1965). Dynamic analysis of structural systems using component modes. *AIAA Journal vol. 3, no. 4*, pp. 678–685.
- [59] Hussein, A., L. Hao, C. Yan, and R. Everson (2013). Finite element simulation of the temperature and stress fields in single layers built without-support in selective laser melting. *Materials and Design vol. 52*, pp. 638–647.
- [60] Idelsohn, S. R. and A. Cardona (1985). A reduction method for nonlinear structural dynamic analysis. *Computer methods in Applied Mechanics and Engineering vol. 49, no. 3*, pp. 253–279.
- [61] Jamshidinia, M., F. Kong, and R. Kovacevic (2013). Numerical modeling of heat distribution in the electron beam melting of Ti-6Al-4V. *Journal of Manufacturing Science and Engineering vol. 135, no. 6*.
- [62] Jiang, W., K. Dalgarno, and T. H. C. Childs (2002). Finite element analysis of residual stresses and deformations in direct metal SLS process. *Solid Freeform Fabrication Symposium*, pp. 340–348.
- [63] Kempen, K., L. Thijs, J. V. Humbeeck, and J.-P. Kruth (2012). Mechanical properties of AlSi10Mg produced by selective laser melting. *Physics Procedia vol. 39*, pp. 439–446.
- [64] Knol, M. F. (2016). Thermal modelling of selective laser melting: a semi-analytical approach. Master’s thesis, Delft University of Technology (TU Delft).
- [65] Kolossov, S., E. Boillat, R. Glardon, P. Fischer, and M. Locher (2004). 3D FE simulation for temperature evolution in the selective laser sintering process. *International Journal of Machine Tools and Manufacture vol. 44, no. 2-3*, pp. 117–123.
- [66] Konrad, C., Y. Zhang, and B. Xiao (2005). Analysis of melting and resolidification in a two-component metal powder bed subjected to temporal gaussian heat flux. *International Journal of Heat and Mass Transfer vol. 48, no. 19-20*, pp. 3932–3944.
- [67] Koric, S. and B. Thomas (2008). Thermo-mechanical model of steel solidification based on two elastic visco-plastic constitutive laws. *Journal of Material Processing Technology vol. 97, no. 1-3*, pp. 408–418.
- [68] Körner, C., E. Attar, and P. Heintl (2011). Mesoscopic simulation of selective beam melting processes. *Journal of Materials Processing Technology vol. 211, no. 6*, pp. 978–987.
- [69] Körner, C., A. Bauereiß, and E. Attar (2013). Fundamental consolidation mechanisms during selective beam melting of powders. *Modelling and Simulation in Materials Science and Engineering vol. 21, no. 8*, pp. 1–18.
- [70] Krishnamurthy, H. (2002). Application of Duhamel’s theorem to problems involving oscillating heat source. Master’s thesis, Louisiana State University.

- [71] Kruth, J., L. Froyen, J. V. Vaerenbergh, P. Mercelis, M. Romboutsb, and B. Lauwers (2004). Selective laser melting of iron-based powder. *Journal of Materials Processing Technology* vol. 149, no. 1-3, pp. 616–622.
- [72] Kruth, J.-P., M. Badrossamay, E.Yasa, J. Deckers, L. Thijs, and J. V. Humbeeck (2010). Part and material properties in selective laser melting of metals. In *16th International Symposium on Electromachining (ISEM XVI)*.
- [73] Kruth, J.-P., J. Deckers, E. Yasa, and R. Wauthlé (2012). Assessing and comparing influencing factors of residual stresses in selective laser melting using a novel analysis method. *Journal Engineering Manufacture* vol 226, no. 6, pp. 1–12.
- [74] Kruth, J.-P., B. Vandenbroucke, J. V. Vaerenbergh, and I. Naert (2005). Digital manufacturing of biocompatible metal frameworks for complex dental prostheses by means of SLS/SLM. *Proceedings of the VRAP*, pp. 139–145.
- [75] Kumar, K. S. (2014). Analytical modeling of temperature distribution, peak temperature, cooling rate and thermal cycles in a solid work piece welded by laser welding process. *Procedia Materials Science* vol. 6, pp. 821–834.
- [76] Lanczos, C. (1950). An iteration method for the solution of the eigenvalue problem of linear differential and integral operators. *Journal of Research of the National Bureau of Standards* vol. 45, no. 4, pp. 255–282.
- [77] Laohaprapanon, A., P. Jeamwatthanachai, M. Wongcumchang, N. Chantarapanich, S. Chantaweroad, K. Sitthiseripratip, and S. Wisutmethangoon (2012). Optimal scanning condition of selective laser melting processing with stainless steel 316L powder. *Advanced Materials Research* vol. 341-342, pp. 816–820.
- [78] Laoui, T., E. Santos, K. Osakada, M. Shiomi, M. Morita, S. Shaik, N. Tolochko, F. Abe, and M. Takahashi (2006). Properties of titanium dental implant models made by laser processing. *Journal of Mechanical Engineering Science* vol. 220, no. 6, pp. 857–863.
- [79] Li, C., C. Fu, Y. Guo, and F. Fang (2015). Fast prediction and validation of part distortion in selective laser melting. *Procedia Manufacturing* vol. 1, pp. 355–365.
- [80] Li, C., J. Liu, Y. Guo, and Z. Y. Li (2015). A temperature-thread multiscale modeling approach for efficient prediction of part distortion by selective laser melting. In *The 26th Annual International Solid Freeform Fabrication Symposium, At Austin, TX*.
- [81] Li, J., L. Li, and F. H. Stott (2004). Thermal stresses and their implication on cracking during laser melting of ceramic materials. *Acta Materialia* vol. 52, no. 14, pp. 4385–4398.
- [82] Liu, H. (2014). Numerical analysis of thermal stress and deformation in multi-layer laser metal deposition process. Master’s thesis, Missouri University of Science and Technology.

- [83] Liu, H., T. E. Sparks, and F. W. Liou (2013). Numerical analysis of thermal stress and deformation in multi-layer laser metal deposition processes. In *Solid Freeform Fabrication Symposium*, pp. pp. 577–591.
- [84] Liu, Z., Z.-X. Qin, F. Liu, X. Lua, and H.-M. Wang (2014). The microstructure and mechanical behaviors of the Ti-6.5Al-3.5Mo-1.5Zr-0.3Si alloy produced by laser melting deposition. *Materials Characterization vol. 97*, pp. 132–139.
- [85] Loh, L.-E., C.-K. Chua, W.-Y. Yeong, J. Song, M. Mapar, S.-L. Sing, Z.-H. Liu, and D.-Q. Zhang (2015). Numerical investigation and an effect modelling on the selective laser melting (SLM) process with aluminium alloy 6061. *International Journal of Heat and Mass Transfer vol. 80*, pp. 288–300.
- [86] Lopez-Botello, O., U. Martinez-Hernandez, J. Ramirez, C. Pinna, and K. Mumtaz (2017). Two-dimensional simulation of grain structure growth within selective laser melted AA-2024. *Materials & Design vol. 113(5)*, pp. 369–376.
- [87] Ma, L. and H. Bin (2006). Temperature and stress analysis and simulation in fractal scanning based laser sintering. *The International Journal of Advanced Manufacturing Technology vol. 34, no. 9*, pp. 898–903.
- [88] Mercelis, P. and J.-P. Kruth (2006). Residual stresses in selective laser sintering and selective laser melting. *Rapid Prototyping Journal vol. 12, no. 5*, pp. 254–265.
- [89] Mertens, A., S. Reginster, H. Paydas, Q. Contrepois, T. Dormal, O. Lemaire, and J. Lecomte-Beckers (2014). Mechanical properties of alloy Ti-6Al-4V and of stainless steel 316L processed by selective laser melting: influence of out-of-equilibrium microstructures. *Powder Metallurgy vol. 57, no. 3*, pp. 184–189.
- [90] Mills, K. C. (2002). *Recommended values of thermophysical properties for selected commercial alloys*. Woodhead Publishing Limited.
- [91] Nedjar, B. (2002). An enthalpy-based finite element method for nonlinear heat problems involving phase change. *Computers and Structures vol. 80, no. 1*, pp. 9–21.
- [92] Nguyen, N. T., A. Ohta, K. Matsuoka, N. Suzuki, and Y. Maeda (1999). Analytical solution for transient temperature of semi-infinite body subjected to 3-D moving heat sources. *Welding research*, pp. 265–274.
- [93] Niendorf, T., S. Leuders, A. Riemer, H. A. Richard, T. Tröster, and D. Schwarze (2013). Highly anisotropic steel processed by selective laser melting. *Metallurgical and Materials Transactions B vol. 44, no. 4*, pp. 794–796.
- [94] Ning, Y., Y. S. Wong, and J. Y. H. Fuh (2004). Effect and control of hatch length on material properties in the direct metal laser sintering process. *Proc. Inst. Mech. Eng., Part B vol. 219, no. 1*, pp. 15–25.
- [95] Nour-Omid, B. (1984). Dynamic analysis of structures using Lanczos coordinates. *Earthquake Engineering and Structural Dynamics vol. 12*, pp. 565–577.
- [96] Nour-Omid, B. (1987). Lanczos method for heat conduction analysis. *Internal Journal for Numerical Methods in Engineering vol. 24*, pp. 251–262.

- [97] Paige, C. (1972). Computational variants of the Lanczos method for the eigenproblem. *Journal of the Institute for Mathematics and its Applications* vol. 10, pp. 373–381.
- [98] Papadakis, L., G. Branner, A. Schober, K.-H. Richter, and T. Uihlein (2012). Numerical modeling of heat effects during thermal manufacturing of aero engine components. In *Proceedings of the World Congress on Engineering*, Volume Vol III.
- [99] Parlett, B. and D. S. Scott (1979). The Lanczos algorithm with selective orthogonalization. *Mathematics of computation* vol. 33, no. 145(145), pp. 217–238.
- [100] Patil, R. B. and V. Yadava (2007). Finite element analysis of temperature distribution in single metallic powder layer during metal laser sintering. *International Journal of Machine Tools & Manufacture* vol. 47, no. 7-8, pp. 1069–1080.
- [101] Powar, S. B., P. M. Patane, and S. L. Deshmukh (2016). A review paper on numerical simulation of moving heat source. *International Journal of Current Engineering and Technology Special Issue 4*, 63–66.
- [102] Rappaz, M. (1989). Modelling of microstructure formation in solidification processes. *International Materials Reviews* vol. 34, no. 1, pp. 93–124.
- [103] Razvan, P. and P. Ancuta (2016). Applications of the selective laser melting technology in the industrial and medical fields. *New Trends in 3D Printing, Prof. Igor V Shishkovsky (Ed.), InTech*.
- [104] Riedlbauer, D., P. Steinmann, and J. Mergheim (2015). Thermomechanical simulation of the selective laser melting process for PA12 including volumetric shrinkage. In *AIP Conference Proceedings 1664*.
- [105] Roberts, I., C.J.Wang, R.Esterlein, M.Stanford, and D.J.Mynors (2009). A three-dimensional finite element analysis of the temperature field during laser melting of metal powders in additive layer manufacturing. *International Journal of Machine Tools and Manufacture* vol. 49, no. 12-13, pp. 916–923.
- [106] Roberts, I. A. (2012). *Investigation of residual stresses in the laser melting of metal powders in additive layer manufacturing*. Ph. D. thesis.
- [107] Rombouts, M. (2006). *Selective laser sintering/melting of iron-base*. Ph. D. thesis, Katholieke Universiteit Leuven.
- [108] Rombouts, M., J. Kruth, L. Froyen, and P. Mercelis (2006). Fundamentals of selective laser melting of alloyed steel powders. *CIRP Annals - Manufacturing Technology* vol. 55, no. 1, pp. 187–192.
- [109] Rosenthal, D. (1941). Mathematical theory of heat distribution during welding and cutting. *Welding Journal* vol. 20, no. 5, pp. 220–234.
- [110] Rudnyi, E. B. and J. G. Korvink (2004). Model order reduction for large scale engineering models developed in ANSYS. *Applied Parallel Computing. State of the Art in Scientific Computing*, pp. 349–356.

- [111] Saad, Y. (1994, June). *SPARSKIT: a basic tool kit for sparse matrix computations-Version 2*.
- [112] Samuel, H. H., P. Liu, A. Mokasdar, and L. Hou (2013). Additive manufacturing and its societal impact: a literature review. *The International Journal of Advanced Manufacturing Technology* vol. 67, no. 5, pp. 1191–1203.
- [113] Seabra, M., J. Azevedo, A. Araujo, L. Reis, E. Pinto, N. Alve, R. Santos, and J. P. Mortagua (2016). Selective laser melting (SLM) and topology optimization for lighter aerospace components. *Procedia Structural Integrity* vol. 1, pp. 289–296.
- [114] Shamsundar, N. and E. Sparrow (1975). Analysis of multidimensional conduction phase change via the enthalpy model. *Journal of Heat Transfer* vol. 97, no. 3, pp. 333–340.
- [115] Shiomi, M., K. Osakada, K. Nakamura, T. Yamashita, and F. Abe (2004). Residual stress within metallic model made by selective laser melting process. *Annals CIRP* vol. 53, no. 1, pp. 195–198.
- [116] Simon, H. (1984). The Lanczos algorithm with partial reorthogonalization. *Mathematics of computation* vol. 42, no. 165, pp. 115–142.
- [117] Slaats, P. M. A., J. de Jongh, and A. Sauren (1995). Model reduction tool for nonlinear structural dynamics. *Computers and structures* vol. 54, no. 6, pp. 1155–1171.
- [118] Song, B., S. Dong, S. Deng, H. Liao, and C. Coddet (2014). Microstructure and tensile properties of iron parts fabricated by selective laser melting. *Optics and Laser Technology* vol. 56, pp. 451–460.
- [119] Swaminathan, C. and V. Voller (1993). On the enthalpy method. *International Journal of Numerical Methods for Heat and Fluid Flow* vol. 3, no.3, pp. 233 – 244.
- [120] Tiso, P. (2011). Optimal second order reduction basis selection for nonlinear transient analysis. *Modal Analysis Topics* vol. 3, pp. 27–39.
- [121] Tolochko, N. K., M. K. Arshinov, A. V. Gusarov, V. I. Titov, T. Laoui, and L. Froyen (2003). Mechanisms of selective laser sintering and heat transfer in Ti powder. *Rapid Prototyping Journal* vol. 9, no. 5, pp. 314–326.
- [122] Tolochko, N. K., T. Laoui, Y. V. Khlopkov, S. E. Mozzharov, V. I. Titov, and M. B. Ignatiev (2000). Absorptance of powder materials suitable for laser sintering. *Rapid Prototyping Journal* vol. 6, no. 3, pp. 155–161.
- [123] Toyserkani, E., A. Khajepour, and S. Corbin (2004). 3-D finite element modeling of laser cladding by powder injection: effects of laser pulse shaping on the process. *Optics and Lasers in Engineering* vol. 41, no. 6, pp. 849–867.
- [124] Tseng, W. and J. Aoh (2014). Experimental validation of a laser heat source model for laser melting and laser cladding processes. *The Open Mechanical Engineering Journal* vol. 8, pp. 370–381.

- [125] Verhaeghe, F., T. Craeghs, J. Heulens, and L. Pandelaers (2009). A pragmatic model for selective laser melting with evaporation. *Acta Materialia* vol. 57, no.20, pp. 6006–6012.
- [126] Voller, V. R., M. Cross, and N. Markatos (1987). An enthalpy method for convection/diffusion phase change. *International Journal for Numerical Methods in Engineering* vol. 24, no. 1, pp. 271–284.
- [127] Vrancken, B. (2016). *Study of Residual Stresses in Selective Laser Melting*. Ph. D. thesis, KU Leuven-Faculty of Engineering Science.
- [128] Vrancken, B., L. Thijs, J.-P. Kruth, and J. V. Humbeeck (2014). Microstructure and mechanical properties of a novel β titanium metallic composite by selective laser melting. *Acta Materialia* vol. 68, pp. 150–158.
- [129] Wang, R.-J., L. Wang, L. Zhao, and Z. Liu (2007). Influence of process parameters on part shrinkage in SLS. *The International Journal of Advanced Manufacturing Technology* vol. 33, no. 5, pp. 498–504.
- [130] Weeger, O. (2015). *Isogeometric Finite Element Analysis of Nonlinear Structural Vibrations*. Ph. D. thesis, Technischen Universität Kaiserslautern.
- [131] Weeger, O., U. Wever, and B. Simeon (2014). Nonlinear frequency response analysis of structural vibrations. *Comput Mech* vol. 54, no. 6, pp. 1477–1495.
- [132] Weeger, O., U. Wever, and B. Simeon (2016). On the use of modal derivatives for nonlinear model order reduction. *International Journal for Numerical Methods in Engineering* vol. 108, no. 13, pp. 1579–1602.
- [133] Wilson, E. L., M.-W. Yuan, and J. M. Dickens (1982). Dynamic analysis by direct superposition of Ritz vectors. *Earthquake Engineering & Structural Dynamics* vol. 10, no. 6, pp. 813–821.
- [134] Withers, P. J. and H. Bhadeshia (2001). Residual stress Part 1- measurement techniques. *Materials Science and Technology* vol. 17, no. 4, pp. 355–365.
- [135] Wong, M., S. Tsopanos, C. J. Sutcliffe, and I. Owen (2007). Selective laser melting of heat transfer devices. *Rapid Prototyping Journal* vol. 13, no. 5, pp. 291–297.
- [136] Wu, L. and P. Tiso (2014). Modal derivatives based reduction method for finite deflections in floating frame. In *11th World Congress on Computational Mechanics (WCCM XI)*.
- [137] Wu, L. and P. Tiso (2016). Nonlinear model order reduction for flexible multibody dynamics: a modal derivatives approach. *Multibody System Dynamics* vol. 36, no. 4, pp. 405–425.
- [138] Xiao, B. and Y. Zhang (2006). Partial melting and resolidification of metal powder in selective laser sintering. *Journal of Thermophysics and Heat Transfer* vol. 20, no. 3, pp. 439–447.

- [139] Xiao, B. and Y. Zhang (2007a). Analysis of melting of alloy powder bed with constant heat flux. *International Journal of Heat and Mass Transfer* vol. 50, no. 11-12, pp. 2161–2169.
- [140] Xiao, B. and Y. Zhang (2007b). Marangoni and buoyancy effects on direct metal laser sintering with a moving laser beam. *Numerical Heat Transfer, Part A: Applications* vol. 51, no. 8, pp. 715–733.
- [141] Yadroitsev, I., A. Gusarov, I. Yadroitsava, and I. Smurov (2010). Single track formation in selective laser melting of metal powders. *Journal of Materials Processing Technology* vol. 210, no. 12, pp. 1624–1631.
- [142] Yap, C. Y., C. K. Chua, Z. L. Dong, Z. H. Liu, D. Q. Zhang, L. E. Loh, , and S. L. Sing (2015). Review of selective laser melting: Materials and applications. *AIP Publishing* vol. 2, no. 4.
- [143] Yilbas, B. S. and S. S. Akhtar (2011). Laser cutting of alloy steel: Three-dimensional modeling of temperature and stress fields. *Materials and Manufacturing Processes* vol. 26, no. 1, pp. 104–112.
- [144] Yin, J., H. Zhu, L. Ke, W. Lei, C. Dai, and D. Zuo (2012). Simulation of temperature distribution in single metallic powder layer for laser micro-sintering. *Computational Materials Science* vol. 53, no. 1, pp. 333–339.
- [145] Yuan, P. and D. Gu (2015). Molten pool behaviour and its physical mechanism during selective laser melting of TiC/AlSi10Mg nanocomposites: simulation and experiments. *Journal of Physics D: Applied Physics* vol. 48, no. 3.
- [146] Zäh, M. F. and S. Lutzmann (2010). Modelling and simulation of electron beam melting. *Production Engineering* vol. 4, no. 1, pp. 15–23.
- [147] Zeng, K., D. Pal, and B. Stucker (2012). A review of thermal analysis methods in laser sintering and selective laser melting. In *Solid Freeform Fabrication Symposium*.
- [148] Zhang, . L., D. Klemm, J. Eckert, Y. Hao, and T. Sercombe (2011). Manufacture by selective laser melting and mechanical behavior of a biomedical Ti-24Nb-4Zr-8Sn alloy. *Scripta Materialia* vol. 65, no. 1, pp. 21–24.
- [149] Zhang, D., Q. Cai, J. Liu, and d. Ruidi Li 1 (2010). A powder shrinkage model for describing real layer thickness during selective laser melting process. *Advanced Materials Research* vol. 97-101, pp. 3820–3823.
- [150] Zhang, Y., A. Faghiri, C. W. Buckley, and T. Bergman (2000). Three-dimensional sintering of two-component metal powders with stationary and moving laser beams. *Heat Transfer in Manufacturing* vol. 122, no. 1, pp. 150–158.
- [151] Zhang, Y. and A. Faghri (1999). Melting of a subcooled mixed powder bed with constant heat flux heating. *Int. J. Heat Mass Transfer* vol. 42, no. 5, pp. 775–788.